QUANTIFICATION OF SEISMIC REGIMES IN KANGRA-CHAMBA REGION OF HIMACHAL HIMALAYA

A THESIS

Submitted in partial fulfilment of the
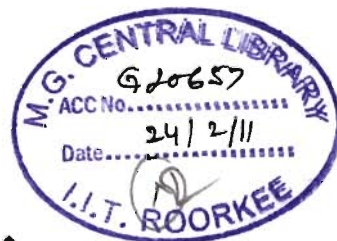*requirements for the award of the degree*
of
DOCTOR OF PHILOSOPHY
in
EARTH SCIENCES

by

NARESH KUMAR

DEPARTMENT OF EARTH SCIENCES
INDIAN INSTITUTE OF TECHNOLOGY ROORKEE
ROORKEE-247 667 (INDIA)
JUNE, 2010

INDIAN INSTITUTE OF TECHNOLOGY ROORKEE
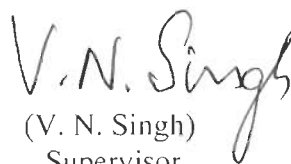## ROORKEE

CANDIDATE'S DECLARATION

I hereby certify that the work which is being presented in the thesis entitled **QUANTIFICATION OF SEISMIC REGIMES IN KANGRA-CHAMBA REGION OF HIMACHAL HIMALAYA** in partial fulfilment of the requirements for the award of the Degree of Doctor of Philosophy and submitted in the Department of Earth Sciences of the Indian Institute of Technology Roorkee, Roorkee is an authentic record of my own work carried out during a period from August, 2005 to June, 2010 under the supervision of Dr. S. Mukhopadhyay, Professor, Dr. V. N. Singh, Professor, Department of Earth Sciences, Indian Institute of Technology Roorkee, Roorkee and Dr. B. R. Arora, Professor and Emeritus Scientist, Wadia Institute of Himalayan Geology, Dehradun.

The matter presented in the thesis has not been submitted by me for the award of any other degree of this or any other Institute.

(NARESH KUMAR)

This is to certify that the above statement made by the candidate is correct to the best of our knowledge.

(B. R. Arora)	(V. N. Singh)	(S. Mukhopadhyay)
Supervisor	Supervisor	Supervisor

Date: June | 5, 2010

The Ph.D. Viva-Voice Examination of **Mr. NARESH KUMAR**, Research Scholar, has been held on _____

Signature of Supervisors   Signature of External Examiner

ABSTRACT

The Kangra-Chamba region of NW Himalaya is seismo-tectonically active and geologically one of the most complex region of the world. Fresh compilation of seismic catalogue of NW Himalaya reveals that though Kangra-Chamba region witnessed only one great earthquake (M8.0 Kangra earthquake of 1905) the region has been a zone of intense seismicity evidenced by clustering of epicenters and energy release irrespective of the duration and period of observation. A distinctive aspect of this part of the Himalaya is that the region is transgressed by the extended Chamba Nappe (CN). The weakly metamorphosed strata of the CN are similar in facies to the Tethys Himalaya (TH) and are considered to have resulted from southwestward sliding of the TH sediments from the north over the metamorphic Higher Himalayan Crystalline (HHC) along the south dipping Chenab Normal Fault (CNF) that separates the CN from the HHC. The Kistwar (KW) and Rampur (RW) windows are large antiformal folds to the NW and to the SE of the present study area. The present thesis describes the design, processing, results and interpretation of a special local seismic network undertaken to improve our understanding of the structures and seismotectonics of the region.

The high quality local earthquake data is first used to investigate the 1D and 3D variation of crustal velocity structure. The inversion of travel-time paths could resolve velocity structure for the upper 20 km or so as > 85% earthquakes are confined to depth less than 20 km of the upper crust. Therefore, the determination of the thickness and velocity up to Moho and upper mantle were supplemented independently by travel-time-distance plot using data of regional seismic networks and scanning epicentral distances up to 550 km. The minimum 1-D velocity model divides the average 44 km thick crust into four layers. The top ~10 km thick layer represents the metamorphosed sediments of the CN that dominates the surface geology of the study area in the central part. A thin low velocity layer at 15 km depth, after allowing for the station corrections, portrays the geometry of the detachment zone separating the down-going Indian plate from the overriding wedge. In addition to the expected relative high station corrections over the Siwalik, the single most anomalous feature indicates unambiguous presence of a structural discontinuity in the southeast corner striking NE-SW.

While inverting the data for 3D crustal structure investigation using Local Earthquake Tomography (LET), a systematic and significant variation up to 14% in Vp and Vs along with up to 6% in the Vp/Vs ratio has been observed across the major

tectonic units. The low velocity perturbations (LVP) largely overlap with known exposure of the Siwalik and Lesser Himalaya, while relative high velocity area correspond to metamorphosed sedimentary sequence of TH and thus helps to map the spatial extent of the CN at different depths. It is clearly seen that the southward extent of the CN on the western part of the study area is limited by the Chamba Thrust (CT) whereas on the eastern part the CN extends right up to the Panjal Thrust/Main Boundary Thrust (PT/MBT). This varying limit of southward extension of the CN helps to resolve the long standing structural puzzle that the CT bordering the Chail formation to the north is well marked west of Chamba whereas this contact is not traced east of Chamba. Another distinctive feature of velocity tomograms is a narrow NE-SW aligned LVP in the eastern part, confined to depth interval of 2 to 5 km and is underlain by a high velocity zone in tomograms at 10 km depth. The presence of a structural discontinuity striking NE-SW is coincident with the sharp terminus of positive station delays. The distribution of hypocenters in specific depth intervals clearly depict that most of the hypocenters are concentrated at the boundary between low-high velocity couplets correlating with crustal heterogeneity. Since such linkages are better developed and outlined in Vs tomograms, part velocity variability may reflect rheological changes associated with varying degree of saturation.

As an independent mode to constrain the seismotectonic model, the fault plane solutions (FPS) of 42 well located events (RMS value of <0.1s and M>2.5) are computed and analysed. The complex tectonic setting of the sector is immediately evident from the fact that three dominant focal mechanisms noted are: (1) thrust fault mechanism with strike slip component, (2) strike slip movement with thrust component and (3) normal fault motion with strike slip component. The FPSs of the past earthquakes located at detachment highlight the dominance of the thrust environment of the region on a broad tectonic scale. The earthquakes occurring along the shallow sections of the MBT and PT are characterized by thrust mechanisms with varying component of strike slip movement. The decreasing dip of the nodal planes with increasing depths on these thrusts favor the tectonic hypothesis that steeply dipping thrusts near the surface flatten out at depth to merge with the detachment plane zone marking top of the down-going Indian Plate. The normal fault mechanism along the plane which is seen as a subsurface extension of the CNF is consistent with the tectonic model which postulates NE-SW directed extensional tectonics responsible for the southward displacement of the CN along the normal fault. Earthquakes located beneath

the detachment zone in a localized cluster northeast of the epicenter of the Kangra earthquake are dominated by normal fault mechanism or the NE-SW directed structural discontinuity.

The source parameters of the earthquakes are obtained using Brune's circular model through the corrected amplitude spectra based on geometrical spreading and site effect. For these earthquakes the determined corner frequency of the spectrum is in the range 1 to 10 Hz. The seismic moment and source radius of these events is $7.0 \times 10^{17} < M_0 < 7.0 \times 10^{22}$ dyne-cm and between 0.1 to 1.2 km respectively with larger values for higher magnitude earthquakes. The specified relation of Brune is used to convert the seismic moment into moment magnitude (M_w). The linear regression analysis is performed to obtain relations between M_w and the local magnitude M_L as well as coda magnitude M_C. The empirical linear relation shows that the variation in M_L is equal to 0.70 times change in the value of M_w whereas, this change in M_C is 0.86 times relative to M_w. The obtained stress drop has a different characteristic for micro-earthquakes compared to bigger size events. The maximum stress drop is 27 bar with a majority in the range 0.1 bar to 10 bar showing increase in value with the earthquake size. The low stress drop near the plate boundary is related to high levels of earthquake activity with typically weak fault rheology.

This work is among the first studies to provide both spatial and temporal analysis of seismic data for quantification of seismic regime in Kangra-Chamba region of Himachal Himalaya. Given the shallow character of seismicity, the limitation of not imaging the velocity structures for full thickness of the crust can be circumvented by the application of global tomography using receiver function approach. Further, given the significance of imaging the true character and geometry of the BTF, both in the tectonic evolution and seismicity in the Himalayan collision zone, active seismic and high resolution broadband magneto-telluric surveys would be timely and rewarding.

ACKNOWLEDGEMENTS

Extra special thanks go to the Director, the Abdus Salam International Centre of Theoretical Physics (ICTP), Trieste, Italy. It is impossible to exaggerate the amount of assistance I have from ICTP for my research work. I owe a great vote of thanks to Dr. Imtiyaz A. Parvez, Scientist, CSIR, Center for Mathematical Modelling and Computer Simulation (CMMACS), Banglore, India who has always been available to discuss the finer points of seismology and geophysics related to Indian continent.

I would like to express my sincere gratitude to Dr. V. M. Choubey, Head Geophysics Group, WIHG, Dehradun, India for his continuous inspirations, motivations, valuable suggestions and to allow me to avail the facilities of the Geophysics Group to carry out this research work. I always enjoy scientific discussion with him.

I would like to thank my best friends and companions of my Geophysics Group, in no particular order, Mr. Guatam Rawat, Mr. P. R. K. Gautam, Drs. D. K. Yadav, Devajit Hazarika, A. K. Mahajan, A. K. Mundepi, Ajay Paul, V. Sriram, Sushil Kumar, Rajesh S and Mr. D. D. Khandelwal. I also like to thanks my colleagues, namely, Drs. Pradeep Srivatava, B. K. Mukherjee, Narendra Meena and S. S. Thakur for memorable discussions on geological aspects and suggestions. Thanks to all those who helped with the field work of START 2004 experiment along with seismic data collection, retrieval and analysis. Special appreciation goes to Mr. Chandan Bora and Dr. D. K. Yadav.

At this moment, it is a great pleasure for me to acknowledge the immense help and encouragement rendered by my friends at IIT Roorkee, especially Dr. Krishna Kumar and Dr. Ramesh. I want to express thanks to Mr. Birinder Singh, Mr. Sabyasachi Dash and Mr. Bhupendra Bahadur Singh who helped me to wind this work in the present form of Thesis.

My vocabulary utterly fails in expressing my accolade to my parents, **Shri. Dina Nath Diwan** and **Smt. Satya Devi,** because of whom I am what I am today. My regards go to each and every family member for their trust and love for me. Last but not least, my deepest gratitude goes to my wife, Smt. Anjna Kumari, son, Anish and daughter, Anusha for their unflagging love and support; this thesis would have been simply impossible without them.

(NARESH KUMAR)

LIST OF PUBLICATIONS

1. Shashidhar, D., **Kumar N.**, Mallika, K., and H. K. Gupta (2010). Characterstics of Seismicity Pattern prior to the M ~ 5 Earthquakes in the Koyna Region, Western India – Application of the RTL Algorithm. **Episodes** (Accepted)

2. Mukhopadhyay, S., Sharma, J., Del-Pezzo, E. and **Kumar N.** (2010). Study of attenuation mechanism for Garhwal-Kumaon Himalayas from analysis of coda of local earthquakes. **Physic. Earth. Planet. Inter.**, 180, pp. 7-15.

3. **Kumar N.**, Sharma, J., Arora, B. R., and S., Mukhopadhyay (2009) Seismotectonic model of the Kangra-Chamba sector of NW Himalaya: Constraints from joint hypocenter determination and focal mechanism. **Bull. Seismol. Soc. Amer.** Vol. 99(1), pp. 95-109 February 2009, doi: 10.1785 0120080220.

4. Choubey V. M., **Kumar N.**, and B. R., Arora (2009). Precursory signatures in the radon and geohydrological borehole data for M4.9 Kharsali earthquake of Garhwal Himalaya. **Science Tot. Environ.**, 407, pp. 5877-5883.

5. Yadav, D. K., **Kumar N.**, A., Paul (2009). Recent Seismicity and Stress pattern in NW Himalaya. **Him. Goelogy**, Vol 30(2), pp. 139-145.

6. Arora, B. R., **Kumar N.**, Rawat, G., and A., Paul (2008). A Peep into the Himalayan Seismicity. **Mem. Geol. Soc. Ind.**, 72, 29-46.

7. Arora, B. R., Kamal, Kumar, A., Rawat, G., **Kumar N.**, and V. M., Choubey (2008) First Observations of Free Oscillations of the Earth (FOE) from Indian Superconducting Gravimeter in Himalaya. **Current. Sci.**, 2008, **95**(11) pp. 1611-1617

8. Gitis, V., Yurkov, E., Arora, B., Chabak, S., **Kumar N.**, and P., Baidya (2008). Analysis of seismicity in North India. **Russian Jour. of Earth Science**, 2008 (10), ES5002, doi:10.2205/2008ES000303.

9. Mahajan, A. K, **Kumar N.**, and B. R., Arora, (2006). Quick look isoseismal map of 8 October 2005 Kashmir earthquake. **Current Science,** 91(3), pp 356-361.

10. **Kumar N.,** Sharma J., Arora B.R., and S., Mukhopadhyay (2006). Imaging deep structure through the inversion of earthquake data: An example from Kangra-Chamba Region of Himachal Himalaya. **DST, DSC News Letter**, 2006, 16(1), pp 7-10.

11. **Kumar N.**, Imtiyaz, A., and H. S., Virk (2005). Estimation of coda wave attenuation for NW Himalaya region using local earthquakes. **Physic. Earth Planet. Inter.**, 151, pp 243-258.

LIST OF ABBREVIATIONS

Abbreviation	Meant for
1D/1-D	One Dimensional
3D	Three Dimensional
ART	Algebraic Reconstruction Technique
BTF	Basement Thrust Fault
BVP	Boundary Value Problem
CMT	Centroid Moment Tensor
CN	Chamba nappe
CNF	Chenab Normal Fault
CRT	Checkerboard Resolution Test
CSIO	Central Scientific Instruments Organisation
CT	Chamba Thrust
DWS	Derivative Weight Sum
FM	Focal Mechanism
FMSI	Focal Mechanism Solution Inversion
FPS	Fault Plane Solution
GPS	Global Positioning System
GSI	Geological Survey of India
HFT	Himalayan Frontal Thrust
HH	Higher Himalaya
HHC/GHC	Higher/Greater Himalayan Crystalline
HSB	Himalayan Seismic Belt
HVZ	High Velocity Zone
IMD	Indian Meteorological Department
INDEPTH	International DEep Profiling of Tibet and Himalaya
ISC	International Seismological Center
ISZ	Indus Suture Zone
ITSZ	Indus-Tsangpo Suture Zone
IVP	Initial Value Problem
JHD	Joint Hypocenter Determination
KW	Kistwar Window
LET	Local Earthquake Tomography
LH	Lesser (Lower) Himalaya
LTA	Long Term Average
LVL	Low Velocity Layer
LVP	Low Velocity Perturbations
LVZ	Low Velocity Zone
MBT	Main Boundary Thrust
MCT	Main Central Thrust
MHSB	Main Himalayan Seismic Belt
MMI	Modified Mercalli Intensity
MSL	Mean Sea Level
PIZ	Panjal Imbricate Zone
PMT	Palampur Thrust
Rb-Sr	Rubidium-Strontium
RMS	Root Mean Square
RRT	Restoring Resolution Test

RW	Rampur Window
S/N	Signal-to-Noise Ratio
SAM	Signal Acquisition Module
SEISAN	SEISmic ANalysis
SH	Shiwalik Himalaya
STA	Short Term Average
STDS	Southern Tibet Detachment System
THS	Tethyan (Tibetan) Himalayan Sequence
USGS	United States Geological Society
UTC	Universal Time Coordinate
WIHG	Wadia Institute of Himalayan Geology
WWSSN	World Wide Seismic Standard Network
ZSZ	Zanskar Shear Zone

LIST OF SYMBOLS

Symbols	Meaning
$\Delta\sigma$	Change in stress drop
a, b	Parameters of G-R Relationship.
A_{max}	Maximum ground displacement amplitude
$C(\Delta)$	Distance correction factor
C_r	Regional Source correction factor
C_s	Site effect correction factor
db	Decibel
DIM(f)	Diminution function due to anelastic attenuation
GI	Geometrical spreading corrections
I	Incidence angle
M	Magnitude
M_0	Seismic moment
M_b	Body wave magnitude
M_d	Coda duration magnitude
M_L	Local Magnitude
M_s	Surface wave magnitude
M_w	Moment magnitude
Q	Quality factor
Q(f)	Coda wave quality factor for frequency f
S(f)	Amplitude source spectrum
β	Shear wave velocity
δ	Dip of the fault
λ	Rake
ρ	Average density
σ	Stress Drop
τ	Dimension of the fault
Ω	Amplitude
ω	Angular frequency
Φ	Azimuth angle
γ	Asymptotic high frequency spectral decay exponent
μ	Modulus of rigidity
f_0	Corner frequency
Ω_0	Low frequency level

LIST OF TABLES

moment, Mw – moment magnitude, Lati. – Latitude, Long. – Longitude, f_0 – corner frequency, SR – source radius, SD – stress drop.

LIST OF FIGURES

MSL stands for Mean sea level.

the principle stress axes (after Anderson, 1951, and Zoback, 1992)

duration magnitude of Kangra-Chamba region.

TABLE OF CONTENTS

CHAPTER 1

INTRODUCTION

1.1. INTRODUCTION

The 2500 km long Himalayan arc (**Figure 1.1**) is about 250 km wide and extends from Kashmir in the west (longitude 74°E) to Arunachal Pradesh in the east (longitude 93°E). The Himalaya contains spectacular mountain ranges along the northern margin of India and was formed due to collision of the Indian and Asian (**Figure 1.2a**) landmasses around 50 m.y. ago (Gansser, 1964; Le Pichon, 1968; Mc Kenzie and Scalter, 1971; Le Fort, 1975; Mitchell, 1981; Curray *et al.*, 1982; Molnar and Lyon-Caen, 1988). It has been reported by several investigations (Seeber and Armbruster, 1981; Baranowski *et al.*, 1984; Ni and Barazangi, 1984; Molnar, 1990; Hauck *et al.*, 1998) that India is under-thrusting Asia along a gently northward dipping plane called the detachment plane and the many thrust planes observed in the Himalaya (e.g., Main Central Thrust, Main Boundary Thrust, Himalayan Frontal Thrust) are splay branches of this thrust plane and one produced due to continent-continent collision, the convergence process shown in **Figure 1.3**. Movement along these thrust planes and other subsidiary faults cause high seismic activity in the Himalaya. The reason of high seismic activity in the Himalaya, the convergence tectonics and the thrusting of the Indian sub-continent along the detachment was explained by Seeber and Armbruster, (1981), based on the information of big sized earthquakes, in terms of a steady state model. This model suggests that the detachment surface under-thrusting Himalayan front within crust under the great Himalaya is the locale of the recent seismic activity. The concentration of the small magnitude earthquakes is also high along this zone. Continuous improvements in earthquake monitoring network shows clear segmentation of seismicity along the Himalayan arc with well-defined segments of intense/low seismicity (Srivastava *et al.*, 1987; Gaur *et al.*, 1985; Kumar *et al.*, 2009), seismic gaps (Khattri and Tyagi, 1983) or tectonically stable zones (Kayal, 2001, 2003). Such space-time segmentations of earthquake activity signify complexities of the tectonic setting and crustal structures controlling strain accumulation/release that may be responsible for varied earthquake mechanisms in different parts of the Himalaya (Pandey *et al.*, 1995; Bollinger *et al.*, 2004). Thus the Main Himalayan Seismic Belt (MHSB) is described as

1

an approximately 50 km N-S extended zone between Main Central Thrust (MCT) and Main Boundary Thrust (MBT) that is intersected by transverse features dividing this belt into discrete blocks of similar seismic behavior. Records (Chandra, 1992) of about last 120 years shows that the Himalayan region has experienced four great earthquakes, e.g., the 1897 Shillong (M8.7). The 1905 Kangra (M8.0), the 1934 Bihar (M8.4) and the 1950 Assam (M8.7) earthquakes, the location of these earthquakes are shown in **Figure 1.1a**. These earthquakes have ruptured a wide area around their epicenters suggesting that whole Himalayan region is vulnerable for seismic hazard. Hence, there is urgent need to investigate different parts of the Himalaya using multi-disciplinary seismological studies for seismic hazard mitigation. In this study, I applied different methodologies to quantify the highly active seismic regime of Kangra-Chamba region of the Himachal Himalaya which is the meizoseismal area of the great 1905 Kangra earthquake. The present work includes the investigation of historical and recent ongoing seismic activity, imaging the crustal structure and subsurface features and quantifying the earthquake source processes.

The Kangra-Chamba region in NW Himalaya, the center of devastating 1905 great Kangra earthquake (M8.0), falls in the risk zone V on the seismic zoning map of India (http://www.gsi.gov.in/zonation.htm). Geo-tectonically also the Kangra-Chamba region exhibits certain distinctive characters and is dominated by Nappes and Windows and is well marked by highly undulating topography. The lack of good regional velocity model coupled with limited azimuthal distribution of seismological stations, particularly north of the high seismicity zone, restrict the robust determination of the hypocenters and, thus, inhibit detailed insight into the tectonic setting associated with localized zone of high seismicity. To generate area specific seismic velocity model and improvement in earthquake location for better understanding of seismicity and seismotectonics of the Kangra-Chamba segment of the NW Himalaya (Kumar *et al.*, 2006, 2009, Arora *et al.*, 2008), a special experiment with an array of closely spaced seismometers was started in April 2004. This thesis discusses and presents the various aspects of the experiment, starting from the basic rationale, distinctive tectonic setting, design and upgradation of seismic network, data acquisition and application of more advanced processing tools to derive local velocity models, robust determination of hypocenters and their bearing on the tectonic interpretation to evaluate the seismotectonic model for the Kangra-Chamba region.
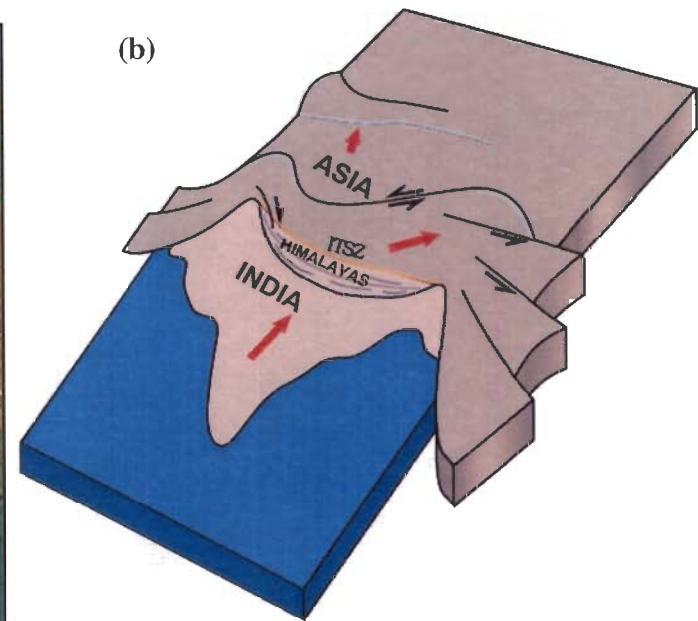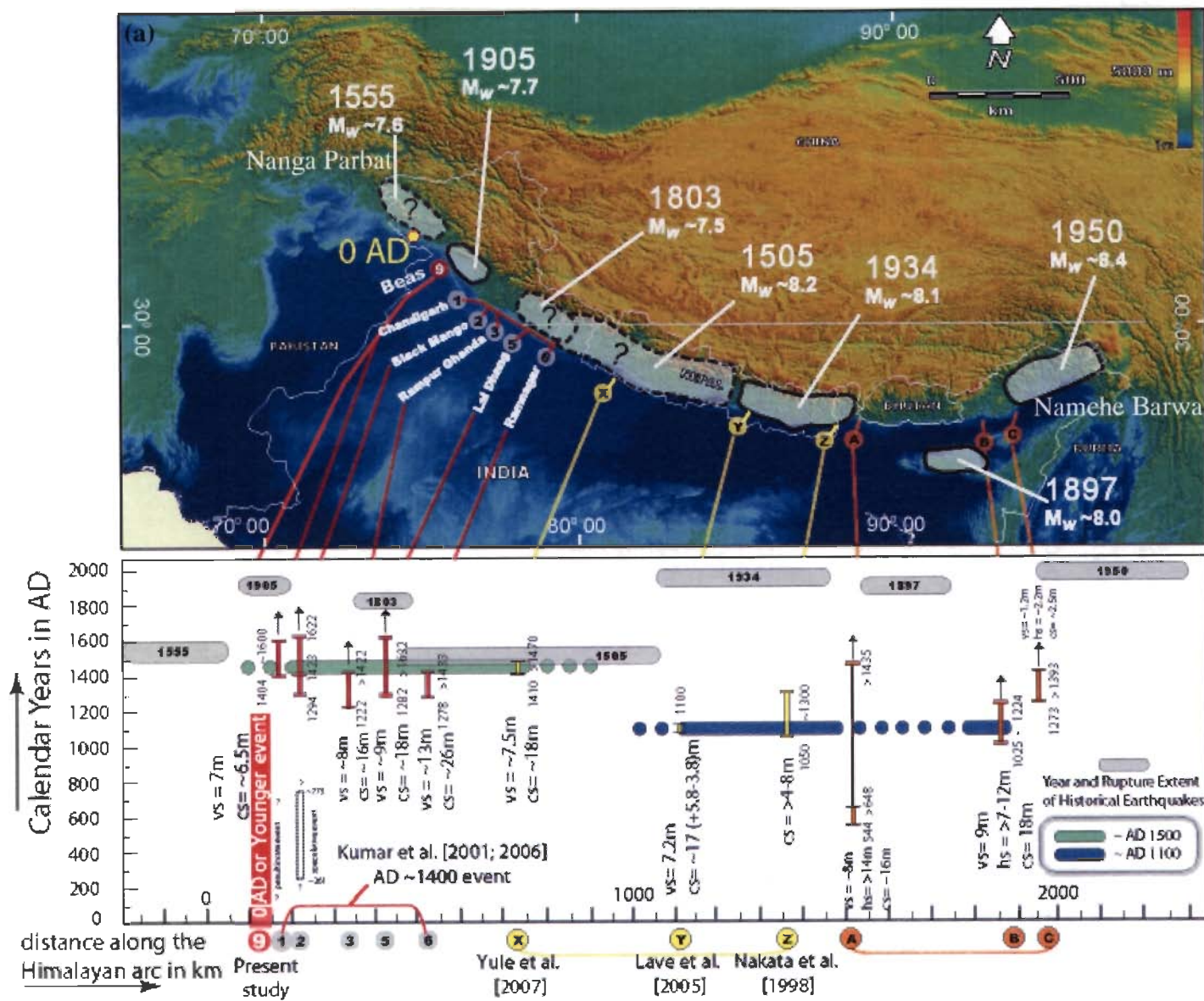
Figure 1.1: (a) Map showing rupture region in the Himalaya for large magnitude earthquakes. Question mark indicates that the exact extents of meizoseismal for some earthquake are not shown after (Kumar *et al.*, 2010). Lower panel shows the amount of slip due to large magnitude earthquakes since 0 AD. (b) Schematic representation of India-Asia Collision (after Auvoc, 2003).

3

Seismically the study area falls in zone V where plenty of moderate magnitude earthquakes occur and the concentration of micro-earthquake activity is always high. This trend of micro- to moderate size earthquake is prevalent throughout the Himalayan belt occurring in the upper crust beneath the topographic front of the Higher Himalaya. Most of these moderate-magnitude earthquakes occur at shallower depth (10-20 km), above the "plane of detachment" (Seeber *et al.*, 1981; Ni and Barazangi, 1984; Kayal, 2001; Kumar *et al.*, 2005; Kumar *et al.*, 2009). The Indian plate is under-thrusting the Eurasian plate along a low-angle (~5°-15° dip) thrust plane called the detachment plane (Molnar *et al.*, 1977; Seeber *et al.*, 1981; Ni and Barazangi, 1984; Molnar, 1988). It is suggested that below MCT lies the basement thrust front (ramp), the transition zone between the plane of detachment and the basement thrust, which acts as a geometrical asperity for stress concentration (Pandey *et al.*, 1995). The interface between the down going Indian plate and overriding Tethyan slab is described as basement thrust (Bhattacharya and Kayal, 2005). These aspects are studied and investigated based on a designed experiment of a dense seismic network in one of the most seismically active regions of the Himalaya, viz., Kangra-Chamba region of NW Himalaya. This small portion in the central part of NW Himalaya is highly deformed containing a variety of active tectonic features where high concentration of seismic activity can be found in any period of observation.

I have first of all reviewed few aspects of the northwest Himalayan tectonics along with historical and recent seismic aspects in Chapter 2 having relevance with present study. The review of historical along with recent seismicity in the NW Himalaya indicates a high concentration of seismic activity in the Kangra-Chamba region that can be observed at any period of study. The recent seismic network in the study region and its importance is discussed in Chapter 3 highlighting the new findings in the region. The highly accurate micro-earthquakes data obtained through a dense seismic network are utilized to obtain 1D velocity model and refinement of the earthquake source locations. In Chapter 4, the same data set is used for local earthquake tomography to obtain 3D velocity structures and further refinement of the earthquake locations. Then this refined data is utilized for characterizing the seismic regime of study region through fault plane solutions, earthquake source parameters and stress pattern in Chapters 5 and 6 respectively. The combined interpretation of the whole work is given in Chapter 7 with suggestion for future work.

1.2. REGIONAL GEOLOGICAL SETUP

The collision between India and Eurasia continents produced the complex structures and lithology existing presently in the Himalayan region (**Figure 1.2**). In this continent-continent convergence tectonics, the Indian tectonic plate is moving to NNE and under-thrusting the SSW moving Eurasian tectonic plate. The highly deformed and geologically complex Himalayan ranges are the elevated region striking in eastwest direction and lies between eastern and western syntaxes known as Namche Barwa and Nanga Parbat respectively (**Figure 1.2b**). To the west of the Himalaya, adjoining to Nanga Parbat, the Hindu Kush Mountains exist while to the eastern side of the Namche Barwa are the Indo-Burma ranges. The Karakoram Mountains and the Tibetan Plateau are situated in the north while the Indo-Gangetic planes are in the south. According to Gansser (1964), the southern boundary of the Himalaya has a high contrast making a sudden change between the strata of Indian Shield and the Himalayan ranges (**Figure 1.2b**). Just to the south of the Himalaya lies the foredeep region that contains the alluvial covered low lands of Indus, Ganges and Brahmaputra river basins.

In the continent-continent convergence tectonics, a series of continuous thrusts (**Figure 1.3**) have developed that divide Himalayan arc into four tectonically distinct and stratigraphically contrasted nearly east-west extended parallel lithotectonic zones (**Figure 1.2b**). These zones are Tethyan (Tibetan) Himalayan Sequence (THS), Higher (Greater) Himalaya Crystalline (HHC), Lesser (Lower) Himalaya (LH) Sequence and Siwalik (Sub-) Himalaya (SH) Sequence. To the north of these units, the Indus Suture Zone (ISZ) and Trans-Himalayan batholiths exist that separate the Himalaya from the Eurasian belt. These litho-tectonic units are separated by major thrust planes dipping to north or north-east. These units are prevalent throughout the Himalayan region, however their dimensions are not same and many longitudinal inequalities exist along the Himalayan arc. The dimensions as well as composition of these lithotectonic units change along the trend of the Himalaya, however at a very slow rate. The brief geological description of different units is as follow:

Trans-Himalayan Batholith: It is a plutonic complex that is partly covered by forearc rocks and continental molasses sedimentary rocks. It was formed due to partial melting of a subducting Neo-Tethyan slab beneath the Asian plate (Sorkhabi et al., 1999). The existing geological composition was derived from the uplifted magmatic rocks and their subsequent erosion due to tectonic deformation. It represents as island arc environment in the western Himalaya (**Figure 1.2a**) formed on

5
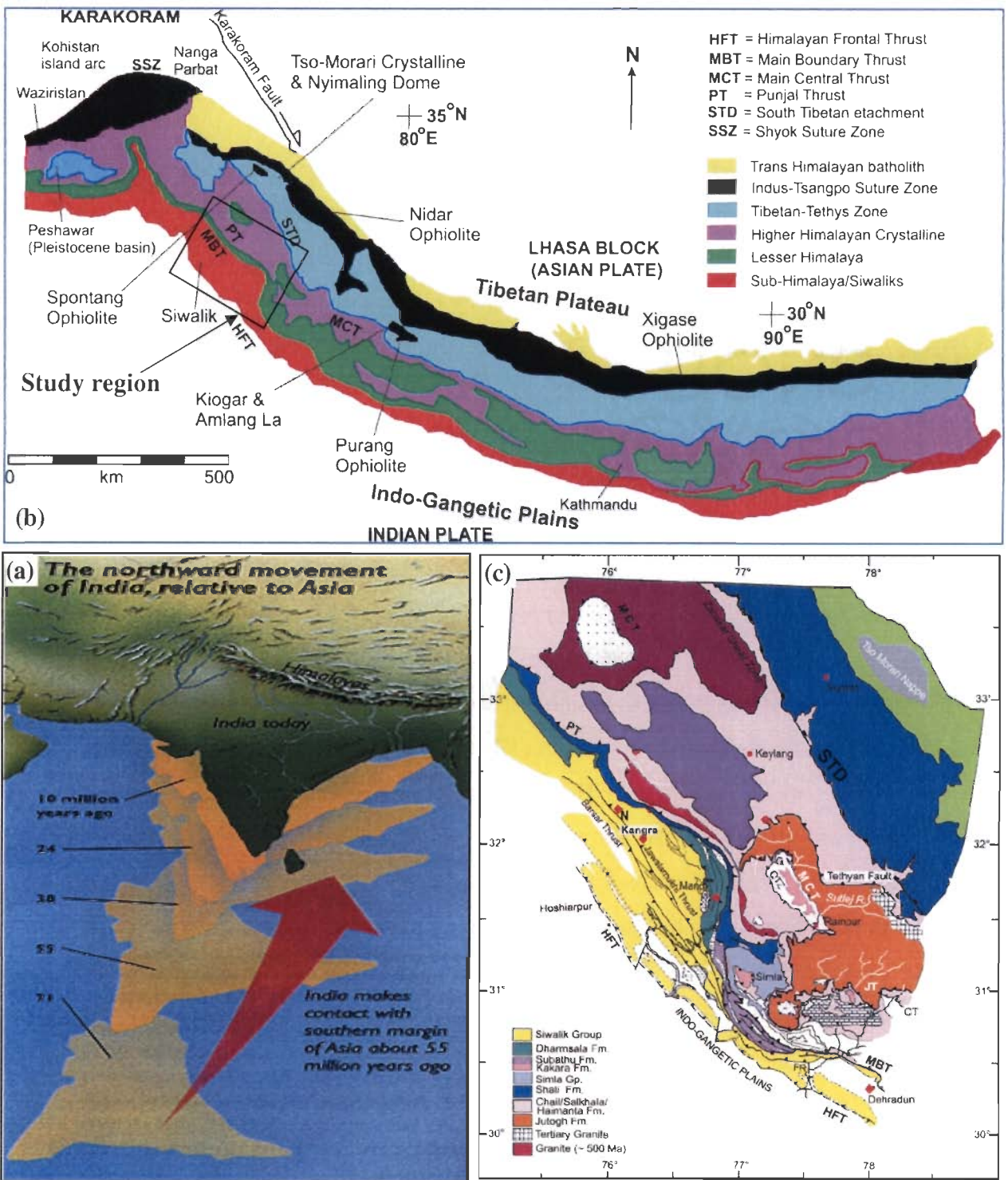
Figure 1.2: The geotectonics of the Himalaya produced by India-Eurasia continent-continent collision (a) the relative position of Indian continent with Asia, the direction of Indian continent movement and the concept of Himalayan formation (b) the geo-tectonic subdivision of Himalaya (after Corfield *et al.*, 2001) (c) the geotectonic subdivision of Kangra-Chamba region and adjoining regions of NW Himalaya (after Thakur, 1998).

the northern side of the Neo-Tethys and became trapped in between Asia and India (Windley, 1995).

Indus Tsangpo-Suture Zone: The areas of collision between Indian and Asian plates are described as Indus-Tsangpo Suture Zone (ITSZ) where the Tethys Ocean was consumed by subduction processes (Windley, 1995). This zone hosts a variety of rock types describing the orogen of Himalaya such as complete successions of ophiolites suggesting high pressure during subduction and rapid extrusion. The Spongtang Ophiolite in the Ladakh Himalaya consists of a thrust sheet of upper mantle and oceanic crustal rocks obducted onto the northern passive continental margin of India during the Late Cretaceous (Pedersen et al., 2001). A wide variety of rock types along this zone indicates that the collision of plate boundaries was complex.

Tethyan Himalayan Sequence: Tectonically the Tethys Himalaya is resting over Precambrian Higher Himalayan Crystalline (HHC); the boundary of these two units is marked by Tethyan Tectonic Thrust as the basement of Tethys Himalaya. This zone comprises over 10 km thick sequence of sedimentary rocks which are predominantly fossiliferous ranging from Late Precambrian to Cretaceous and even Eocene age group (Sinha, 1989). The sedimentary rocks are also inter-beded with Paleozoic and Mesozoic volcanic rocks (Garzanti, 1999; Brookfield, 1993; Steck *et al.*, 1993; Critelli and Garzanti, 1994). In the NW Himalaya, the post-lower Cambrian stratigraphic break related to the Pan-African orogeny is also recorded. Using Rb-Sr dating, Miller *et al.* (2001) has dated mylonitic orthogenesis unit (Baragaon gneiss) ~ 1840 Ma in the Kullu-Larji-Rampur Window that is the basement of Tethyan Himalayan sequence (THS). However, its lithostratigraphy changes both along and perpendicular to the Himalayan orogen (Brookfield, 1993).

Higher or Greater Himalayan crystalline (HHC): The Higher or Greater Himalayan crystalline lie on the Lesser Himalayan sequence as a thrust sheet and is also described as Central Crystalline zone. It generally consists of Paleoproterozoic to Ordovician (1800 - 480 Ma) high grade and deformed metamorphic rocks that forms a continuous belt south of THS and marks the existence of orogenic uplift. The thrusting of HHC started around 23 - 20 Ma with the development of Main Central Thrust (Hubbard and Harrison, 1989) bringing higher Himalaya on top of lower Himalaya. The HHC also exist as isolated patches in the Zanskar and Tso-Morari strata of NW Himalaya where it is surrounded by THS (Honegger *et al.*, 1982; Steck *et al.*, 1998; DiPietro and Pogue, 2004). The occurrence of major thrust fault within this zone and

convergence ad caused a shortening of about 600 to 650 km here in which the part of Indian plate shortened to form the Greater Himalaya.

Lesser Himalaya Sequence (LHS): The rocks of LHS consist of Precambrian-Lower Paleozoic and Tertiary sediments and low grade meta-sediments with volcanic and granitic components. These are the non-fosssiliferous low-grade metasedimentary rocks (Gansser, 1964; LeFort, 1975) which are overlain by Permian to Cretaceous Sequence (Gansser, 1964). Lithologically, the metasedimentary rocks, metavolcanic rocks and augen gneiss are in the age group of 1870-850 Ma (Yin, 2006). These are primarily sedimentary rocks from the Indian platform and these rock units also show a series of anticlines and synclines. This belt is very narrow in the western Himalaya including the present study region.
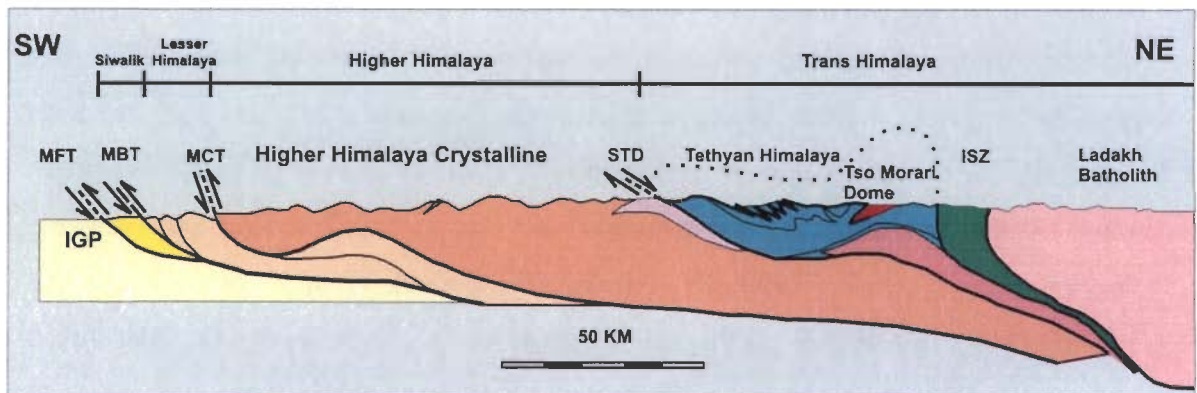
Figure 1.3: The continent-continent convergence mechanism. The convergence tectonics due to the collision of two tectonic plates such as India and Asia (after Dezes 1999)

Sub or Outer Himalaya Sequence: The Outer or Siwalik Himalaya comprises the low altitude Siwalik Hills with flat-floored structural valleys consisting of about 9500 m thick Cenozoic sedimentary pile characterized by folds and faults (Thakur, 1992). The Sub-Himalayan basin has the composition of eroded and denudated thick deposition of terrigeneous sequence of Miocene age produced by the uplift and subsequent erosion of the Himalaya deposited by rivers. It consists of Neogene Siwalik and Paleogene-early Miocene strata (Yin, 2006). It comprises of Siwalik Molasse conglomerates that extend southwards up to the Gangetic basin. The sedimentary basin of Sub-Himalaya has good prospect of petroleum. In contrast to LHS, the sub-Himalaya is wide in the western Himalaya.

Active Himalayan foreland basin: The region south of the Outer Himalaya also called Indo-Gangetic plains is the foredeep depression where the sediments exported from the Himalaya through Indo-Gangetic Rivers are deposited. These sediments reside on the Indian Plate and have a thickness of about 4-5 km. The basement is not flat and has irregular topography with several ridges in the Peninsular India lying transverse to the trend of the Himalaya. These ridges control Cenozoic sedimentation and are locally associated with seismicity. The Delhi-Muzaffarnagar ridge divides the drainage between Indus and Ganges rivers in NW India. This ridges influences tectonics and seismicity perpendicular to Himalayan pattern and has an impact on variation of these two factors along the strike of the Himalayan ranges (Johnson, 1994; Pandey et al., 1999; Avouc, 2003).

These different geological units show differences in their geographical, stratigraphical and structural characteristics. In addition to these major subdivisions, the Himalaya are highly deformed and folded belt due to which many regional scale nappes and windows are also present. In addition of these major eastwest extended geological units also show variation in width along the strike of the Himalaya. For example, the portion of LH sequences is very narrow in the Himachal Himalaya compared to the Garhwal Himalaya that lie to its east. However the other sequences are comparatively wider (**Figure 1.2b**). On the other hand, the SH sequences is wide in the Himachal Himalaya and narrow in the Garwhal Himalaya.

The study region covers the Himalayan mountains ranges between the Indus River in the west and the Satluj River in the east, mostly the part comes in the Himachal Himalaya. The geological and tectonic setup of this region (**Figure 1.2c**) was given in detail by Thakur (1992, 1998), Steck (2003) and Yin (2006). The region to the north of the MBT is mainly covered with Kashmir and Chamba Nappes, the units contain rocks that have moved from the north over the HHC through topographic uplift. These contain the thick sequences (~ 8 km thick Chamba nappe, Thakur, 1998) of Late Precambrian to Jurassic age rocks. These occur between HHC and LH formation and to the south the LH formations is a very narrow zone (few km) described as Panjal Imbricate Zone (PIZ) that is bound in the south by Cenozoic belt of Siwalik Himalaya. In this region the Kistwar and Rampur windows reveal orthoquartzite, volcanic and carbonate rocks and granitic gneiss of Proterozoic age (Thakur, 1998). These windows contain the LH formations that are surrounded by medium grade metamorphics of HHC.
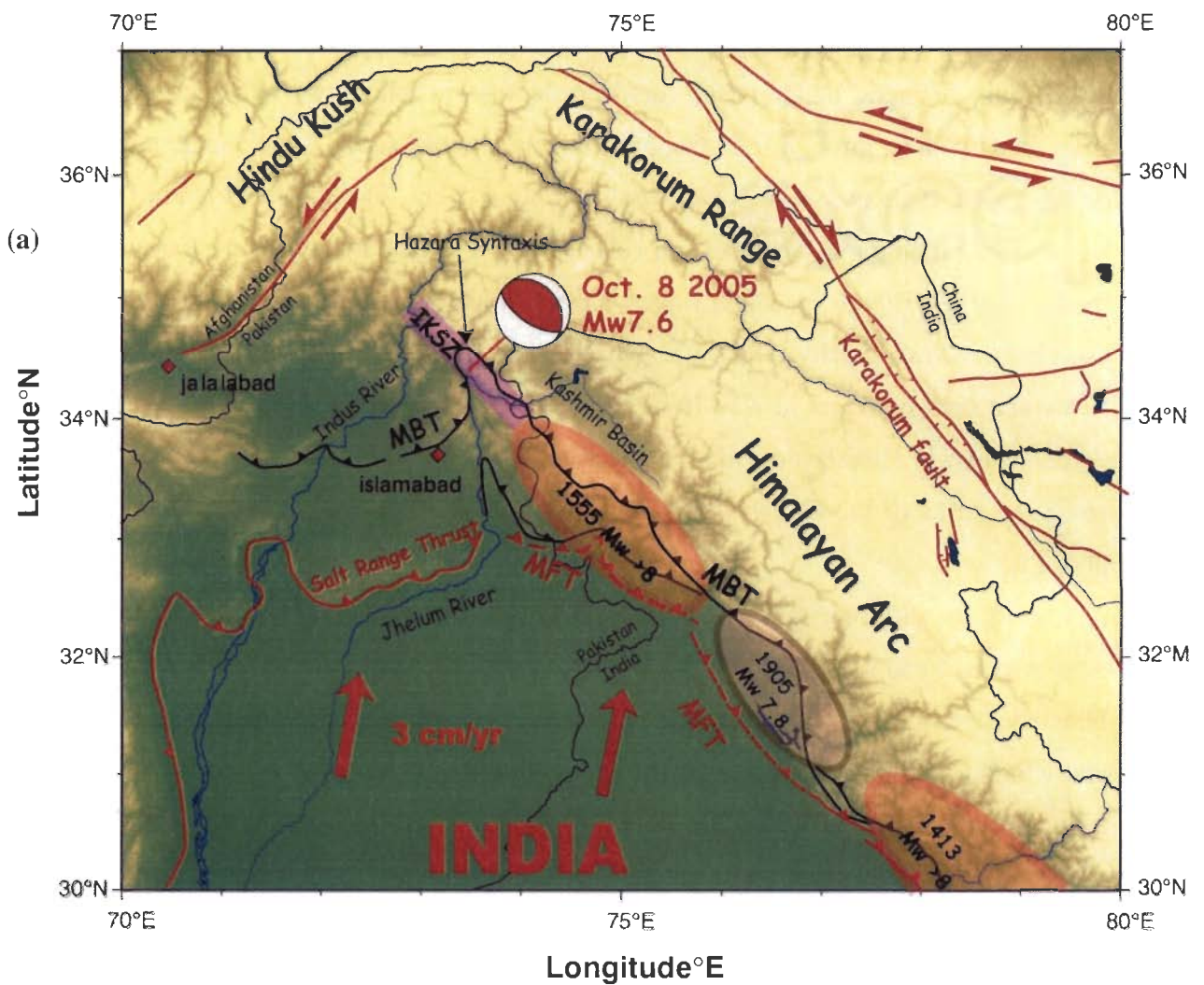
Figure 1.4: (a) The movement direction of the Indian plate and the rupture region due to large magnitude earthquakes occurred in Kangra-Chamba and adjoining region since 1413 AD. **(b)** The collision forms high mountain range as the Dhauladhar ranges of NW Himalaya.

1.3 TECTONIC FEATURES OF THE REGION

The typical cross section of the Himalaya bounded by the Himalayan Frontal Thrust (HFT) in the south and the Trans Himalayan ITSZ to the north is usually divided into SH, LH, HHC and THS respectively (**Figure 1.2b**). These lithological subdivisions from south to north are separated respectively by MBT, MCT and the Southern Tibet Detachment (STD); also referred as the Tethyan Fault (**Figure 1.2b**). This generalized geological and tectonic subdivision of the Himalaya, in the present study area of Kangra-Chamba section is swamped by the extended Chamba nappe (Thakur, 1992; Thakur, 1998). The other significant differences are: The roughly 80 km wide meta-sedimentary sequence of LH in the Garhwal-Kumaon-Nepal thins out in Kangra-Chamba region to a narrow belt of a few km, and represented by Panjal Imbricate Zone dominantly comprised of phyllites, slates and limestone (Rautela and Thakur, 1992, Thakur, 1998). Also the MCT along which the HHC sequence thrust over the LH sequence almost loses its identity in this area. Instead the Panjal thrust (PT) north of the Panjal imbricate zone can be traced for a long distance to the west in Kashmir Himalaya that connects to the Chail thrust in the southeast and is collectively designated as the MCT. The weakly metamorphed sediments of the Chamba nappe (CN) are similar in facies to the Tethys Himalaya and are considered to result from the southwestward sliding of the THS from north over the metamorphic HHC along the south dipping Chenab Normal Fault (CNF) that separates the CN from the HHC. Synchronous with southward thrusting, CN has undergone regional scale folding, e.g. Chamba syncline. In the western part (Chamba sector) of the study area, based on structural fabric and strain pattern, Singh (1994) has identified the Chamba thrust (CT) along which the Chamba succession rides over the Chail formations of the LH. No clear markers suggesting continuation of the CT to the eastern part (Kangra sector) are reported. Here in Kangra-Chamba sector the Dhauladhar ranges, immediately north of closely spaced MBT and the PT, rise abruptly attaining an average altitude of 4000 m (**Figure 1.4b**) and form the center of intense seismicity. The Kistwar (KW) and Rampur (RW) Windows are large antiformal folds (Thakur, 1992) to the NW and to the SE of the present study area.

Tectonically, the western Himalaya is divided from north to south into following tectonic units:

1. The Indus-Tsangpo Suture (ITS): The boundary between Himalaya or Indian landmass with Eurasia is marked by the Indus-Tsangpo Suture Zone (ITSZ) that is formed about 50 Ma starting the Himalayan convergence tectonics (Molnar

and Tapponnier, 1975). The suture is made up of imbricated mélanges of flysch sediments, pillow lavas, volcanic and the basic and ultrabasic rocks, which are cut by steep faults (Allegre *et al.*, 1984).

2. The South Tibet Detachment System (STDS): This is also known as the North Himalayan Normal Fault (Burg *et al.*, 1984a; Searle, 1986; Herren, 1987; Pecher, 1991; Buchfiel *et al.*, 1992). In the present study region of NW Himalaya, HHC around Rampur window (RW) has northern boundary as the extension of STD/Malari fault from Garhwal Himalaya. The eastern boundary of Chamba nappe is separated from the HHC by the STD that is nearly perpendicular to major tectonic units here and also described as Manali fault in the seismotectonic atlas of Geological society of India by Dasgupta *et al.*, (2000).

3. The Main Central Trust (MCT): The MCT is the major tectonic discontinuity, which divide the two contrasting structures of LH and HH. The relative movement of the blocks across this tectonic discontinuity has caused the development of crustal buckles in which the Palaeogene and Neogene sediments were deposited. In the Kumaon and Garhwal Himalaya (SE of present study region), the MCT is also described by some researches as Munsiari thrust that is traced up to Kullu-Larji-Rampur window in the present study region (Heim and Gansser, 1939). To its west the MCT is missing, i.e. replaced by Panjal Thrust (PT) and has been described as MCT in many publications (e.g. Gansser, 1981). In this region the MCT is folded and found in windows as Kistwar window in the NW and Kullu-Larji-Rampur window in SE where the age of MCT around Kistwar window is between 22 – 16 Ma (Walker *et al.*, 1999, Stephenson *et al.*, 2001).

4. The Panjal Thrust (PT): This thrust represents the original flat-over-flat relationship between the THS and LHS before the HHC that has been squeezed between two units. According to Valdiya (1980), it is the western continuation of the MCT extending the Chail Thrust to the west of Garhwal Himalaya. It is the northern boundary of the narrow belt of the LH containing rocks of Panjal Imbricate Zone (PIZ) where it has placed Salkhala Formations of CN over LH (Thakur, 1998).

5. The Chenab Normal Fault (CNF): it is the south dipping fault having ductile shear zone up to several kilometers containing high-grade HHC in the footwall

(Frank *et al.*, 1995). The GHC has Zanskar Shear Zone (ZSZ) in the northern side where the GHC has been separated from THS (Dezes, 1999). The CNF separated the CN from HHC along which the CN has moved Chamba sequence to the south over HHC (Thakur, 1998). At the surface it is steeply dipping but in the bottom has gentle slope coinciding with PT and it is described as gravity-controlled collapse of the Himalaya Miocene topographic front.

6. The Main Boundary Thrust (MBT): The MBT is the tectonic boundary between the Lesser Himalaya nappes lying to its north and the Outer Himalaya Tertiary foreland basin to its south (Gansser, 1964; Meigs *et al.*, 1995; Powers *et al.*, 1998; Decelles *et al.*, 2001). The majorities of the earthquakes in the NW Himalaya are concentrated in the Lesser Himalaya zone confined between MBT and MCT and have shallow focal depths. The evolutionary model of Himalaya (Le Fort, 1975) states that MBT lying to the north of HFT is the younger tectonic discontinuity as compared to MCT, which is more active currently. However, both the MCT and MBT have been treated as the contemporaneous features in the steady-state model of Seeber and Armbruster (1981).

7. The Himalayan Frontal Thrust (HFT): This tectonic unit is well exposed in the western Himalaya as compared to central Himalaya (Thakur, 2004). The average slip rate along this fault is ~ 8-10 mm/yr (Kumar et al., 2001). The HFT is the southernmost, youngest and neo-tectonically active thrust, which gives a topographic break to the Himalaya against the Indo-Gangetic alluvium planes.

The major tectonic boundaries are shown in **Figure 1.2c** that accommodates the strain through thrusting occurring in NE direction. The slip rate along the thrusts can be estimated indirectly using the size of the past large earthquakes, elapsed time since the last great earthquake and the convergence rate of about 18mm/yr (Gahalaut, 2008). According to Seeber and Armbruster (1981) all the above mentioned discontinuities merge with each other at depth with a common detachment surface. The detachment surface is developed along a detachment discontinuity, which separates the under-thrusting Indian plate from the Himalayan sedimentary wedge in the southern part and the Eurasian plate in the northern part. The geotectonic subdivision of the study region, a part of NW Himalaya is shown in **Figure 1.2c** taken from Yin (2006). The main regional tectonics has been shown in **Figure 1.4** showing the movement of the Indian plate at a rate of 3 cm/yr to NNE direction. The rupture areas due to large magnitude

earthquakes that occurred in this region since 1413 to 2005 are also shown.

1.4 PREVIOUS GEOPHYSICAL STUDIES IN THE HIMACHAL, HIMALAYA

The formation of the Himalaya and ongoing geodynamic processes can be revealed in a better way if a combined analysis of various parameters like, gravity, magnetic, Global Positioning System (GPS) records, topographic elevation and seismicity is performed. Combining different geophysical methods in the INDEPTH (Alsdorf *et al.*, 1998) have helped in understanding the geodynamics of the Nepal Himalaya and Tibet. It provides a clue that the Indian plate is under-thrusting northward along gently dipping decollement showing the crustal thickness of 70-75 km under Tibet. In the NW Himalaya the sinuous nature of MBT, PT and PMT, nearly transverse alignment of these thrusts in Kulu-Bilaspur region, existence of Kangra and Dehradun re-entrant, lateral basement ramp and different lineaments (Powers et al., 1998; Banerjee and Burgmann, 2002) suggest segmentation of frontal Himalaya. The brief description of the previous geophysical studies carried out in the northwest Himalayan region has been discussed here.

1.4.1. The Study of Topography

The elevation of the topographic surface in the northern India is highly variable (**Figures 1.1 and 1.3**). The Indo-Gangetic plains have low elevation and the Himalayan region contains most of the highest mountain peaks of the world. The Himalaya exists between Ganga fore land basin to its south and Tibetan Plateau to its north (**Figure 1.2a**). The topographic elevation starts gradually increasing from the Ganga foreland basin (Gansser, 1964). The high topography of the Himalaya and Tibetan Plateau has a good correlation with the free air anomaly (Rajesh and Mishra, 2004). In the Kangra-Chamba sector of NW Himalaya, the topography suddenly increases along the Dhauladhar ranges having high mountain peaks north of it. South of these ranges, the wide zone of SH has gentle increase in elevation from south to north.

The relation between gravity anomaly and isostatic imbalance with variation in topography in the western Himalaya was studied by many scientists (Lyon-Caen and Molnar, 1985; Bilham *et al.*, 2003; Rajesh and Mishra, 2004; Jordan and Watts, 2005; Mishra and Rajasekhar, 2006; Tiwari *et al.*, 2009). In the present study region, it is quite obvious that the topography is variable as it shows foredeep depression in the Indo-

Gangetic plains and increases slowly in the SH (**Figures 1.2a and 1.5**). Then from the LH, the topographical height increases suddenly along the Dhauladhar ranges where some of the highest peaks of the world are present. According to Lyon-Caen and Molnar (1985), along a profile from Ganga basin to Higher Himalaya, the variation in topography deviate from the local isostatic equilibrium based on bouguer gravity anomalies. This has been concluded on the basis of four profiles (Figure 1 of Lyon-Caen and Molnar, 1985) taken in NW Himalaya. It shows mass deficit at Ganga basin and excess mass under the Lesser and Higher Himalaya, which shows that Ganga basin is overcompensated and Himalaya are undercompensated by about 100 mGals. This indicates flexing of the Indian lithosphere under Himalayan front. Gradient of gravity anomalies is very high across the Himalaya in this region. The mean elevation and load in this region is almost twice that of the adjoining parts in the Higher Himalaya.

1.4.2. The Study of Gravity Field

The variation in free air anomaly (free-air correction due to changes in elevation) is interpreted as the compensation of isostatic effect for the loaded crustal mass (Telford *et al.*, 1976). In contrast to the Bouguer anomaly (attraction due to added material) the free air anomaly is negative in the Indo-Gangetic foredeep region showing a thin crustal layer which has been also described as the effect of flexure (Lyon-Caen and Molnar 1983, 1985; Bilham et al., 2003) on the Indian crust in this part. The flexure effect represent a filled-up foredeep basin (**Figure 1.5**) formed due to subsidence of Indian plate following its collision with Asia. The gradient of Bouguer gravity anomaly suddenly increases to 2 mGal/km over Higher Himalaya as compared to 1 mGal/km along SH and LH indicating that Moho dips more steeply (10°–15°) beneath Higher Himalaya (Lyon-Caen and Molnar, 1985). This slope is gentle under LH (only 2°-3°) and it has been proposed that the Indian plate is flexed down by the load of the Himalayan Mountains. The Indo-Gangatic plain has been created as foredeep basin (Figure 5 of Bilham and Szeliga, 2008) due to this deflection of Indian plate and it is directly related both to the strength of the plate and the loading amount of the mountains. According to Bilham and Szeliga (2008), these flexural stresses are the causes of occurrence of the earthquakes in the Himalayan region. The Bouguer gravity anomaly is useful for elaborating the dipping Indian crust beneath the Himalaya. According to Rajesh and Mishra 2004) the transverse central Himalaya shows several gravity highs and lows indicating variation in the sub-surface strata. They show that the

gravity gradient mainly coincide with different tectonic discontinuities such as Altyn Tagh Fault (ATF), ITSZ, MCT and MBT.

1.4.3. The Study Using GPS Data

The present convergence rate between India and Eurasia varies along the trend of the Himalaya as observed from analysis of GPS data. It is about 65 mm/y to the eastern end of the Himalaya and about 40 mm/y to its western end (Burg and Chen, 1984). The other GPS study (Banerjee and Burgmann, 2002) indicates these rates as 44 mm/y and 37 mm/y respectively. Similar results have been given by Bilham and Gaur (2000) and these observations show that the Indian plate is rotating in anti-clockwise direction. Due to this convergence the high Himalayan mountain ranges and elevated Tibetan Plateau were formed because some part of the convergence is accommodated in the shortening and thickening of the crust. These studies show that about 50% of the convergences between India and Eurasia are occurring along the Himalayan arc. According to Powers et al. (1998), the shortening along the Tertiary Siwalik molasse at Kangra (near 76°E) is 14 ± 2 mm/y and across Dehradun reentrant (77.5°E) is 11 ± 5 mm/y. However England and Molnar (1997) has given the convergence rate of 17 ± 8 mm/y for the NW Himalaya between 74°–78°E and 10 ± 2 mm/y to the western part in Pakistan. Banerjee and Burgmann (2002) have used the recent dense GPS network in NW Himalaya, mainly around Kangra and Dehradun regions showing relatively decreasing velocity of convergence towards southwest for this region. They compared two cross sections along these two regions indicating a gentle dip of the Indian plate north of Naddi station that is close to MBT in the Kangra region. However in the Dehradun region the Indian plate is comparatively steeply dipping to the north of Dehradun which too is close to MBT (Figure 3 of Banerjee and Burgmann, 2002). Much of the shortening is taking place within nearly 100 km wide zone where the present day micro-earthquake activity is also high. In the central part of the Himalaya in Nepal, the velocities of convergence obtained through GPS (Bilham et al., 1997; Cattin and Avouac, 2000) are in agreement with inter-seismic elastic strain accumulation north of a locked zone which is about 100 km wide and this strain is released through earthquake occurrence.

1.4.4. The Paleo-Seismic and Magneto-telluric Studies

With the advancement of crustal deformation measurement using GPS geodesy in the Indian continent starting from 1990, the convergence rate between India-Eurasia is now known accurately. On these measurements the building and release of stress associated with northward translation of the Indian plate has been correlated with great size earthquakes since historical time (Iyengar and Sharma, 1998; Ambraseys and Jackson, 2003; Bilham and Ambraseys, 2004; Kumar *et al.*, 2006; Feldl and Bilham, 2006; Bilham and Szeliga, 2008). These studies indicate two possible scenarios. In one case using the well know records of four great earthquakes (1887, 1905, 1934 and 1950), Bilham and Gaur (2000) shows that the Himalayan region is deficient of many such type of earthquakes. In the other case using palaeo-seismic investigations Bilham and Szeliga (2008) reveal that three bigger size earthquakes with slip exceeding 20 m have occurred in Medieval India (**Figure 1.5a**). The earthquakes of these sizes have a potential of total devastation and require an elapsed time of more than 1100-1300 years for recurrence in the Himalaya. The seismic and the magneto-telluric studies have revealed the presence of low seismic wave velocity layer in the mid-crust where the conductivity is also high (Arora, 1993). On the basis of analysis of electrical conductivity structures in the NW Himalaya Arora (1993) suggested that a Trans Himalayan Conductor (THC), an anomalous feature, exist perpendicular to the Garhwal Himalaya. The magneto-telluric studies along a profile across the major litho-tectonic units in northwest Himalaya (Arora *et al.*, 2007) has portrayed a north dipping low resistivity layer above the under-thrusting Indian plate. This low resistivity is attributed to the presence of fluids representing accreted sedimentary rocks under Himalaya and Tibet.

1.4.5 Study of Structure of Moho

Based on P-wave receiver function approach Rai *et al.*, (2006) obtained the Moho geometry under NW Himalaya after taking a transect from Indo-Gangetic Plains (Delhi) to the Karakoram. The Moho is dipping towards north having nearly 40 km depth at Delhi that increases to nearly 75 km at Taska at the Karakoram. Based on a gravity profile for the same region of Laen-Caen and Molar (1985) proposed presence of dipping Moho at a depth of about 48 km beneath the present study region.

These documented anomalous behavior in topography, gravity, electrical conductivity, seismic wave velocities suggest different characteristic of crust. The

present work added a tool of micro-earthquake studies to support and validate these anomalous characteristics in the Kangra-Chamba region of NW Himalaya.
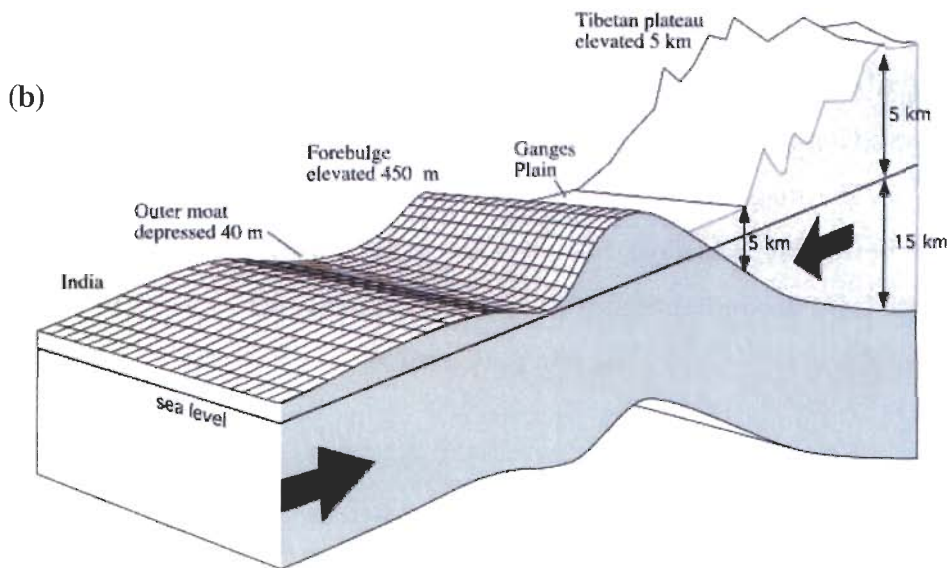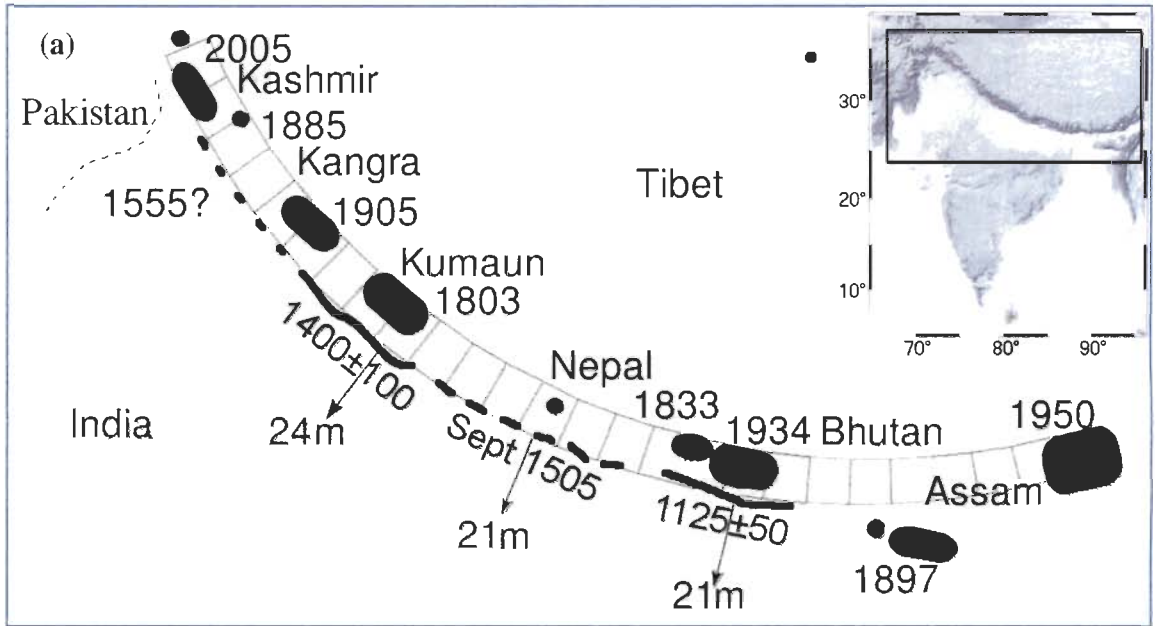
Figure 1.5: The Himalayan arc (shown in inset of upper panel) showing the amount of slip and rupture areas due to devastating earthquakes. (b) Flexure produced in the Indian plate due to continent-continent collision (after Bilham and Szeliga, 2008).

1.5 PURPOSE OF THE PRESENT WORK AND INTRODUCTION OF DIFFERENT METHODS USED

The Kangra-Chamba sector of NW Himalaya is one of the seismo-tectonically most active regions of the Himalaya. It is the source zone of 1905 devastating earthquake (M8.0) that killed more than 20,000 people. This region is located in seismic zone V on national seismic zoning map and is governed by two different directed stress regimes that include various faults, folds, lineaments and other tectonic features (Kumar *et al.*, 2009). High altitude Dhauladhar ranges exists just north of the MBT. This region shows intense seismic activity. However, lack of a good seismic velocity model and limited azimuthal coverage of earthquake sources from northern side has hampered the process of obtaining reliable location of hypocenters which is required for accurate tectonic interpretation. The analysis of recent micro-earthquake data addresses the understanding of seismotectonic processes, physical process of earthquake generation along with seismogenic process on regional basis. The big size earthquakes help to specify the state of movement while their study along with that of smaller and micro-earthquakes provide the understanding of physics of earthquake processes and completely quantify the regional seismic regime. The crustal structural investigation is necessary for complex Himalayan region that helps to improve the location of the earthquake sources. An attempt is made to utilize the catalogue of historical and current seismicity for Kangra-Chamba region of NW Himalaya to quantify its seismic regime on the basis of seismicity, crustal structure, fault plane solutions, earthquake source parameters and active fault geometry. A brief review of the work done is as follows:

In Chapter 2, the attempt is made to characterize the seismic regime of the Himalayan collision zone by examining the space time distribution of seismic catalogue from historical time (1550) to recent time (2005) for the entire NW Himalaya (26°N-34°N and 74°E-82°E). This catalogue indicates rarity of great earthquakes. Yet, another feature of the space-time distribution of seismicity in this belt is its highly heterogeneous segmentation with well defined sections of high seismicity centered on Kangra-Chamba, Kinnaur, Garhwal and Dharchula regions. This picture becomes more apparent in the post 1999 period when the minimum detection threshold of earthquake further reduced to M=2.5 following addition of new local seismic stations. One of the most anomalous features of space time distribution has been that the Kangra-Chamba region in NW Himalaya has persistently been a zone of intense seismicity as revealed by the clustering of epicenters, energy released irrespective of the duration and period of

records examined. This chapter further reviews the distinctive geotectonic setting of the study region in the background of generalised litho-tectonic subdivisions and major mega-thrusts of the Himalaya. In the background of this existing knowledge of tectonic setting and spatial behavior of seismicity, the incorporation and upgradation of local seismic network has been discussed. The design of the network and the threshold of the seismic events recorded have been explored. The layout of total 21 stations (14 three-component digital and remaining 7 single vertical component analog stations) covered densely a 2° x 2° area bounded by 31.5°-33.5°N and 75.5°-77.5°E. Further, this network, when combined with already functional 15 stations in the Garhwal-Kumaon Himalaya provides a network of 36 stations to study the regional seismicity in the NW Himalaya.

The central focus of Chapter 3 is the determination of area specific 1D velocity model of the region. Well tested algorithm VELEST (Kissling, 1995) is adopted for simultaneous estimation of velocity structure and to improve the locations of the earthquakes. The station corrections obtained as a byproduct of the approach provides nature of deviation from 1D structure. Total 906 P- and 773 S-phases pertaining of 172 earthquakes were selected for inversion. The inversion of travel-time could resolve velocity structure for the upper 20 km or so as > 85% of the recorded earthquakes were confined to depth less than 20km of the crust. Therefore, the determination of the thickness and velocity up to Moho and upper mantle were supplemented independently by travel-time-distance plot using data of earthquakes recorded by all 36 stations and scanning epicentral distances up to 550 km. The minimum 1D velocity model divides the average 44 km thick crust into four layers. The top ~10 km thick layer represents the metamorphosed sediments of the CN that dominates the surface geology of the study area. A thin low velocity layer at 15 km depth, after allowing for the station corrections, portrays the geometry of the detachment zone separating the down-going Indian plate from the overriding wedge.

Given that contour plots of station corrections warrant significant deviation from 1D velocity structure, which can not be explained by surface topography as well as by near-surface heterogeneities. The P- and S-wave travel time data, inverted above to derive the optimum 1D velocity structure, is further processed to deduce high-resolution 3D velocity structures using the well proven technique of local earthquake tomography (LET) (Thurber, 1993) in Chapter 4. This Chapter includes a brief description of the basic principle of LET and how it proceeds for simultaneous estimation of hypocenter parameters along with Vp and Vp/Vs structure. The true nature of inverted 3D

variations in Vp, Vs and the ratio Vp/Vs for the central block, well resolved by LET, are shown as horizontal slices corresponding to depths of 0, 2, 5, 10 15 and 18 km. Systematic and significant variations up to 14% in Vp and Vs along with up to 6% in the Vp/Vs ratio have been observed across the major tectonic units. Another distinctive feature of velocity tomograms is a narrow NE-SW aligned low velocity layer (LVL) in the eastern part, confined to depth interval of 2 to 5 km and is underlained by a high velocity zone in tomograms at 10 km depth.

As an independent mode to constrain the seismotectonic model of the Kangra-Chamba region, Fault Plane Solutions (FPS) of some 42 well located events (RMS value of <0.1s and M>2.5) were carried out (Chapter 5). These are computed using P-wave first polarity motions for earthquakes recorded at more than eight stations with maximum azimuthal station gap of less than 100°. The complex tectonic setting of the sector is immediately evident from the fact that three dominant fault mechanisms noted are: (1) thrust fault mechanism with strike slip component, (2) strike slip movement with thrust component and (3) normal fault motion with strike slip component. The FPSs of the earthquakes located at detachment highlight the dominance of the thrust environment there. The earthquakes occurring along the shallow sections of the MBT and PT are characterized by thrust mechanisms with varying component of strike slip movement. The normal fault mechanism along the plane which is seen as a subsurface extension of the CNF is consistent with the tectonic model which postulates NE-SW directed extensional tectonics responsible for the southward displacement of the CN along the normal fault. Earthquakes located beneath the detachment zone in a localized cluster NE of the epicenter of the Kangra earthquake are also dominated by normal fault mechanism. Orientation of P- and T-axes, obtained by tensor of the focal mechanism indicates that stress pattern in the region is governed by two distinct tectonics.

In Chapter 6 earthquake source parameters are inverted using the refined locations of the local seismic events recorded in magnitude range $1.5 < M_L < 4.7$ in the study region for which over 2000 S-wave spectra of digital seismograms are used. The source parameters of the earthquakes are obtained using Brune's circular model (Brune, 1970) through the corrected amplitude spectra based on geometrical spreading and site effect.

In Chapter 7 the integration of all the above results has been done to quantify the seismic regime of the Kangra-Chamba region. The key results of this work have

been summarized. Also the importance and the requirement of future work relating to this have been discussed.

CHAPTER 2

SEISMIC REGIME, DISTINCT TECTONIC FEATURES AND DESIGN OF OBSERVATION NETWORK

2.1. INTRODUCTION

In this work I have made an attempt to characterize the seismic regime of the Himalayan collision zone by examining the space time distribution of seismicity from historical time (1550) to recent time (2005) for the entire NW Himalaya (26°N-34°N and 74°E-82°E). It is observed that great earthquakes are very rare in this area, only earthquake reported from this area is the great 1905 Kangra earthquake of magnitude 8.0. However, the evidence of major (M>6) earthquakes over the entire NW Himalaya can be traced for nearly five centuries, indicating this region has been repeatedly fractured and affected by major events (Lyubushin et al., 2010). Most of the events are confined to a narrow belt between surface trace of the MCT and MBT. This narrow belt, named MHSB (Ni and Barazangi, 1984) is better defined on the epicentral distribution map for earthquakes with M>4.5, the minimum detection magnitude for which earthquake catalogues are complete only for the post 1965 period. In more recently developed seismotectonic models for the Himalaya, this MHSB is viewed as a ramp structure (Pandey et al., 1995) in the detachment zone separating Indian plate and overriding Himalayan wedge or the locked portion of the Main Himalayan Thrust (MHT) fault (Bilham et al., 1998; Banerjee and Burgmann, 2002; Bollinger et al., 2004). Yet, another feature of the space-time distribution of seismicity in this belt is its highly heterogeneous segmentation with well defined sections of high seismicity centered on Kangra-Chamba, Kinnaur, Garhwal and Dharchula regions. This picture become more apparent in the post 1999 period when the minimum detection threshold of earthquake further reduced to M=2.5 following addition of new local seismic stations. One of the most anomalous features of space time distribution has been that the Kangra-Chamba region in NW Himalaya has persistently been a zone of intense seismicity as revealed by the clustering of epicenters and energy released irrespective of the duration and period (Kayal, 2001; Kumar et al., 2009; Thakur et al., 2000) of records examined.

This chapter further reviews the distinctive geotectonic setting of the study region in the background of generalized litho tectonic subdivisions and major mega-thrusts of the Himalaya. It is highlighted that generalized cross-section is transgressed by the extended CN (Thakur, 1992; 1998). The weakly metamorphosed sediments of the CN are similar in facies to the Tethys Himalaya sediments and are considered to have resulted from southwestward sliding of the TH sediments from the north over the metamorphic HHC along the south dipping CNF that separates the CN from the HHC. The Kistwar (KW) and Rampur (RW) windows are large antiformal folds (Thakur, 1992) to the NW and to the SE of the present study area. In the background of this existing knowledge of tectonic setting and spatial behavior of seismicity, the existing seismic network of 9 stations was suitably upgraded by adding 12 new stations. The layout of total 21 stations (14 three-component digital and remaining 7 single vertical component analog stations) covered densely a $2°$ x $2°$ area bounded by $31.5°$- $33.5°N$ and $75.5°$ -$77.5°E$. The station spacing between pair of stations varied from 3-7 km in the southern part where the Lesser Himalaya (LH) pinches out to a narrow belt of only few km (Thakur, 1998; Rautela and Thakur, 1992), average value of 20 to 30 km over the central part and 50-70 km for select pair of stations on the northern border to cover regional scale tectonic features present in the study area. Further, this network when combined with already functional 15 stations in the Garhwal-Kumaon Himalaya provides a network of 36 stations to study the regional seismicity in the NW Himalaya.

2.2. SEISMIC CATALOGUE AND DISTRIBUTION OF EPICENTERS

High seismic activity is occurring in the Himalaya as compared to the adjoining regions due to high stress build up at the boundary of India-Eurasian convergence. The recent compilation of seismic catalogue from historical time (1550) to recent years (2005) for whole of NW Himalaya has more than 6000 entries for the region $26°$-$34°N$ and $74°$-$82°E$ (Gitis *et al.*, 2008; Lybbusin *et al.*, 2010). This catalogue is compiled using different sources of earthquake information taken from the International Seismological Center (ISC) United Kingdom, Indian Meteorological Department (IMD) New Delhi, India, Wadia Institute of Himalayan Geology (WIHG) Dehradun, India and Kumaon University, Uttarakhand, India. The catalogue includes great 1905 Kanga earthquake along with 6 great earthquakes having magnitudes in the range of 7.0 -7.9 and 26 major earthquakes of magnitude range 6.0-6.9. Most of these events are confined

in a narrow zone between MBT and MCT where the elevation of surface above mean sea level (MSL) is higher than the adjoining parts immediately south of it. With successive up gradation of seismic networks, the minimum magnitude threshold was 4.5 in 1965 and came down to 2.5 in 1999. This seismic catalogue data is also utilized since 1999 to observe the spatio-temporal variation of seismicity, b-value and minimum magnitude representation using the software Geo-information (**http://eearth.viniti.ru**). This analysis shows that seismicity is high in the Kangra-Chamba region with 0.8 and higher b-value and minimum representative magnitude is 2.5 (Gitis *et al.*, 2008).
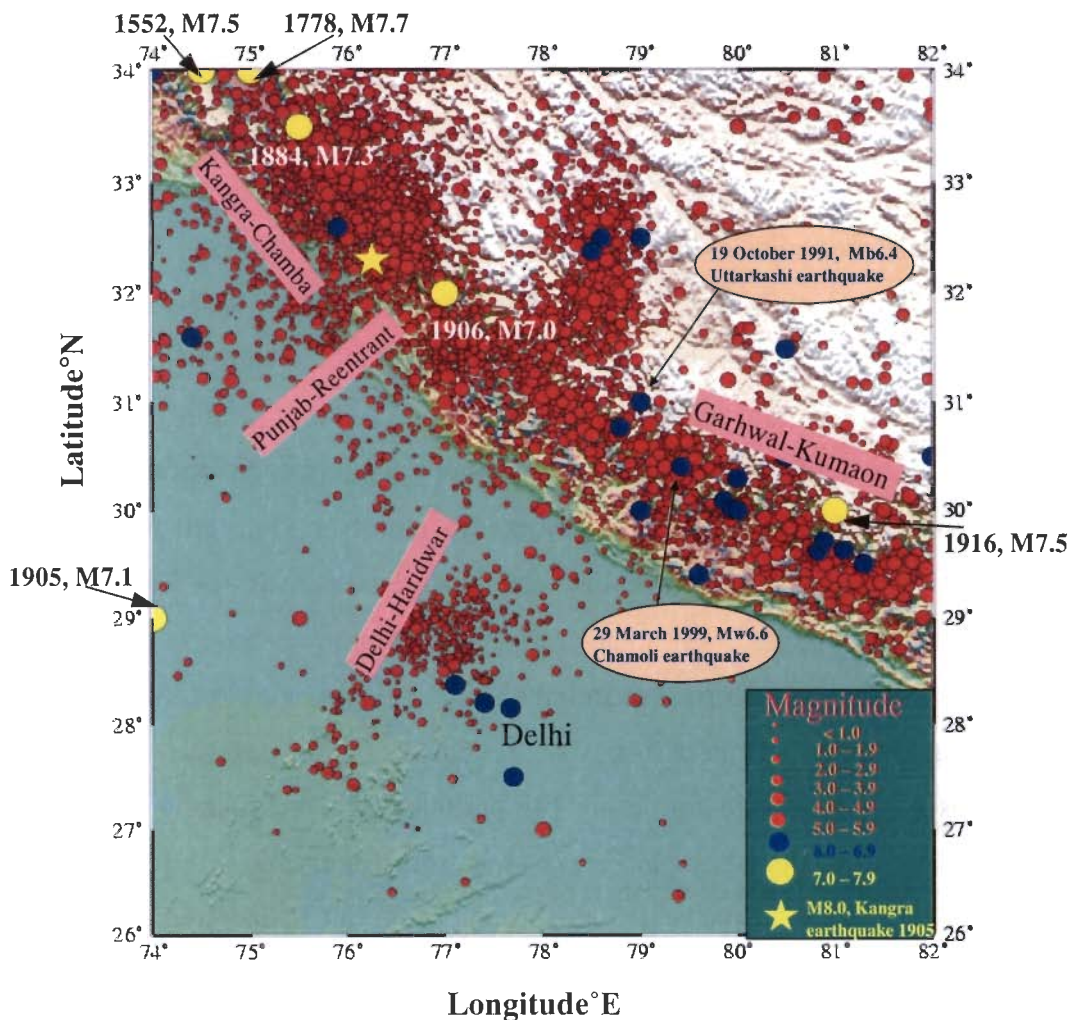
Figure 2.1: The earthquake epicenter distribution in the western Himalaya. Star indicates the location of devastating M8.0 Kangra earthquake. Yellow circles are the epicenters of earthquakes in magnitude range 7.0 – 7.9. Blue circles are the epicenters of earthquakes in magnitude range 6.0 – 7.0. The red circles show the seismicity of M < 6.0 with increasing size of the circle for increasing magnitude.

The seismic catalogue of western Himalaya was obtained using the information from different sources for a period of 1550 to 2005. **Figure 2.1** gives the epicentral distribution of all the earthquakes obtained from the sources mentioned on page 24 of this section. The epicentral location of devastating M8.0 Kangra earthquake that occurred on 4th April 1905 is indicated by a star. This is the only recent large magnitude earthquake of the region, which has claimed more than 20,000 casualties and caused lots of damage to the property near the epicenter zone. However, in 2005 another earthquake of M7.6 occurred in Kashmir very close to and towards northwest of the present study region. The other large earthquakes that occurred in this region earlier to Kangra earthquake is indicated by yellow circles in **Figure 2.1**. The listing of these earthquakes in magnitude range 6.0 – 6.9 in the catalogue indicates that only three earthquakes of M > 6.0 occurred during the last five centuries in the Kangra-Chamba region while more events occurred in the adjoining regions. The density of epicenters of lower magnitude earthquakes (M<5.0) is higher in the Kangra-Chamba region compared to the other parts of the western Himalaya. Therefore, the seismicity of low magnitude earthquakes is higher while that of high magnitude earthquakes is lower in the Kangra-Chamba region compared to that of the adjoining parts in the western Himalaya. This non-uniform distribution of seismicity highlights the difference between different seismic regimes in the western Himalaya indicating the need for performing different analysis to differentiate the seismotectonic characteristics of Kangra-Chamba region from the other parts. In this chapter, different approaches have been adopted for the analysis of recent and historical seismicity.

The distribution of these big size earthquakes indicates that the region is vulnerable as a potential site for future big earthquakes. The shaking effect in this region due to these earthquakes can be assessed from **Figures 2.2 and 2.3** where the intensity variations with distance in and around Kangra-Chamba region have been reported. In **Figure 2.3**, the isoseismal contours (taken from seismotectonic atlas of India prepared by GSI, 2003) have been incorporated for different big size earthquakes that occurred here during the last century. These isoseimal maps are validated through the damage scenario of M7.6 Kashmir-Kohistan earthquake that occurred on 8th October, 2005. Mahajan *et al.*, (2006) has prepared the Quick look isoseismal map of this earthquake taking the damage assessment at different parts of the northern India. According to this analysis, the Kangra, Chamba and other places in the current study

region of Kangra-Chamba felt intensity V under MMI intensity scale. This is based on Eurasian Macroseismic scale 98 for assessing the damage patterns.
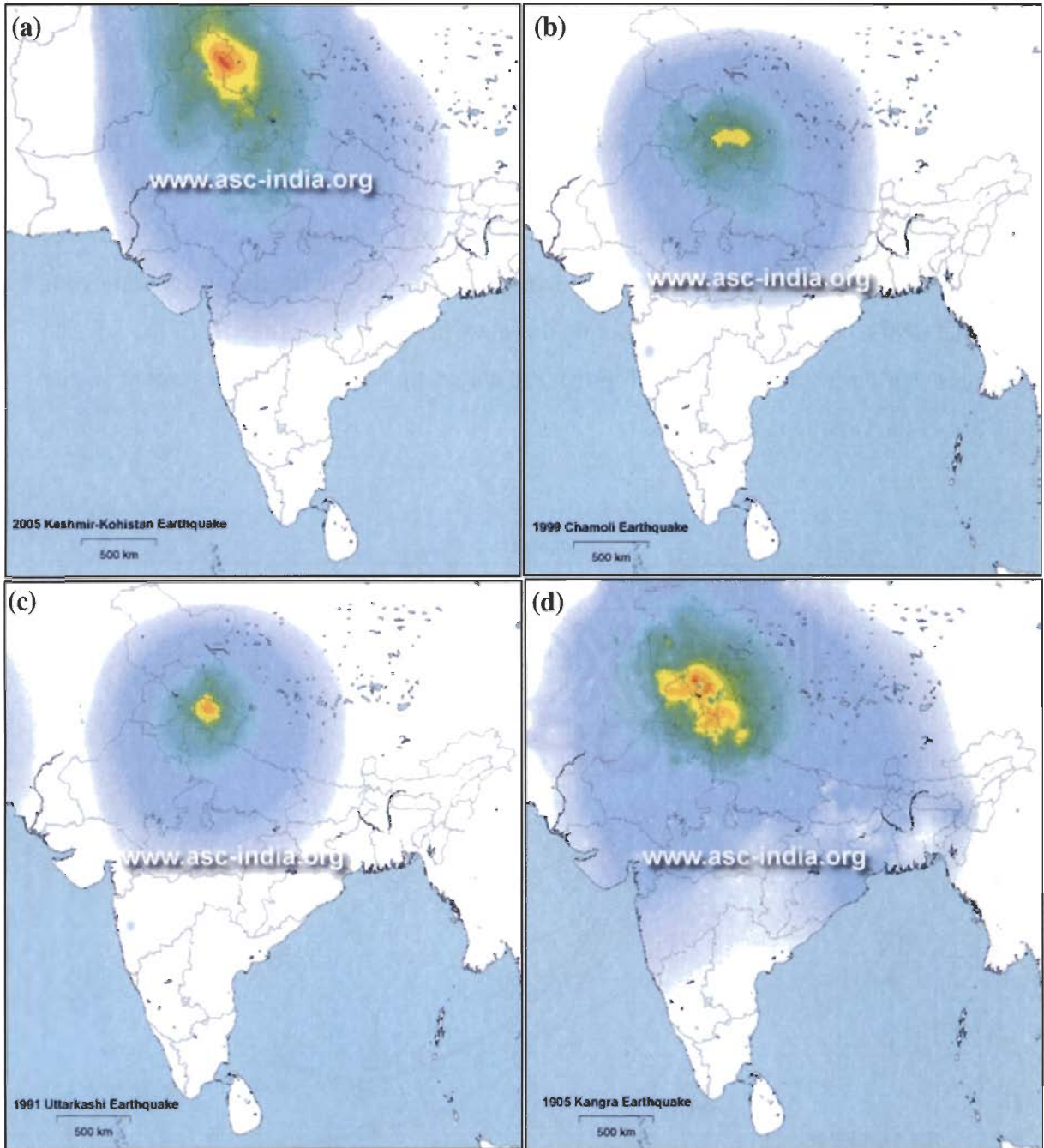
PERCEIVED SHAKING	Not felt	Weak	Light	Moderate	Strong	Very strong	Severe	Violent	Extreme
POTENTIAL DAMAGE	none	none	none	Very light	Light	Moderate	Moderate/Heavy	Heavy	Very Heavy
PEAK ACC.(%g)	<.17	.17-1.4	1.4-3.9	3.9-9.2	9.2-18	18-34	34-65	65-124	>124
PEAK VEL.(cm/s)	<0.1	0.1-1.1	1.1-3.4	3.4-8.1	8.1-16	16-31	31-60	60-116	>116
INSTRUMENTAL INTENSITY	I	II-III	IV	V	VI	VII	VIII	IX	X+

Figure 2.2: Isoseismal maps prepared by amateur seismic centre (www.asc-india.org), Pune India for (a) the M7.6 Kashmir earthquake of 2005, (b) the M6.4 Chamoli earthquake of 1999, (c) the M6.8 Uttarkashi earthquake of 1991 and (d) the M8.0 Kangra earthquake of 1905.

The catalogue can be divided in to three time periods, the period from 1550 to 1962 is taken as the historical time period for which the instrumental data is absent but the events are officially documented. The size of the earthquakes in terms of magnitude is not much reliable for this period. The records of seismic events of big earthquakes are available for the period of 1963 to 1976 with well known documents and instrumental data. The threshold of this period can be easily achieved for magnitude 4.5 and this threshold goes down to magnitude 2.5 after 1999. After 1965 the threshold for the study region is 4.5 due to the introduction of World Wide Seismic Standard Network (WWSSN), while this threshold goes down to 2.5 in 1999 with the up gradation of regional IMD network and introduction of new networks of other institutes. These changes can be easily noticed in **Figure 2.4** which highlight the improvement in the quality of the catalogue with time.
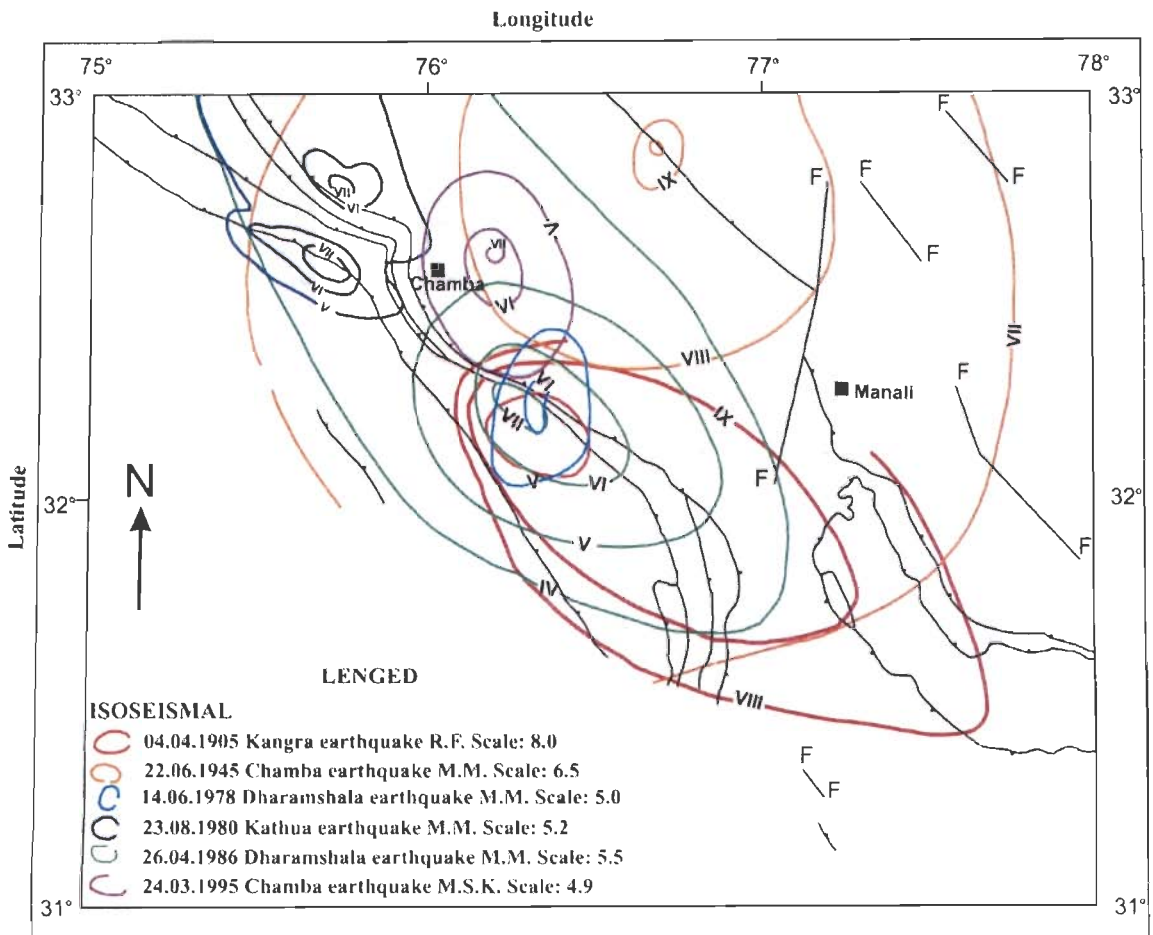
Figure 2.3: The isoseismal maps of different earthquakes of Kangra-Chamba region obtained from the seismotectonic atlas of India prepared by Geological Society of India (GSI) in 2002.

2.3. SIGNIFICANT EARTHQUAKES (M ≥ 5.0) OF THE REGION

During last century, the Kangra-Chamba region of NW Himalaya was jolted by a number of large-magnitude earthquakes. The most devastating was the Kangra earthquake of 4th April 1905 (**Figure 2.1** and **Table** 2.1) that caused a huge loss of human life and property. The isoseismals of this earthquake for intensities IX and VIII are shown in **Figure 2.3**. In the Himalayan region, three other great earthquakes (1897 Shilong, 1934 Bihar and 1950 Assam) has been reported during last 120 years and the recurrence period of these types of earthquakes are from one century to few centuries (Bilham and Szeliga, 2008). The historical records of such great earthquakes are very few and the information about their location and timing is not very reliable. The investigation of paleo-seismological (**Figure** 1.1) studies offers some hope for increasing the numbers of pre-instrumental period records that are helpful in improving the estimates of recurrence interval and for macro-seismic studies. However, the records of larger size earthquakes of damaging nature exist for every part of the Himalaya. The study of these earthquakes is useful to obtain the damage pattern and probable source mechanisms. The intermediate size earthquakes (4 ≤ M < 6) occur frequently in Kangra-Chamba region of NW Himalaya, the shaking due to which were observed and reported many times in the recent years. A number of times I too got the chance to experience the shaking effect due to these earthquakes. The recurrence period of M5 earthquake in the study zone is of the order of 3 to 5 years and for M4 earthquake it is nearly 1 year. The salient findings of the recent big size earthquakes of this region have been gathered to investigate the seismic regimes. The epicentre locations of these earthquakes are shown in **Figure 2.5** where 1 (star) represents the location of M8.0 Kangra earthquake of 1905, 2 is the location of M6.5 Chamba earthquake of 1945, 3 is the M5.1 Dharamshala earthquake of 1968, 4 is Kinnaur earthquake of 1975, 5 is the epicenters of and M5.4 Dharamshala earthquake of 1978, 6 represents the epicentre of M5.4 Jammu-Kathua of 1980 and 7 is the M5.7 Dharamshala of 1986. Detail description of individual event is as follows.

2.3.1. The Great Kangra Earthquake of 4th April 1905

The Kangra earthquake in the western Himalaya was an interesting event for scientists as it occurred merely 7 years after the 1897 great Assam earthquake that occurred just south of the eastern Himalaya (**Figures 1.1**). Although, it was about 1800 km away from the Assam earthquake but the increase of post-earthquake observation,

the addition of instruments and the latest literature revamping helped this time to improve the knowledge of Himalayan seismicity. The maximum intensity reported was X on Rossi-Forel scale near Kangra and Dharamsala region and also VIII intensity near Dehradun at about 250 km towards SE of the source zone. The numbers of causalities (~20,000) during this earthquake were about 4 times more as compared to that for the Assam earthquake. The casualty was also higher than that for the other two great earthquakes (1934 Bihar and 1950 Assam earthquakes) of the Himalayan region. Perhaps the comparison of loss of this earthquake with Assam event and the extended VIII intensity from Kangra to Dehradun has compelled Richter to assign its magnitude 8.0 that is lowered to 7.8 by Ambraseys and Douglas (2004). Middlemiss (1910) and Molnar (1987) also reported about 100 km rupture in the Kangra region of Himachal Himalaya and a smaller rupture in Dehradun region. The available intensities of big size earthquakes in the Kangra-Chamba region are shown in **Figure 2.3** that are given in the atlas seismotectonics of India by GSI (2000).

2.3.2. The Chamba Earthquake of 22nd June, 1945

It is the largest magnitude earthquake reported in this region after the occurrence of M8.0 Kangra earthquake of 1905. However, there is limited reported information about this earthquake. Mahajan and Virdi (2005) has assessed the macroseismic study of this earthquake indicating a similar decay trend of rapid decay towards northwest compared to southeast as has been reported for the Kangra earthquake. As shown in **Figure 2.3**, the maximum observed intensity during this earthquake was IX on the MM scale enclosing an area of 192.08 km^2. The area enclosing intensity VI zone in that study is 240,000 km^2 which follow elongated pattern parallel to the strikes of major tectonic features. However, the higher isoseismal are circular in pattern matching the shape of the Kistwar window.

2.3.3. The Kinnaur Earthquake of 19th January 1975

This earthquake of M7.0 occurred in the upper Sutlej valley on 19th January, 1975. The epicentral location of this earthquake is 32.45°N and 78.43°E (**Figure 2.1**) as per the information by Bangar (1976) followed by a big size aftershock of M6.0 after 10 minutes to its occurrence. The high Himalayan region with topographical elevation of 4000 m from the mean sea level was jolted in mid winter. Due to severe cold and snowfall during this time the sufferings of inhabitants of this region increased many
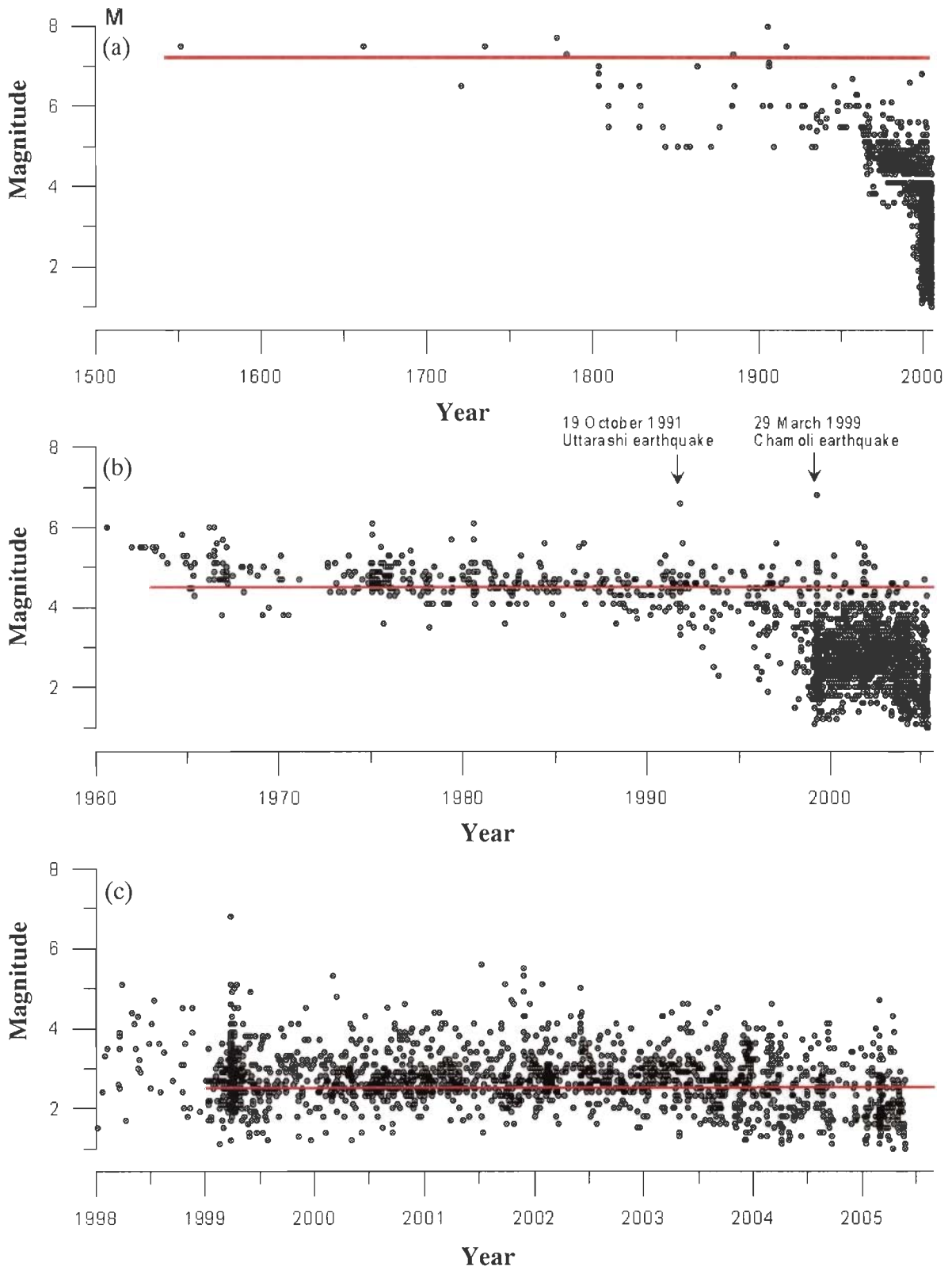
Figure 2.4: Distribution of earthquake magnitudes at different time intervals. Red horizontal lines give statistically significant magnitude threshold for catalogue completeness during specific interval.

Table 2.1: Chronological distribution of seismic events of M ≥ 5.0.

Abbreveriations: Sno – Serial number, dd/mm/yyyy – day/month/year, hr:min:sec – hour/minute/second, Mag – Magntiude, M Type – Magntitude type, SRC – Source

Sno	Date (dd/mm/yyyy)	Time (hr:min:sec)	Latitude	Longitude	Depth	Mag	M Type	SRC
1	00/00/1552	-	34.000	74.500	-	7.5		ISC
2	00/00/1662	-	34.000	75.000	-	7.5		ISC
3	15/07/1720	-	28.370	77.100	-	6.5		ISC
4	00/00/1735	-	34.000	75.000	-	7.5		ISC
5	00/00/1778	-	34.000	75.000	-	7.7		ISC
6	00/00/1784	-	34.000	75.000	-	7.3		ISC
7	00/00/1803	-	30.000	80.000	-	6.5		ISC
8	00/00/1803	-	34.000	75.000	-	7.0		ISC
9	01/09/1803	-	27.500	77.700	-	6.8		ISC
10	00/00/1809	-	30.000	79.000	-	6.0		ISC
11	00/00/1809	-	30.700	78.500	-	5.5		ISC
12	26/05/1816	-	30.000	80.000	-	6.5		ISC
13	00/09/1827	-	32.500	76.000	-	5.5		ISC
14	24/09/1827	-	31.600	74.400	-	6.5		ISC
15	06/06/1828	-	34.000	74.000	-	6.0		ISC
16	16/01/1842	-	27.000	78.000	-	5.5		ISC
17	05/03/1842	-	30.000	78.000	-	5.5		ISC
18	11/04/1843	-	30.000	80.000	-	5.0		ISC
19	21/01/1851	-	32.000	74.000	-	5.0		ISC
20	07/04/1856	-	31.000	77.000	-	5.0	Ms	IMD
21	11/08/1858	-	31.120	77.170	-	5.0		ISC
22	00/00/1863	-	33.500	75.500	-	7.0		ISC
23	00/04/1871	-	34.000	76.000	-	5.0		ISC
24	12/12/1875	-	31.600	74.400	-	5.5		ISC
25	30/05/1883	-	29.400	79.600	-	6.0		ISC
26	30/05/1884	-	33.500	75.500	-	7.3		ISC
27	06/06/1885	-	34.000	75.000	-	6.5		ISC
28	16/06/1902	-	31.000	79.000	-	6.0		ISC
29	04/04/1905	05:00:00.00	32.300	76.250	25	8.0	Ms	IMD
30	26/09/1905	01:26:09.09	29.000	74.000	-	7.1	Ms	ISC
31	28/02/1906	-	32.000	77.000	-	7.0	Ms	IMD
32	13/06/1906	-	31.000	79.000	-	6.0		ISC
33	11/12/1908	-	31.000	79.000	-	5.0		ISC
34	28/08/1916	06:29:30.30	30.000	81.000	-	7.5		ISC
35	28/04/1918	11:12:40.40	30.500	82.000	-	6.0		ISC
36	06/11/1925	19:20:45.45	26.500	81.500	-	5.5		ISC
37	27/07/1926	07:23:36.36	30.500	80.500	-	6.0		ISC
38	08/10/1927	10:34:28.28	30.500	80.500	-	6.0		ISC
39	11/05/1930	11:30:36.36	31.700	77.000	-	5.5		ISC
40	04/03/1932	23:50:55.55	33.500	81.000	-	5.0		ISC
41	14/04/1934	00:00:00.00	29.000	75.500	-	5.0		ISC
42	19/10/1934	20:58:20.20	33.600	82.000	-	5.7		ISC
43	05/03/1935	22:15:59.59	29.600	80.400	-	5.8		ISC
44	15/03/1935	10:33:52.52	29.600	80.400	-	5.4		ISC
45	30/04/1937	19:32:55.55	30.000	81.500	-	5.6		ISC
46	20/10/1937	01:23:46.46	31.100	78.100	-	5.9		ISC

47	10/04/1940	08:17:39.39	30.000	81.500	-	5.5		ISC
48	10/01/1941	07:38:14.14	34.000	77.000	-	5.7		ISC
49	04/06/1945	12:08:55.55	30.300	80.000	-	6.5		ISC
50	22/06/1945	18:00:51.51	32.600	75.900	60	6.5	Ms	ISC
51	10/07/1947	10:19:20.20	32.600	75.900	-	6.2	Ms	IMD
52	19/08/1947	20:07:06.06	31.200	79.900	-	5.9		ISC
53	05/02/1949	08:55:20.20	31.200	79.900	-	5.5		ISC
54	12/08/1950	03:59:06.06	32.600	75.900	-	5.5	Ms	IMD
55	13/08/1950	05:59:07.07	33.500	80.000	-	5.5		ISC
56	17/08/1950	03:26:15.15	33.500	80.000	-	5.5		ISC
57	12/09/1951	20:41:48.48	33.300	76.500	-	5.5		ISC
58	27/12/1952	18:45:37.37	31.200	74.800	-	5.5		ISC
59	23/02/1953	00:46:08.08	29.500	81.300	-	6.0		ISC
60	27/06/1955	10:14:09.09	32.500	78.600	-	6.0		ISC
61	10/10/1956	15:31:36.36	28.150	77.670	-	6.7		ISC
62	28/12/1958	05:34:38.38	30.010	79.940	-	6.3		ISC
63	31/12/1958	03:45:15.15	30.090	79.860	-	6.0		ISC
64	12/05/1959	00:35:46.46	32.500	79.000	-	6.3		ISC
65	27/08/1960	15:58:59.59	28.200	77.400	109	6.0		ISC
66	24/12/1961	07:13:30.30	29.430	80.830	59	5.5		ISC
67	17/06/1962	04:39:39.39	33.740	75.830	88	5.5		ISC
68	13/07/1962	05:01:06.06	30.640	79.480	-	5.5		ISC
69	14/07/1962	15:58:54.54	30.640	79.320	17	5.5		ISC
70	15/09/1962	12:35:08.08	31.900	76.200	-	5.5	Ms	IMD
71	30/01/1963	10:33:50.50	29.500	80.900	-	5.5		ISC
72	12/04/1963	00:41:29.29	32.000	78.790	36	5.4		ISC
73	22/04/1963	00:51:09.09	31.500	74.000	-	5.5		ISC
74	02/09/1963	01:34:30.30	33.960	74.730	23	5.3		ISC
75	27/11/1963	21:10:40.40	30.800	79.100	33	5.1		ISC
76	26/09/1964	00:46:03.03	29.960	80.460	50	5.8		ISC
77	06/10/1964	20:19:32.32	29.400	80.980	11	5.3		ISC
78	02/12/1964	08:21:42.42	29.580	81.100	3	5.1		ISC
79	20/12/1964	03:31:32.32	29.350	81.100	9	5.3		ISC
80	18/03/1965	02:41:30.30	29.550	80.260	67	5.0		ISC
81	31/05/1965	02:04:43.43	32.650	77.990	28	5.1	Mb	ISC
82	06/03/1966	02:10:52.52	31.510	80.550	5	5.3		ISC
83	06/03/1966	02:15:57.57	31.490	80.500	50	6.0		ISC
84	27/06/1966	10:41:08.08	29.620	80.830	33	6.0		ISC
85	27/06/1966	10:47:45.45	29.550	80.990	43	5.3		ISC
86	27/06/1966	10:49:51.51	29.500	80.900	72	5.4		ISC
87	27/06/1966	10:59:18.18	29.710	80.890	36	6.0		ISC
88	27/06/1966	11:21:42.42	29.570	80.820	26	5.2		ISC
89	27/06/1966	13:55:49.49	29.620	80.930	18	5.3		ISC
90	29/06/1966	00:42:10.10	29.690	80.860	21	5.2		ISC
91	05/08/1966	01:03:02.02	32.760	79.610	31	5.2		ISC
92	15/08/1966	02:15:28.28	28.670	78.930	5	5.6		ISC
93	16/12/1966	20:52:16.16	29.620	80.790	19	5.7		ISC
94	21/12/1966	22:10:59.59	29.650	80.790	21	5.2		ISC
95	20/02/1967	15:18:39.39	33.630	75.330	20	5.5		ISC
96	21/02/1967	12:37:43.43	33.650	75.440	20	5.0		ISC
97	18/12/1967	10:51:36.36	29.460	81.710	42	5.0		ISC
98	05/01/1968	06:42:44.44	30.410	79.250	7	5.0		ISC
99	31/05/1968	03:01:36.36	29.910	79.920	33	5.0		ISC
100	03/03/1969	06:20:21.21	30.040	79.840	18	5.0		ISC

101	12/02/1970	01:51:48.48	29.240	81.570	25	5.3		ISC
102	17/08/1972	18:14:25.25	30.750	78.420	33	5.2		ISC
103	06/09/1972	02:51:28.28	32.490	78.510	14	5.0		ISC
104	16/01/1973	21:31:26.26	33.290	75.830	39	5.1		ISC
105	01/04/1973	09:45:27.20	32.12	77.83	90	5.6	Mb	ISC
106	24/10/1973	05:23:51.51	33.150	75.920	37	5.3		ISC
107	24/10/1973	19:57:17.90	33.060	75.730	52	5.0	mb	USGS
108	23/12/1974	09:45:42.42	29.320	81.380	45	5.2		ISC
109	19/01/1975	08:00:18.18	32.300	78.660	-	5.1		ISC
110	19/01/1975	08:01:58.58	32.380	78.500	1	6.2		ISC
111	19/01/1975	08:12:10.10	31.940	78.530	49	5.8		ISC
112	19/01/1975	13:04:36.60	32.130	78.640	33	5.0	Mb	USGS
113	27/01/1975	08:10:18.70	32.460	78.730	33	5.0	Mb	USGS
114	02/02/1975	19:14:10.10	32.560	78.500	21	5.1		ISC
115	19/07/1975	06:10:54.54	31.950	78.590	-	5.1		ISC
116	29/07/1975	02:40:51.51	32.570	78.490	-	5.5		ISC
117	06/09/1975	04:44:33.33	29.210	81.950	-	5.1		ISC
118	19/09/1975	17:59:33.00	31.970	78.480	33	5.1	Mb	USGS
119	30/10/1975	14:36:42.50	32.900	75.990	34	5.2	Mb	USGS
120	05/11/1975	00:35:57.57	32.070	78.740	21	5.0		ISC
121	05/12/1975	07:37:11.11	33.100	76.130	24	5.3		ISC
122	10/12/1975	03:26:06.06	32.950	76.100	5	5.3		ISC
123	10/12/1975	05:03:42.30	32.830	76.190	33	5.0	Mb	USGS
124	11/12/1975	10:09:50.50	33.000	76.170	42	5.0		ISC
125	07/01/1976	00:24:53.53	32.970	76.120	40	5.3		ISC
126	08/01/1976	22:34:24.90	33.020	76.190	33	5.0	Mb	USGS
127	05/02/1976	12:04:31.31	31.240	77.030	5	5.0		ISC
128	10/05/1976	18:43:53.53	29.330	81.460	-	5.2		ISC
129	06/07/1976	02:55:49.49	32.440	78.350	24	5.1		ISC
130	08/09/1976	20:13:01.01	32.030	78.760	-	5.3		ISC
131	29/09/1976	02:51:27.00	29.820	81.390	33	5.0	Mb	USGS
132	29/09/1976	07:47:17.50	31.770	78.350	29	5.0	Mb	USGS
133	19/02/1977	06:15:25.25	31.800	78.430	40	5.4		ISC
134	27/03/1977	05:36:49.49	32.670	78.660	26	5.1		ISC
135	21/12/1977	02:08:10.00	32.840	76.630	33	5.1	Mb	USGS
136	14/06/1978	16:12:05.05	32.240	76.610	6	5.0	Mb	ISC
137	20/05/1979	22:59:11.11	29.930	80.270	-	5.7		ISC
138	28/12/1979	01:59:18.18	30.820	78.570	23	5.0		ISC
139	01/05/1980	05:43:12.70	33.020	75.920	33	5.0	mb	USGS
140	22/06/1980	14:38:53.53	30.130	81.760	-	5.1		ISC
141	29/07/1980	12:23:08.08	29.340	81.210	3	5.7		ISC
142	29/07/1980	14:58:42.42	29.630	81.090	-	6.1		ISC
143	23/08/1980	21:36:49.49	32.960	75.750	3	5.2	Mb	ISC
144	23/08/1980	21:50:01.01	32.900	75.800	12	5.2	Mb	ISC
145	22/09/1980	20:37:48.48	32.650	78.510	3	5.0		ISC
146	10/10/1980	14:02:26.70	29.170	81.210	33	5.0	mb	USGS
147	06/03/1981	05:58:48.48	29.800	80.660	23	5.1		ISC
148	15/05/1981	17:22:43.43	29.460	81.930	33	5.1		ISC
149	28/05/1981	23:14:05.05	31.830	78.430	-	5.2		ISC
150	13/06/1981	00:56:56.33	31.700	78.330	33	5.0	mb	USGS
151	27/02/1983	20:33:04.04	32.660	78.500	3	5.2		IMD
152	19/02/1984	15:46:26.26	29.840	80.540	21	5.1		ISC
153	14/03/1984	01:32:11.11	29.180	81.120	14	5.0		ISC
154	23/03/1984	00:34:08.72	29.990	78.870	33	5.1	mb	USGS

155	18/05/1984	04:28:52.52	29.520	81.790	-	5.6		ISC
156	26/04/1986	07:35:15.15	32.210	76.310	2	5.7		IMD
157	16/07/1986	23:03:07.07	31.050	78.000	40	5.6		ISC
158	21/09/1990	16:08:19.19	29.980	79.910	19	5.1		ISC
159	25/12/1990	03:56:46.46	33.310	75.760	51	5.3		ISC
160	19/10/1991	21:23:15.15	30.770	78.790	13	6.6		ISC
161	20/10/1991	05:32:26.85	30.790	78.690	26	5.3	ml	IMD
162	09/12/1991	01:02:42.42	29.510	81.610	3	5.6		ISC
163	02/06/1992	22:07:45.45	29.000	81.900	56	5.2		ISC
164	15/09/1993	15:08:14.14	33.400	75.700	-	5.0		ISC
165	17/07/1994	17:40:48.30	29.150	81.370	29	5.0	mb	USGS
166	26/03/1996	08:30:22.22	30.600	79.000	33	5.0		ISC
167	08/11/1996	00:54:13.13	29.300	81.640	33	5.0		ISC
168	05/01/1997	08:47:25.25	29.840	80.530	33	5.6		ISC
169	17/12/1997	05:52:31.31	33.480	74.900	52	5.8		IMD
170	30/03/1998	23:55:45.45	28.200	76.200	10	5.2		ISC
171	29/07/1998	18:11:07.07	30.820	75.980	15	5.0		IMD
172	28/03/1999	19:05:54.54	32.230	76.590	15	6.5		IMD
173	28/03/1999	19:36:06.06	30.270	79.330	3	5.1		IMD
174	30/03/1999	21:02:09.09	30.380	79.440	3	5.0		IMD
175	06/04/1999	19:37:24.24	30.480	79.560	16	5.0		IMD
176	14/04/1999	17:24:29.29	30.340	79.380	9	5.1		IMD
177	03/03/2000	02:58:01.01	33.960	81.730	33	5.3		IMD
178	19/10/2000	01:49:51.51	33.460	75.980	15	5.2		IMD
179	11/07/2001	19:44:35.35	29.380	81.260	10	5.6		IMD
180	27/11/2001	07:31:53.53	29.530	81.760	33	5.5		IMD
181	27/11/2001	08:53:58.58	29.360	81.700	33	5.3		IMD
182	27/11/2001	17:56:55.11	29.510	81.740	33	5.1	mb	USGS
183	27/01/2002	22:33:44.44	33.110	75.830	10	5.1		IMD
184	04/06/2002	14:36:06.06	30.420	81.430	10	5.0		IMD
185	04/09/2002	16:11:51.51	31.740	77.910	66	5.1		IMD
186	26/10/2004	02:11:36.36	30.780	81.030	10	6.1		IMD
187	06/11/2005	01:36:56.67	29.730	81.870	49	5.0	mb	USGS
188	14/12/2005	07:09:54.19	30.480	79.250	44	5.1	mb	USGS
189	05/05/2006	08:00:28.78	29.500	81.00	17	5.0	mb	USGS
190	26/05/2006	00:41:41.66	33.150	76.240	66	5.0	mb	USGS
191	22/07/2007	23:02:13.22	30.910	78.316	15	4.9	Ml	WIHG

times. The shaking of this earthquake was felt in the whole northern Indian region including New Delhi, the capital and highly populated city of India. It was preceded by M5 magnitude earthquake, intermediate magnitude foreshock occurred few minutes before its occurrence. About 20 aftershocks of M≥4.0 were also reported by Bangar (1976). The Meizoseismal area lies to the northeast from Kangra-Chamba region and covers an area of 89 sq. km (Narula and Shome, 1992). In this survey 42 casualties were reported and about 278 houses were damaged. Besides landslides and some ground

fissures were also reported. The isoseimals of this earthquake were reported by Narula and Shome (1992) and were shown in Figure 2 of their paper.

The Fault plane solutions of the main shock and big sized aftershocks showed normal fault mechanism with strike of nodal planes oriented in N-S or NNW-SSE directions (Chaudhary and Srivastava, 1976; Molnar and Tapponnier, 1978). The strikes of these nodal planes coincide with that of the Kaurik-Change fault (Chaudhary and Srivastava, 1976) and also match with the trends of the isoseismal lines of the mainshock.

2.3.4. The Dharamsala Earthquake of 14th June 1978

An earthquake of M_L 5.4 occurred in the night of 14th June 1978 that shook the Kangra valley and was felt in the entire Himachal Himalaya as well as adjoining areas. Its epicenter was located just north of the epicentre of Kangra earthquake of 1905 under the Dhauladhar ranges (**Figure 2.5**). According to Narula and Shome (1992), this event was also preceded by smaller size foreshocks. No casualty was reported, however some old buildings collapsed around Dharamsala town and many stone masonry buildings developed cracks. The maximum intensity assigned to this earthquake was VI (Kumar *et al.*, 1981). The isoseismals were elongated in N-S direction. Kumar *et al.* (1981) obtained a source mechanism showing strike slip movement along N-S direction. On the other hand Das Gupta *et al.* (1982) inferred thrust fault mechanism with similar strike direction that is perpendicular to the major tectonic trends of the Himalayas. This earthquake was located in a region where seismic activity is always very high (**Figure 2.5**). The anomalous mechanism of this earthquake and the clustering of seismicity could be related to local stress accumulation and release behavior. This local stress buildup may be treated as the consequences of interaction of two transverse features in this part of the study region where the thrusts PT, MBT and PMT are dipping towards northeast, while RW and STD in the eastern part are dipping.
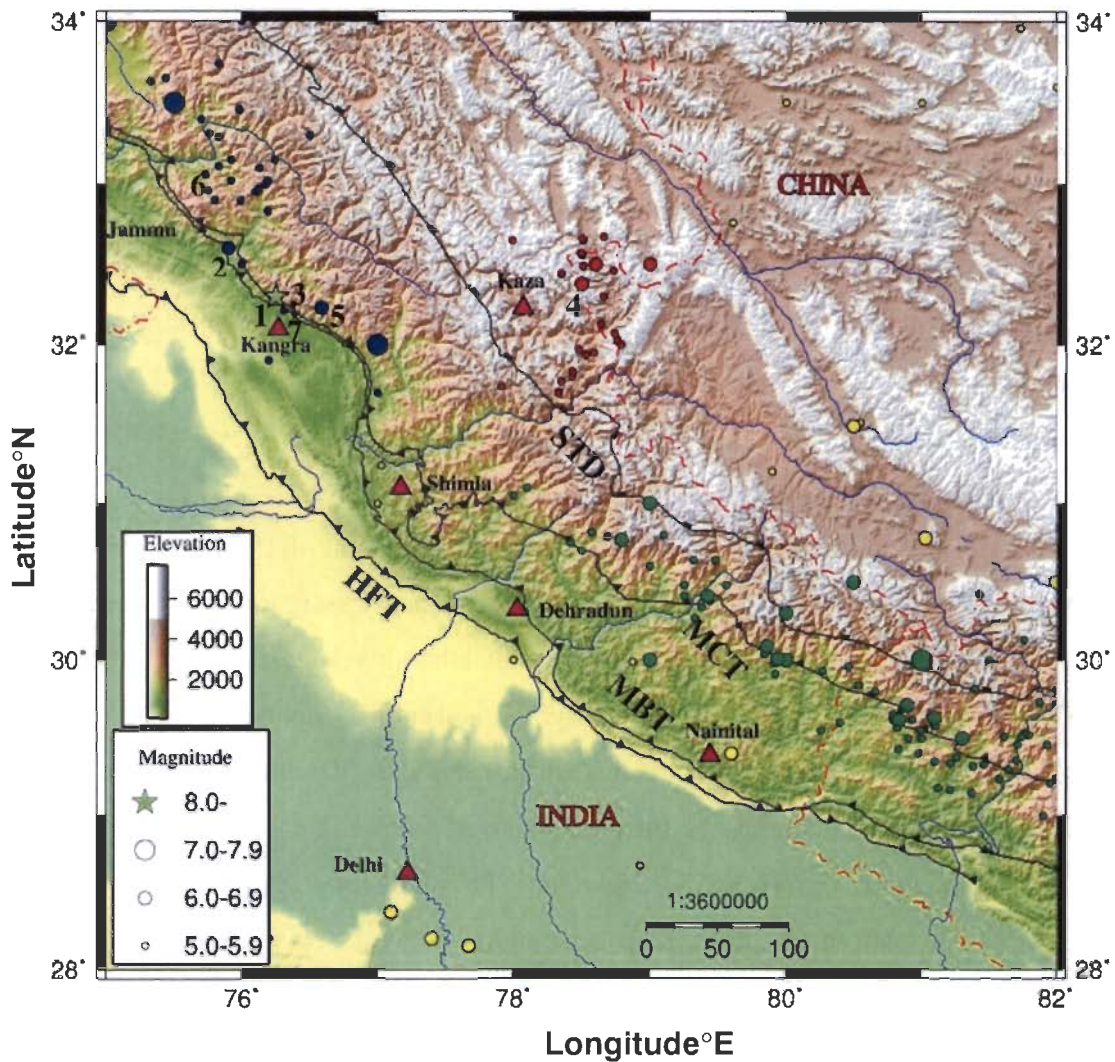
Figure 2.5: The map showing the epicentral distribution of earthquakes M ≥ 5.0 that occurred in NW Himalaya since 1552. The star (1) denotes the location of devastating M8.0 Kangra earthquake of 1905. Blue color represent the distribution of epicentres in Kangra-Chamba region, green color in Garhwal-Kumaon and western Nepal region, red color Kinnaur region and yellow color is the location in other parts. HFT: Himalayan Frontal Thrust, MBT: Main Boundary Thrust, MCT: Main Central Thrust and STD: South Tibetan Detachment. Epicentral locations of different earthquakes as 2: M6.5 Chamba, 1945; 3: M5.1 Dharamshala, 1968, 4: M6.5 Kinnaur, 1975, 5: M5.4 Dharamshala, 1978, 6: M5.4 Jammu-Kathua, 1980, 7: M5.7 Dharamshala, 1986.

2.3.5. The Jammu-Kathua Earthquake of 24th August 1980

This earthquake occurred at the NW part of the Kangra-Chamba region on 24th August 1980. This is a bifocal event because two events of similar magnitude (M5.5 and M5.4) (Narula and Shome, 1992) occurred within 12 minute interval having epicentre location distance of only 21 km with each other. Two isoseimals were reported, both elongated in same direction along the major tectonic trend of the region having maximum intensity VII on MM scale. The isosiesmals of these two events were drawn

to the north and south of the MBT. These two events are related with the twin sources, the asperities at the intersection of MBT and the basement fault in extension of surface trace of Suruin-Mastgarh anticlinal axis with the detachment surface (Narula and Shome, 1992). However based on the time gap of about 12 minutes between the occurrence of these two events, Narula and Shome (1992) categorized them as two separate events instead of a bifocal event and opined that the first one triggered the second one.

2.3.6. The Dharamsala Earthquake of 26ᵗʰ April, 1986

The epicentral locations of this M5.7 event, M5.0 event of 1978 and M8.0 event of 1905 are very close to each other. The maximum intensity assigned to this earthquake is VIII on MM scale that caused damage around Dharamsala in the Kangra-Chamba region of Himachal Himalayas. The intensity VII isoseismal encloses an area of about 100 sq. km. The trend of isoseismal for this earthquake was different as compared to the above mentioned 1978 event as the inferred strike of source fault was along the major tectonic units aligned N55°W-S55°E. However, the attenuation characteristic obtained from the damage pattern of different isoseismals also favors co-seismic motion along N-S direction, which again indicates the complex nature of the tectonic environment due to presence of two transverse tectonic features. The frequent occurrence of 5M earthquakes in this part of Kangra-Chamba region in the epicentre zone of Kangra earthquake may be attributed to the oblique local convergence of crustal structures.

2.4. MACROSEISMIC STUDIES AND DAMAGE ASSESSMENT

The amount of shaking of earth's surface during strong earthquake depends on the size of the earthquake. The intensity of shaking is highest in the epicentre zone of the earthquake and it goes on decreasing while moving away from this zone. Bigger the size of the earthquake stronger the shaking effect. Also deeper the earthquake source lower is the amount of shaking but larger is the area of impending effect. In general in the NW Himalaya, the seismicity is shallow focused (Seeber *et al.*, 1981; Ni and Baraznagi, 1984; Khattri, 1987; Kayal, 2001; Bhattacharya and Kayal, 2005; Kumar *et al.*, 2009) and hence the big size earthquakes mentioned in the previous section were mostly located in the upper crust upto 25-30 km depth from the earth's surface.

The intensities of the earthquakes are measured through the assessment of ground shaking, the damage scenario of manmade structures and human casualities after

the occurrence of the earthquake and used for macroseismic studies. Based on the collected data from different places near to the epicentre of the earthquake, the isosiesmal intensities are connected to obtain isoseismal maps. These maps are important for regional earthquake hazard studies which can be utilized for future planning, development and settlement. The macroseismic studies have been done in the study region during the occurrence of big size earthquake in last century and during the recent Kashmir earthquake of 2005. These studies have been performed by Middlemiss (1910), Kaila and Sarkar (1978), Kumar *et al.* (1981), Kumar and Mahajan (1990), Narula *et al.* (1995, 2000), Ambrayes and Douglas (2004), Mahajan and Virdi (2005) and Mahajan *et al.* (2006) for different earthquakes. The amateur seismic centre (www.asc-india.org), Pune India is also maintaining the records of published isoseismal maps for the Indian earthquakes. The isoseismal maps collected from this web site are shown in **Figure 2.2** for the M7.6 Kashmir earthquake of 2005, the M6.4 Chamoli earthquake of 1999, the M6.8 Uttarkashi earthquake of 1991 and the M8.0 Kangra earthquake of 1905 where the variation of shaking effect has been shown with different colors. These maps indicate that a strong effect was observed in the present study region during these earthquakes. It is clear that the strongest effect in this region was observed during Kangra earthquake of 1905 when wide spread damage and causalities occurred.

In the seismotectonic atlas of India (prepared by Geological Society of India (GSI in 2002) the isoseismal maps of different intensities reported during the bigger size earthquakes of this region are shown. These maps of the earthquakes mentioned in the previous sections are shown in **Figure 2.3**. On an average these maps indicate that the isoseimals are elongated to NW-SE coinciding with the strikes of the major tectonic faults of the region which has been also reported by Mahajan et al. (2006) for the recent M7.6 Kashmir earthquake of 2005. Therefore the shaking effect attenuates fast perpendicular to the strike of major tectonic features in this region. During M8.0 Kangra earthquake of 1905 the shaking effect was attenuated fast in the westward direction and extended towards southeast.

2.5. CATALOGUE COMPLETENESS

The assessment of the seismic hazard and other studies mainly depends upon the magnitude range of the earthquakes of any region. The uniform validity of this magnitude range is described as the completeness of the seismic catalogue or the identification of minimum magnitude threshold. **Figure 2.4** presents a plot of magnitude

versus earthquake origin time obtained from the catalogue compiled by WIHG highlighting the magnitude threshold for different time periods. It includes all the earthquakes up to a maximum focal depth of 100 km. However, most of these events occurred within crust. With the up gradation of global and regional seismic networks the threshold level of seismic events changed from time to time (**Figures 2.4a, b and c**). It is obvious that the completeness of the catalogue varies greatly from time to time and especially during the last century. One can easily observe remarkable increase in the registration of seismic events in 1965, 1988 and 1999 (**Figure 2.4b**). The recent data are evidently more regular and complete (**Figure 2.4c**).

2.5.1. Completeness of Catalogue

With the inclusion of local networks, up gradation of existing network and reshuffling of seismic stations, the seismic scenario of a region is changed. Based on statistical approach, Gutenberg and Richter (1944) have developed the relation of number of earthquake occurrence for different magnitudes for a region that is valid only if the recording is for longer period. This is a logarithmic relation in which the number of earthquakes decreases logarithmically with the increase of magnitude. **Figure 2.6** presents the histograms obtained using the empirical relations for two time intervals of 1963-2005 and 1999-2005 for which complete data set for earthquakes with certain magnitudes are available. The value of argument for which the empirical distribution function has a straight line behavior till the maximum observed magnitudes gives statistically significant minimum value of magnitude. This minimum value is known as threshold magnitude above which the catalogue is complete. The threshold magnitudes 4.5 and 2.5 were derived from the reliability of reported seismic events in the catalogue of western Himalaya. The empirical relation for 1963-2005 indicates two types of relations between magnitude and the frequency of their occurrence. For magnitude 4.5 and above it gives a straight line of least square fit between the frequency and the magnitude of the earthquake, this straight line can also be obtained for lower magnitude with lower slope which shows that the data is complete for lower magnitude for small regions or it is complete for lesser time period. On this basis the analysis for time period of 1999-2005 is done separately.

Figure 2.7a presents spatial distribution of earthquake epicenters for all events within the catalogue in which the earthquakes of magnitude more than 6.0 are shown with blue color circles. The seismic events belonging to time interval 1963-2005 and

having magnitudes more than 4.5 are plotted in **Figure 2.7b** in which the earthquakes of M6.0-6.5 are represented with purple color small circles and the earthquakes of magnitudes 6.5 and above are shown with purple color double circles. These seismic events are utilized for further analysis in the present study. The distribution of big size earthquakes (**Figure 2.5**) and related seismic energy (**Figure 2.8**) shows the segmentation of seismic activity in NW Himalaya. Based on this, the two zones of high seismic activity shown with polygons Q1 and Q2 are compiled separately to observe the presence of any hidden periodicity. Besides that **Figure 2.7b** presents partition of the region into 2 polygonal parts: northwestern Q1 and southeastern Q2, the intermediate region along the adjoining boundaries of these polygons has less seismic activity.
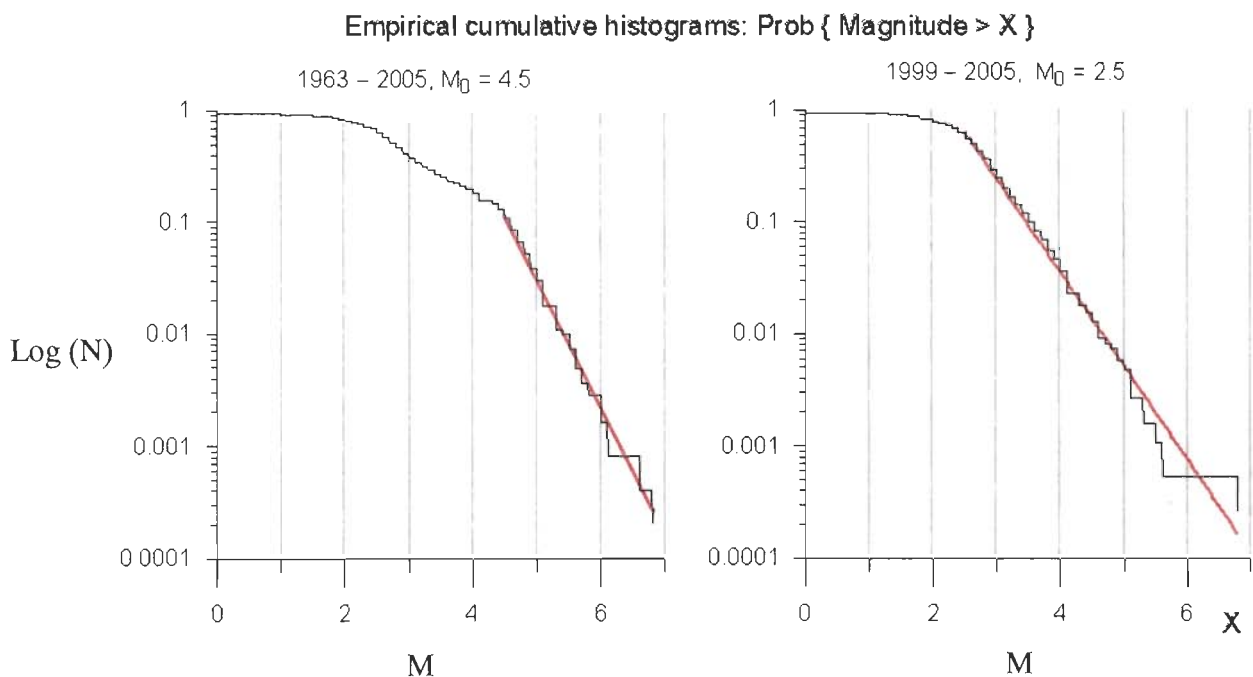
Figure 2.6: Empirical functions of distribution of magnitudes values for periods 1963-2005 and 1999-2005. The values M_0 are statistically significant values of lower magnitude. Here M is the magnitude and N is the number of earthquakes with magnitude less than or equal to M.

2.5.2. Removal of Aftershock Activity

The inclusion of aftershock events disturbs the randomness behavior of main sequence events of any catalogue. Different procedures are tested to completely identify the aftershock density at a distance 'r' from the location of a main shock. For analysis of hidden periodicities, it is necessary to exclude the aftershock activity of the main big earthquakes. For this purpose the simplest method (Gardner and Knopoff, 1974) was

used. The advantage of this method is that it is casual, i.e. does not use the future information for decision whether the considered event is main shock or aftershock. This property is important for applications to earthquake prediction. Let t_j, M_j be the origin time and the magnitude of the main shock. The seismic event t_k, M_k (origin time and magnitude) is considered its aftershock and removed from the catalog if it satisfies the criteria of $M_k < M_j$, $t_j < t_k < t_j + \tau(M_j)$ and the distance ρ_{jk} between epicenters of events j and k obeys the condition of $\rho_{jk} < r(M_j)$ within radius r from the location of the main shock M. For culling the aftershocks of any event, the small step of time duration from the origin time of main shock is obtained using the relation, $\tau(M) = \tau_0 \cdot 10^{a(M-M_0)}$ and its value for distance from the source origin of the main shock is taken as $r(M) = r_0 \cdot 10^{b(M-M_0)}$. Following the procedure and criteria of Gardner and Knopoff (1974) we tested this data set and obtained the parameters of $M_0 = 4$, $\tau_0 = 30$ days, $r_0 = 10$ km, $a = b = 0.5$ to remove the aftershocks. The first event in the catalog is regarded as a main shock, which may or may not be the largest event.

2.6. SPATIO-TEMPORAL MODELING OF SEISMOLOGICAL PARAMETERS

After depletion of aftershocks data as described in the previous section, the compiled seismic catalogue consists of 2628 seismic events that occurred during 1550 - 2005. However, before 1960 only few seismic stations existed in India and adjoining regions. Therefore only big magnitude earthquakes were documented. For these events also the epicentral location is not very accurate and in few cases the location was approximated using iso-seismal data obtained through information about loss of human life and property. The seismological network was significantly improved after 1960 due to which magnitude threshold obtained in 1965 showing complete documentation of seismic events for earthquakes came down to 4.5. This threshold came down to 4.3 in 1985, 3.3 in 1990 and 2.5 in 1999 with the improvement of seismological networking in the NW Himalayas. The complete catalogue for M>2.5 have 1856 earthquakes for a period of 1999 to 2005. These 1856 earthquakes are used for most of the modeling parameters of seismology using spatio-temporal variation. However, few additional analyses have also been done using the whole catalogue data from historical time for only major earthquakes.

The compiled catalogue of WIHG having historical and instrumental earthquakes from 1552 till 2005, the digital elevation model in grid 30″ x 30″ and linear tectonic structures containing active thrusts and non-active thrusts are used to develop different seismic models. These data were used for compiling the following three models based on grid methodology:

1. Spatial model of seismic network sensitivity.

2. Spatial model of seismic activity.

3. Spatial model of b-value.

4. Spatial model for Earth's surface elevation relief.
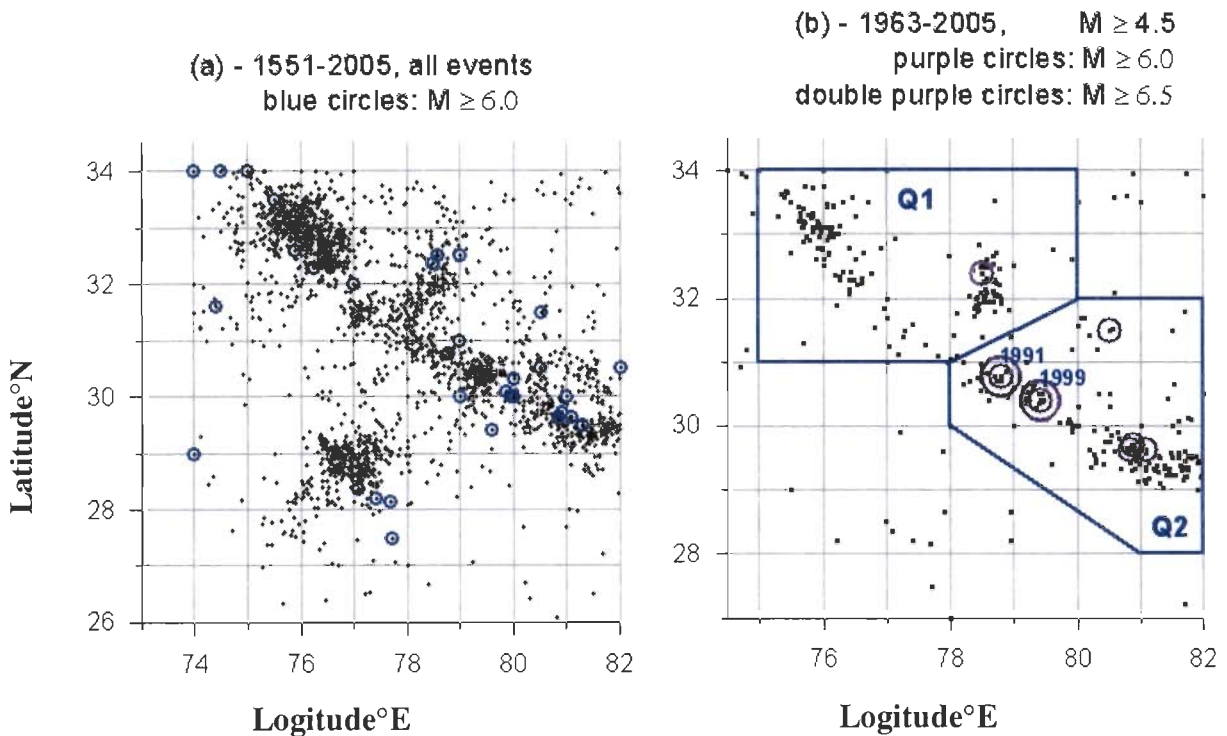
Figure 2.7: Space-Time distribution of seismic events since historical times (a) All events from historical to 2005, Blue circles represent earthquakes with M ≥ 6.0; (b) Earthquakes of M ≥ 4.5 for time interval 1963-2005, Purple double circles represent earthquake of M ≥ 6.5 while single purple circles represent earthquakes with M 6.0-6.5; Most seismic active region is split into 2 parts (Q1 and Q2).
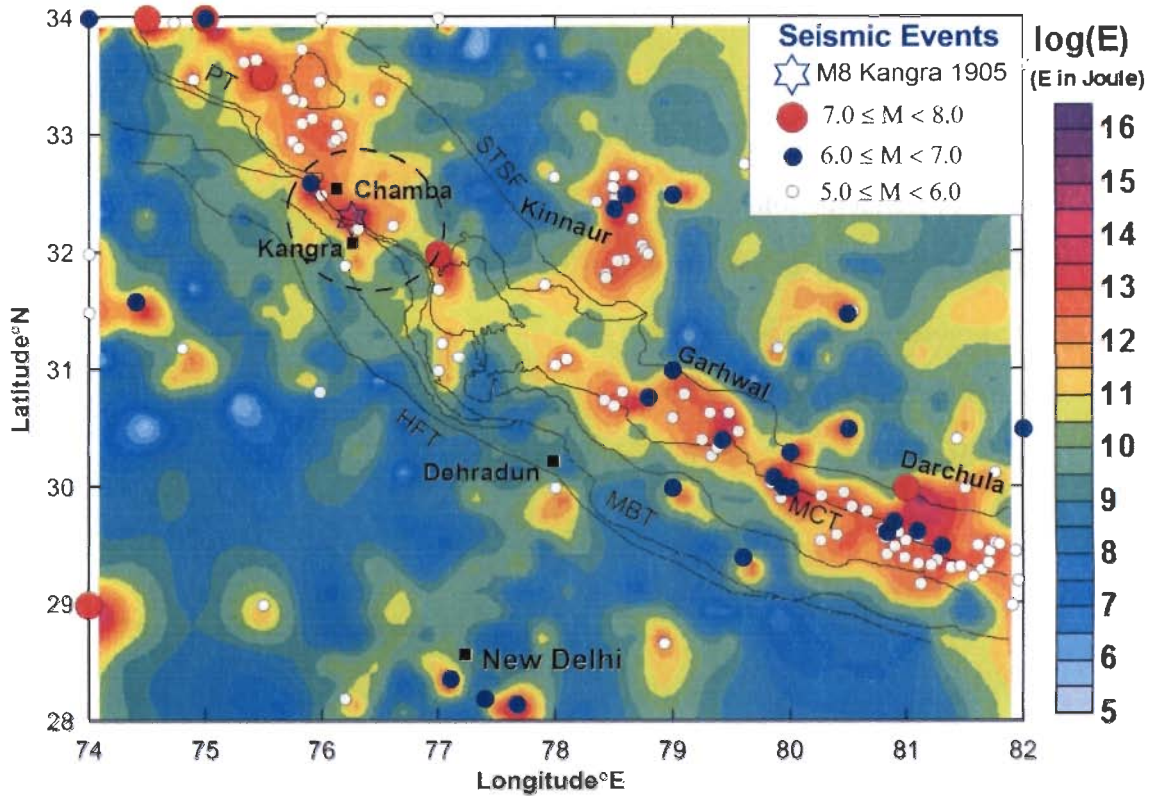
Figure 2.8: Map of NE Himalaya showing the cumulative seismic energy released from all magnitude earthquakes during 1551-2005. The spatial distribution is mapped by computing the cumulative energy for circular area of radius 20 km with 10 km overlap. The epicenters of big size earthquakes (M ≥ 5.0), including 1905 great Kangra earthquake, are marked with circles. Well defined zones of intense seismicity are centred on Kangra-Chamba, Kinnaur, Garhwal and Dharchula regions. Despite very few big earthquakes, the Kangra-Chamba region remains zone of intense seismicity even when examined for shorter data sub sets.

To compile these models the seismic records are scanned with moving spatial window for specified time window. The different seismic parameters are estimated from the earthquake records taking epicenters inside the window. Evidently, the accuracy of estimates depends on the density of epicenters. The initial analysis of catalogue completeness is taken in to consideration to fulfill the condition of statistical uniformity for a set of epicenters inside the window. Therefore, the window must cover homogeneous area for seismotectonic parameterization. The window size should be appropriate to the tectonic and seismic homogeneity. If the window size is more then the estimate will be doubtful due to mixing evidences from different probabilistic distributions. However, very small window size produces uncertainties because of small number of a sample set. Using different data sets, a compromise is adopted for adaptive

fitting of the window size. Therefore, the analysis procedure adopted the criteria of smaller window size for the region of more dense seismic events and wider region for the part having sparse seismicity.
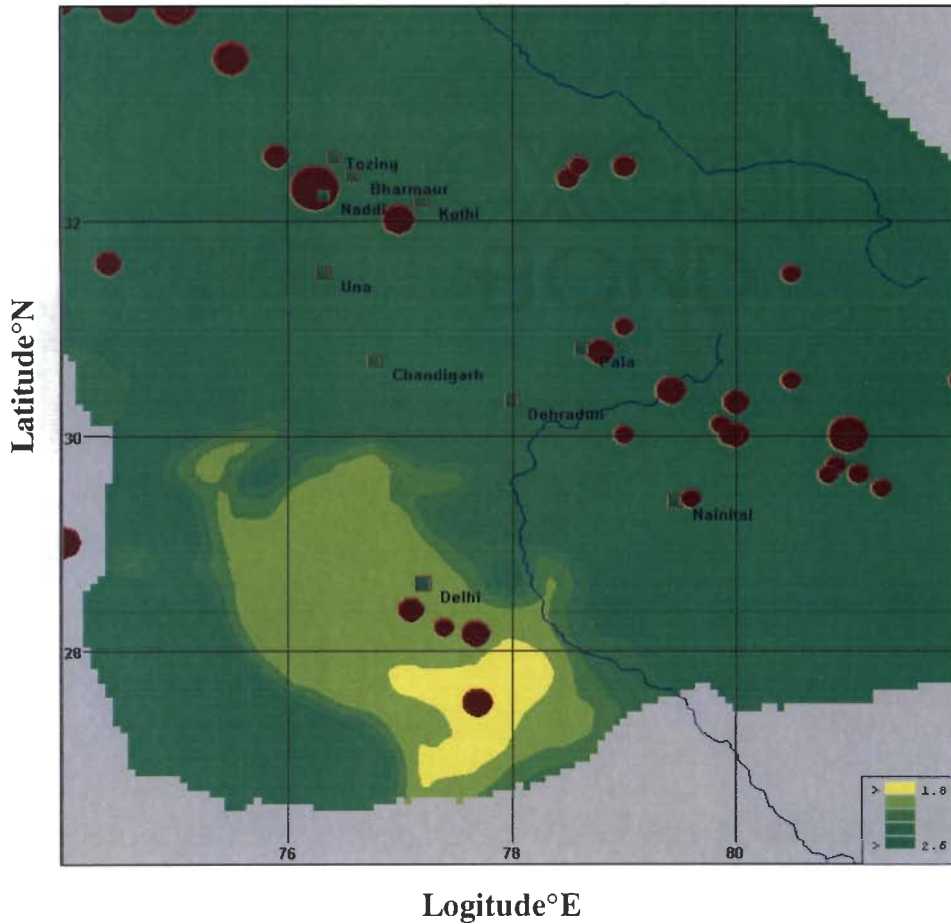
Figure 2.9: Spatial pattern of minimal magnitude representation estimated for the catalogue for a period of 1999 - 2005. Red circles represent the location of large earthquake with increasing radius for increasing magnitude. Location of cities and towns are shown by green rectangles.

For smoothing the effect of seismic parameters for different regions of NW Himalaya, the moving window is taken for cylindrical region with fixed height equal to temporal interval for the data of the period of 1999 to 2005. The radius of cylinder varies from R_1 to R_2, the two limits of the radius of circular area. The minimal number of seismic records in a window is N_{min} and the nominal number of events is specified as N. In the adaptive window algorithm (Gitis *et al.*, 2008), the axis of the cylinder is coincident with a grid point (λ, φ, t), where λ is the latitude, ϕ is the longitude and t represents the time respectively for the seismic catalogue. If the number of events in a

45

cylinder of radius R_1 is $n \geq N$ only then the data is used for estimation. If the number of events in cylinder of radius R_2 is $n < N_{min}$ then the data is rejected. However, if the number of seismic records in cylinder of radius R_2 is $N_{min} \leq n \leq N$, then it is included for estimation of parameter. If number of events in cylinder of radius R_2 is $n > N$, then to select N the nearest events to the grid point (λ, φ, t) are used.
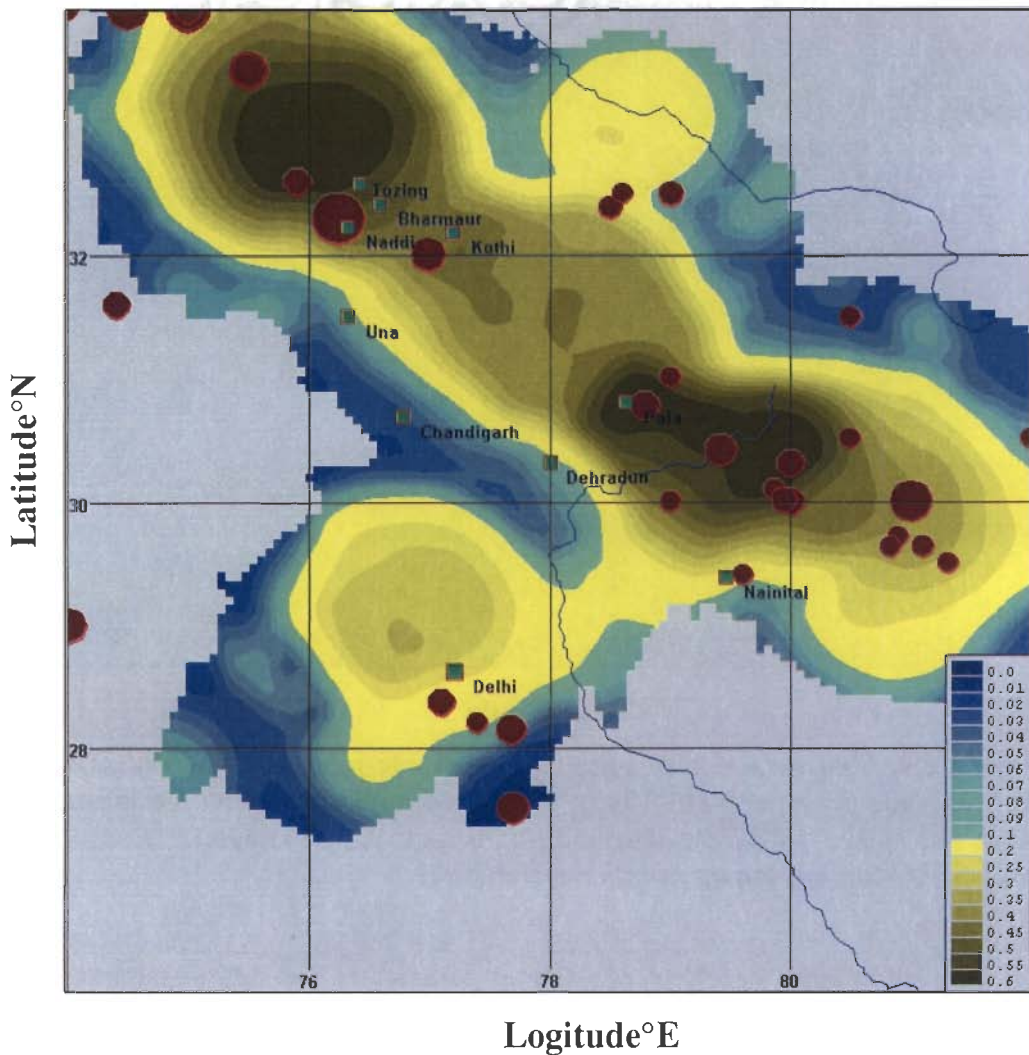
Figure 2.10: Spatial pattern of seismic activity estimated by the WIHG earthquake catalogue for a period of 1999 - 2005. Red circles represent the location of large earthquake with increasing radius for increasing magnitude. Location of cities and towns are shown by green rectangles.

2.6.1. Spatial Model of Seismic Network Sensitivity

The foremost requirement of these models is homogeneity of the catalogue for each part of the investigated region. For time domain requirement, the catalogue is uniform for M2.5 and above from 1999 to 2005. The minimal representative magnitude of earthquakes 'M_0' is the smallest magnitude of the compiled data in the Gutenberg-Richter (Gutenberg and Richter, 1944) relation of frequency and magnitude above which the relation is valid. For the specified period of particular region, the numbers of earthquakes decrease logarithmically above M_0 as per the relation given below

$$\log_{10}N = a - b\ M_0 \qquad\qquad \text{------------ 2.1}$$

where a and b are the constants that define the seismic behavior of the region. However, the value of M_0 depends on number of seismic stations, their spatial distribution, and sensitivity from one part to other in particular region of study. For this analysis, the recent catalogue is processed to check the variability in minimum magnitude representation in the NW Himalaya for spatial variability. The methodology for spatial calculation of M_0 is based on testing of statistical hypothesis. This moving window calculation method was developed by Pisarenko (1989), which was modified by Smirnov (1995) to develop an algorithm for calculation. Smirnov and Gitis introduced this algorithm in the year of 1994 for GIS GeoTime (Gitis *et al.*, 1994) using which the present processing and analysis has been done.

For developing the spatial model of M_0 for the NW Himalayas using seismicity from 1999 to 2005, a grid of size 4' x 4' is taken with the following parameters: R_1=50 km, R_2=200 km, N_{min}=25, N=75. In this calculation the grid-based model of M_0 is smoothed with moving window of R=20 km. The obtained results of earthquake magnitude representation variation are shown in **Figure 2.9.** It indicates that the minimum magnitude representation for NW Himalaya is 2.5 for most of the parts after 1999. Only a small area that includes New Delhi (capital of India) and adjoining region has the minimum magnitude in the range of 1.0 – 1.5 due to a local network of Indian Meteorological department (IMD). IMD has been operating this local network from last few years. The minimum magnitude representation for the Kangra-Chamba region is 2.5. The red circles in **Figure 2.9** show the location of major earthquakes since historical time and the rectangle represent few well known places of the region.
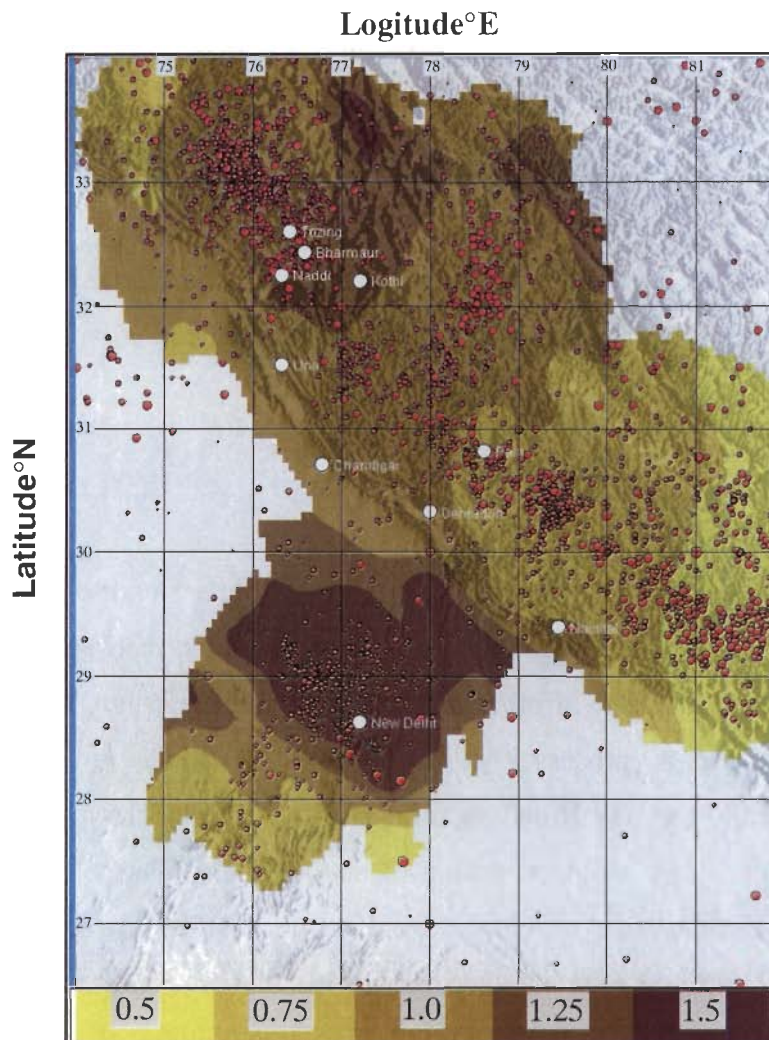
Figure 2.11: The Spatial model of b-value for 1999 – 2005 estimated for NW Himalaya. The seismicity is shown with red circles. Location of cities and towns are shown by white circles.

2.6.2. Spatial Model of Seismic Activity

The Himalayan region has high seismic activity and hence each part in the Himalayas and adjoining region should have micro earthquake activity that can be obtained using dense local networks if the duration of investigation is at least one year. Therefore the present study of minimum magnitude representation highlights the strength of local seismic networks. If the minimum magnitude representation for a particular region is up to micro earthquake level for a given time duration, then the seismic records above this magnitude can be used to check the variability in seismicity during this time. Therefore, the catalogue data of NW Himalaya from 1999 to 2005 is

used to observe the density of the seismic event. The seismic activity $A(\lambda, \varphi, t)$ is taken as normalized based on spatio-temporal window for the number of earthquakes adjusted to magnitude, $m \in (m_A - \dfrac{\delta m}{2},\ m_A + \dfrac{\delta m}{2})$ for all the events above minimum magnitude that is 2.5 as described in previous section. The calculation of seismicity is based on the following relation (Gitis $et\ al.$, 2008).

$$A(\lambda, \varphi, t) = kN_{m_0}(\lambda, \varphi, t)[\exp(-\beta(\lambda, \varphi, t)(m_A - \frac{\delta m}{2} - m_0(\lambda, \varphi, t)))$$
$$- \exp(-\beta(\lambda, \varphi, t)(m_A + \frac{\delta m}{2} - m_0(\lambda, \varphi, t)))]$$

------------ 2.2

where: $N_{m_0}(\lambda, \varphi, t)$ is the number of earthquakes of magnitudes $m \in (m_0(\lambda, \varphi, t),\ M_{max}(\lambda, \varphi, t))$, $k = \dfrac{1}{ST}$, S is a spatial size of the window and T is the temporal interval of the window.

This spatial model of seismic activity in grid of 4′ x 4′ is calculated with the parameters: R_1=50 km, R_2=120 km, N_{min}=20, N=70. Grid-based model of seismic activity smoothed with moving window R=20 km is shown in **Figure 2.10**. The calculation shows that highest density of seismicity is represented by 0.6 in the NW Himalaya. The NW-SE trend coinciding with major tectonic features (**Figures 2.10 and 2.1**) of the region shows high seismic activity in the Himalayan region compared to the adjoining parts. However, almost a vertical zone that passes through New Delhi and crosses the Himalaya also has more seismic activity compared to its surroundings (**Figure 2.1**). The high seismic activity of this zone is also supported by major events that occurred near New Delhi and Tethyan sequences near Kinnaur in Himalaya. This section passes through the Delhi-Haridwar ridge that may be the one reason for high seismic activity. This investigation shows that the Kangra-Chamba region has highest seismic activity. The Garhwal-Kumaon region also has higher seismicty although less dense than Kangra-Chamba region but the major events are more frequent in the Garhwal-Kumaon region compared to the Kangra-Chamba region. The other result of this study is that the intermediate part between Kangra-Chamba and Garhwal-Kumaon through which the Delhi-Haridwar ridge passes has less seismic activity than adjoining regions.

2.6.3. Spatial Model of b-Value

The next investigation includes *b*-value which is an important parameter of Gutenberg-Richter relation given in equation 2.1. The procedure adopted for Maximum likelihood estimation (*Gitis et al.*, 2008) of *b*-value is as follow:

$$b(\lambda, \varphi, t) = \beta(\lambda, \varphi, t) \lg e \approx 0.43\beta(\lambda, \varphi, t) \qquad \text{------------ 2.3}$$

where $\beta(\lambda, \varphi, t) = (\frac{1}{N_{m_0}} \sum_{m_i \geq m_0} (m_i - m_0(\lambda, \varphi, t)))^{-1}$, $N_{m_0} = N_{m_0}(\lambda, \varphi, t)$ is the number of

earthquakes for $m \in (m_0(\lambda, \varphi, t), M_{max}(\lambda, \varphi, t))$.

Spatial model of *b*-value in grid of 4′ x 4′ is calculated with the parameters: R_1=50 km, R_2=120 km, N_{min}=20, N=70. For this calculation, the Grid-based model of *b*-value was smoothed with moving window of R=20 km. As shown in **Figure 2.11**, the spatial variation of *b*-value is calculated only for that part of NW Himalaya which has sufficient events satisfying the procedure of calculations for different windows. The observed variation of *b*-value for this region is from 0.5 to 1.6 indicating higher number of big size earthquakes than small magnitude earthquakes for low *b*-value and vice-versa. A considerable part adjoining to NW Himalaya near to New Delhi has high *b*-value which also shows a lowest minimum magnitude representation as shown in **Figure 2.9**. This indicates that most of the stored tectonic stress in this part is released due to frequent occurrence of small magnitude earthquakes. The Kangra-Chamba part also has higher *b*-value than other part of Himalayan region of the NW Himalaya while the Garhwal-Kumaon region has lowest value in the study region. It is also quite obvious in **Figure 2.8** that the number of small magnitude earthquakes is more in the Kangra-Chamba than Garhwal-Kumaon. However, the scenario of occurrence of bigger size earthquakes is opposite for these two parts of the NW Himalaya. It indicates that the stored stress in the Kangra-Chamba is released by frequent occurrence of smaller size earthquakes and the region has less strength to hold the energy for the rupture due to big earthquake.

2.6.4. Spatial Model for Earth's Surface Elevation Relief

The modeled digital elevation map of northern India and the location of the bigger size (M $\geq$ 6) earthquakes are shown in **Figure 2.12**. The Himalayan seismicity is mostly correlated with heterogeneities of Earth's crust, which are manifested by Earth surface

relief in the lithosphere as shown in **Figure 2.12**. Taking into account this hypothesis we calculated root mean square (RMS) of the Earth surface elevations with moving window R=15km. The surface elevation in northern India clearly indicates a higher surface relief with RMS deviation > 500 m from the average value in the Himalayan region identifying different Himalayan peaks. There is good correlation of location of bigger size earthquakes and elevations. Most of Himalayan earthquakes with M ≥ 6 are located in zone with RMS deviation in elevation > 500 m.
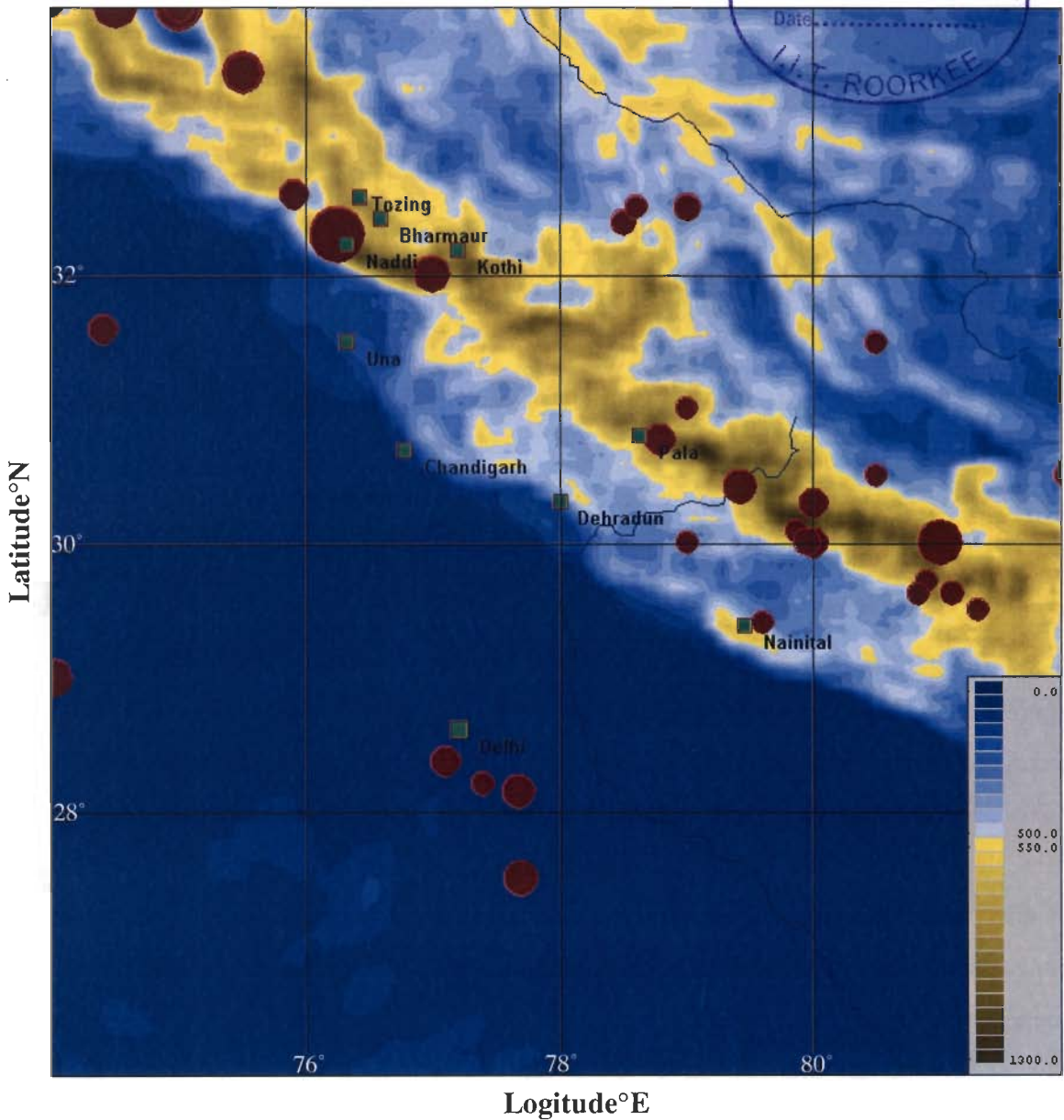
Figure 2.12: The grid-based model of root mean square of the Earth surface elevations with moving window R=15km and the epicenters with M >= 6 of WIHG earthquake catalogue from 1552 - 2005.

This is the zone where Himalayan mid-crustal ramp under the southern Higher Himalaya has been proposed on the basis of various geophysical studies (Gahalaut and Kalpna, 2001; Yeats and Thakur, 1998). Throughout Himalaya and mainly in NW Himalaya, a narrow belt between Higher and Lesser Himalaya shows intense seismic activity. The region is close to the ramp and better known as Himalayan Seismic Belt (HSB). Yeats and Thakur (1998) has given a fault-bend fold model where the megathrust drives southward and upward over the ramp and the axial surface of the fold is active only at crustal scale. The central Himalaya moves southward as a fault bend fold due to slip by earthquakes that nucleate at the detachment under Himalaya of this region. That study also shows maximum relief over the structural ramp indicating high uplift rates over the ramp. Therefore a high uplift rate in the central Himalaya above the frontal ramp is due to thrust movement during megathrust earthquakes identified by recent compiled seismic catalogue.

2.7 PURPOSE OF PRESENT WORK AND DESIGN OF OBSERVATION NETWORK

The Kangra-Chamba sector of NW Himalaya is one of the seismo-tectonically most active regions of the Himalaya. It is the source zone of 1905 devastating earthquake (M8.0) that killed more than 20,000 people. This region is located in seismic zone V on national seismic zoning map and is governed by two different directed stress regimes that include various faults, folds, lineaments and other tectonic features. Recently two moderate size earthquakes (M ≥ 5.5) occurred in this region in 1968 and 1976 (Srivastava *et al.*, 1987). High altitude Dhauladhar ranges exists just north of MBT. This is the region under which always an intense seismic activity can be found for any period of observation. However lack of a good regional velocity model and limited azimuthal control of earthquakes from northern side has hampered getting better location of hypocenters and tectonic interpretation. In 2004, WIHG put a dense seismic network around this high seismicity zone for understanding the geodynamic process using modern technology and processing techniques. The data of seismic stations of other networks being operated in this region is also combined to improve the station coverage and getting more reliable data. The current results from micro-earthquake data in this seismic regime gives new insights of complex tectonic settings that are different from previous studies obtained based on big size earthquakes. Similar observations of

deviation of results by micro-earthquakes and big sized earthquakes have also been reported in other parts of the Himalaya.

In India, the reduction of seismic risk still requires additional basic research on all aspects of Seismology. The analysis of micro-earthquake data addresses the understanding of seismotectonic, physical process of earthquake along with seismogenic process on regional basis. The spatial distribution of micro-earthquakes can be used to delineate the tectonic discontinuities in deeper part that is helpful to understand the intra-continental tectonics in the Himalayan region. The big size earthquakes help to specify the state of movement while their study along with smaller and micro-earthquakes provide the understanding of physics of earthquake processes and completely quantify the regional seismic regime. The crustal structure investigation is necessary for complex Himalayan region that helps to improve the location of the earthquake sources mainly for shallow focus earthquakes. An attempt is made to utilize the catalogue of historical and current seismicity for Kangra-Chamba region of NW Himalaya to quantify its seismic regime on the basis of seismicity, crustal structure, earthquake source parameters and active fault geometry.

CHAPTER 3

DATA ACQUISITION, SELECTION OF SEISMIC EVENTS FOR JHD AND 1-D VELOCITY INVERSION

3.1. INTRODUCTION

The seismotectonic studies (LeForte, 1975; Seeber et al., 1981; Khattri and Tyagi, 1983; Ni and Barazangi, 1984; Kayal, 2001) have significantly improved our understanding of subsurface structures and define better the collision processes of Himalayan orogeny. However, as reported by Tandon (1992) and Kamble *et al.* (1974) only few studies have been conducted for crustal velocity structure determination of the Himalayan regions compared to the other parts of the Indian plate. It may be due to complex crustal structure of the Himalayas which can be resolved through highly sophisticated procedures. The other reason may be the difficulty to deploy dense local seismic networks due to harsh conditions in the high altitude mountainous region. Recently, Rai *et al.* (2006) carried out receiver function analysis across NW Himalayas and was able to locate the north dipping Moho discontinuity with variable depth of 40 km at Delhi and 75 km beneath Taksha and Karakoram. However they could not resolve the crustal velocity structure due to its complex behavior caused by collision tectonics, which is simple in case of Indian shield region (Rai *et al.*, 2003; Sarkar *et al.*, 2003). The crustal velocity structure investigations for some parts of the NW Himalaya is performed by Kamble et al., (1974); Ni and Ibenbrahim (1991); Mukhopadhyay and Kayal (2003). However, the crustal velocity structure of the Kangra-Chamba region, the source zone of devastating M8.0 Kangra earthquake of 1905 is not known in detail. This causes significant error in determining earthquake locations, especially in the northern part where the station coverage is poor. The deployment of a dense seismic network in a high seismicity area by WIHG helped me to get sufficient data in a short duration. This data was used to determine the crustal velocity and to obtain more accurate earthquake location. This in turn helps in deciphering details of the tectonic deformation and kinematics of this region.

The central focus of this Chapter is the deployment of the local seismic network and its utilization to determine area specific 1-D velocity model for the Kangra-Chamba region of NW Himalaya. Well tested algorithm VELEST (Kissling, 1995), is adopted because it allows simultaneous estimation of velocity structure as well as improved

locations of hypocenters by the inversion of travel times of large number of high quality local earthquakes. The approach incorporates an iterative simultaneous inversion of hypocenter-velocity coupling to obtain the velocity model and refine the earthquake locations. The final velocity model is taken as the minimum 1-D velocity model of the region. The station corrections obtained as a byproduct of the approach provide nature of deviation from 1-D structures. The well-calculated 1-D velocity model will be an efficient model for the relocation/location of the earthquakes and determine other source parameters.

With a main focus of generating area specific seismic velocity models and to improve the location of the seismic events for better understanding of the seismicity and seismotectonics of the Kangra-Chamba segment of the NW Himalaya, a special experiment with an array of closely spaced seismometers was started in 2004. This section highlights the objectives of the array, operational strategy adopted for acquiring the data and the analysis of the data. The main focus is given to analyses of the acquired local micro-earthquake data. A brief overview of the obtained 1-D velocity model and location of the earthquakes is given that high lights the importance of new seismic network. The improved locations of epicenters show close clustering of seismic events immediately northeast of the epicenter of 1905 Kangra earthquake, while away from this zone the seismicity in the Chamba sector has more even distribution (Kumar *et al.,* 2009).

3.2. THE START EXPERIMENT 2004

Over the last decade, micro-earthquake data collected from temporary seismic networks in the Himalayas show a broad zone of concentrated epicenters bounded between MCT and MBT, named Main Himalayan Seismic Belt, extending over the entire length of the Himalayan arc. These concentrations of seismicity suggest complex tectonic activities responsible for varied earthquake mechanisms in different parts of the Himalayas (Pandey *et al.,* 1995; Kayal, 2003; Bollinger *et al.,* 2004). The space-time patterns of seismicity are also highly variable over the Himalayan arc with well-defined segments of intense/low seismicity, seismic gaps or tectonically stable zones (Srivastava *et al.,* 1987; Khattri and Tyagi, 1983; Gaur *et al.,* 1985, Khattri *et al.,* 1989; Kayal 2001; 2003). The Kangra-Chamba region of NW Himalaya in the epicentral zone of devastating 1905 Kangra earthquake has intense seismic activity. Two moderate size earthquakes (M≥5) have also occurred in the years 1968 and 1978 in this segment of the

Himalayas (Srivastva *et al.*, 1987). The lack of good regional velocity model coupled with limited azimuthal distribution of stations from north of the high seismicity zone restricted the robust determination of the hypocentral locations and, thus, inhibited detailed insight into the tectonic setting associated with localized zone of the high seismicity. The special campaign mode arrays operated either to monitor local seismicity (Thakur *et al.*, 1997; Pandey *et al.*, 1995) or aftershock activities of 1991-Uttarkashi and 1999-Chamoli earthquake (Kayal, 2001) have proved effective tool to analyze the complex seismotectonic environment of the NW Himalaya.
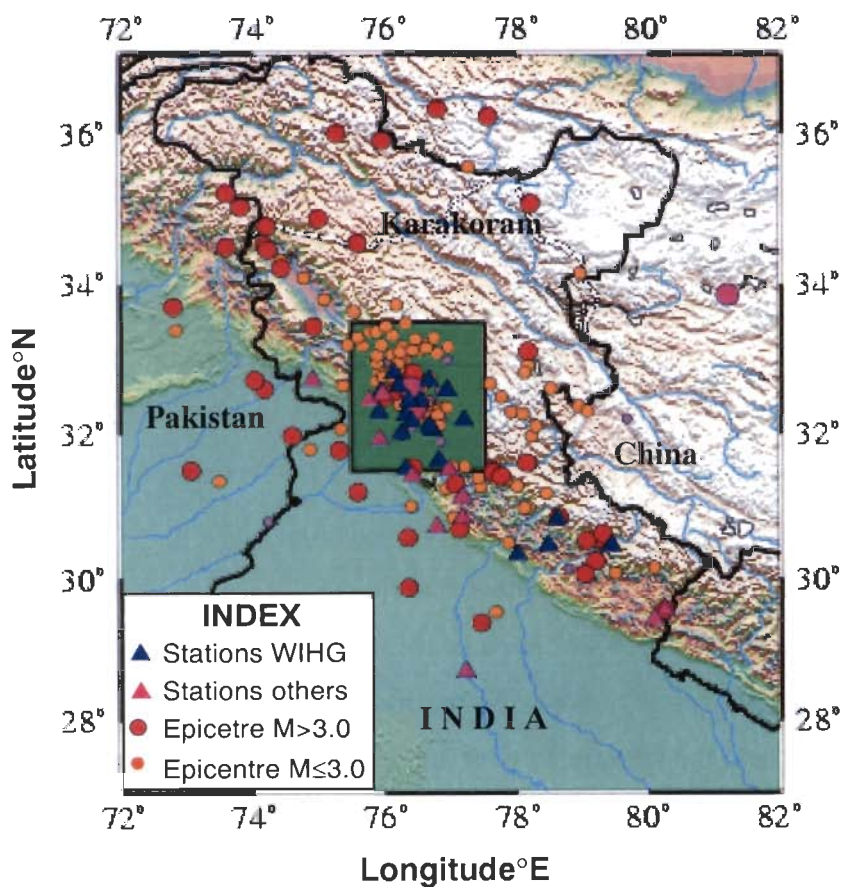
Figure 3.1: The plot of epicenters and stations used for the travel time analysis to obtain the 1-D velocity model.

3.2.1. Objectives of the Network

- To record the local micro-earthquake data using temporary broadband seismic stations along with the permanent short-period stations of Wadia Institute of

Himalaya Geology (WIHG), Dehradun, seismic stations deployed by the Indian Meteorological Department (IMD), New Delhi and other agencies.

- To develop the area specific velocity models using micro-earthquake data and use the new velocity model to constrains the hypocenter locations.

- To develop the seismotectonic models using micro-earthquake activity and quantify the seismic regimes.

- To develop the characteristics of earthquake sources using refined locations.

3.2.2. Seismic Networks Before 2004

As a part of the National Seismic Network, the IMD has been operating 8 seismic stations in the NW Himalaya since 1963 (**Figure 3.1**). Beginning 1984, the WIHG, Dehradun also started monitoring seismic activity in NW Himalaya after installing 7 analog seismic stations in the Himachal and Garhwal Himalayas to monitor the seismic activity on regional scale. In addition the WIHG installed four short period seismic stations in Kangra-Chamba region of Himachal Pradesh and three short period seismic stations in the Garhwal Himalayas. As discussed in the previous chapter, the earthquake catalogue compiled afresh from historical time (1550) to 2005 shows complete/homogeneous seismic events of M ≥ 4.5 for a period of 1965-2005 and M ≥ 3.8 for 1988-2005. Since 1999, this magnitude threshold for the northwest Himalaya has come done to 2.5 and now the data is complete for M ≥ 2.5. After 1963 the 4.5 magnitude threshold for the NW Himalaya is due to the introduction of World Wide Seismic Standard Network (WWSSN) in India and adjoining Asian countries. The WWSSN established the seismic network throughout world that was sufficient to record and locate the earthquakes having magnitude more than 4.5. Therefore this threshold level of acquiring seismic data on regional basis would match with the world wide seismicity. The addition of WIHG network in 1984 has improved the seismic network in the NW Himalaya and hence the magnitude threshold lowered down from 4.5 to 3.8. After 1985 and before 2004 few more temporary seismic networks were started in this region on local scale by Kumaon University, Kumaon, Central Scientific Instruments Organisation (CSIO), Chandigarh and Guru Nanak Dev University, Amritsar. In addition IMD has also operated few temporary networks to record the seismic activity around hydro-projects and also to record the aftershock activity of moderate to strong earthquakes that occurred during this period. Therefore, the local networks of limited

durations operated in Himachal Pradesh to cater to special needs of major river valley projects and geothermal explorations along with aftershock activity show that Kangra-Chamba sector has remained active at all times although the source/seismotectonics of this intense cluster remained elusive (Chatterjee and Bhattacharya, 1992). The magnitude threshold in 1999 came down to 2.5 for whole NW Himalaya (Lyubusin *et al.*, 2010) and even less than 2.5 in the Kangra-Chamba region (Gitis *et al.*, 2008) with the introduction of new stations after occurrence of M6.4 Chamoli earthquake (its epicentre shown in **Figure 2.1**) in the Garhwal Himalaya.

3.2.3. Deployment of Seismometers through START2004 Experiment

WIHG launched campaign mode array operation in this highly seismically active Kangra-Chamba sector beginning 2004. As a part of this array, 12 three-component digital stations were added in the Kangra-Chamba region of NW Himalaya (**Figures 3.1 and 3.2**). A special feature of this seismic array is that four stations (Kothi, Tozing, Udiapur and Tissa) are located north of Dhauladhar ranges and, thus, ensure good constrain on the location of seismic events seated beneath the Chamba Nappe, a zone of high seismic activity. These stations are on the exposed hard rock in the higher Himalayas. The exposed hard rock is clearly visible in **Figure 3.3**, where the seismometer was installed on a small concrete pillar made on hard bedrock.

Two types of broad band seismometers were deployed in the START2004 seismic array. After this new installation, the network of 21 stations (stations including WIHG, IMD and CSIO) are equipped with portable high quality three-components broadband CMG-3T seismometers having natural period of 120s (flat response from 0.033 – 50 Hz), broadband CMG-40T with natural period 30s (flat response 0.33 – 50 Hz) and short period seismometer CMG-40T1 of 1s natural period (flat response from 1.0 – 100 Hz). This upgraded network of 21 digital and analog seismic stations is given in **Table 3.1** and shown in **Figures 3.1 and 3.2**. In **Figure 3.2**, the location of stations having digital seismograph are shown with a hut of blue color and the stations containing analog seismograph with the hut of red color. All these digital seismometers are of GURALP (Guralp System Limited, United Kingdom). The digitizer and recording equipments are of GURALP and REFTEK (Refraction Technology Limited, United State America) with high accuracy GPS synchronized timing system. GURALP digitizers also contain Signal Acquisition Modules (SAMs) utilized for better handling the data acquisition. The digitizers were set to record velocity variation at a rate of 100

samples per second at all the three components. The 24 bit digitizers have a high dynamic range of more than 138 db. Universal Time Coordinate (UTC) timing for each system was being provided by the GPS system that synchronized the instrument clock at every minute. The GPS also provided the location of the station with elevation from the Mean Sea Level (MSL). The station location along with the time error in instrument clock was provided in the auxiliary file after an interval of one hour. The analog seismographs contain only vertical component seismometer along with a digital clock. The analog recorder of this seismograph is an indigineuous designed one by the Central Scientific Instrument Organigatio (CSIO), Chandigarh, India and it is attached with vertical seismometer of SS-1 short period Ranger Seismometer of Kinemetrics. The digital clock of this seismograph is synchronized with an external and digital clock developed by CSIO. Power to the instrument was supplied through a regulator by a combination of two parallel connected 12 volt truck batteries. Those were connected in parallel with the solar panel for charging during day time.

Table 3.1. Details of seismic stations with station corrections

Name	Code	Latitude (°N)	Longitude (°E)	Elevation (m)	P-Wave Correction (Sec)	S-Wave Correction (Sec)
Naddi	NAD	32.250	76.315	1995	-0.24	-0.46
Bharmaur	BRM	32.434	76.543	2100	-0.41	-1.10
Deol	DEO	32.094	76.672	700	-0.61	-1.07
Tozing	TZG	32.590	76.935	1700	-0.64	-1.25
Udapur	UDA	32.723	76.669	1710	-1.15	-2.43
Banikhet	BNK	32.547	75.940	1960	-0.29	-0.65
Chhatrari	CHT	32.441	76.373	1800	-0.48	-1.00
Lagore	LGR	32.292	75.908	800	-0.11	-0.02
Rajiyana	RJA	32.000	76.252	430	-0.50	-0.68
Tissa	TSA	32.822	76.138	1040	-0.76	-1.35
Rewalsar	RWS	31.632	76.825	1310	-0.67	-0.99
Beed	BED	32.047	76.723	600	-0.67	-1.04
Kothi	KOT	32.176	77.200	2520	-0.69	-1.30
Una	UNA	31.521	76.319	550	-0.83	-0.57
Jadera	CHM	32.644	76.205	1710	-0.50	-1.01
Sundernagar	SDN	31.500	76.972	1000	-0.83	-1.30
Thin	THN	32.445	75.763	640	-0.55	-0.44
Pong	PNG	31.917	75.917	490	-0.16	1.63
Shimla	SML	31.128	77.167	1750	-0.25	-0.74
Dalhausei	DLH	32.542	75.967	2100	-0.33	-0.39
Bhakhra	BHK	31.417	76.417	510	-0.47	-0.78
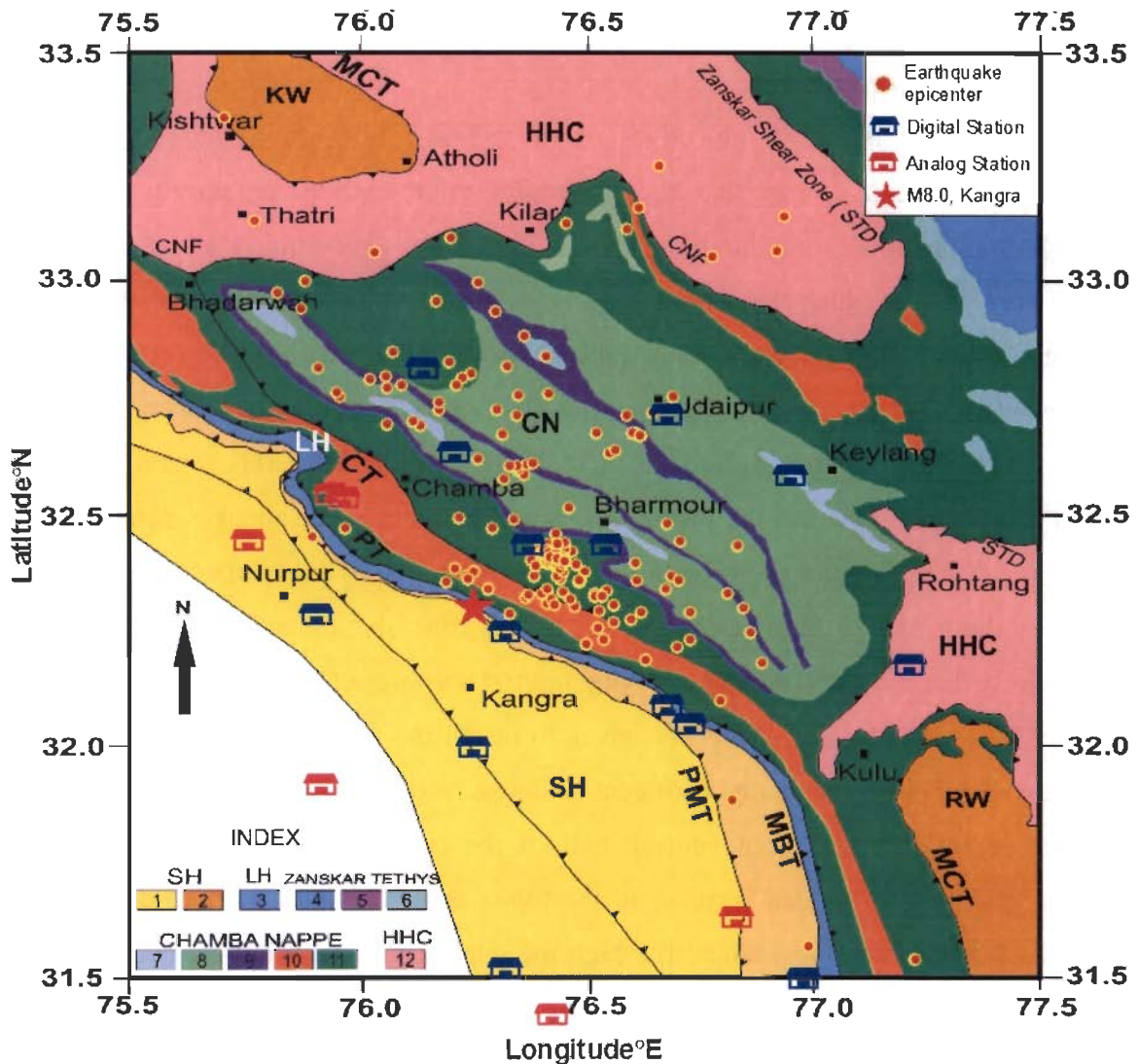
Figure 3.2: Locations of seismic stations and epicenters of local earthquakes used in this study on a map of the geology and tectonic elements of the Kangra–Chamba sector of northwest Himalaya (after Thakur, 1998). The star shows the epicenter of the devastating 1905 Kangra earthquake. Labels used are as follows: SH, Siwalik Himalaya; LH, Lesser Himalaya; HHC, High Himalayan Crytallines; KW, Kistwar window; RW, Rampur window; STD, southern Tibetan detachment; CNF, Chenab Normal Fault; CT, Chamba thrust; MCT, main central thrust; MBT, main boundary thrust; PT, Panjal thrust and PMT, Palampur Thrust

This upgraded network of 21 digital and analog seismic stations (**Figure 3.2;** **Table 3.1**) in the Kangra-Chamba sector of Himachal Himalayas combined with already functional 15 stations in the Garhwal-Kumaon Himalayas makes a network of 36 stations to study the regional seismicity of the NW Himalayas. The location of 36 stations is given in **Figure 3.1**.

3.2.4. Station Distributions

To fulfill the main objectives of the START2004 array, the stations were distributed in such a way that the maximum micro-earthquake activity could be recorded within small time duration. The distribution of the seismic stations covers the study area well in which the station spacing is minimum around crustal heterogeneity. The analysis of earthquake catalogue data reported in the previous chapter shows that the seismicity is highest in the Kangra-Chamba region, which is the epicenter zone of devastating M8.0 Kangra earthquake. It has been observed that this region is always seismically active because the micro- and small-magnitude earthquakes can be found here every year. Therefore, this region was also monitored by many agencies in the past to study the causes of high seismic activity. This time also the array was deployed in such a way that it covers the region having highest seismic activity within the network.

This time more emphasis was given to install the seismic station in the northern side in Dhauladhar range, the stringent and less accessible region as its maximum portion is covered with snow during half of the calendar year. In this part of the Himalayas, there is sudden increase in the topographic elevation in the northern side towards Dhauladhar range, where the high mountain peaks are having elevation about 4000 m from mean sea level. It is clearly evident in **Figure 3.4** where the mountain peak is covered with snow in summer in the month of June. The snow starts melting during May-June and the region is accessible only from June to October every year during which period the data collection, instrument installation or repairing of the station is possible. This is a big hindrance for deploying seismic instruments and continuous collection of the seismic data. In this part of the study region the major problem is being faced to provide a stable power supply for the installed seismic equipments. Although, a suitable power pack of batteries is provided and these batteries are being recharged with solar panel. However, the region is covered with snow and clouds most of the time and as a consequence the battery goes dead quite often. This time four stations have been deployed in the northern side (Kothi, Tozing, Udiapur and Tissa) even then only 172 seismic events could be properly located and further used for tomography from the data of more than 300 recorded events during the period of 2004 and 2005.
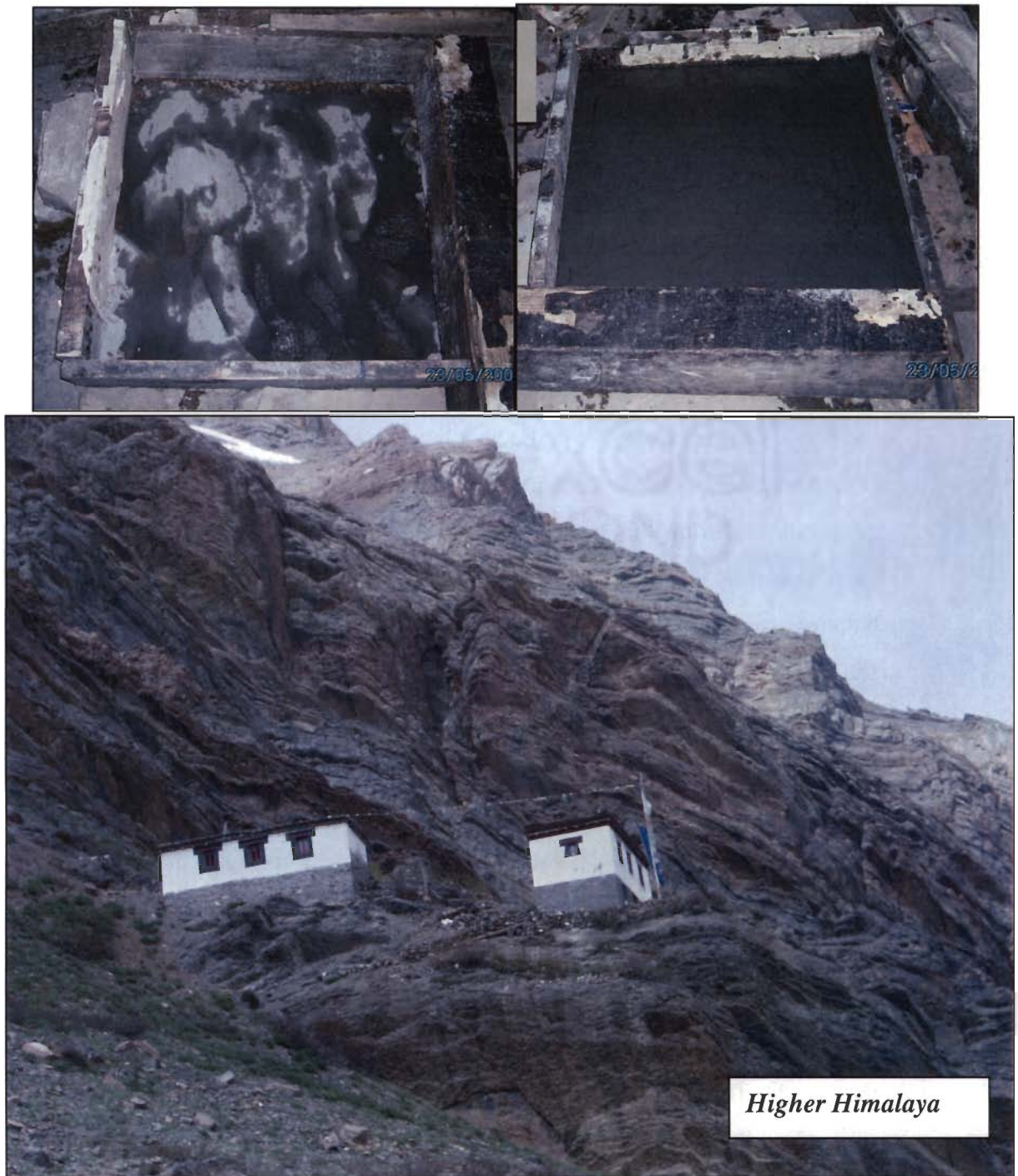
Figure 3.3: Seismological station in the Higher Himalaya installed at hard bed rock. Upper left panel shows the exposed hard rock and right upper panel is the view of constructing the Pillar on this bed rock.

3.2.5. Problem Faced in Data Collection

The Kangra-Chamba region, where the stations of START2004 were installed is very far away from WIHG headquarters Dehradun and is located in the difficult Himalayan terrain, a large part of which remains snow covered for many months and

therefore remain inaccessible. Therefore, frequent visit to these stations were not possible. The data from these stations were collected after duration of two to three months and from few stations after four to five months in winter, which is brought to Wadia Institute, Dehradun for analysis. Sometimes at few stations problems were encountered due to power failure or malfunctioning of the equipments. The main problems faced were as follows:

- **Power problem:** These stations are located in the higher Himalayan terrain where the power supply is possible only through solar charger battery backup. In the winter season, the time duration of day is less than night and sunshine intensity is lower. Quite often the weather remains cloudy and snowfall occurs. As a consequence, at some stations the batteries go dead leading to no recording of the data. During this period few stations are also covered with thick snow even covering the solar panels or destroying the stand of solar panels. The batteries were not fully charged and sometimes during night or even day time for cloudy weather the power failure caused shutdowns of the systems.

- **SAM failure of GURALP systems**: Few stations containing the SAM for data handling were also not functioning properly due to SAM failure. Tissa station was encountering this problem many times. Sometimes due to poor handshaking between SAM and digitizer, the data were not collected properly showing gaps in the continuous data. Due to this problem at 2 to 3 stations, the downloaded data contains huge number of 1 kb files containing no information that introduced many gaps. Due to this it was also difficult to transport the data. To remove this problem, I have developed small software package to delete these 1 kb files automatically from the downloaded data because it is time consuming to perform this task manually.

3.3. DATA RECORDED BY THE WIHG NETWORK

3.3.1. Data Acquisition

The velocity of particle motions at the seismic station are recorded by the seismometer and these variations are converted into voltage based on electromagnetic induction method (simple sensor as mass-coil combination). The sensitivity of the seismometer depends upon the generator constant of the sensor. Latest seismic sensors are more sensitive having high generator constant in wide frequency range known as

broadband sensor and its working principle is based on force balance method. This converted voltage of earth vibration is digitized by the attached digitizer in digit values. In this conversion, the analog signal is converted to digital signal through A/D converter attached to the data acquisition system (DAS). The range of conversion in digit values depends on the bit resolution of the digitizer. All the latest digitizers have a high resolution of 24-bit that is sufficient to record all size of earthquakes occurring near the station. The 24 bit digitizer gives a wide dynamic range of more than 138 db for recording data at a rate of 100 samples per second. The digitizer stores the digit values in the storage unit through DAS (Havskov and Alguacil, 2004).

The seismic data acquisition and processing software were provided by the firms from where the systems were purchased. The DAS, first store the data in the attached random access memory (RAM) and it is subsequently automatically transferred to the attached portable disk at specified interval or when the RAM is filled 70 percent. In the GURALP system, the raw data is stored in Guralp Compressed Format (GCF) in the attached portable disk. This disk is easily replaced with the spare one at the seismic station without any loss as the RAM has sufficient storage. From the portable disks the raw data was downloaded in the lab through the PCMCIA bus unit that accesses the disk.

3.3.2. Continuous Seismic Data and Events Retrieval

In the GURALP system the raw data was downloaded in GCF format from the portable disk. This continuous data was downloaded in the computer making a file of one hour interval. This full data was subsequently archived in the WIHG server that has a database of all the seismic stations. The database was designed in such a way that data files of all the stations were converted into uniform duration of one hour files irrespective of recording instrument system. The recording time of data obtained from the GPS attached to all the stations is uniform as all the stations have timing in UTC.

To retrieve the events from the continuous data the autoderm software was used to plot the 24 hour data at a time. The visual inspection of 24 hour data show the occurrence of the earthquake where the signal to noise (S/N) ratio suddenly changed. If this S/N ratio is high for longer period only then the data is considered as that of an earthquake. For small duration the high S/N ratio might be due to external noise near the stations produced by cultural noise, heavy wind and rock-falls etc. An automated detection of seismic events method was also designed using a simple STA (Short Term

Average) and LTA (Long Term Average) algorithm. The data were band pass filtered at 1-5 Hz to calculate the STA and LTA values. The STA was calculated for 2 second and the LTA was calculated for 20 second to obtain the STA/LTA trigger ratio. Trigger threshold of 5 was used to detect a seismic event (Havskov and Alguacil, 2004).

Higher Himalayan Peaks partially covered with snow in peak summer
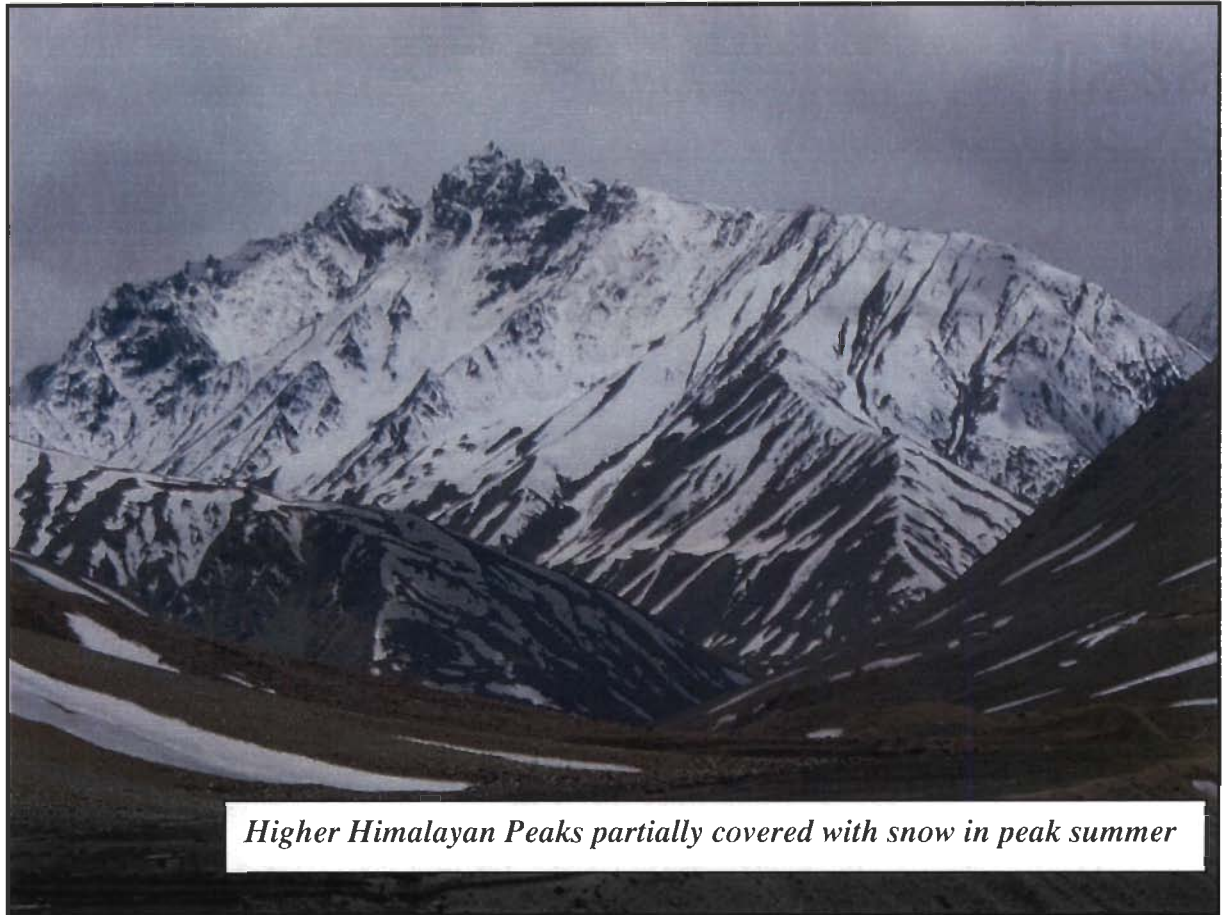
Figure 3.4: Dhauladhar peaks covered with snow during summer.

3.3.3. Data Processing and Analysis

A specific requirement of data processing was to determine the seismic event location, its occurrence time and magnitude accurately and rapidly so that relates the earthquake data with tectonic features of the region. Initially the P- and S-phase data of 360 regional events (events having focal depth less than 10 km) were picked and initial earthquake source locations obtained using HYPO71 (Lee and Lahr, 1975). The uncertainty in picking these phases from digital data was less than 0.05s and that from analog records was less than 0.5s. In this provisional estimation three layer 1-D velocity

model of Kamble *et al.* (1974) was used adopting a constant Vp/Vs ratio of 1.74 ± 0.08, obtained by Wadati's plot (**Figure 3.5**) based on the method of Wadati (Wadati, 1933). The Wadati plots are obtained using two different methods, in one method the S-travel time is plotted with respect to P-travel time as shown with yellow circles in **Figure 3.5a.** The minimum least square linear fit is calculated for this data set shown with straight line using which the average value of Vp/Vs is obtained from the slope of this curve. The correlation coefficient (R^2) of the linear fit is very good (99.6%) showing a good correlation of observed P- and S-phases of this data set. In the second method, the timing difference of S-P is plotted with the timing of P-phase data as shown in **Figure 3.5b**. In this case also the Vp/Vs ratio is obtained through the slope of the linear least square fit and adding a value of 1.0. These events are scattered all over the region covered by the network of 36 stations and epicentral distances out to 550 km (**Figure 3.1**). However, more than 80% earthquakes have epicenter distance less than 200 km (**Figure 3.1**) and their P-wave travel times are less than 40 second. The magnitude of these events ranged between 1 and 5, the seismic events having magnitude more that 3.0 are shown with red circles and the smaller size events are plotted with orange circles. It is clear from **Figure 3.1** that the numbers of micro-earthquakes (M ≤ 3.0) are more as compared to big size earthquakes. The travel time plots of these data sets were used to obtain the average velocity structure of the crust and the uppermost mantle. These are reported in next sections of this chapter. Out of 360 events, 172 events (**Figure 3.2**), constrained by closely spaced network of 21 stations of the Kangra-Chamba sector were fairly well located with average RMS error value of 0.50s. The average error in the initial location of these events was ± 5 km for depth, latitude and longitude. The inversions of P- and S-phase data from these 172 earthquakes were used to obtain the minimum 1-D velocity model and to relocate the events by joint hypocenter determination (JHD) that is reported later on. In the next chapters, the waveform and phase data of these earthquakes are utilized for further analysis. The phase data of P- and S-wave is further analyzed to obtain 3-D model of Vp, Vs and Vp/Vs for the upper crustal part of the region. The best located events are selected for obtaining fault plane solutions using first P-wave polarity motions recorded at sufficient number of stations and it is utilized to infer the stress patterns of the seismic regimes along with seismotectonic model of the region. The digital data of secondary arrivals are also used to study source characteristic like source dimension, stress drop etc.
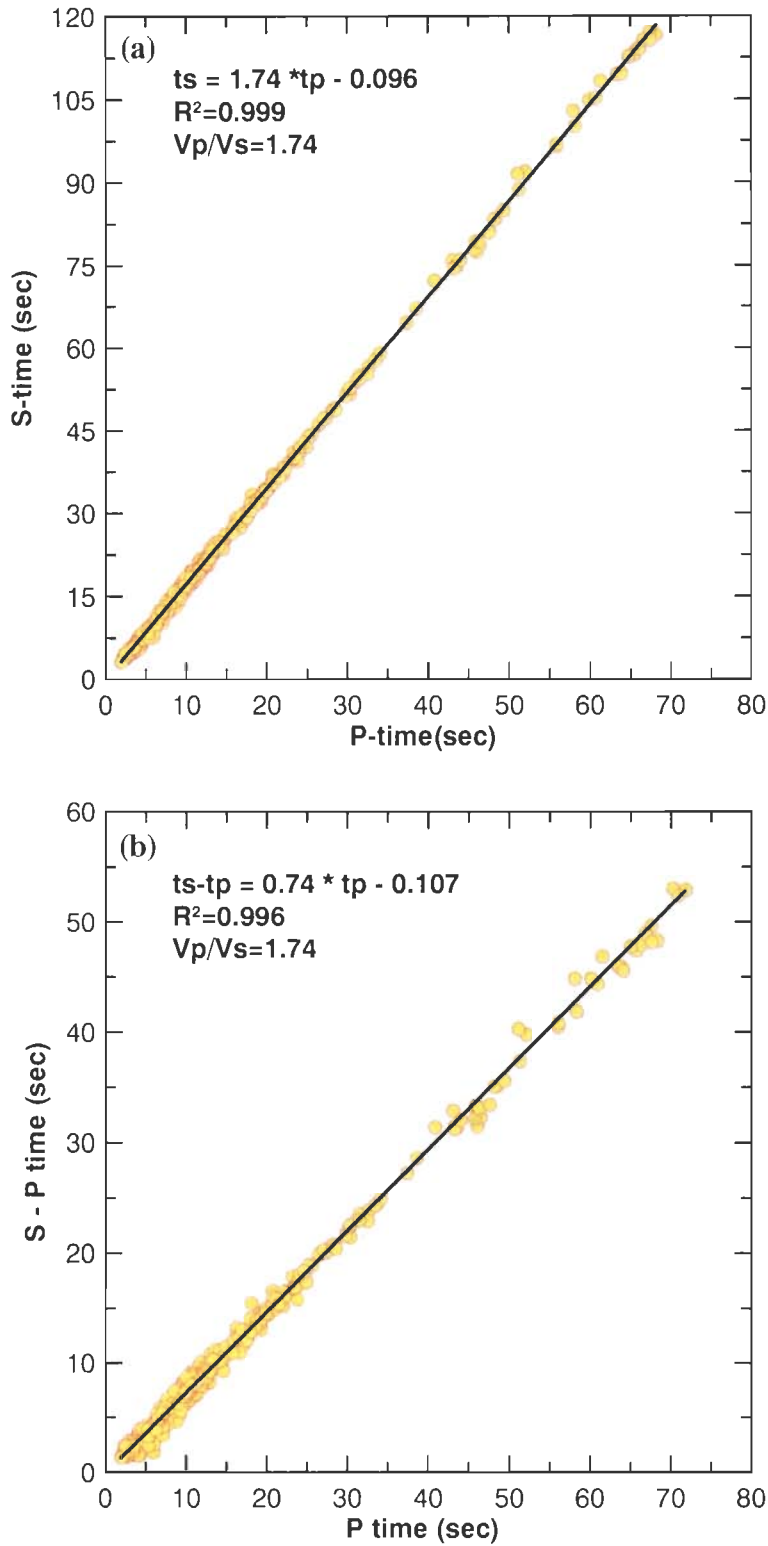
Figure 3.5: Wadati diagrams providing Vp/Vs ratio of 1.74 ± 0.08 for all earthquakes within epicentre distance of 500 km (a) Plots of P-wave time with respect to S-wave time and (b) Plot of P-wave time with respect to S-P travel time.

3.3.4. Seismic Events Recorded by START 2004 array

The Himalayas is seismically active region where mostly shallow focused earthquakes occurred (Kayal, 2001). The Hindukush region, very close to the north-west side of the study region, is one of the most active parts of the world containing intermediate to shallow focus earthquakes. Therefore, each station of the array recorded at least one earthquake daily. During 2004 and 2005 more than 2000 seismic events were recorded from local, regional and tele-seismic range. Most of these seismic events occurred in Hindukush region at a regional distance from the array and have magnitude more than 4.0. The aperture of the START2004 array is about 200 x 200 km^2, therefore a criteria of selecting local events out of all is to limit 40 second maximum time difference between P- and S-wave at the central station. I also included the stations of adjoining Himalayan regions of Garhwal and Kumaon form south-east direction (**Figure 3.1**) to include all the seismic events of NW Himalaya for obtaining 1-D velocity model of the region using travel time plots. I could obtain the initial location of 285 earthquakes using HYPO71 (Lee and Lahr, 1975) and used the travel times for different distances to construct 1-D velocity model.

Out of 360 earthquakes, 172 were taken as the local earthquakes of the START2004 array as a subset based on the S-P time difference. I used the SEISAN (Havskov and Ottemoller, 2008) software to mark the onset of P- and S-wave times. Initially the P-wave times were marked for the data of each station after assigning the weightage based on the S/N or clarity of the onset of the signal. The quality of the phase pick was represented by numbers 0, 1, 2, 3 or 4. 0 denotes a very sharp impulsive arrival while 3 are emergent and 4 is unclear. We have adopted the following criteria of assigning the weightage:

- 0 – S/N ratio excellent with lowest uncertainty and reading accuracy of phase pick ≤ 0.02 second
- 1 – S/N ratio good with reading accuracy of phase pick between 0.02 – 0.05 second
- 2 – S/N ratio fair and picking accuracy of phase pick between 0.05 – 0.10 second
- 3 – S/N ratio poor, accuracy of phase pick between 0.10 – 0.20 second
- 4 – Signal is unclear with uncertainty and reading accuracy of phase pick > 0.20 second

For the highest uncertainty, the data is used only to locate the earthquake for the seismic behavior of the region. However, it is not used for further processing such as developing the velocity structure.

Only vertical component of the seismometer was used to pick the onset of the P-wave. First motion polarities were also marked for the P-wave if the weightage is 0, 1 and 2 only so that the uncertainty is small. S-waves were picked from the horizontal component and only from the digital records. The minimum error in S-phase pick was 0.05 sec.

3.4. EARTHQUAKE LOCATIONS USING 1-D VELOCITY MODEL AND ESTIMATION OF MINIMUM 1-D MODEL

The preliminary location of the earthquake sources (**Figure 3.1**) is obtained by using P- and S-phase arrival times and the earlier existing 1-D velocity model of the region obtained by Kamble *et al.*, (1974) as given in **Table 3.2**. In this velocity model the crust is divided into two layers, the upper crust having P-wave velocity of 5.72 km/s and the lower crust velocity of 6.61 km/s. The P-wave velocity at the crust mantle boundary (Moho discontinuity) is 8.22 km/s. This velocity model by Kamble *et al.*, (1974) was obtained for the Mandi region using local earthquake data. Mandi region is the central part of the NW Himalayas. Therefore the velocity model may represent an average model of the region. The velocity model was used with a simplifying assumption of a constant Vp/Vs ratio of 1.74 ± 0.08, obtained through Wadati's plot (**Figure 3.5**). In the next step minimum 1-D velocity and Vp/Vs model of the study region is obtained using a two-step procedure. In the first step travel time plots for P- and S-phase data are used to obtain the 1-D model of the crust and upper mantle. In the second step a simultaneous inversion algorithm VELEST (Kissling, 1995) is used to further refine the upper crustal velocity and Vp/Vs structure. The procedures and the results are discussed in the next few sections.
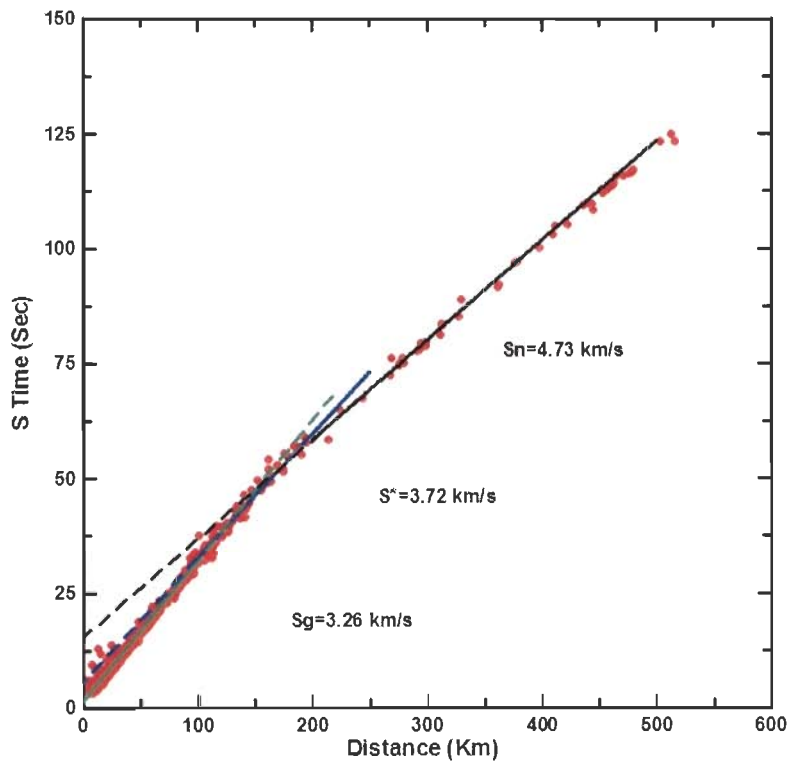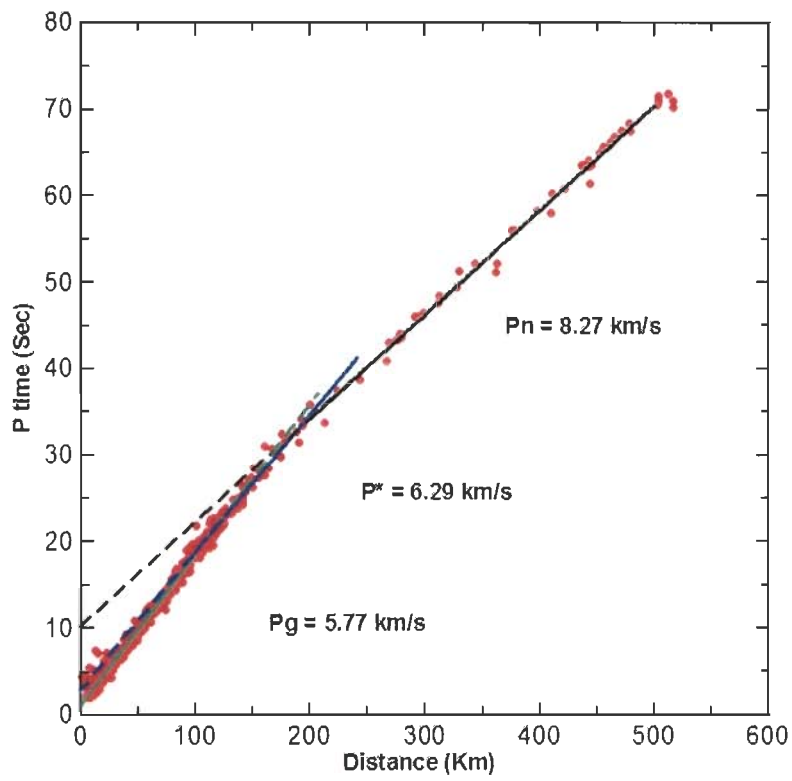
Figure 3.6: Travel time curves of first P-wave arrivals for earthquakes with epicentral distance. The least square regression lines are taken for three distance ranges indicating two layers of the crust and the uppermost mantle.

Table 3.2. Crustal structure and 1-D velocity model obtained by Kamble *et al.* (1974).

Layer	Depth (km)	Thickness (km)	Vp (km/s)	Vs (km/s)
1	0.0	24.0	5.72	3.29
2	24	21.0	6.61	3.72
3	45	Half Space	8.22	4.73

3.4.1. The Concept of the Minimum 1-D Model

The minimum 1-D velocity model of a region is obtained to constrain the location of the earthquakes and evaluate an average model. This model is obtained by taking a priori information from all available sources. This velocity model divides the region (mostly crustal part) depth wise into different layers having similar characteristic related to physical properties. For the minimum 1-D model the region is localized in such a way that it should not have diverse characteristics. Using local seismic data the minimum 1-D velocity model is obtained using hypocenter-velocity coupling. In this method the observed travel times are compared with the calculated (model) travel times. The difference between these travel times is measured as the residual RMS (root-mean-square) misfit for all the events. This procedure is repeated many times by changing the velocity model and locations to obtain 1-D minimum model of the region. The process of obtaining minimum 1-D model is a trial-and-error method for different initial models with internal non-linear inversion procedure.

3.4.2. 1-D Velocity and Vp/Vs Model Using Travel Time Plots

Out of 360 local and regional events, P- and S-phase data of 285 shallow focused (focal depth less than 10 km) events were used for estimation of Vp, Vs and Vp/Vs for the study area. The location of these events and the 36 stations whose data were used in this work is shown in **Figure 3.1,** where the epicentre locations are shown with circle and the station locations with triangle. **Figure 3.6** shows the travel time versus distance plots for P- and S-data of these 285 events having focal depth less than 10 km. Based on the observation of trend of these plots three straight lines were fitted through each plot using linear regression. From the slope of these lines average Pg, P*, Pn, Sg, S* and Sn

velocities were estimated, where slope of each line is equal to the inverse of respective velocity values. The calculation of the velocities of these different phases of P- and S-wave and the thickness of the different layers was done using the relations given below.

(a)

(b)
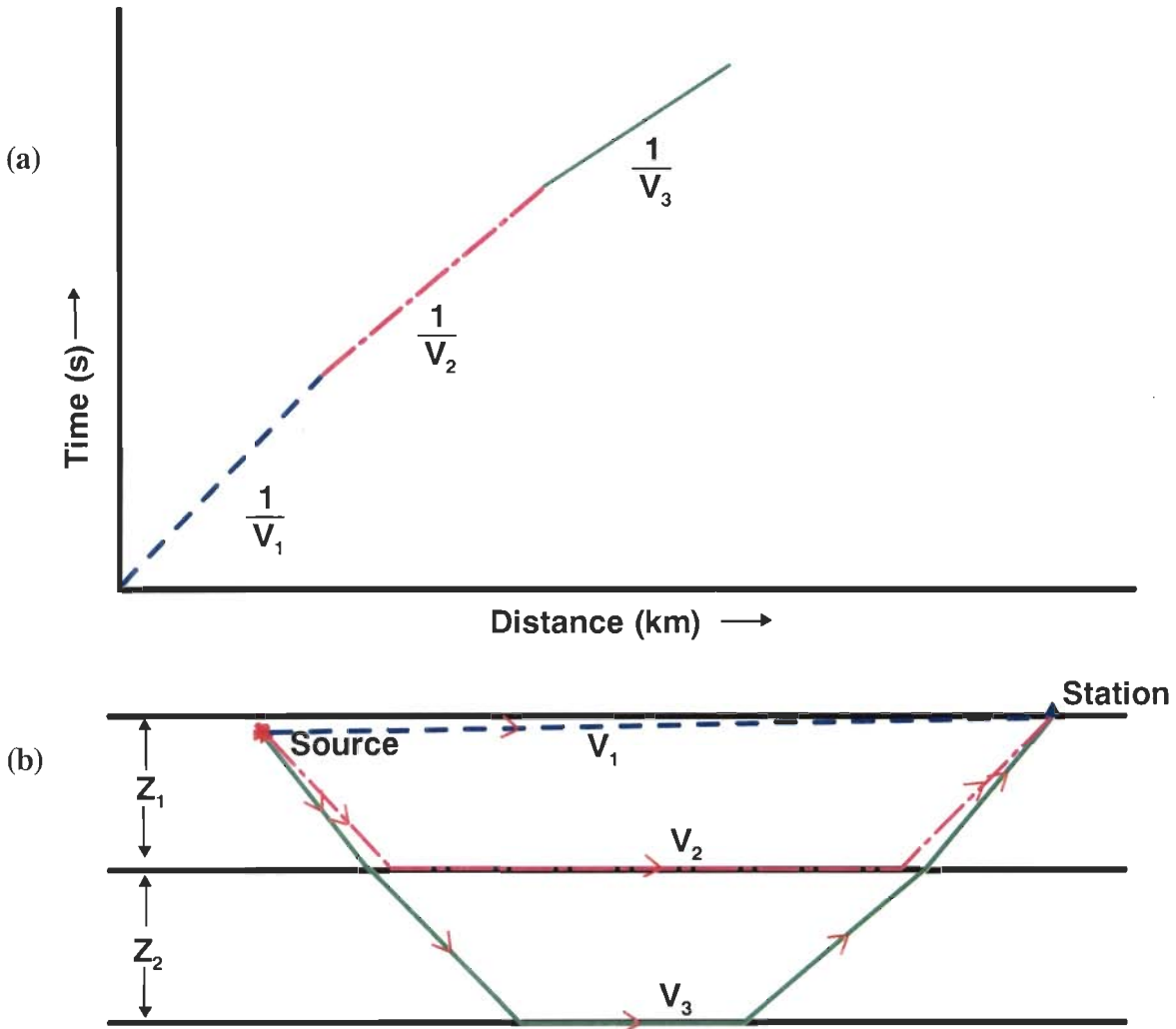
Figure 3.7: The schematic 2-layers crustal model adopted for the time-distance plot of P- and S-wave. (a) Direct and refracted rays of seismic wave passing through 2-layers having thicknesses Z_1 and Z_2. (b) Velocities V_1, V_2 and V_3 obtained from the slopes of time-distance plot.

In the present data set, three linear regression curves are obtained for P- and S-wave dividing the upper structure of the earth into two layers. To calculate the above mentioned parameters the two layers crustal model is shown in **Figure 3.7b** and travel time of the waves passing through these layers is shown in **Figure 3.7a**. If the crust is divided into two layers having thickness Z_1 and Z_2 respectively for upper and lower

crust. V_1, V_2 and V_3 are the velocities of a seismic wave for upper crust, lower crust and uppermost mantle respectively. If X is the epicentre distance for source shown with red color and the seismic station with blue triangle, then the seismic wave will have three possible paths shown with blue, magenta and green colors. The source is taken at a shallow depth in the upper crust so that the distance of propagation for the wave passing through upper layer (blue dotted line) is nearly equal to the epicentre distance. The travel time t_1 of this wave is given by the equation

$$t_1 = \frac{X}{V_1}$$ ---------------- 3.1

The second wave shown with magenta color dotted line is propagating downwards from the source and critically refracted at the boundary of upper and lower crust propagating as head wave (Telford *et al.*, 1976) along the uppermost part of lower crust and then again critically refracted to upper crust to reach the seismic station. Therefore, this wave partially propagates with velocity of upper layer and partially with the velocity of lower layer. As described by Telford *et al.* (1976) the travel time t_2 of this wave is given by

$$t_2 = \frac{X}{V_2} + \frac{2Z_1}{V_1 V_2}\sqrt{V_2^2 - V_1^2}$$ ----------------- 3.2

Similarly, the other wave shown with green color propagates downwards from the source in the upper crust with velocity V_1 and reflected at the boundary of upper and lower crust to penetrate in the lower crust propagating with velocity V_2. This wave is critically refracted at Moho boundary to propagate in the uppermost part of mantle with velocity V_3. Then again it is critically refracted to propagate in the lower crust reflected on the boundary of lower and upper crust to reach to the station. The overall propagation time t_3 of this wave is given by

$$t_3 = \frac{X}{V_3} + \frac{2Z_1}{V_1 V_2}\sqrt{V_2^2 - V_1^2} + \frac{2Z_2}{V_2 V_3}\sqrt{V_3^2 - V_2^2}$$ ---------------- 3.3

As shown in **Figure 3.7**, the velocities V_1, V_2 and V_3 can be obtained from the plots of epicentre distance and travel times of these three waves. These velocities are calculated from the inverse of the slopes of three curves shown with blue, magenta and green colors for these three waves.
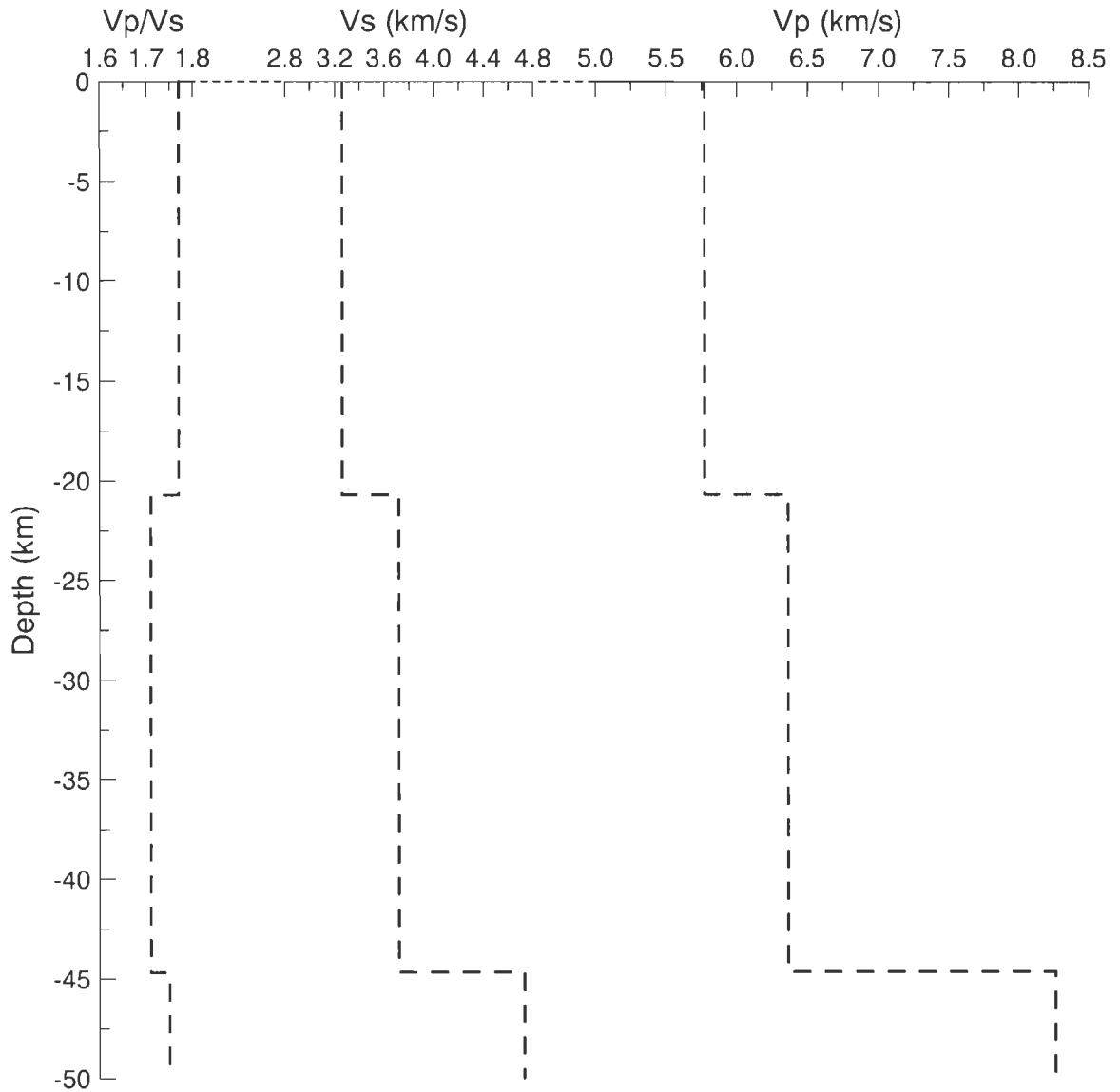
Figure 3.8: The three layer 1-D velocity model obtained using travel time versus distance plot for the 285 shallow focused local and regional earthquakes of NW Himalaya.

It is evident from equations 3.1, 3.2 and 3.3 and **Figure 3.7** that the time t_1 should be minimum and time t_3 should be maximum. However, the velocity of seismic wave usually increases with the increase of depth so that V_1 is the minimum velocity and V_3 is the maximum velocity. Based on this if the source is near to the station then t_1 is less and minimum and t_2 is more but with the increase of the epicentre distance the travel time of wave represented by equation 3.2 will propagate more and more distance through the lower layer (having higher velocity) as compared to its path through upper layer (having less velocity). Therefore after certain epicentre distance t_2 will be less than t_1. In this way when the time of t_1 is equal to t_2 then the epicentre distance is known as critical distance X_{c1} and the thickness of upper layer can be obtained from the equations 3.1 and 3.2 which is given as

$$Z_1 = \frac{X_{c1}}{2}\sqrt{\frac{V_2 - V_1}{V_2 + V_1}} \qquad \text{----------------- 3.4}$$

Similarly for smaller epicentre distance t_3 is more than t_2 while after some time it is reverse as V_3 is more than V_2 and the time t_3 depends on how much portion of propagation path lies in the upper mantle. At the critical epicentral distance (X_{c2}), the times t_2 and t_3 will be equal and using equations 3.2 and 3.3 the thickness of lower layer can be obtained from critical distance as

$$Z_2 = \frac{X_{c2}}{2}\sqrt{\frac{V_3 - V_2}{V_3 + V_2}} \qquad \text{------------------- 3.5}$$

Table 3.3. 1D velocity model obtained using the travel time information.

Layer	P-Wave data			S-Wave data			Vp/Vs
	Depth (km)	Thickness (km)	Vp (km/s)	Depth (km)	Thickness (km)	Vs (km/s)	
1	0.0	20.7	5.77±0.03	0.0	19.60	3.26±0.01	1.77
2	20.7	24.0	6.38±0.14	19.60	23.50	3.72±0.08	1.71
3	44.7	Half Space	8.26±0.11	43.10	Half Space	4.73±0.05	1.75
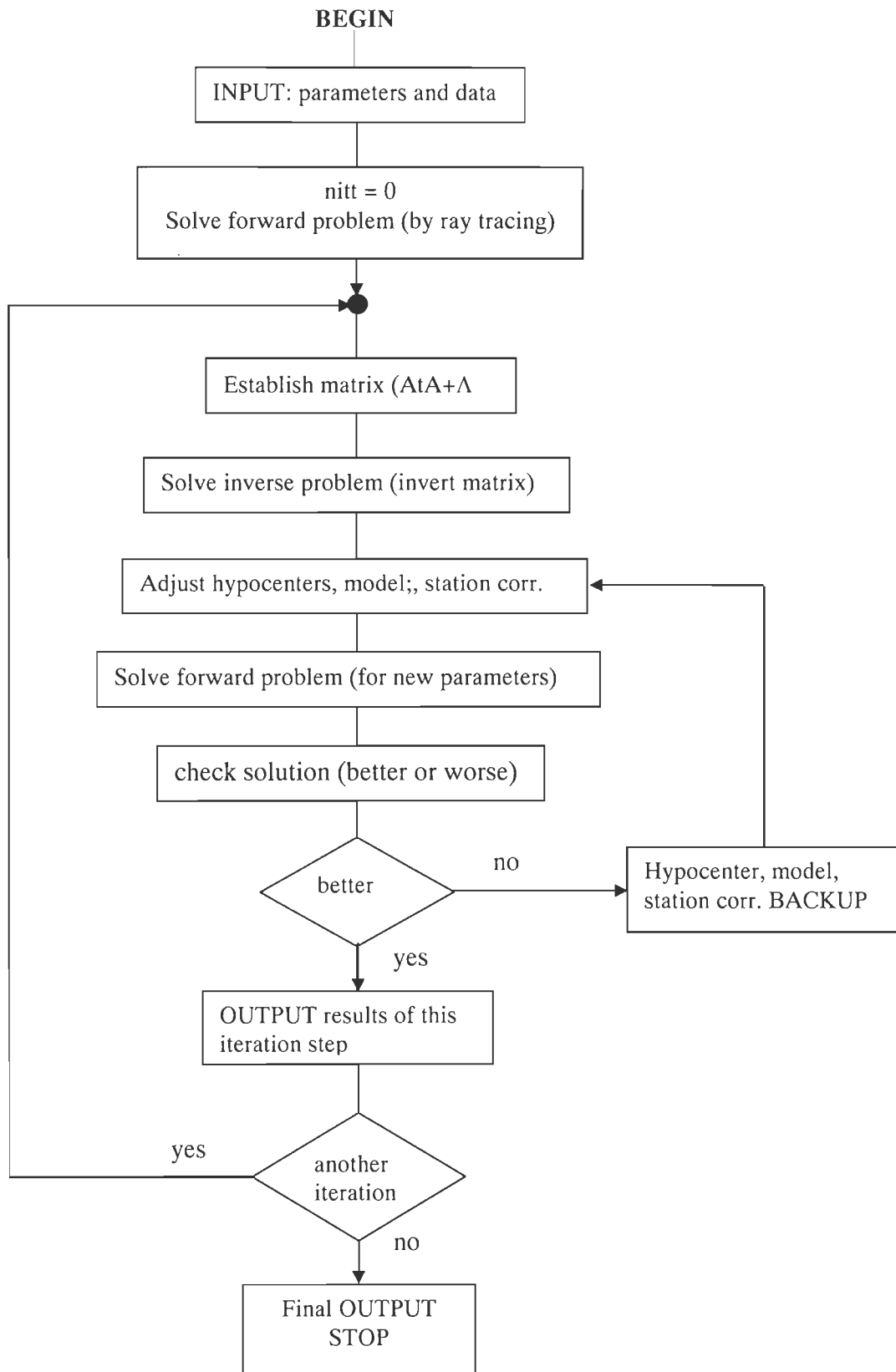
Figure 3.9: Overview of the VELEST algorithm applied for 1D inversion.

The thicknesses of different layers were estimated using these velocity values and the time values where two lines cross each other as shown in **Figure 3.7a**. These values are shown in **Table 3.3**.

Using present data set the estimated average Pg-wave velocity of the upper crust is 5.77 ± 0.03 km/s based on initial travel time of the wave shown with green color line in **Figure 3.6a**. The linear regression fit of middle part of this curve shown with blue color gives the P*-wave velocity of 6.29 ± 0.11 km/s which is the P-wave velocity of the lower crust. These two velocities and the intercept time of these two portions of the curves were used to obtain the thickness of the upper crust as per relation given in equation 3.4. This average thickness of the upper crust is 20.7 km for the present study region. The Pn velocity of the upper mantle was obtained from last section of the curve. The inverse of slope of this section of the curves gives velocity 8.27 ± 0.11 km/s showing a large contrast in velocity at the crust-mantle boundary (**Figure 3.8** and **Table 3.3**). The velocities of middle and last portion of the curve are used along with the intercept times to obtain the depth of Moho discontinuity. The Moho discontinuity between lower crust and upper mantle for Kangra-Chamba region is obtained at a depth of 44.7 km, therefore the thickness of lower crust is 24.0 km. These velocities of upper crust, lower crust and crust-mantle boundary are represented by Pg, P* and Pn as mentioned in **Figure 3.6a**.

Similar linear regressions are performed for the S-wave travel time curve (**Figure 3.6b**) to obtain the S-wave velocities for the crustal layers and and upper mantle for the study region. The slope of the linear regression fit straight line for the initial part of the distance-time curve of S-wave was used to obtain 3.26 ± 0.01 km/s Sg-wave velocity of the upper crust based on distance-time-velocity relation given in equation 3.1. This straight line is shown in **Figure 3.6b** with green color. The middle part of the curve shown with blue color line was used to obtain S*-wave velocity of 3.72 ± 0.08 km/s through the inverse of slope of this part of the curve. Using the relation of equation 3.4, these two velocities and the intercept time of these two straight lines was used to calculate 19.60 km thickness of the upper crust. With this data the upper mantle velocity is 4.73 ± 0.05 km/s calculated for Sn-wave using the last portion of the curve shown with black straight line as a straight line least square fit. Based on relation of equation 3.5, the thickness of the lower crust was obtained as 23.50 km using the intercept time of middle and last part of the curve and the velocities of lower crust and upper mantle.

Therefore using S-wave data of these earthquakes the average depth of Moho discontinuity for this part of the Himalaya is 43.10 km. This analysis gives mean Vp/Vs ratios of 1.77, 1.71 and 1.75 for the upper crust, lower crust and the uppermost mantle respectively. The reduced velocity model and layer parameters are listed in **Table 3.3**.

Plot	Model Name	Initial rms	output inversion rms
M – – – – –	Mukhopadhyay and Kayal	0.5226	0.3867
N ·················	Ni and Ibenbrahim	0.7158	0.4134
T ————	Travel-Time present study	0.5689	0.3712
L — · —	Low Velocity	0.6788	0.4153
H — - - -	High Velocity	0.9008	0.4156
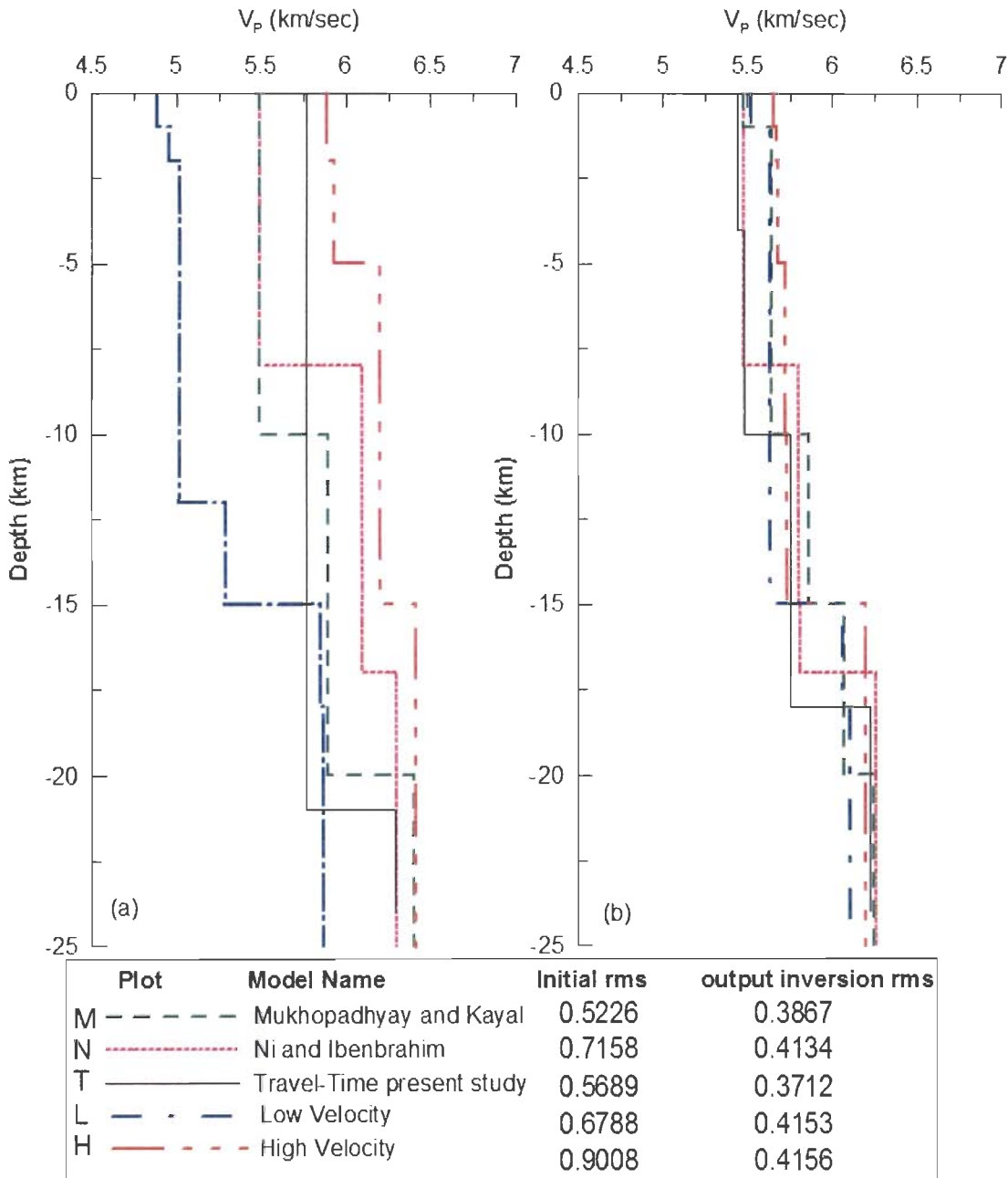
Figure 3.10 (a) Various starting test models used as input for the travel time inversion and (b) corresponding output models.

The thicknesses of the upper and the lower crust and therefore the depth of Moho discontinuity obtained by the data of the phase readings of P- and S-wave obtained using this method are not identical (**Table 3.3**) but a small difference exist. This difference is not significant. In this data set the used number of S-phase was less as compared to P-phase because signal-to-noise ratio in case of S-wave was less as this phase is found in the last portion of P-wave coda. Therefore, layer thickness obtained using P-wave data is considered and the reduced velocity model further used is shown in **Figure 3.8.**

3.4.3. Assessment of Data Quality that can be used for Simultaneous Inversion

When using simultaneous inversion technique to get a reliable estimate of a velocity model one needs to have reliable locations of earthquakes. Whether a particular data set can be used to obtain reliable location of an earthquake or not depends on the accuracy of its phase readings. Besides this the following criteria also determine the quality of the solution.

- **Minimum number of phase data:** to properly locate an earthquake and find its origin time, minimum four phase data are required from different stations. The four unknown earthquake source parameters are three coordinates (x, y and z) of earthquake hypocenter that give its location and one denoting the origin time of the earthquake. However to better constrain the location more number of phases using more number of stations is necessary. In the current data we have taken at least six number of phases recorded for each earthquake, out of which at least two should be S-phase data.

- **Azimuthal gap:** The location of the earthquake is obtained in three dimension space taking the information of recording of the earthquake on only two dimensions, i.e. the seismic stations located on the earth's surface. It is necessary that the epicenter of the earthquake should be within seismic network to properly locate it. Therefore, the earthquake source must be within the periphery of the seismic stations on which it is recorded. Therefore, to improve the quality of the location, the maximum seismic gap between two stations out of the available data for one seismic event is calculated. The smaller is the value of maximum azimuthal seismic gap, better is the location, especially the focal depth. To fulfill this criterion,

maximum azimuthal gap was taken less than 180°. Therefore, the seismicity used for the tomography inversion was within the START 2004 array. Using these selection criteria, in the first step the appropriate seismic events are chosen for further analysis.
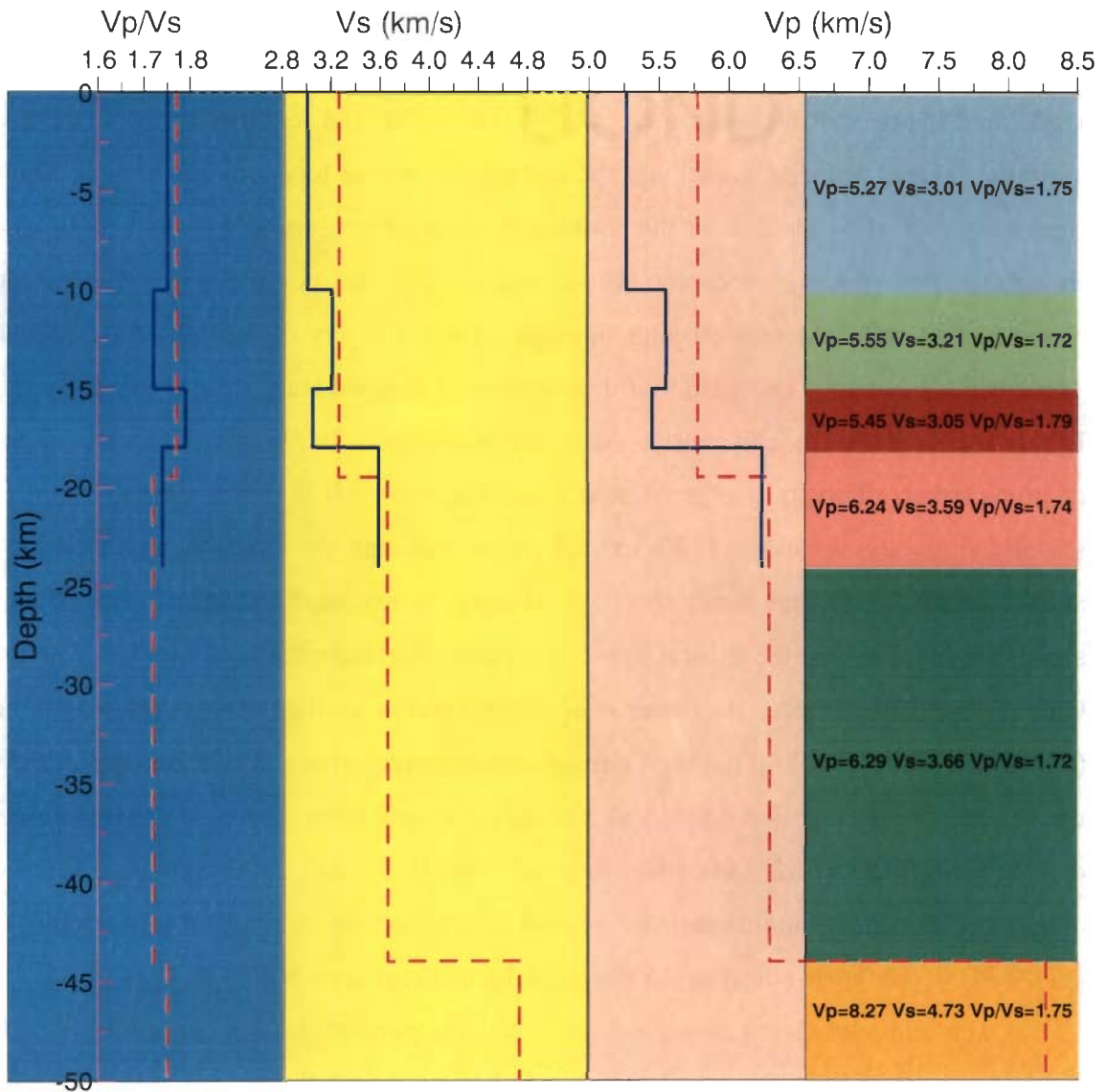
Figure 3.11: 1D velocity model for Vp, Vs, and Vp/Vs derived from travel-time–distance plots (dotted red lines) overlain by a velocity model obtained from travel-time inversion (solid blue lines). In the right side variation of 1D model in depth is shown with different color along with corresponding value.

In this case, the local seismic events are selected using the time difference or the epicenter distance from the central station (Naddi) of the array. This difference of S- and P-wave data is taken as 25 s so that the epicenter distance is approximately 200 km.

3.4.4. Estimation of 1-D Velocity and Vp/Vs Model by Simultaneous Hypocentre-Velocity Inversion

To obtain improved crustal velocity structure, simultaneous inversion, both for 1-D velocity model and earthquake location, was performed using the VELEST algorithm (Kissling, 1988, 1995; Kissling *et al.*, 1994). The overview of the different steps involved for the hypocenter-velocity model coupling is shown in **Figure 3.9** where in one iteration, the forward and inverse problem is solved and the new velocity model and hypocenter locations are obtained. The input data required for processing is an initial layered velocity model and the earthquake source locations (or the controlled source location if available). In the forward problem, the ray tracing are incorporated from source to station (receiver). These ray tracings are computed through direct, refracted and reflected rays passing through different layers of 1-D structure model. The inverse problem is executed by full inversion of damped least square matrix [AtA + L], where A is the Jacobi matrix, At is the transposed Jacobi matrix and L is the damping matrix. This inverse problem is a non-linear one. It is first linealised and then solved iterativelly. As shown in **Figure 3.9** all the modules are solved in single iteration and depending upon the result the next iteration is executed. The efficacy of this algorithm in deducing the crustal velocity structure in seismically active belts of the Gulf of Arta, NW Greece (Haslinger *et al.*, 1999) and in southern part of the Colombia (Ojeda and Havakov, 2001) is well demonstrated among others where the approach is used to get the starting model for local earthquake tomography studies (e.g. Michelini *et al.*, 1998; Raffaele *et al.*, 2006; Nicole *et al.*, 2007). I also utilized this algorithm to obtain the 1D velocity model and that is used in next section as input for tomography to get the 3D velocity variations in the Kangra-Chamba region of NW Himalaya.

The minimum 1-D velocity model with corresponding station corrections results from simultaneous inversion of a large number of travel times from selected high quality-events such that the sum of residual of all events is minimized. For this a set of well-located events meeting the following criteria were selected: individual event RMS lower than 1.0s, azimuthal gap of stations recording the individual event is ≤ 180° and with 6 or more P- and S-phase readings. Finally, 172 events (**Figure 3.2**) with 906 P-phases and 773 S-phases were used for inversion using 1-D inversion algorithm following the procedures given in Kissling *et al.* (1994). The final inverted model
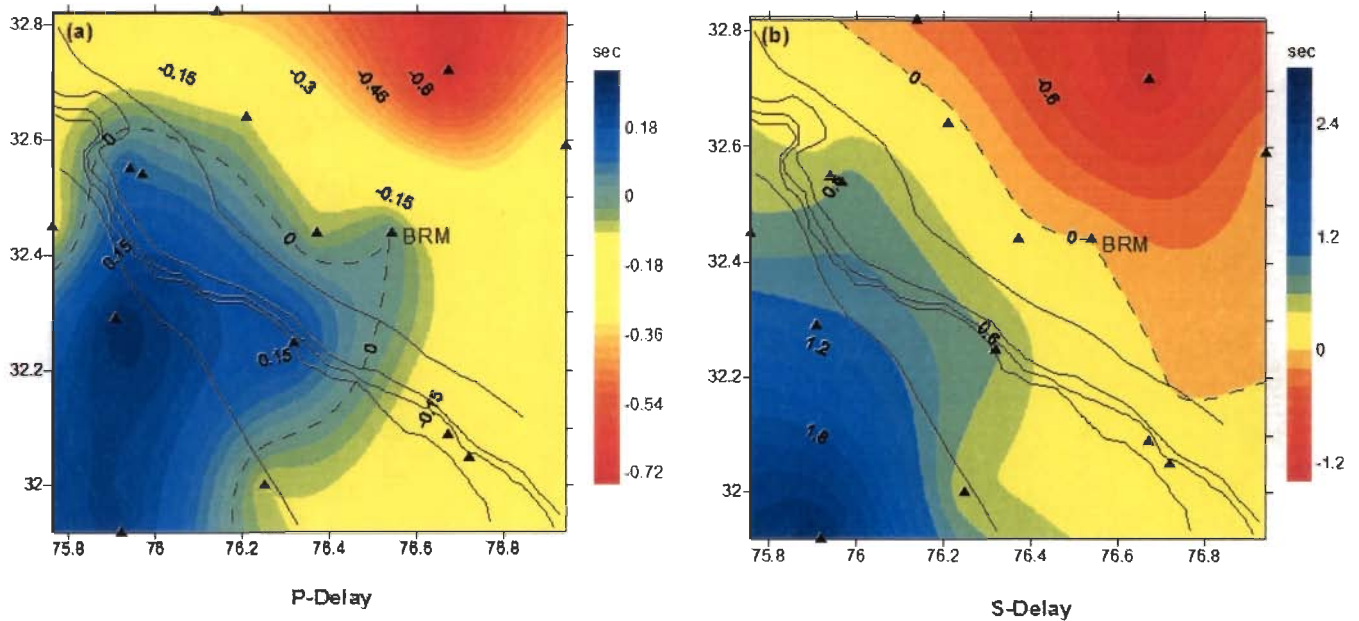
Figure 3.12: Contour plots for station corrections for (a) P-wave and (b) for S-wave with respect to the reference station BRM.

depends upon the spatial distribution of recording stations, seismic sources and a priori initial velocity model. The initial hypocenter location showed that focal depth of recorded earthquakes ranged from near surface down to depths of 40 km but most of the events are confined to upper crust. Therefore, the velocity and thickness deeper than 25 km and the Moho depth is not resolved by these data. The Moho depth of ~45 km, inferred from travel-time plot is used as a priori information. Further given the sensitivity of the inverted model to initial velocity model, we tested several initial a priori velocity models (**Figure 3.10**). The velocity and geometrical distribution, in the range of model tested, were in principle guided by the velocity models of Kamble et al. (1974), Ni and Ibenbrahim (1991), Mukhopadhyay and Kayal (2003) and that obtained using travel time plots (this study). Two synthetically generated models having velocities lower and higher than velocities for other models in most depth levels were also incorporated for this analysis. The five initial velocity models of P-wave velocity variation at different depth levels up to a maximum depth of 25 km are shown in **Figure 3.10a** and the names of these velocity models are given in legend in this figure.
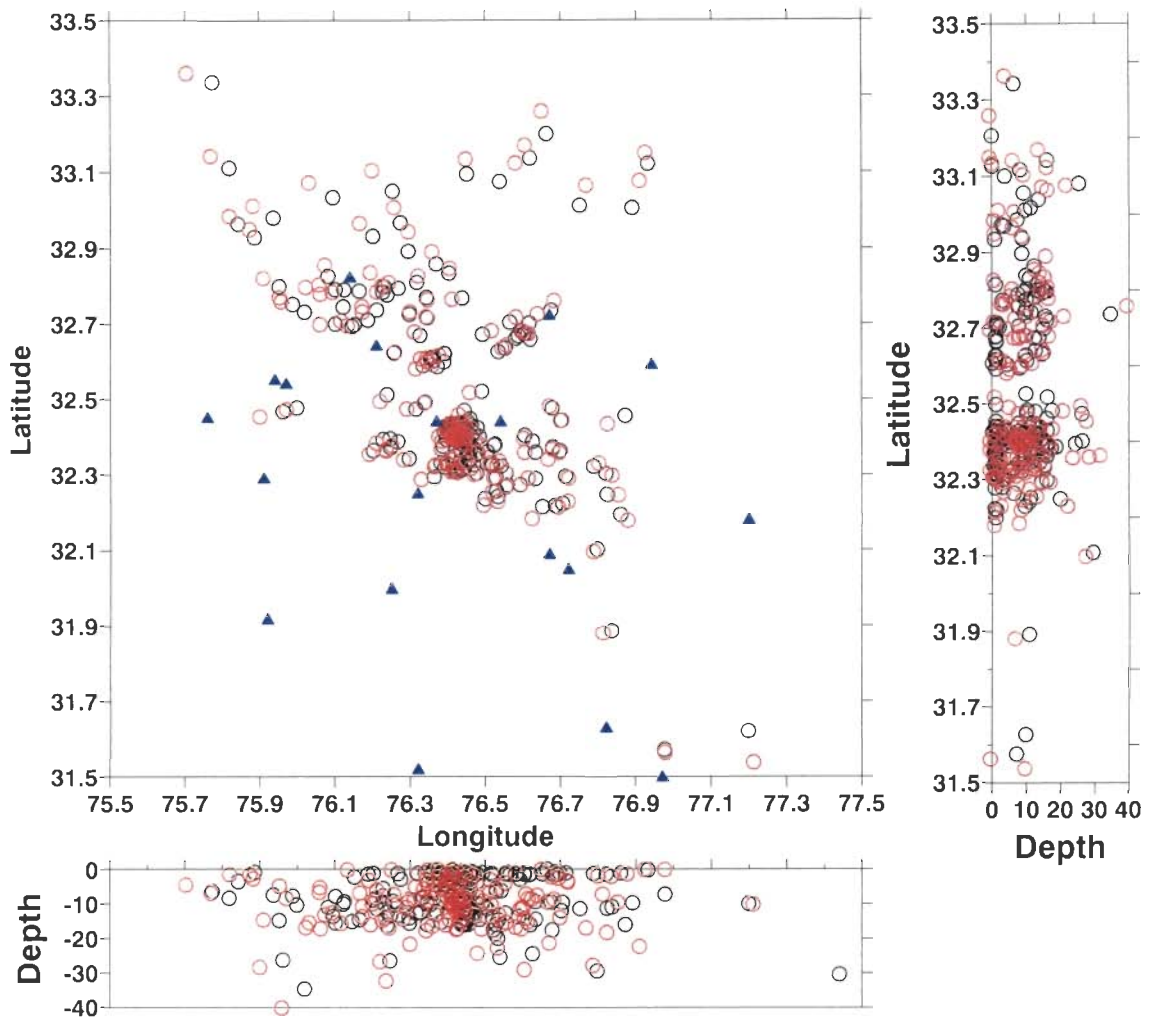
Figure 3.13: Epicntral and hypocentral shift after the final 1-D P- and S-wave inversion relative to the initial velocity model. The initial location is shown with black circle and the final location with red circle.

The new inverted 1-D P-wave velocity model with minimum RMS value obtained from each 1-D initial model are shown **Figure 3.10b**. The reduction from initial RMS to final RMS error for each model is given in the legend of this figure. It is clear that the final velocity models are close to each other for all the depth levels as compared to the initial velocity models. However, for estimation of 3-D variation in velocity and Vp/Vs for this region, I have used the final velocity model obtained from the initial model estimated from travel time plot as this shows the minimum RMS error among all the cases reported.

It is clear from **Figure 3.2** that the region of study has uneven topography where the Dhauladhar ranges of Himalayan peaks are about 4 km high. The location of seismic

84

stations is given in **Table 3.1** in which the height of station from mean sea level (MSL) varies between 500 to 2520 m. Therefore, to incorporate the 1-D velocity model, the layers of this model were started by including 4 km thick strata above MSL. Hence as given in **Tables 3.4** and **3.5**, a layer of -4 to 0 km was also included. In all the cases, we started with large number of thin layers (nearly 2 km thick) and during the inversion process combined those layers in which the velocity values were found similar. Typical initial input velocity models as well as output models estimated from travel time inversion are shown in **Figure 3.10** and include the models defining the upper and lower bound on the range of velocities tested in the given depth range. For each initial model, the inversion was terminated when average RMS did not change significantly for the next iteration. In the selection of final model, beside the minimum average RMS error of all events as a criterion, the errors in earthquake location parameters were also considered. As seen in **Figure 3.10**, inverted velocity distribution shows some variability, however, the velocity interfaces in the depth range of around 10 km and 15 km are persistently indicated by range of models tested. Using these initial models of P-wave and adopting the value of Vp/Vs equal to 1.74 taken from Wadati diagram, the 1-D velocity model of S-wave is also calculated by the same procedure.

It is also noted that in the range of models tested the velocity values increase with depth, the initial RMS errors, which ranged between 0.52s and 0.90s for P-wave, did not drop below 0.37s-0.42s. In this trial and error search for realistic velocity model, it was observed that an introduction of a low velocity layer between 15 and 18 km (**Figure 3.11**) leads not only in reduction of average RMS error to 0.32 s but also greatly improves the earthquake locations which are shown later to be more coherent with the tectonic models of the region. Of course, as cautioned by Ojeda and Havskov (2001), special care was exercised to avert instability in inversion by appropriate choice of damping factor in the inversion scheme.

The new 1-D velocity model of Vp and Vs were used to determine variation of Vp/Vs with depth. The resolution parameters for Vp and Vs of different layers with and without low velocity layer are given in **Table 3.4**. The result indicate that the data is giving less resolution parameter for depth range 10 to 18 km for both the cases however these value are tolerably good for obtaining 1-D velocity model. It is observed that introduction of low velocity layer caused improvement in resolution in the 10 to 18 km depth range, whereas those for other layers were not significantly affected. The final 1-D inverted velocity model, obtained after several runs of the iterations, divides the

upper crust down to a depth of 24 km into four layers, with a thin low velocity layer between 15-18 km and the last layer simulating half space (**Figure 3.11, Table 3.5**). In the inversion analysis, the velocity interfaces at 10 km and 15 km were placed in the initial input model based on the number of preliminary tested models described above. In the final model, the initial average RMS value of 0.50s reduced to lowest value of 0.32s.

Table 3.4: Resolution parameters of various velocity layers obtained from the inversion of P and S-waves

Model including incremental increase in velocity with depth					
Depth (km)	-4	0	10	15	18
P-Resolution	0.9894	0.9699	0.5760		0.8155
S-Resolution	0.9768	0.9868	0.5027		0.9971
Model including low velocity layer					
Depth (km)	-4	0	10	15	18
P-Resolution	0.9856	0.9250	0.6161	0.8087	0.9969
S-Resolution	0.9857	0.9854	0.8377	0.6410	0.9917

The validation and stability of the inverse problem is also defined in respect of total number of observed phases with respect to unknowns. A total of 738 unknowns (4 x 172 hypocentral parameters, 4 layers below MSL with both P and S-velocities and 42 station corrections for both phases). The combined number of observations of P- and S-phase is 1679 giving the formal over determination factor of 2.3 approximately. **Table 3.5** summarizes the parameters of the final 4-layer velocity model below MSL. The bottom layer with average Vp of 6.26 km/s compare well with velocity mapped for lower crust from the travel-time plot. The optimum velocity model for the full thickness of the crust and uppermost mantle, obtained by the combination of time-distance plots and travel-time inversion results, is superimposed on **Figure 3.11** dividing the crust in to five layers with different values of Vp, Vs and Vp/Vs.

Table 3.5: 1-D velocity model obtained using P and S-wave data inversion.

Layer	Depth (km)	Thickness (km)	Vp (km/s)	Vs (km/s)	Vp/Vs
1	-4.0	4.0	5.32 ± 0.09	2.45 ± 0.15	2.65
2	0.0	10.0	5.27 ± 0.13	3.01 ± 0.40	1.72
3	10.0	5.0	5.55 ± 0.12	3.21 ± 0.32	1.74
4	15.0	3.0	5.45 ± 0.37	3.05 ± 0.30	1.80
5	18.0	Half Space	6.24 ± 0.04	3.59 ± 0.50	1.73

3.5. INTERPRETATION AND DISCUSSION

3.5.1. Optimum Crustal Velocity Structure

Regression analysis of travel-time curve shows that crust mainly consists of two layers with P-wave velocities of 5.77 km/s and 6.38 km/s respectively. The P-wave velocity of the second layer and underlying half-space (8.26 km/s) are typical of the continental lower crust and upper mantle material. Therefore, the layer thickness of ~21 km and 24 km for the first and second layer respectively place the Moho at a depth of 45 km. These estimates of crustal layering and velocity are fully in agreement with the velocity model for the Dalhausei-Mandi section (encompassing the present study area) where average crustal thickness of 46 km with P-wave velocities of 5.75 km/s for the 24 km thick upper most crust, 6.73 km/s for the 21 km lower crust and 8.22 km/s for the upper mantle were obtained by Kamble *et al.* (1974). Recently, from receiver function study across NW Himalayas Rai *et al.*, (2006) have located the north dipping Moho discontinuity from the depth of 40 km around Dehli in the Gangetic Plains to 75 km beneath the Higher and Trans-Himalayas. The depth of ~45 km beneath the Kangra-Chamba region estimated in this study is consistent with the above regional depth profile of Moho.

The optimum 1-D vertical velocity model obtained from simultaneous inversion of the arrival times of P- and S-waves permits to divide the upper crustal section to a depth of 25 km in to a 4-layer structure (**Table 3.5**). A salient feature of the inverted velocity model is that both Vp and Vs increase with depth except for the depth range of 15 to 18 km. The proportional enhancement of Vs is lower than the Vp in this layer,

resulting in high Vp/Vs ratio of 1.81. In contrast to third layer, the top two layers marked by distinctive Vp and Vs velocities are characterized by the same Vp/Vs ratio of 1.71. The top 10 km thick layer with P-wave velocity of 5.23 km/s, much lower than the typical velocity of upper continental crust, can be related to the thick sheet of weakly metamorphed sediments of the CN that extensively cover the study area and are similar in facies to the Tethy Himalaya sequence exposed further north of the HHC. This geological attribute strongly supports the view of Thakur (1998) who based on the stratigraphic morpho-tectonic consideration postulated the CN sequence to be approximately 8 km thick. In this tectonic scenario, the 5 km second layer with Vp and Vs of 5.66 km/s and 3.26 km/s respectively can be viewed as meta-sediments of under-thrusted sequence of Lesser Himalaya or the over-thrusted sedimentary wedge of Himalaya overriding the down going Indian plate.

The obtained Vp and Vs values for the second layer of 10 km thickness are 5.23 km/s and 3.04 km/s respectively (**Table 3.5**). The Vp and Vs values for the next layer of 5 km thickness increase to 5.66 km/s and 3.26 respectively. These changes in velocities at 10 km depth can be related to the geological aspects of the study area described by Thakur (1998) who has postulated that CN sequence is approximately 8-10 km thick. Our model reveals a slightly low Vp and Vs velocities for the next layer of 3km thickness in the depth range of 15 to 18 km where the Vp/Vs ratio is slightly higher than the upper layer having a value of 1.81. The low Vp and Vs and high Vp/Vs ratio may indicate the zone of transition from brittle to ductile medium where fluid-filled cracks in the rocks are possible. The change in Vp and Vs is very high at 18 km depth which may be either due to low velocity zone from 15 to 18 km depth or this is the boundary between granitic and basaltic layer. This could also be the boundary of two contrasting section in which a thin layer is residing on the top of the under-thrusting Indian plate. However, the observed velocities of P- and S-waves obtained through travel time curves show a change at 21 km depth. We observe that the Vp and Vs values obtained using travel time curves for the depth range 21 to 25 km are similar to those obtained using simultaneous inversion for depths greater than 18 km. This confirms the fact that the estimated velocity values are reliable. However, the exact location of the boundary between the upper and lower crust is not that well resolved and it may lie somewhere between 18 to 21 km depth. However, for our subsequent analysis we take this boundary at 18 km depth as the data used for simultaneous inversion is much well constrained and hence the results are considered to be more reliable.

The Vp, Vs and Vp/Vs values for the top 3 layers match quite well with the velocity of 21 km thick single upper crustal layer resolved by travel time curves. Both the thickness as well as velocity parameters of the fourth layer in the inverted velocity model is not well constrained by simultaneous inversion as there are very few ray paths emanate from below the 20 km depth that is largely free from earthquakes. We, however, observe that within the error limits associated with velocity determinations, the velocity of the fourth layer as well as underlying half space is comparable to the velocity of lower crustal layer given by travel time curves. Therefore, it can be surmised that crust beneath Kangra- Chamba sector of the NW Himalaya with a total thickness of ~45 km can be divided into 4-layers with Vp (Vs) velocities of 5.23 (3.04) km/s, 5.66 (3.26) km/s, 6.38 (4.73) km/s The merit of this 4-layer velocity model over the simple 2-layer crustal model, obtained either from travel-time plots or that reported in Kamble *et al.* (1974) is immediately obvious from the fact that rms of travel time residual for all 172 events analysed through HYPO71 has reduced from 0.42s to 0.33s.

3.5.2. Lateral Velocity Inequalities and Station Corrections

The contour plots of both P-wave and S-wave station corrections with reference of station BRM (**Figure 3.12**) are dominated by strong relative high travel time delays (signifying true velocities lower than the 1-D model) in the southwest part of the study area that changes to pronounced low (corresponding to relative high velocity) in the northeast corner. The area of relative high broadly encompasses low-velocity alluvial/sediments of Indo Gangetic Plains and Siwaliks whereas the region of low station delays, northeast of the Chamba thrust, is covered by the Tethys sequence of CN. However, this distinctive pattern is either almost absent (P-wave) or is greatly subdued in magnitude (S-wave) in the eastern part of the study area, where similar contrast in lithology prevails across the SH. It seems likely that in addition to surface lithology, a substantial part of station corrections may relate to alternative near surface or deeper crustal velocity structure.
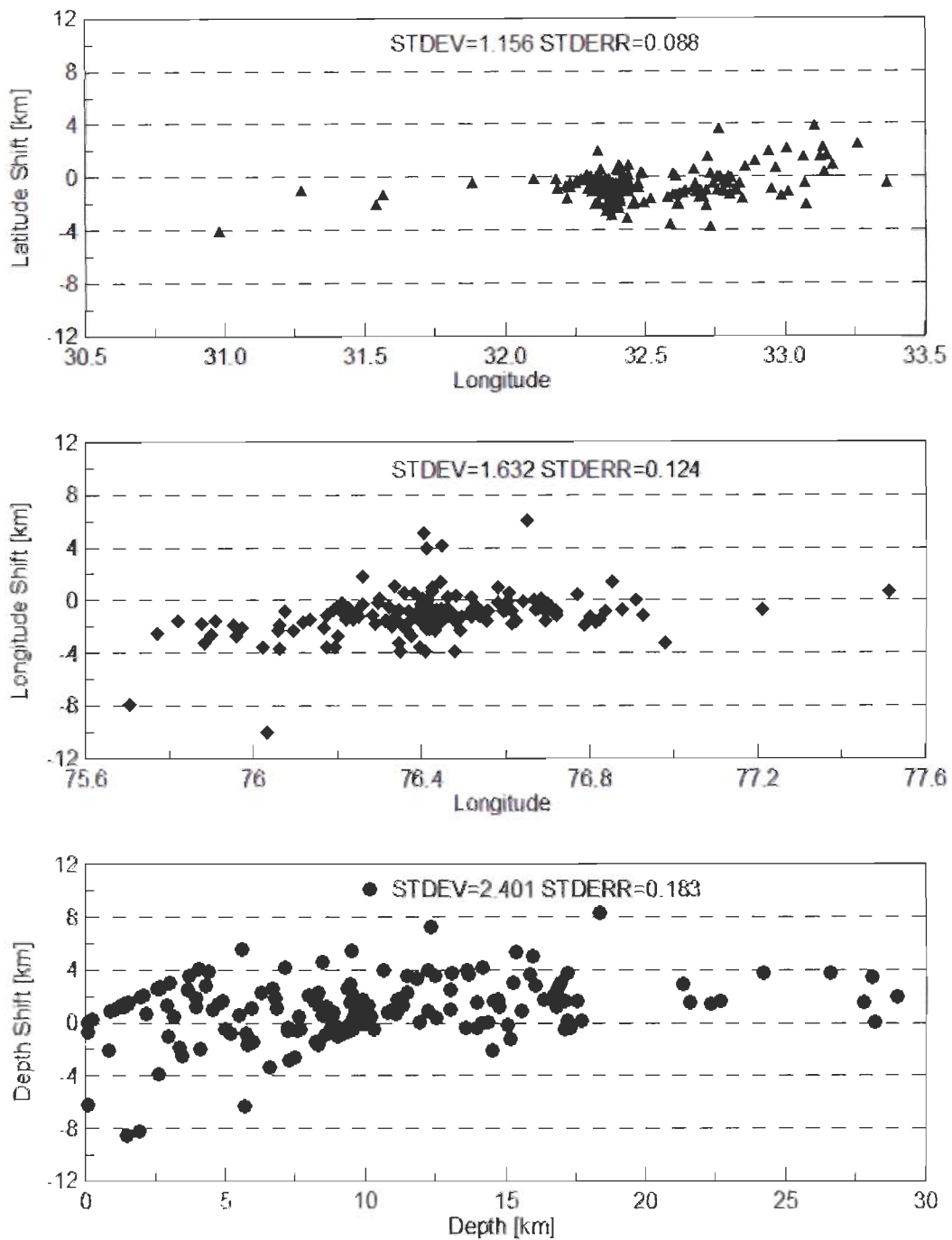
Figure 3.14: The hypocentral shifting after the final 1-D P- and S-wave velocity model relative to initial velocity model. (a) the shift in Latitude (b) the shift in Longitude and (c) the shift in depth.

It is known that in the Himalayan collision regime, the Indian Plate flexes and under thrusts at gentle dip resulting in the increase in the thickness of the overriding wedge from frontal Himalayas to higher Himalayas. The lateral variation in the thickness of overriding wedge is examined as an alternative source of long-term trend in station corrections. The nature of variations in the absolute value of S-wave station

90
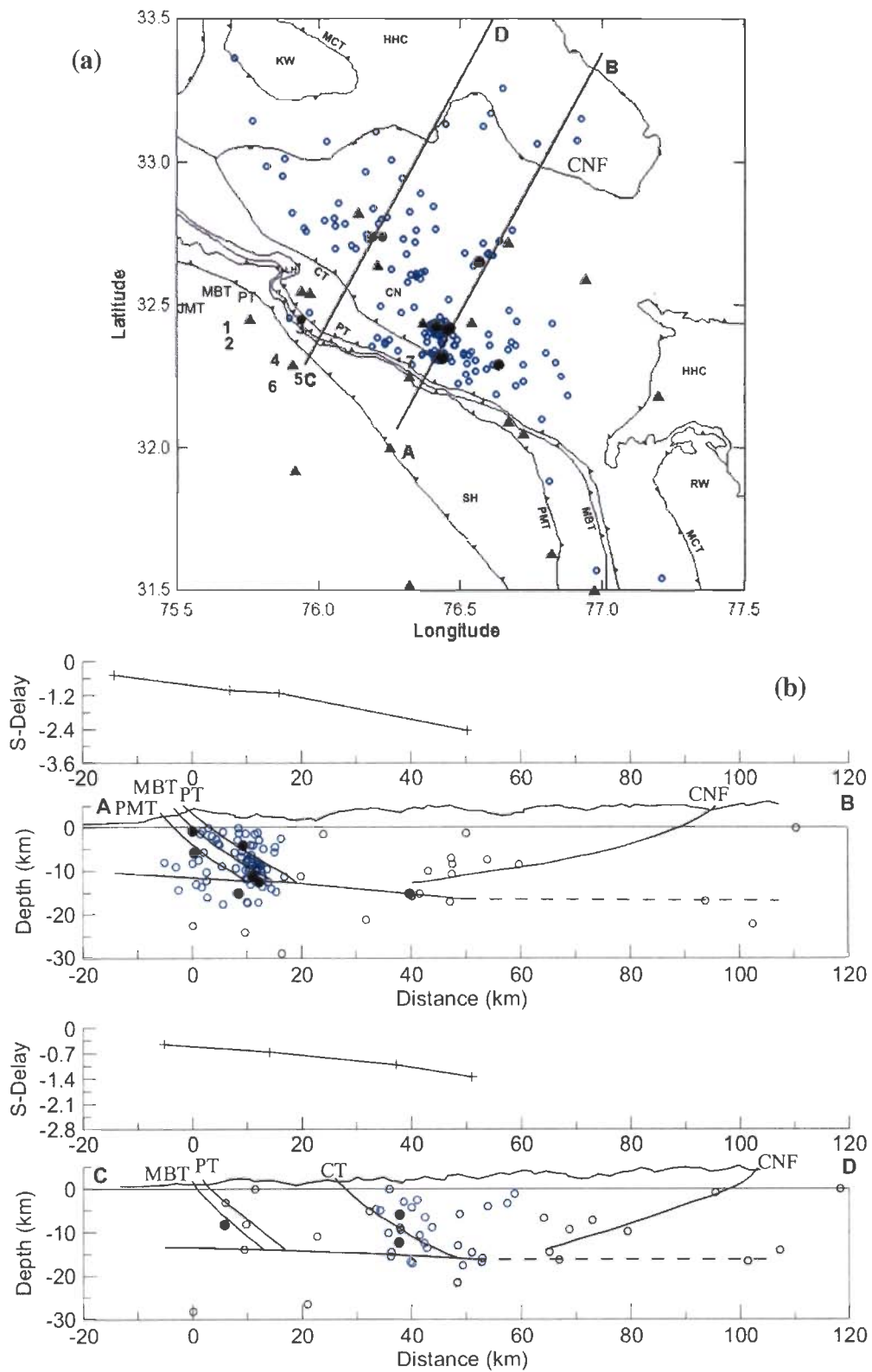
Figure 3.15: Epicentre and hypocentre distribution of well-located 172 earthquakes using JHD in relation to major tectonic feature of the region. (a) The refined epicenter distribution, (b) Depth distribution of refined earthquake location along 50 km wide corridors centered along profiles AB and CD. The distances on both profiles are marked with respect to MBT.

corrections is shown along two selected profiles, AB and CD (upper panels of **Figure 3.15b**). As noted earlier, these long-term trends in station corrections may relate to variation in thickness of the overthrusted sedimentary wedge; the first rough estimate on the geometry of the dipping underthrusting Indian plate is approximated by converting the station corrections to thickness of the wedge corresponding to the average velocity. In such a transformation, the averaged 1D velocity structure can be viewed as northeast dipping layers. As an example, the overall geometry of the upper surface of the mapped anomalous low-velocity layer in the depth range of 15–18 km will be seen as marked in **Figure 3.15** for both profiles. It is interesting to note that, except for a narrow section directly beneath the clustered zone of epicenters, the inferred geometry of the low-velocity layer defines the lower depth boundary of crustal seismicity.

On the P-wave map, the zone of relative high station delays terminates sharply in a prominent NE-SW trend. A critical examination of the delay patterns reveals that the region of transition embeds a zone of local high striking NE-SW, both on the P-wave and S-wave travel time delay plots (**Figure 3.12**). The anomalous trend does not correlate with any topographic or surface tectonic feature. The inversion of present earthquake data sets, using formulation of 3-D local earthquake tomography done in the next Chapter and also reported in Kumar *et al.* (2010), which is best suited to map lateral velocity heterogeneity, do suggest presence of a low velocity zone, coincident with this NE-SW trend, in the depth range of 2- 5 km range, which is underlain by high velocity body.

3.5.3. Joint Hypocenter Determination

The Joint Hypocenter Determination (JHD) performed using the optimum 1-D velocity model allows relocation of hypocenters with higher precision after adjusting for the station corrections. The 172 events were again located using HYPO71 (Lee and Lahr, 1975) and the 1-D velocity model estimated in this work. These earthquake locations are shown in **Figure 3.13** with black circles. These earthquakes were also relocated through JHD for removing the station corrections due to geotectonically complex nature of the region. The epicentral and hypocentral locations obtained by JHD are shown by red circles in **Figure 3.13**. The average RMS error of 0.33 s obtained when the earthquakes are located using HYPO71 and the estimated velocity model is reduced to 0.23 s when they are located using JHD. The improvement in location through JHD is significant in depth direction. To better estimate the difference in the

hypocenter locations by these two methods, the difference in location along latitude, longitude and depth is calculated. These differences are shown in **Figure 3.14** where in (a) the locations are shifted in latitude, in (b) these are shifted in longitude and (c) in the focal depth. The standard deviation obtained in these three different parameters show that the shift of earthquake locations is more along depth as compared to epicentral positions.
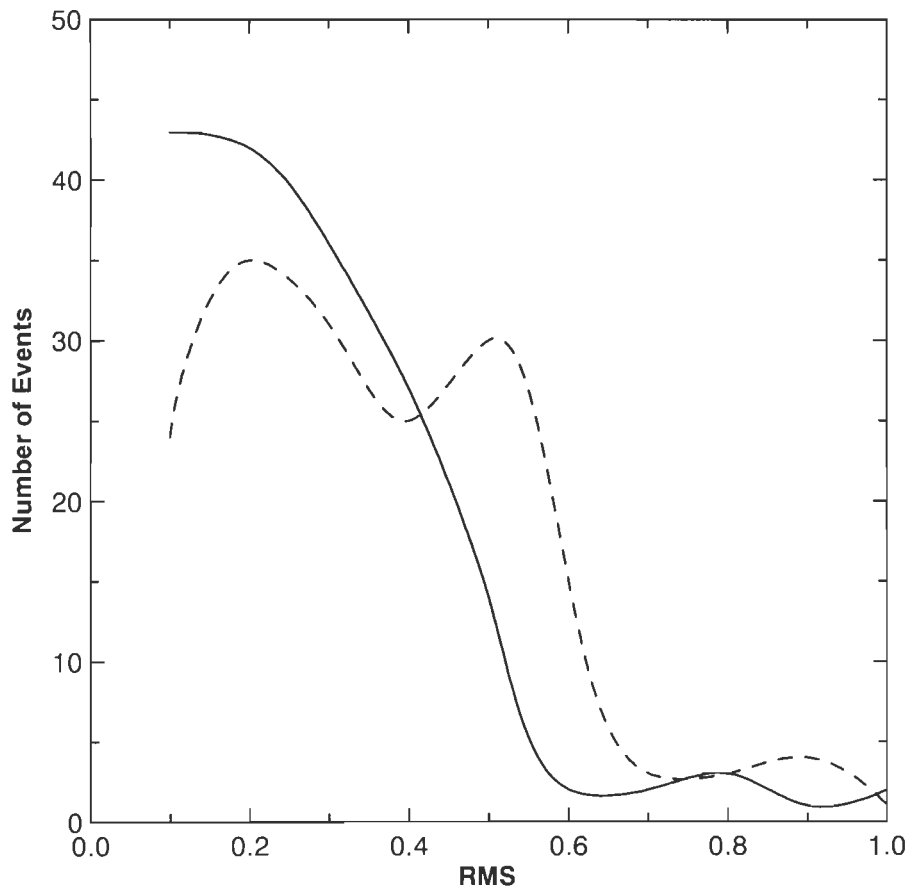
Figure 3.16: The curves showing the Root Mean Square (RMS) error after the final P- and S-wave inversion model relative to initial model. The dashed curve is the RMS variation for initial model and solid curve for final model.

The locations of the earthquakes are also judged from the RMS difference of the time differences of seismic phases obtained between calculated and observed values. In **Figure 3.16**, the variation of RMS values of the present data set obtained using the 1-D minimum velocity model with HYPO71 and JHD are plotted. This RMS value measures the quality of the location; closer is the value to 0 better is the location. The RMS values varies between 0 and 1 for these 172 earthquakes where the variation using 1-D

minimum velocity model and HYPO71 is shown with dashed line and its value based on JHD is shown with solid line. The RMS values are less than 0.7 for most of the earthquakes in the former case and less than 0.6 in case of JHD. In case of JHD the number of earthquakes goes on decreasing with the increasing value of RMS while in case the other numbers of earthquake are almost equal for RMS between 0.1 and 0.6. It shows that the JHD method has improved the location for most of the earthquakes. This may be due to the fact that for JHD station corrections are taken into account when locating earthquakes.

The hypocenters are thus better located by the JHD method in the region having lateral heterogeneity in the velocity structure at shallow depth. The relocated earthquakes reveal a close association of seismic activity with active faults in the study region (**Figure 3.15**). Most of the earthquakes lie in the CN and LH clustering around MBT, PT and Chamba Thrust (CT) and most of the events are located in the top 20 km, i.e. in the upper crust. The earlier status of seismic pattern in the Himalayan region given by Forte *et al.* (1975), Seebar *et al.* (1981), Ni and Barazangi (1984), Molnar (1990), Chandra (1992), and particularly for NW Himalaya by Thakur *et al.* (2000), Kayal (2001) and Kumar *et al.* (2009) have located most of the epicenters between MBT and MCT with shallow focus earthquakes lying along these discontinuities. In order to understand the seismotectonic model of the region, we took two cross sections (mentioned by AB and CD in **Figure 3.15** across the tectonic trends traversing nearly from Southwest to Northeast direction where maximum seismicity is found. The distribution of epicenters shows two close groups of shallow seismic sources belonging to these two cross sections where earthquakes that fall within 25 km on either side of the cross-section lines are considered. The relocated earthquakes along two cross sections show that most of the earthquakes are concentrated near major faults. This shows that these faults are currently active. In the next chapter estimation of 3-D variation in Vp, Vs and Vp/Vs are reported.

3.6. CONCLUDING REMARKS

The earthquake source location in the NW Himalaya used to have higher error due to scattered location of stations and poor coverage from high altitude northern region. The experiment 2004 of WIHG has been perfomed with an aim of removing these two limitations of seismic monitoring in an area of intense micro-earthquake activity in the epicentral region of devastating M8.0 Kangra earthquake of 1905. The

well-calculated 1-D crustal velocity model is an efficient model for the relocation/location of earthquakes. The 1-D velocity model has divided the upper crust below MSL and down to a depth of 24 km into four layers, with a thin low velocity layer between 15 and 18 km. The low Vp and Vs and high Vp/Vs ratio may indicate the zone of transition from brittle to ductile medium where fluid-filled cracks in the rocks are possible.

The change in Vp and Vs is very high at 18 km depth which may be either due to low velocity zone from 15 to 18 km depth or this is the boundary between granitic and basaltic layer. This could also be the boundary of two contrasting section in which a thin layer is residing on the top of the under-thrusting Indian plate. The seismic activity is very low below 20 km depth in this part of Himalaya which may indicate the possibility of second aspect so that underthrusting Indian plate below this depth is comparitivelly ductile as compared to upper part and the occurrence of earthquake is negligible. The improved hypocenters of the micro and low magnitude earthquakes are further refined and better located by the JHD method in the region having lateral heterogeneity in the velocity structure at shallow depth. The relocated earthquakes reveal a close association of seismic activity with active faults. Most of the earthquakes lie in the CN and LH clustering around MBT, PT and CT and most of the events are located in the top 20 km, i.e. in the upper crust. The shallow focused micro-seismic activity belongs to the Punjal imbricate zone at the southern boundary of CN and low magnitude earthquakes are occurring at the upper boundary of northerly low dipping detachment plane.

The seismogenic signification of deduced optimum velocity structures and improved locations of earthquake parameters in constraining the seismo-tectonic model of the region are further discussed in the concluding Chapter 7.

CHAPTER 4

IMAGING 3D VELOCITY STRUCTURES OF KANGRA-CHAMBA REGION USING LOCAL EARTHQUAKE TOMOGRAPHY

4.1. INTRODUCTION

Given that contour plots of station corrections warrant significant deviation from 1D velocity structure, which cannot be explained by surface topography as well as by near-surface heterogeneities, the P- and S-waves, inverted to derive the optimum 1D velocity structure, is further processed to deduce the high-resolution 3D velocity structures using the well proven technique of local earthquake tomography (LET) (Thurber, 1993). This Chapter includes a brief description of the basic principle of LET and how it proceeds for simultaneous estimation of hypocenter parameters along with Vp and Vp/Vs structure. Using the optimum arrived grid spacing, the robustness of the inversion is tested by checkerboard resolution, derivative weight sum and choosing appropriate damping coefficient etc as adopted in earlier works in Indian region (Mukhopadhyay and Kayal, 2003; Mukhopadhyay et al., 2006) and in other parts of the world (Calvert et al., 2008; Pie et al., 2007; Wagner et al., 2005). The true nature of inverted 3D variations in Vp, Vs and the ratio Vp/Vs for the central block, well resolved by LET, are shown as horizontal slices corresponding to depths of 0, 2, 5, 10 15 and 18 km. Systematic and significant variations up to 14% in Vp and Vs along with up to 6% in the Vp/Vs ratio have been observed across the major tectonic units. The low velocity perturbations (LVP) largely overlap with known exposure of the Siwalik and Lesser Himalaya, while relatively high velocity areas correspond to metamorphosed sedimentary sequence of TH and thus help to map the spatial extent of the CN at different depths. It is clearly seen that the southward extent of the CN on the western part of the study area is limited by the Chamba Thrust (CT) whereas on the eastern part the CN extends right up to the PT/MBT. This varying limit of southward extension of the CN helps to resolve the long standing structural puzzle that the CT bordering the Chail formation to the north is well marked west of Chamba, whereas this contact is not traced east of Chamba (Singh, 1994). Another distinctive feature of velocity tomograms is a narrow NE-SW aligned LVP in the eastern part, confined to depth interval of 2 to 5 km and is underlain by a high velocity zone in tomograms at 10 km depth. This

coincides with a structural discontinuity striking NE-SW which is also coincident with the sharp terminus of positive station delays, as noted in previous chapter.

To establish correlation of resolved earthquake parameters with crustal heterogeneity as revealed by velocity structures, the distribution of hypocenters in specific depth intervals are superimposed on the velocity tomograms, which clearly depict that most of the hypocenters at different depths are concentrated at the boundary between low-high velocity couplet. Since such linkages are better developed and outlined in Vs tomograms, part velocity variability may reflect rheological changes associated with varying degree of saturation (Caldwell *et al.*, 2009; Wagner *et al.*, 2006).

This section discusses the results of the 3D tomograhic inversion executed for the Kangra-Chamba region of NW Himalaya. The well-resolved features obtained from the inversion are highlighted in context of crustal structure and tectonic setting of the region. The section concludes with an interpretation of the results of tomography in comparison with geological and other geophysical results obtained by previous studies. First a brief discussion of local earthquake tomography (LET) methodology and problem has been given following the overview of used algorithm of the inversion. The discussion of applied inversion strategy is also included. The final results of velocity inversion are presented for the three-dimensional structure variation. The variation of obtained three-dimensional structure is duly compared with the minimum 1D velocity model obtained in the previous section.

The data is inverted for 3D variation of Vp, Vs and Vp/Vs (proportional to poissons's ratio, σ) using SIMULPS a simultaneous inversion technique of Thurber (1983) using new 1D starting model obtained in the previous chapter with the same data set. Efforts are made to investigate the upper crustal structure in order to understand the collision mechanism in the frontal Himalaya of Kangra-Chamba region. Because the seismic activity is mainly confined to upper crust above 20 km and a limited number of events are found below this depth, therefore only the upper crust could be investigated.

4.2. LOCAL EARTHQUAKE TOMOGRAPHY

In the early 70's, Professor Adam M. Dziewonski, started the tomographic study to map the structure of the earth for the first time. Seismic tomography, obtained as the

analogy of medical CAT-scan, scans the earth structure as the travel time anomalies of seismic waves observed for many ray-paths, criss-cross the Earth between various points near the Earth's surface. These rays passing from different depths can resolve the three dimensional (3D) model.

The earth's tomographic inversion can be done using the information from controlled sources or the natural earthquake sources (Thurber, 1993). The advantages of local earthquakes compared with controlled sources are their substantial excitation of both compression and shear waves and their 3D spatial distribution but the disadvantage is the lack of control on the distribution of the sources, lack of knowledge about their exact location and the origin time. Controlled sources can be used as supplemental data with earthquake hypocenter parameters (Thurber, 1993). The local earthquake tomography (LET) is better over tele-seismic tomography due to higher spatial resolution of structure with increased density of ray sampling, higher wave frequency, and closer station spacing. But depth extent of LET model is limited to the maximum extent of earthquake focal depths as suggested by Aki (1982). Therefore LET can be used for obtaining mostly crustal velocity model up to maximum focal depth of the earthquakes.

4.2.1. Basic Theory

In LET, the imaging of the earth structure is obtained using the ray tracing of body waves within the earth medium as shown in **Figure 4.1**. The body wave travel time T_{ij} from an earthquake i to a seismic station j is the ray path integral given by

$$T_{ij} = \int_{source}^{receiver} u\,ds \qquad \text{---------------- 4.1}$$

where u is the slowness and ds is an element of path length, but the actual observations are the arrival times, t_{ij} given by

$$t_{ij} = \tau_i + T_{ij} \qquad \text{---------------- 4.2}$$

τ_i is the earthquake origin time. In equations (4.1) and (4.2) the known parameters are the receiver locations and the observed travel times but the source coordinates (x_1, x_2 and x_3), origin times τ_i, ray-paths, and slowness field are unknown.

99
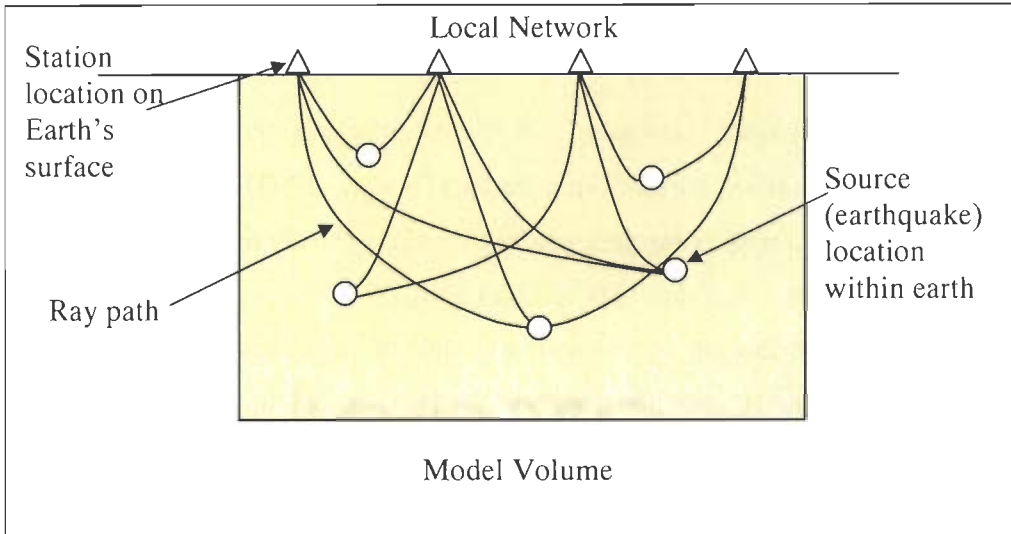
Figure 4.1: Schematic Representation of local earthquake tomography (LET after Thurber, 1993).

The equations 4.1 and 4.2 are used to calculate the residual (misfit) r_{ij} between the observed arrival times t_{ij}^{obs} of body waves and calculated arrival times t_{ij}^{cal} using trial hypocenters, origin times and an initial model of the seismic velocity structure.

$$r_{ij} = t_{ij}^{obs} - t_{ij}^{cal} \qquad \text{----------------- 4.3}$$

The residuals can be related to the perturbations to the hypocenter and velocity structure parameters by a linear approximation

$$r_{ij} = \sum_{k=1}^{3} \frac{\partial T_{ij}}{\partial x_k} \Delta x_k + \Delta \tau_i + \int_{source}^{receiver} \delta u ds \qquad \text{----------------- 4.4}$$

where the hypocenter partial derivatives $\partial T_{ij}/\partial x_k$ are proportional to the components of the ray vector times the seismic slowness at the source (Thurber, 1986).

$$\frac{\partial T_{ij}}{\partial x_k} = -\frac{1}{V}\left(\frac{dx_k}{ds}\right)_{source} \qquad \text{----------------- 4.5}$$

100

The LET can be utilized to improve the estimates of the model parameters (structure and hypocenters) by perturbing them in order to minimize the residuals. Equation 4.4 is the focus of basic methodology for LET but it can be utilized in different ways by using some or all following aspects:

(1) the scheme for the representation of the velocity structure

(2) the technique for travel time and ray-path calculations

(3) the treatment of the hypocenter-velocity structure coupling

(4) the method of inversion

(5) the assessment of solution quality

(6) the use of S-waves.

The methods use the observed waves in terms of the ray paths through the earth medium. However, the amplitude and travel time of the seismic energy traveling through the earth is affected by the properties of the material in a finite volume called the Fresnel volume that surrounds the ray path (Chou and Booker, 1979).

Using the finite parameterization of the velocity field, the travel time integral of equation 4.4 can be replaced with a first order approximation:

$$r_{ij} \approx \sum_1^3 \frac{\partial T_{ij}}{\partial x_k} \Delta x_k + \Delta \tau_i + \sum_{i=1}^L \frac{\partial T_{ij}}{\partial m_l} \Delta m_l \qquad \text{----------------- 4.6}$$

The m_l is the Lth parameter of the velocity model and $(\partial T_{ij}/\partial m_l)$ is the model partial derivate along the ray path.

4.2.2. Representation of Structure

The LET methods are used to model the 3D velocity structure of the body waves for the earth's crust and upper mantle up to the maximum focal depth of the earthquakes for the study region. The Earth's crust and upper mantle contain heterogeneities and displays anisotropy due to many discontinuities, faults, intrusions, varying temperature with some partial molten material and random geologic heterogeneity. The minimum spatial scale of

101

heterogeneity that can be imaged using LET is determined by the density of ray paths in a given region.
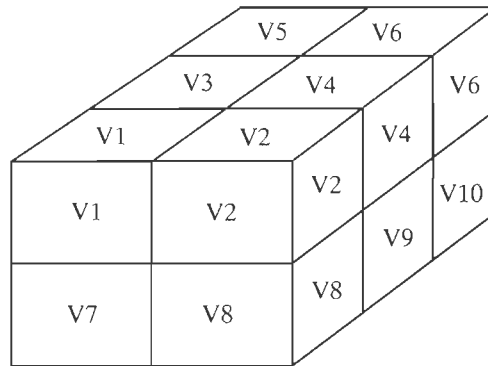
Figure 4.2: Schematic of 3D velocity model representation (after Aki and Lee, 1976).

The 3D velocity structure modeling with LET can be done by representing the earth medium by different types of models. Aki and Lee (1976) used a simple constant-velocity block structure (**Figure 4.2**) dividing the region into different blocks in which each block has constant velocity. However, this method lacks the ability to represent heterogeneities faithfully. The other approaches were given by Crosson (1976), Hawley *et al.* (1981), Thurber (1983), each of which has some pros and cons. Crosson's model of constant-velocity layers also has the limitations of inadequate representation of heterogeneous part. Instead Hawley *et al.* (1981) divided the region into vertical constant velocity layers and interpolation is used to calculate the intermediate velocity of two vertical lines. Hence the variations on the discrete block parameterization include laterally varying layers. Thurber (1983) used the 3D grid spacing approach for which the velocity varies continuously from grid to grid in all three directions. Within the grids the values are taken with linear B-spline interpolation among nodes. The gradients of velocity or the effect of discontinuities, a limitation in the model of Aki and Lee (1976) has been lowered by taking thousands of blocks and introducing gradual or rapid velocity changes from one block to other (Nakanishi, 1985; Walck and Clayton, 1987; Lees and Crosson, 1989). Therefore, the earth structure can be modeled in LET with a variety of ways and mostly the grid or many block approach is taken. In the present analysis the velocity models are parameterized using a 3D

grid of nodes at the points of intersection of x, y and z orthogonal axes as was proposed by Thurber (1983).

The model must be represented with finite set of numbers for doing the calculations. The structure can be represented with velocity and Vp/Vs values at large number of grid nodes (over parameterization), which has the advantage of reducing smoothness. However, computation time increases many fold, thus reducing efficiency. Hence, the proper parameterization is very helpful for computation and structure inversion.

4.2.3. Ray-Path and Travel Time Calculation

The ray tracing and the calculation of travel times are the fundamental approach in LET, which depend on the seismic wave propagation between source and receiver. The ray tracing is the forward problem in LET which is used for calculation of travel time residuals and their partial derivatives. **Figure 4.3** shows the density of rays for straight line ray-paths for the present study area in plane view and in sections. Such ray-paths are used to calculate the travel time residual, the hypocenter parameters and the velocity model partial derivatives. The computational approach involved can be one out of shooting, bending, approximate ray tracing or finite-difference method. For ray-tracing formulation, two-point boundary value problem (BVP) is taken by defining the end-points (source and receiver positions) and traversing a propagation path. The shooting methods solve the two-point BVP by iteratively solving an initial value problem (IVP) with one fixed end-point and the initial ray trajectory varied, while bending methods solve the BVP directly by keeping the end-points fixed and perturbing the path connecting them. But both these methods may converge to ray paths that give local rather than global travel time minimum. Thurber and Ellsworth (1980) have developed an approximate ray-tracing scheme that computes rays and times in a local layered average of the 3D structure. Thurber (1983) developed a fast, simple, brute-force search technique that allowed for laterally refracted rays taking a constant curvature along any one trial ray. The finite-difference method of Vidale (1990) and the network theory method of Moser (1991) can be used to determine both the global minimum time path and crude estimation of the arrival amplitude.
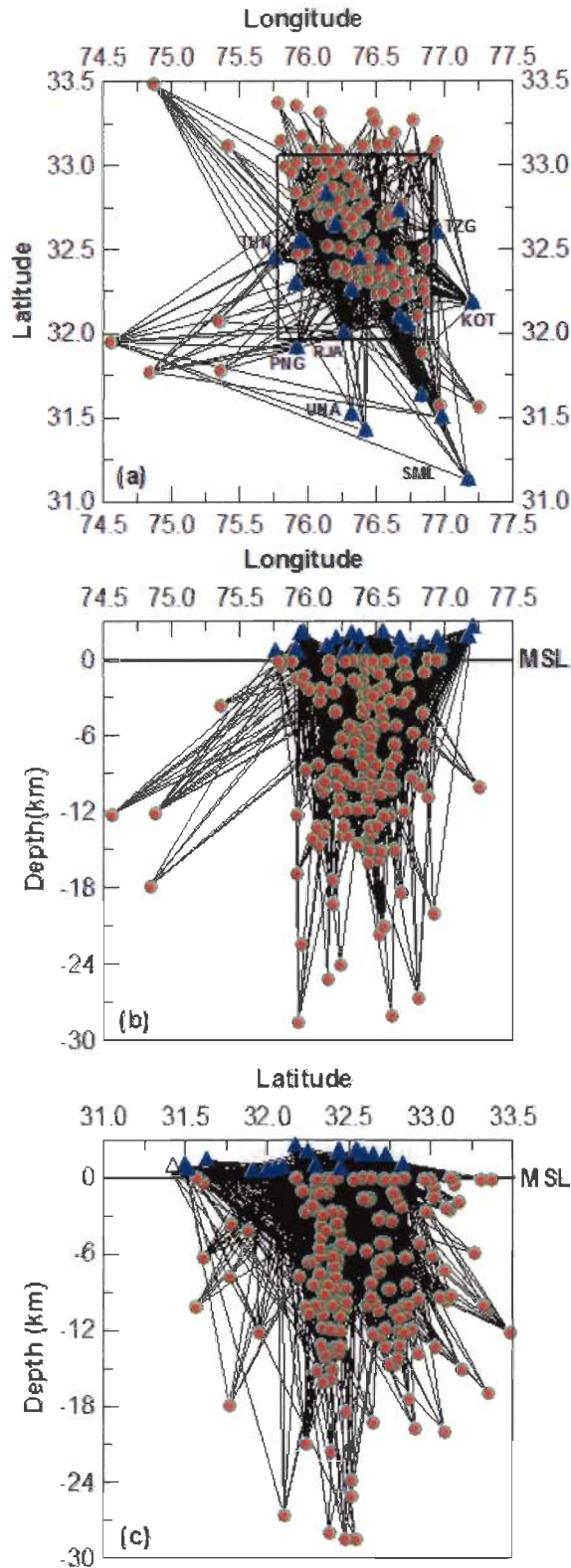
Figure 4.3: Ray path coverage for straight line ray paths: (a) surface projection, (b) east–west depth section, and (c) north–south depth section. Stations of the seismic network are represented by blue triangles, and earthquake locations are shown by green circles filled with red color. Ray paths in the central block bounded between 31.8° N and 33.0° N and 75.5° E and 77.2° E have been used for travel-time inversion. MSL stands for Mean sea level.

104

4.2.4. Hypocenter-Velocity Structure Coupling

The hypocenter parameters and the velocity structure model are re-evaluated alternatively iteratively in the LET method. Traditionally, the term local earthquake 'tomography' usually implied the determination of velocity structure using fixed hypocenter parameters, while simultaneous inversion was usually constructed to mean an explicit treatment of the hypocenter-velocity structure coupling. This can be solved through a matrix of approximately (L x N) by (4N + M) size containing a data set and model of L stations, N earthquakes, and M velocity parameters. The complete system of simultaneous inversion equations can be written in the (discrete) form as

$$r = H\nabla h + M\nabla m \qquad \text{----------------- 4.7}$$

Where r is the residual vector, H and ∇h are the matrix and vector of hypocenter parameter partial derivatives and perturbations, respectively, and M and ∇m are the matrix and vector of velocity parameter partial derivatives and perturbations, respectively. For the ith event, we have the set of equations

$$r_i = H_i\nabla h_i + M_i\nabla m_i \qquad \text{----------------- 4.8}$$

The 3D LET method of Thurber (1983) uses above equation for simultaneous estimation of hypocentral location, origin time, Vp and Vp/Vs. For this, the initial parameters can be derived from a laterally homogeneous (1D) velocity model, with or without station corrections, with no explicit treatment of the hypocenter-velocity structure coupling so that the term $H\nabla h$ in equation (4.7) can be ignored. Kissling (1988) has also highlighted the importance of tomographical inversion using hypocenter-velocity structure coupling.

4.2.5. Inversion Methods

The unknown parameters of the inversion method are known as the model parameters, which are compared with the collected data for inversion procedure. The inverse theory is the process of predicting the results of the data on the basis of some

general principle or model using a set of specific relevant conditions. Therefore, the inverse theory solves the reverse problem, starting with data and a general principle or model to estimate the model parameters. The inverse and forward problem can be stated as

Forward Problem:
model parameter → mode l → prediction of data
Inverse problem:
data → model → estimation of model parameter

The LET uses an iterative damped least square inversion scheme inverting simultaneously for hypocentral and velocity parameters. In this inversion, the recorded phase data, the station location and hypocenter location are taken to be the data and velocities of the seismic phases at different points in the earth's structure that are taken to be the model parameters at first step. While in the second step, the hypocenter parameters are the model parameters and the velocities are the data. An iterative approach for its solution is required because the LET problem is basically a nonlinear one and because it is linearized for solving the problem. At each iteration, the residuals are minimized in a least square sense by calculating the model perturbations. Due to non-uniform distribution of rays, certain parameters are underdetermined (less rays) while some parameters are over-determined (heavily sampled). The overall problem is considered as mixed-determined with some parts underdetermined and some over-determined. A useful method for minimizing the underdetermined part and avoiding numerical instabilities of inversion is to combine parameter separation with construction of the normal equations and the incorporation of damping. It is done using the equation

$$\nabla m = \left[(M')^T M' + \varepsilon^2 I \right]^{-1} (M')^T r' \qquad \text{----------------- 4.9}$$

Where ε is the damping parameter and I is the identity matrix. The resultant matrix size is fixed by the number of velocity model parameters (Spencer and Gubbins, 1980; Thurber, 1983). The given approach is useful for controlling the size of the matrix for large number of earthquakes and therefore the equation (4.9) is called the damped least squares inversion.

Thurber (1983) developed this algorithm and used a 3D grid of nodes to represent the velocity structure. However, the method has the following limitations:

(1) the loss of singular value information,

(2) the sensitivity of the solution to the choice of damping value and

(3) squaring of the condition number of the matrix to be inverted.

Kissling (1988) made use of parameter separation and applied Algebraic Reconstruction Technique (ART) type of approximation of equation for better solution. This representation may be given as

$$\nabla m_j = \frac{\left[(M)^T r' \right]_j}{\left[(M)^T M + \varepsilon^2 I \right]_{jj}}$$
---------------- 4.10

where the subscripts j and jj indicate the jth vector element and the jjth diagonal element of the corresponding vectors and matrix.

The other two important concepts, which have been applied to LET problem, are the uses of a priori information and smoothness constraints. The a priori information includes a suitable initial model from which the deviations are penalized (Jackson and Matsu'ura, 1985) for the stability and uniqueness of the solution. The use of S-data also aids the LET problem by increasing constraints on earthquake source depths and providing information that helps to decouple the hypocenters from the structure in the inversion.

4.3. PRE-INVERSION CONSIDERATIONS

Before inverting the body wave travel paths of P- and S-waves, several parameters are evaluated for fulfilling the criteria of inversion. They are discussed in this section

4.3.1. Input Data and 1D Initial Velocity Model

The well located seismic events recorded at five or more than five stations are considered for the inversion. 172 earthquakes in the magnitude range 1.0 and 5.0 fulfill this criterion. Also, the minimum 1D velocity model estimated by me (reported in the previous
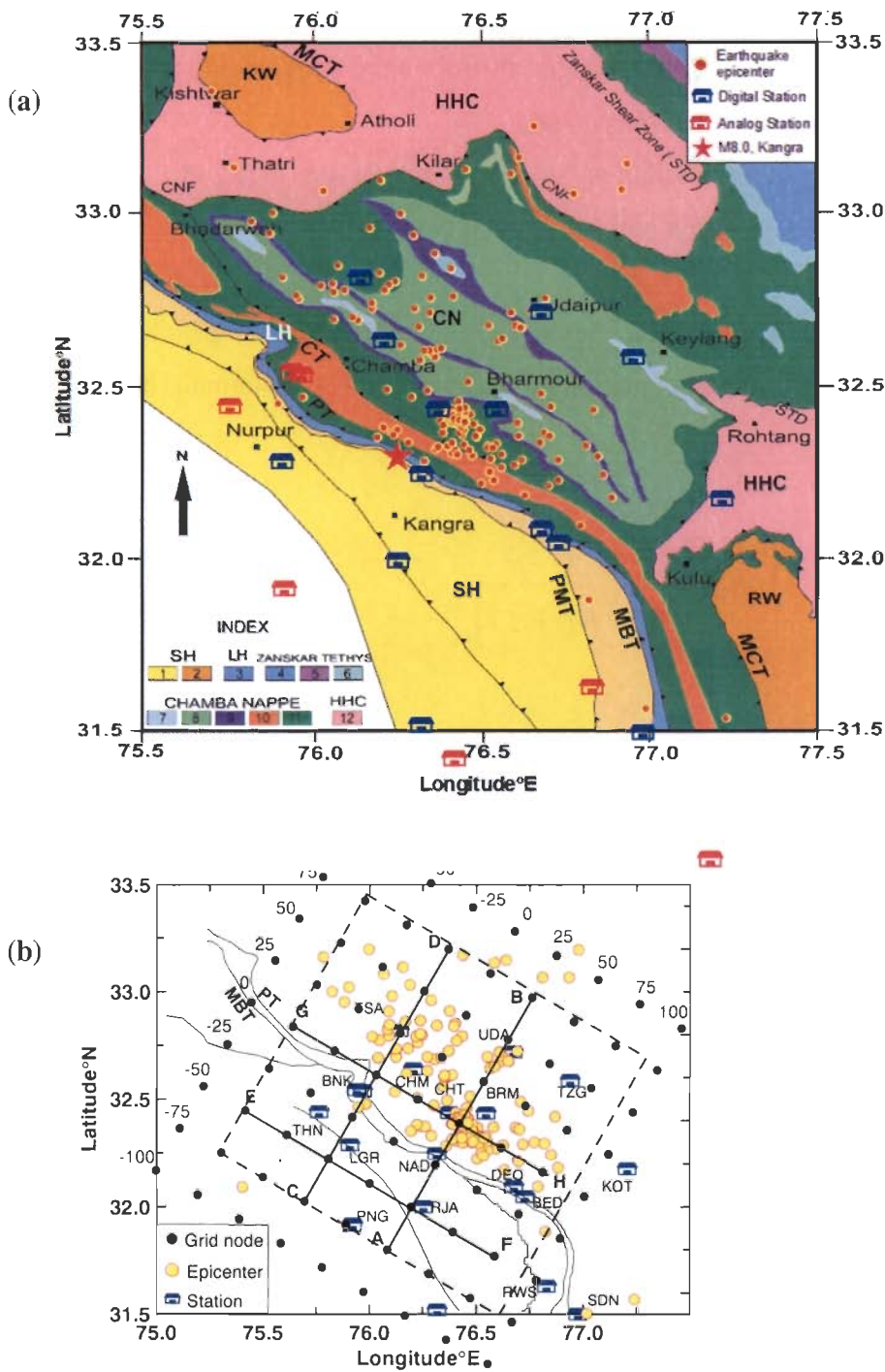
Figure 4.4. (a) On the geotectonic map, the station locations are shown with hut (Blue hut having digital seismograph and red analog) and epicenters of the earthquakes with red circles. (b) Map showing location of grid nodes (black dots) superimposed on seismicity map. Earthquake epicenters and station locations are shown with yellow circles and blue huts respectively. The bold straight lines show locations along which vertical sections for Vp, Vs and Vp/Vs models are obtained. The dotted box is the area where the 3D velocity inversion is well resolved.

chapter) is used as the initial input for LET to obtain 3D velocity variations. The hypocenters obtained using Joint-Hypocenter-Determination (JHD) method and reported in the previous chapter are used as the preliminary locations for starting LET.

4.3.2. Selection of Grid Node Separation

The inversion procedure is started by selecting grid nodes in three dimensions with appropriate velocity values taken from initial 1D model obtained in previous chapter. The spacing of the nodes depends upon density of seismic rays in three dimensions. **Figure 4.3** shows the coverage of the study area by straight line ray-paths. It shows that an area lying between 31.8° N and 33.0° N and 75.5° E and 77.2° E and up to a depth level of 18 km is well covered by criss-crossing ray paths. Velocity and Vp/Vs values are estimated for this region. **Figure 4.3** shows that the density of ray path varies from one part to other. A large number of inversions are carried out to determine optimal grid spacing. The grid spacing shown in **Figure 4.4** provides the best resolved results. Considering the ray density (**Figure 4.3**), the topographic elevation (**Figure 3.1**), the seismicity and tectonics (**Figures 3.1 and 3.2**) a horizontal grid with 25 x 25 km^2 node spacing covering an area of 200 x 200 km^2 was taken for 3D inversion (**Figure 4.4**). These nodes are aligned in the NW-SE direction. The grid point locations with respect to central coordinate 32.50° and 76.32°E are taken as 0, ±25, ±50, ±75 and ±100 km in the NW-SE direction and at similar spacing in the NE-SW direction. In the depth direction grid nodes are positioned along the boundaries between layers of 1D model used as the initial model for this study, i.e. at -4, 0, 2, 5, 10, 15 and 18 km depths. 0 km represents mean sea level. The SIMULPS algorithm works when all the ray paths are enclosed in a volume covered by grid nodes. As all the stations are located above mean sea level, this entails that a plane containing grid nodes must lie above the station having highest elevation. With this consideration I have kept a layer boundary containing grid nodes at an elevation of 4 km. As the z-axis is taken to be positive in the downward direction, the z-value for this level is taken to be -4 km. The grids are chosen to be aligned with the regional structural trend. In this selection the y-axis is aligned to NE-SW direction. The estimates of model parameters at grid points at depths greater than 18 km are not reliable as ray coverage (**Figure 4.3**) below this depth is poor due to limited

number of seismic sources. With these considerations, a reliable image of 3D crustal structure can be obtained for the study area up to a depth level of 18 km.
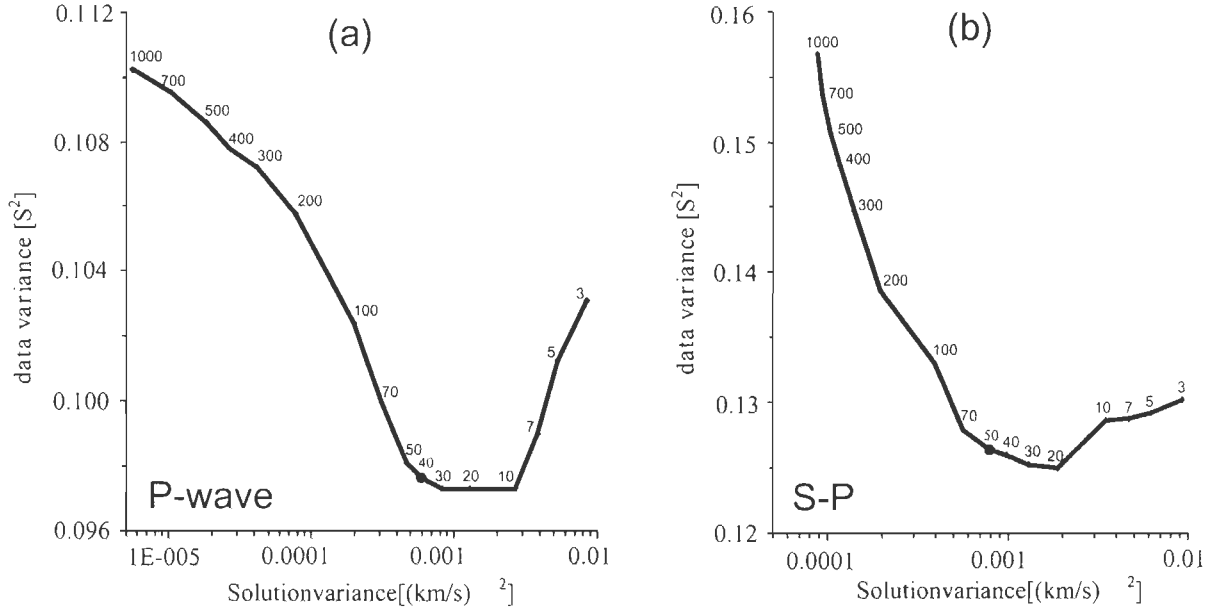
Figure 4.5. Curves showing model variance versus data variance for damping values between 1000 and 3 to obtain optimum damping values. The data and model variance are computed after one iteration for indicated damping values. Damping values of (a) 40 (solid circle) for P-wave and (b) 50 (solid circle) for S-P are used for further processing.

4.3.3. Determination of Damping Parameter

For tomographic inversion the solution stability also depends upon the damping parameters. The damping parameter for both Vp and Vp/Vs is obtained based on a series of tests on the trade-off between model variance (roughness) and data variance (Eberhart-Phillips, 1986). As shown in **Figure 4.5(a)** and **(b)**, for a large range of damping (3 – 1000) values, one iteration inversion was conducted. We empirically obtained the damping parameters by plotting the data variance (misfit) with respect to model variance as explained by Eberhat-Philips (1986). As shown in **Figures. 4.5(a)** and **(b)** for P and S-P respectively, there is a significant reduction in data variance with moderate increase in solution variance when damping values decreases. However, it is observed that when damping is less than 10 for Vp and 20 for Vp/Vs, the data variance increases. Following the

110

procedure of Eberhart-Philips (1986), we choose the damping values at the point of inflexion of these curves. Therefore, the optimum damping values for P and S-P are taken to be 40 and 50 respectively.
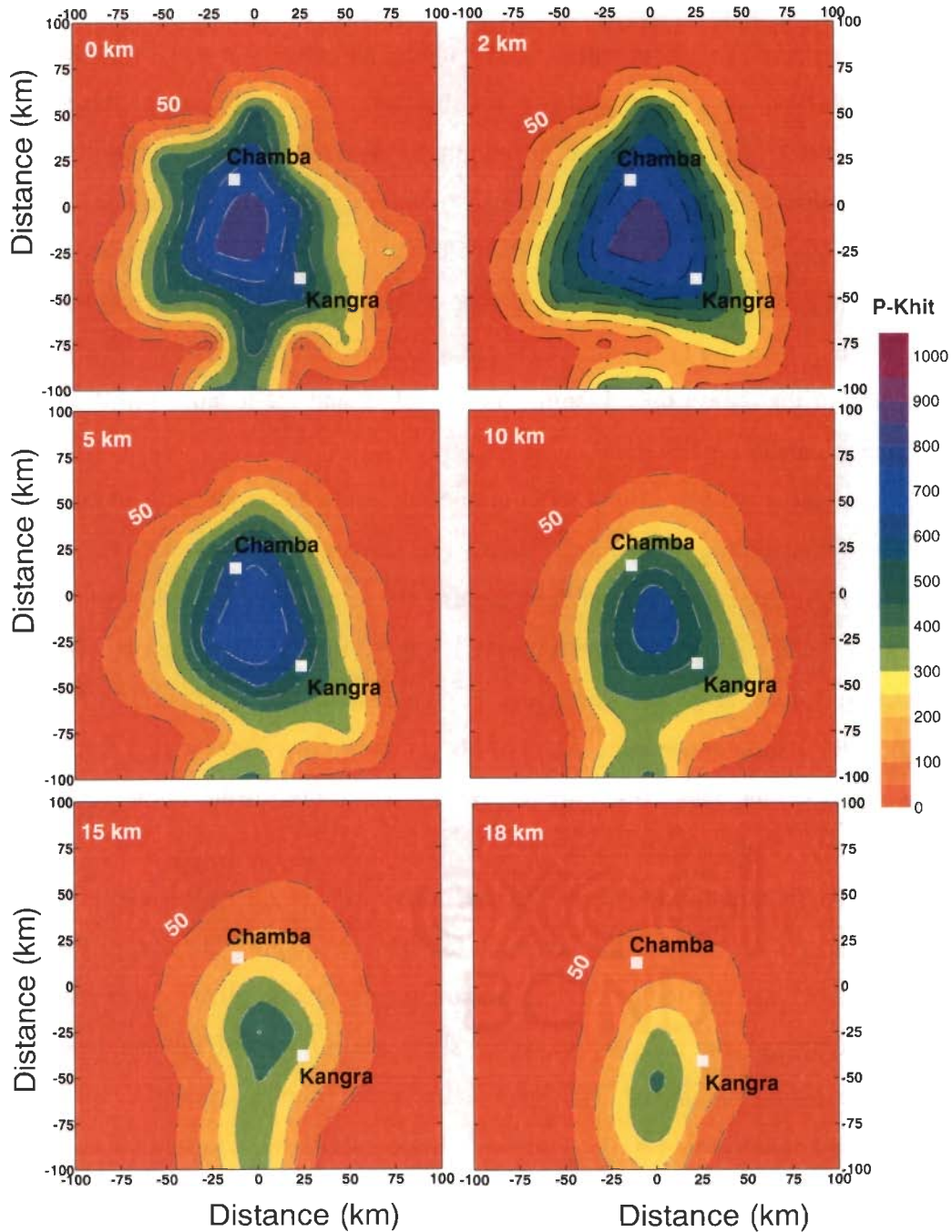
Figure 4.6. Plots of number of ray-paths (khit numbers) of P-phase data used for inverting 3D structure at different nodes. Depths at which horizontal slices are taken are 0, 2, 5, 10, 15 and 18 km.

111

4.3.4. Resolution of the Model

The 3D tomographic inversion is done by taking great care of resolving power of the data set. Different statistical approaches are performed for data suitability for which an estimate of hit count at particular node is used. Hit count represents the number of rays whose travel time data is used for estimation of model parameters at a given node. The hit counts were observed for P-wave and S-P for this data set and the values are shown in **Figures 4.6 and 4.7** respectively. The hit counts for P- and S-P has maximum value of nearly 1000 for this dataset. In the central part of this region, the hit count value is very high indicating good resolution for that part. These hit counts also decrease with the increase of depth because in this data the number of sources goes on decreasing with depth. It is clear that minimum 50 hit count values are available for about 150 x 150 km^2 area in the central part of the region for all depths up to 10 km, and are localized in the centre of the study area at greater depths.

The derivative weight sum (DWS) is another parameter used as a more sensitive measure of spatial sampling of the model space. The DWS quantifies relative ray density in the volume of influence of a model node, weighing the importance of each ray segment by its distance to the model node (Toomey and Foulger, 1989). The plot of DWS values (**Figures 4.8 and 4.9**) shows that this value is greater than 100 in about 100 x 100 km^2 central part of the region and up to a depth of 18 km. As shown in these Figures, the DWS values for depths greater than 10 km are localized in the center of the study area only and therefore this region is used for the inversion.

Another parameter used to check the reliability of the results is the resolution matrix (R), which estimate the quality of the inversion for 3D tomography. The row of R indicates the dependency of solution for one model parameter on all the other model parameters. However, the diagonal elements of R (RDE) show the amount of independence in the solution of one model parameter. The RDE value varies between 0 and 1 with highest resolution being 1. The portion of the study area having RDE value more than 0.1 both for P- (**Figure 4.10**) and S-P (**Figure 4.11**) is considered for further analysis of 3D inversion. All the above described tests are taken in consideration for the inversion to obtain three dimensional crustal structure of the Kangra-Chamba region as it is the most complex part of the Himalaya with highest variability in composition and tectonics. Based on

112

observations of these parameters, 3D structure of the upper crust is obtained for the central part of the study area (100 x 100 km^2) where DWS $\geq$100, khit $\geq$100 and resolution $\geq$0.1.
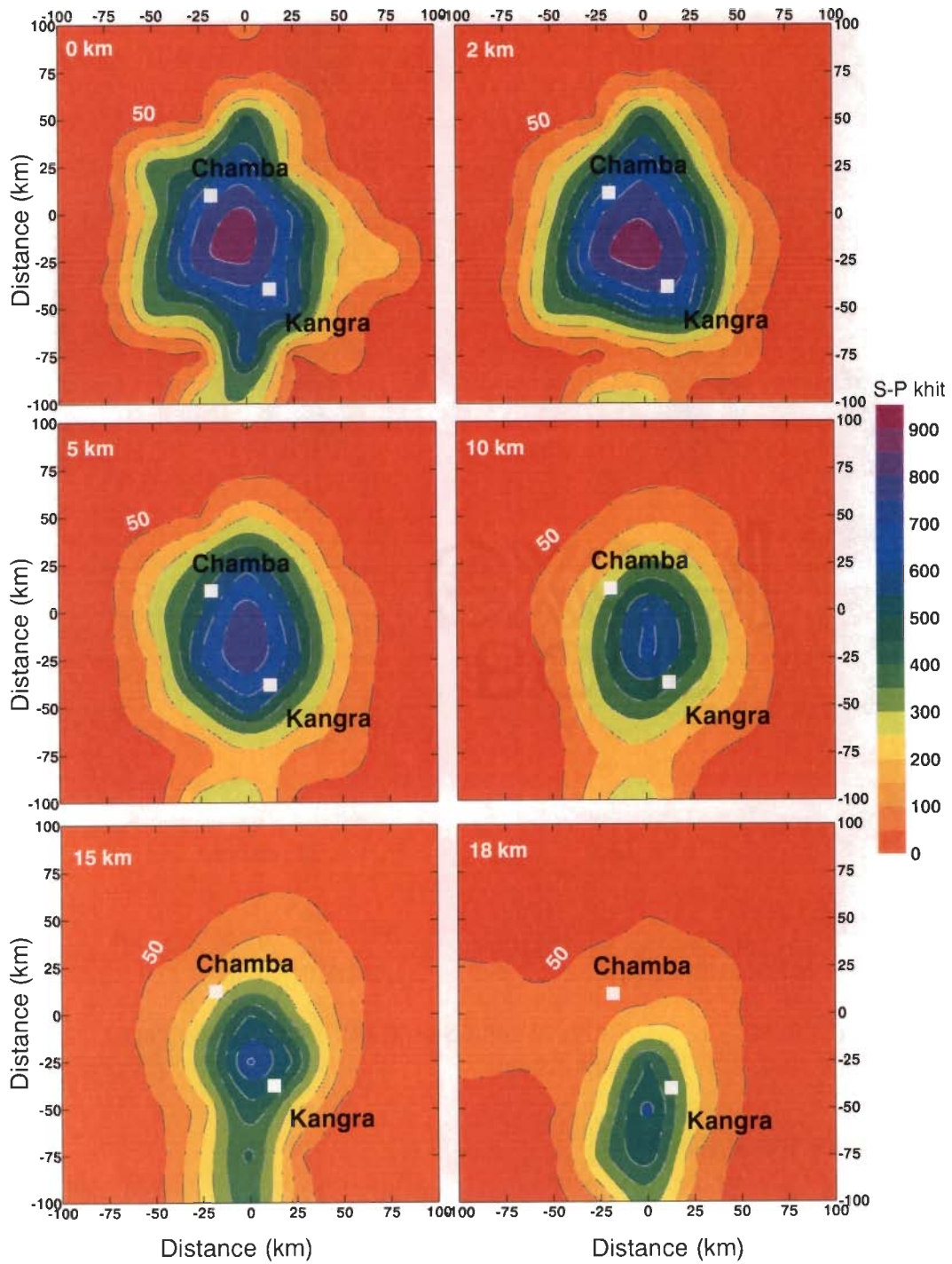
Figure 4.7. Plots of number of ray-paths (khit numbers) for S-P. Depths at which horizontal slices are taken are 0, 2, 5, 10, 15 and 18 km.
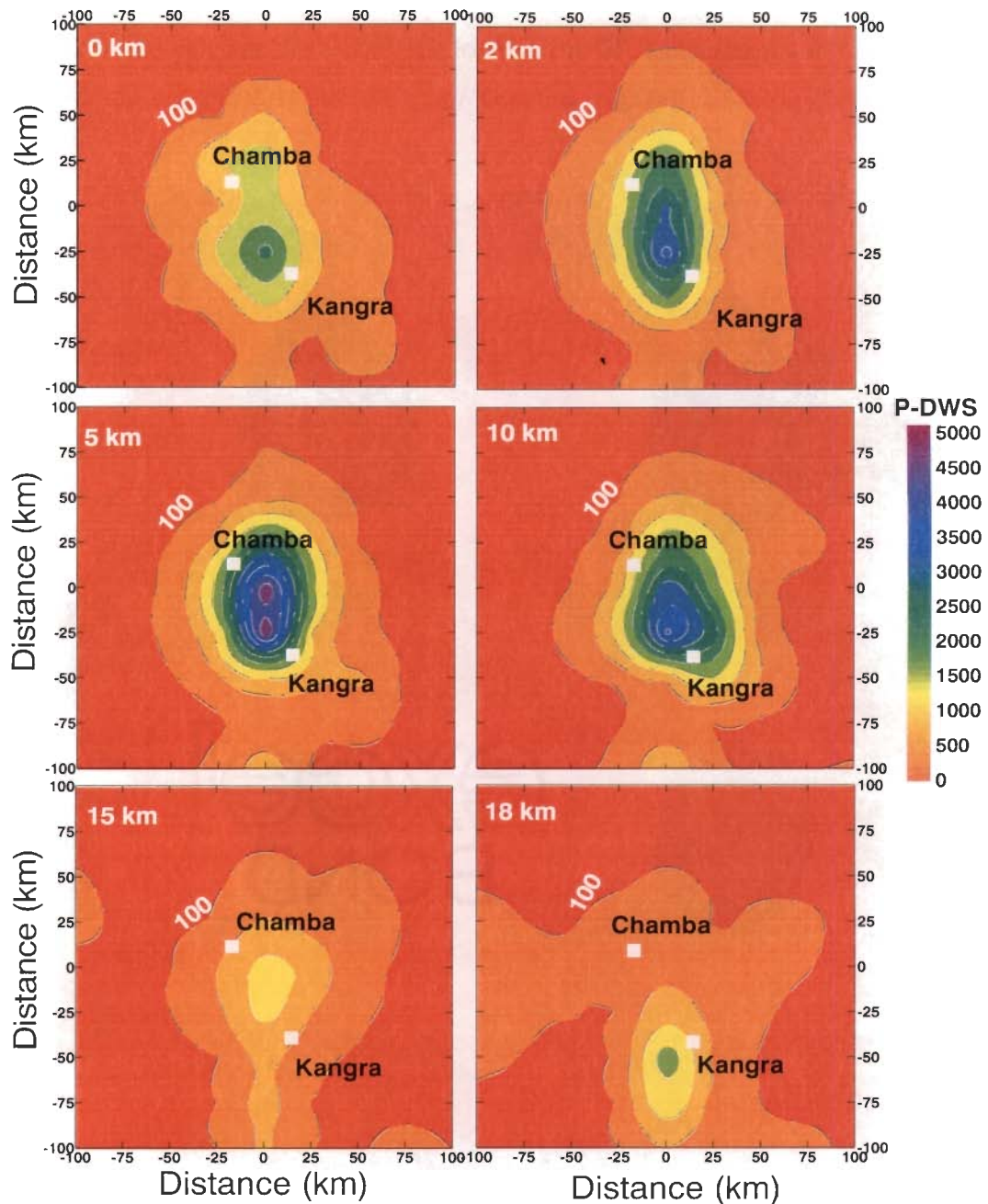
Figure 4.8. Plots of Derivative Weight Sum (DWS) for P-phase data at depths of 0, 2, 5, 10, 15 and 18 km.

4.3.5. Additional Resolution Tests

In order to further check the solution quality I performed both Checkerboard Resolution Test (CRT) and Restoring Resolution Test (RRT). How well the velocity structure of a region is resolved depends on how well sampled the volume is by criss-crossing rays. The CRT is an efficient and widely used method that gives an indication of

resolution. CRT is carried out by putting positive and negative perturbations in the initial velocity model (Zhao *et al.*, 1992). How well the final model recovers such variation gives an indication of resolvability of the data. It is a quick, efficient and widely used test for checking the resolving capacity of the data. In the present data ±14% variation of P-wave and ±6% of S-P at alternate grid nodes for CRT test in 3D space is applied to test the resolving capacity of the data. Therefore, synthetic velocity model is constructed and it is inverted with the earthquake data and on the basis of recovery of the initial model for different points it is observed where the resolution is good and at which point it is poor. The inverted recovery of velocities gives good resolution at a spacing of 25 km in horizontal direction and 2-5 km in vertical direction spacing both for Vp and Vp/Vs for the central part of the region. The CRT of Vp at 25 km spacing at different depths (**Figure 4.12**) of the region shown with dotted box area in **Figure 4.4b** also shows good resolution. However, for smaller grid spacing the resolution becomes poor. Therefore it is clear from **Figure 4.12** that the region 150 x 150 km^2 is well resolved by the CRT method. Similarly, the CRT analysis for S-P has been shown in **Figure 4.13** for the area where the resolution is good. Both these tests verify appropriate central region of the study area for 3D tomographic inversion.

In some cases it is observed that small-sized structures can be resolved well using prevalent and widely accepted CRT method. In this method some times the larger structures are poorly resolved (Leveque *et al.*, 1993). For giving strength to CRT method, RRT was proposed by Zhao *et al.* (1992). In this method, the estimated 3D velocity structure is used as a synthetic input model. A synthetic data set similar to the available data set with added random error (±0.2 s) used for CRT is used to carry out inversion. The obtained 3D velocity models for Vp and Vp/Vs has been tested here by taking these as synthetic input mode. The synthetic input for Vp is shown in the left panel of **Figure 4.14a** and observing the restoring capability of the data, the output restoring model is shown in the right panel. As it is clear from **Figure 4.14b,** the Vp and Vp/Vs anomalies are well recoverable in the study area for the grid spacing chosen in this study.
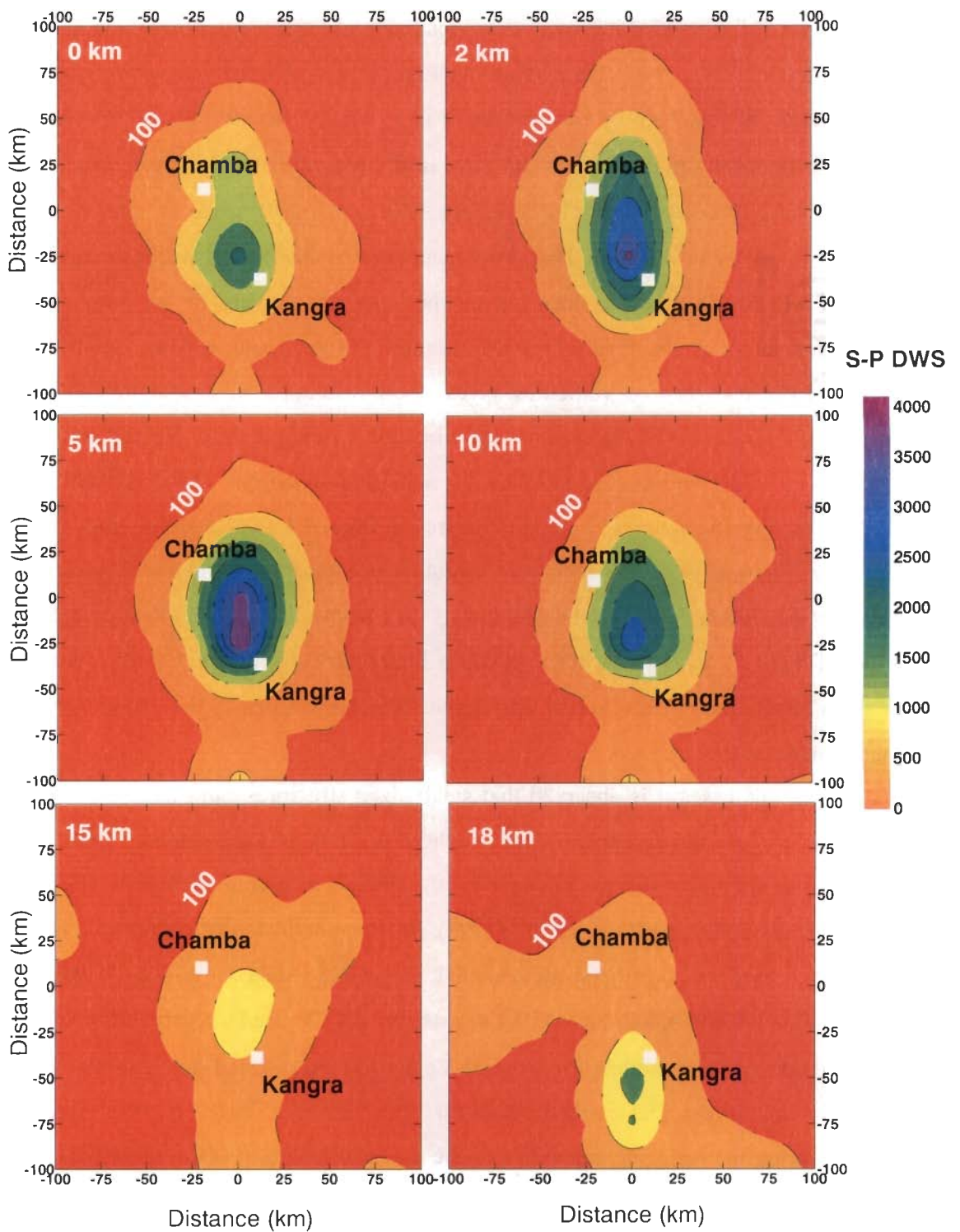
Figure 4.9. Plots of Derivative Weight Sum (DWS) parameter for S-P. Depths at which horizontal slices are taken are 0, 2, 5, 10, 15 and 18 km.

116
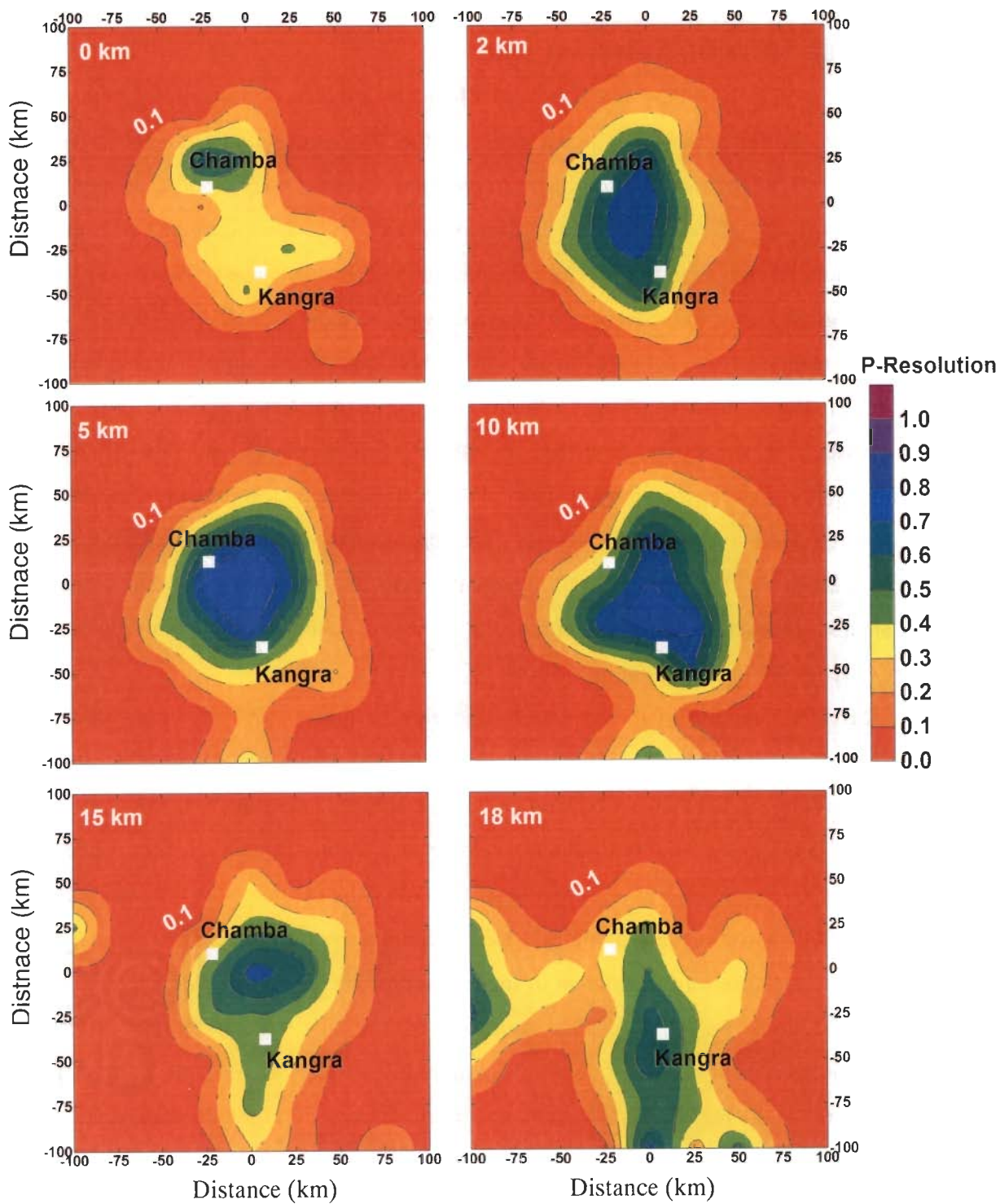
Figure 4.10: Plots of resolution parameter for P-wave velocity. Depths at which horizontal slices are taken are 0, 2, 5, 10, 15 and 18 km.

117

4.4. ADOPTED METHOD AND ANALYSIS

Well tested and widely used method of local earthquake tomography (Thurber, 1993; Eberhart-Phillips, 1993) is adopted to derive the 3D velocity model for the Kangra-Chamba region. The method relies on the iterative simultaneous inversion of large numbers of travel times from well recorded local earthquakes. Out of 172 seismic events used in 1D velocity model calculation in the previous chapter only 159 well located events were used for 3D tomography inversion. Hence, the P- and S-phase data of well located 159 local earthquakes recorded by a network including 14 three-component digital and 7 vertical component analog stations were used for this study. S-arrival times are read only from digital records. Overall, a data set of 831 P- and 734 S-phases with selection criteria of minimum 6 phase readings, azimuthal gap $\leq 180°$ and rms error lower than 0.5 s for the individual event were available for inversion. The seismic activity in this region is confined to the upper 20 km of crust with most of the events occurring within upper 10 km. Because of this shallow character of the seismicity, the inversion scheme could resolve velocity structure only for the upper 18 km of the crust.

SIMULP12 version of the inversion algorithm (Thurber, 1993; Eberhart-Phillips, 1993) was used for simultaneous estimation of hypocentral parameters along with Vp, Vs and Vp/Vs structures. The Vs is obtained at the last step of iteration from the estimated values of Vp and Vp/Vs. The optimum 1D velocity model obtained in Chapter 3 and by Kumar *et al.,* (2009) was used as an initial input model for the 3D inversion attempted here. We first verified the robustness of the 3D LET technique by numerical tests to examine whether the present data set is sufficient to image the real 3D crustal structure as discussed in previous section. We observed the variation of the 3D structure along different horizontal slices as well as along four different profiles taken across and along major tectonic features of the region. The obtained results are discussed in the following sections.

4.4.1. The Variation of Velocity at Different Depth Levels

The inversion reduced the data variance considerably from 0.000956 to 0.000328 $\sec^2$ that accounts for 65% reduction in data variance. A systematic and significant variation up to 12% in velocity and 6% in Vp/Vs (Poisson's ratio) are observed across the major tectonic units. The percentage variations of Vp, Vs and Vp/Vs at depths of 0, 2, 5,

10, 15 and 18 km are shown in **Figure 4.15** (a, b and c respectively) that are obtained for the well resolved central area. To exhibit the true nature of even weak lateral velocity variation at any given depth, all model parameters are plotted as percentage perturbation relative to the initial 1D layer model parameters.
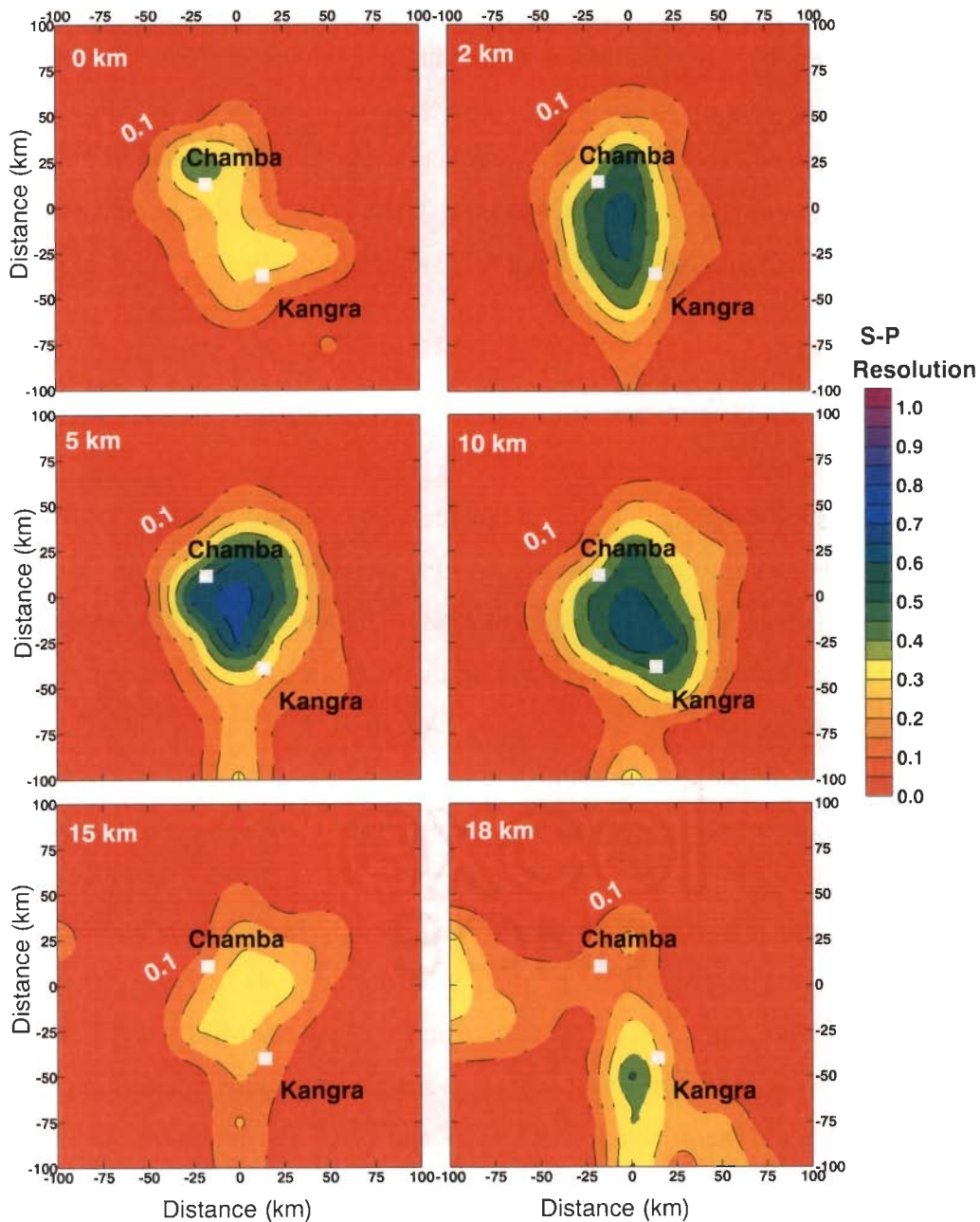
Figure 4.11. Plots of resolution parameter for S-P. Depths at which horizontal slices are taken are 0, 2, 5, 10, 15 and 18 km.

The 3D variations in Vp are shown in **Figure 4.15a** as slices at depths of 0, 2, 5, 10, 15 and 18 km. These images obtained at different depths clearly indicate the presence of strong lateral heterogeneities in this region. The Vp tomography structures show an east-west trending low velocity zone (LVZ) in the south western part which is consistent from surface up to 10 km depth. While from 2 to 5 km depth, the LVZ also extends towards NE-SW in the eastern part. In the northern part of higher Himalaya, a high velocity zone (HVZ) is present that is adjacent to the LVZ, which extends in east-west direction. This HVZ is observed at all the depth levels up to 10 km, while Vp/Vs imaging depicts a high Poisson's ratio structure at the above mentioned depths. The Vp/Vs can also be related to Poission's ratio as per the relation given in equation 4.11, where r = Vp/Vs.

$$\sigma = \frac{0.5(r^2 - 2)}{r^2 - 1}$$ ---------------- 4.11

The results show that east-west extended adjacent low and high velocity zones are prevalent in the central part of the region from surface to 10 km depth. Mainly, the low velocity zone (LVZ) is in the Siwalik and Lesser Himalaya and high velocity zone (HVZ) is in the Higher Himalaya that is divided by major thrust zones of the region. The Vp and Vs tomograms **(Figure 4.15)** show that the LVZ in the SW part is aligned with the MBT and PT and the division of low and high velocity is at the MBT or PT thrust tectonic boundaries. However, in the eastern part there is also a low velocity intrusion in the NEE direction across these tectonic units that are observed at 2 and 5 km depth levels. This might be the intrusion of sediments which has been developed due to two tectonic regimes exerting force perpendicular to each other. From **Figure 4.4a**, it is clear that one tectonic regime is developed due to NE directed movement along the MBT and PT while the other tectonic regime is caused due to the west ward thrusting movement along the RW and HHC. In this region the orientation of the PT and MBT discontinuities also change to NS from NW-SE orientation in the western part. Therefore crustal deformation, variation of composition/velocity and high seismicity of the region can be explained in terms of the tectonic framework of the study region.
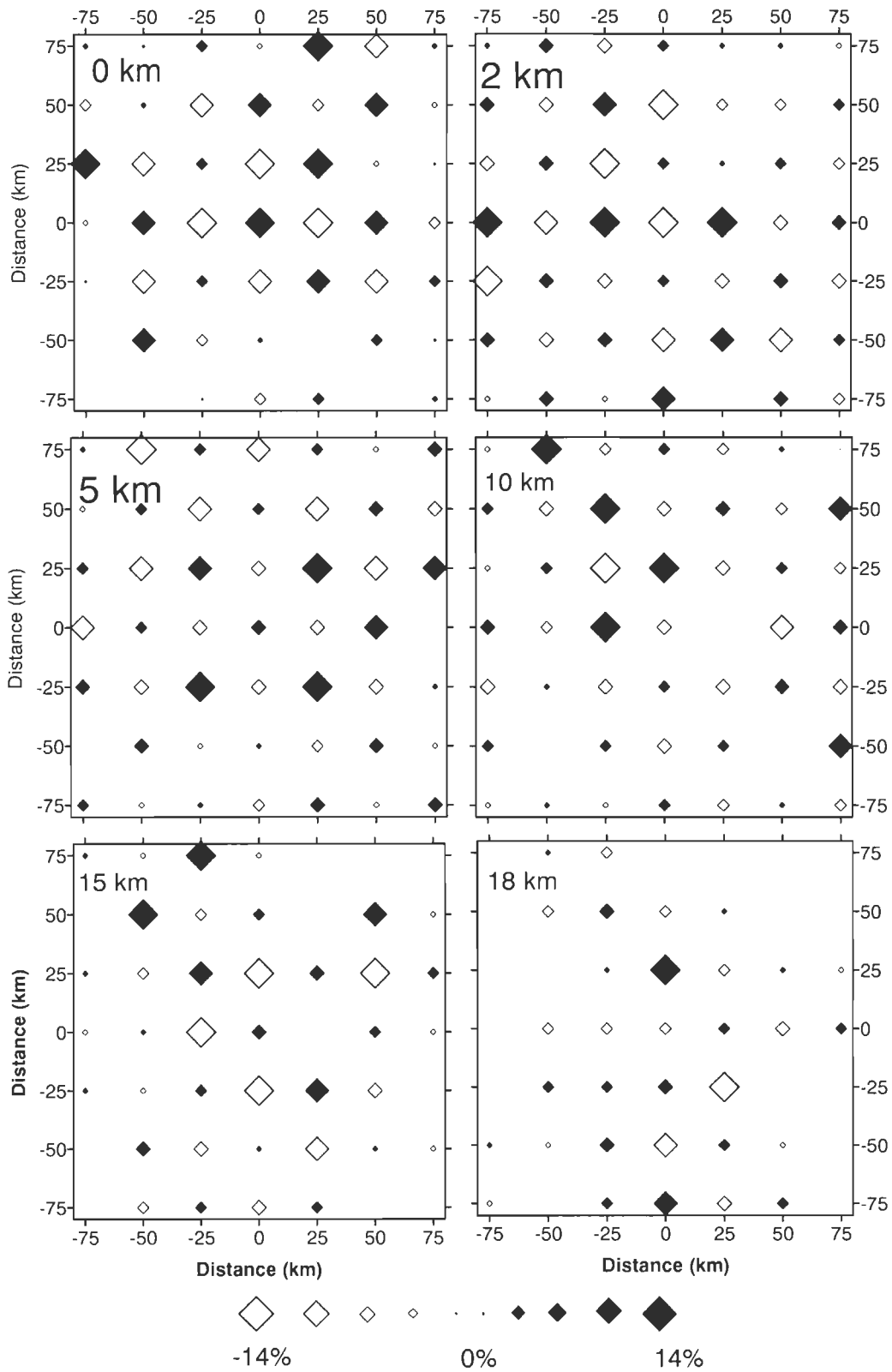
Figure 4.12. The results of the checkerboard resolution tests (CRT) for horizontal grid spacing of 25 km at different depths for P of the dotted region shown in Figure 4.2b.

121
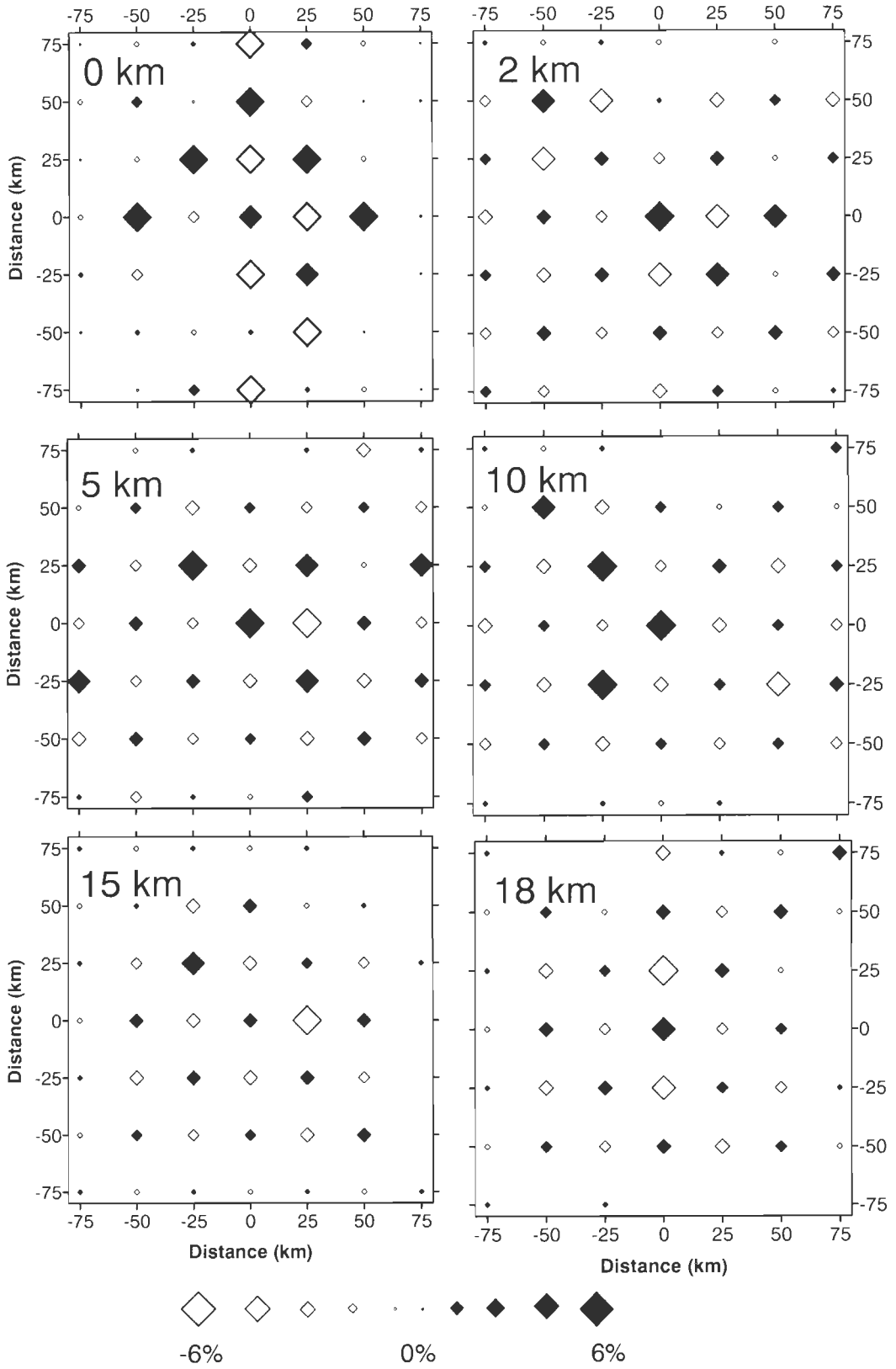
Figure 4.13. The results of the checkerboard resolution tests (CRT) for horizontal grid spacing of 25 km at different depths for S-P of the dotted region shown in Figure 4.2b.

122
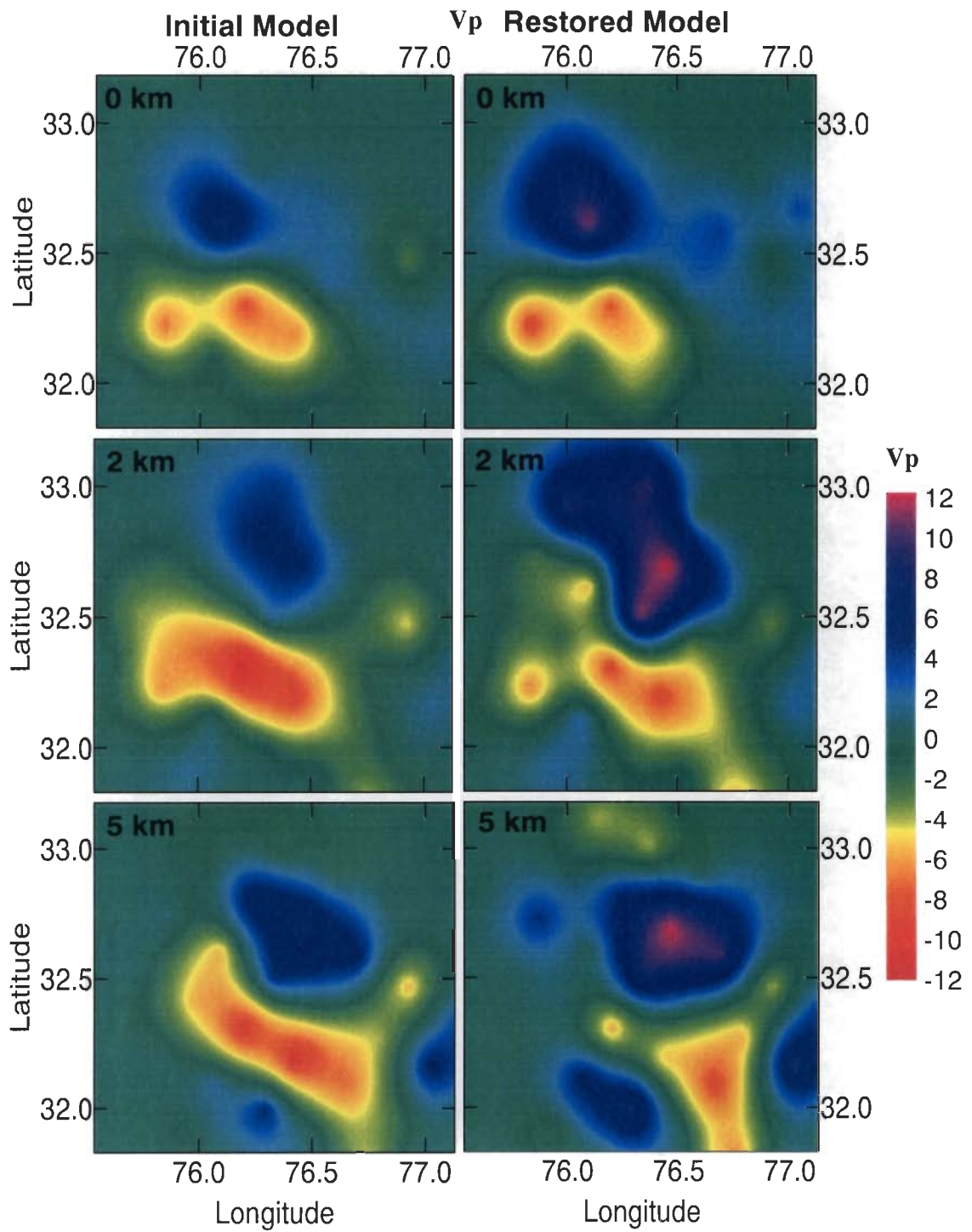
Figure 4.14a. Result of RRT for Vp, left hand panel shows input models and right hand panel shows restored models at different depths of 0, 2, 5, 10, 15 and 18 km by inverting 3D structure.
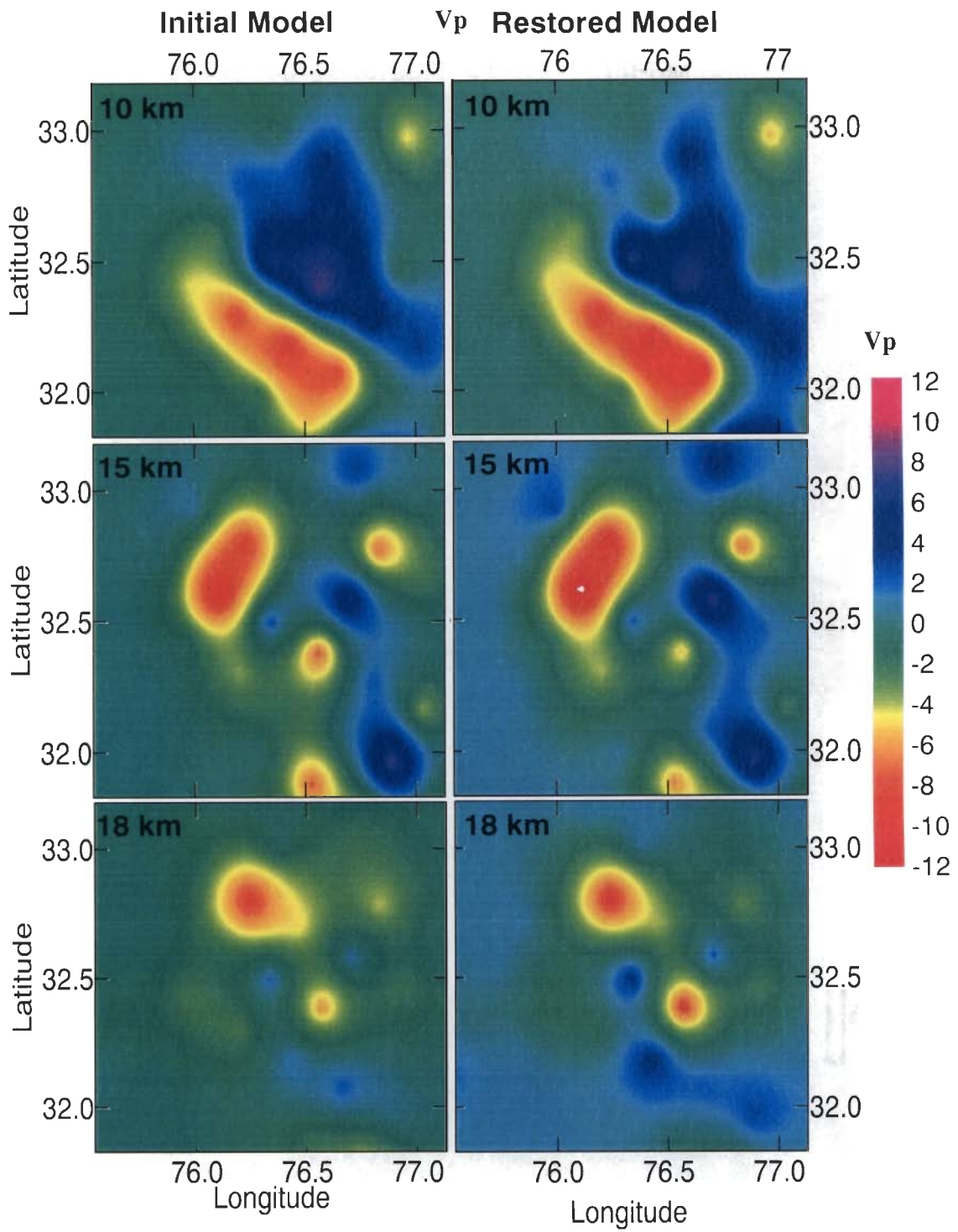
Figure 4.14a: Continue

124
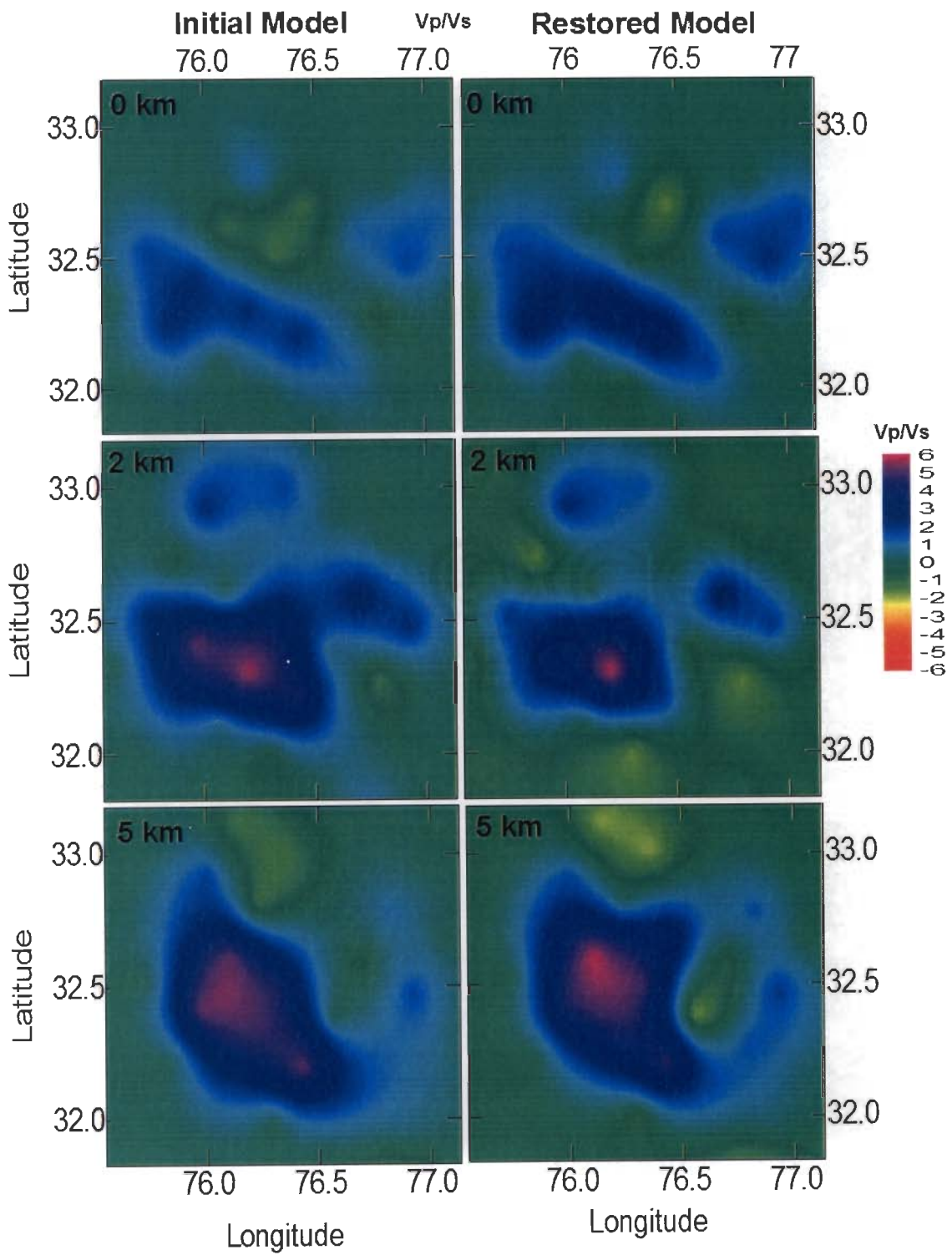
Figure 4.14b. Result of RRT for Vp/Vs, left hand panel shows input models and right hand panel shows restored models at different depths of 0, 2, 5, 10, 15 and 18 km by inverting 3D structure.

125
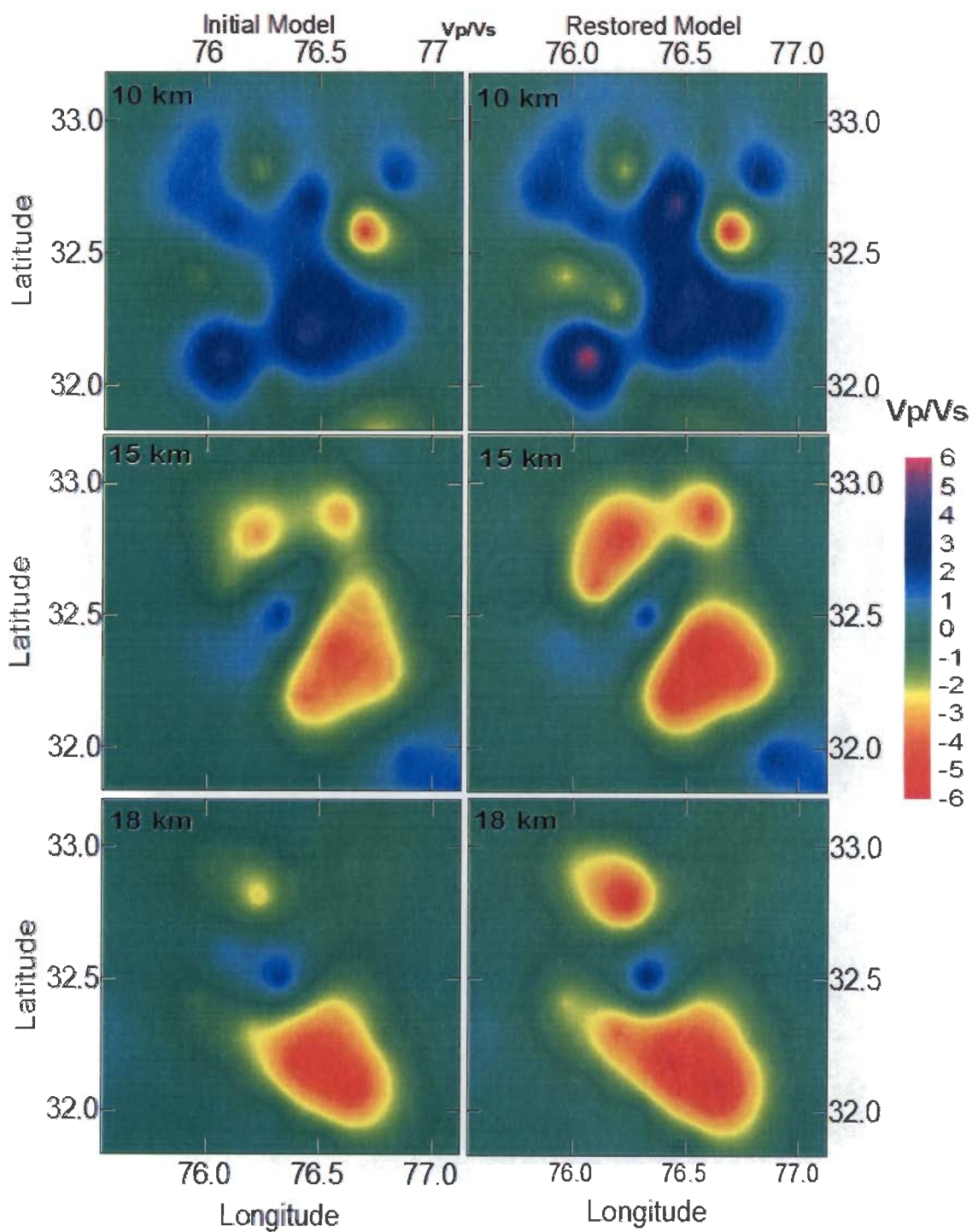
Figure 4.14b: Continue

126

After obtaining the 3D Vp, Vs and Vp/Vs models, a series of profiles are also selected to resolve the main geological structures. Two profiles are taken along NNE-SSW (AB and CD, **Figure 4.4b**) which pass through major tectonic units and different geological features of the region. In addition two profiles are selected parallel to the major tectonic features of the region (**Figure 4.4b**). These two profiles (EF and GH) pass through different geological features (**Figure 4.4**). These profiles are:

- Profile AB- passing through the dense cluster in the eastern part of the region across major tectonic units.
- Profile CD- passing through scattered seismicity and across the major tectonic units in the western part.
- Profile EF- parallel to the tectonic units in the southern part along SH.
- Profile GH- parallel to the tectonic units in the northern part along CN.

The 2-D variation of Vp, Vs and Vp/Vs along the profiles taken across and along the tectonic units of the region at 50 km distance apart from each other are shown in **Figures 4.16** and **4.17** respectively.

The deduced 3D velocity model is characterized by dipping low Vs and High Vp/Vs (visible in Vp/Vs plots in **Figure 4.16**) bodies in the upper crustal section portraying the geometry and depth extent of NE dipping thrust zones of the region. The NE dipping major faults of thrusting nature are on the boundary of high and low values of Vp/Vs plots in **Figure 4.16**. This low Vs and high Vp/Vs present in the SW part of the study region in the upper 10 km of the crust can be related with the sedimentary sequence of Siwalik and its near sub-vertical sub-surface extension.

The Vp variation along the tectonic trend of the area (along profile GH) shows that at the center of the profile we get a HVZ which forms an anticlinal structure from 10 to 15 km depth (**Figure 4.17**). From these profiles it is clear that in the southwest part the variation in Vs is higher as compared to Vp (profile CF). The two profiles EF and GH are selected parallel to the major tectonic units in such a way that they pass through different geological features and lie in the centre of the well resolved region. As clear from **Figure 4.4b**, the profile EF passes through the Siwalik Himalaya that can be related with the low

127

velocity sedimentary sequence of Siwalik and its near sub-vertical sub-surface extension. In case of Vs the depth section shows low velocity region compared to average velocity of the region up to much deeper extent (**Figure 4.17**). The other profile, GH has been selected in the northern part of the study area and passes through CN containing mostly metamorphosed sedimentary sequence. It is clear from the Vp tomogram that the velocity along this depth section is higher compared to profile EF. Similar results are visible in case of Vs variation along depth section. In this case we are also able to separate the thick sheet of weakly metamorphosed sediments of the CN (about 10 km thick) from the lower part of the crust and it may be present in the whole northern part as the CN extensively cover the study area. The depth sections of Vp/Vs also show different structure along these two profiles highlighting the difference of geological composition. However in case of Vp/Vs, its average value is higher for the strata along the EF profile as compared to profile GH. Therefore, the variation of Vs is much more than that of Vp which is also visible in the individual tomograms and has strong geological and compositional difference for different parts of this region.

Further given that the LVZ is better developed and outlined in Vs tomograms, part velocity variability may be related to varying degree of saturation (Mishra *et al.*, 2003). In addition, another LVZ running approximately at right angles to the general geological strike is mapped in the eastern part as a narrow NE-SW aligned part (**Figure 4.15**), on the first appearance seen as local extrusion of the primary NW-SE trending LVZ. However, this LVZ (high intensity in Vs) is confined to depth interval of 2 and 5 km and is underlain by HVZ in the tomogram of 10 km depth. The presence of structural discontinuity striking NE-SW (**Figure 4.4a**), coincident with the LVZ, was also evident from the contour plots of station corrections obtained as a by product of JHD performed to obtain optimum 1D velocity model in Chapter 3. It was seen that zone of positive station delays, coinciding with low-velocity Siwaliks in the SW quadrant, terminates sharply in NE-SW trend. It seems that an intrusion of low velocity material took place in perpendicular direction of the general trend of tectonic and geological features which is controlled by a transverse tectonic thrusting discontinuity dipping to west direction. This shows that the velocity structure may be the result of interaction of two tectonic regimes present in this area (**Figures 4.4 and 4.15**).

In the adjoining region, away from these LVZs, much of northern and northwestern part of the study area is characterized by relatively high velocity zone where both Vp and Vs are higher by ~12-14 % from surface down to 10 km. This part of top 10 km thick layer is related to the thick sheet of weakly metamorphosed sediments of the Chamba Nappe (CN) that extensively cover the study area which has higher velocity compared to southern part of Lesser Himalaya. Nature of relative HVZ display the space-depth extent of the CN metamorphosed sedimentary sequence. From the surface to 5 km depth, it is seen that spatial expanse of the relatively high CN sequence to the south and southeastern part extent is limited by the LVZ. The vertical extent of the Siwalik, characterized by relatively low velocity, and the CN, marked by relative high velocity, do not seem to extend beyond the depth of 10 km as both the LVZ and HVZ show somewhat scattered picture in the velocity tomogram of 10 km. The tomograms of Vp/Vs show complimentary picture in agreement with the independent plots of Vp and Vs. The change in litho-composition of crust in the depth range of 10 km is supported by the transition in Vp/Vs ratio from a uniformly high value in the upper 10 km to diffused low values below the depth of 10 km.

4.4.2. Seismicity-Velocity Structure Linkage

The efficacy of the LET derived 3D velocity model in providing the improved estimation of earthquake parameters is demonstrated by the fact that RMS of travel time residuals reduced by 34.38% from 0.32 s to 0.21 s. To establish correlation of resolved earthquake parameters with crustal heterogeneity as revealed by velocity structures, the distribution of hypocenters in specific depth intervals is superimposed on the velocity tomograms in **Figure 4.15** that depicts the seismicity-velocity linkage. It is clear that most of the hypocenters at different depths are concentrated at the boundary between low-high velocity zones and in the high Vp/Vs zones or near its boundary. Little diffused seismicity patterns are scattered in relatively high velocity sections while low velocity sections are largely free from seismicity. To further highlight the linkage of seismicity with mapped velocity structure, the depth distribution of hypocenters in relation to variation in Vp, Vs and Vp/Vs ratio along two represented profiles (AB, CD) across major structural/tectonic grain of the study region **(Figure 4.16)** is plotted. The Vp/Vs being direct measure of the Poission's ratio clearly trace the boundaries related with intrinsic lithologic transitions
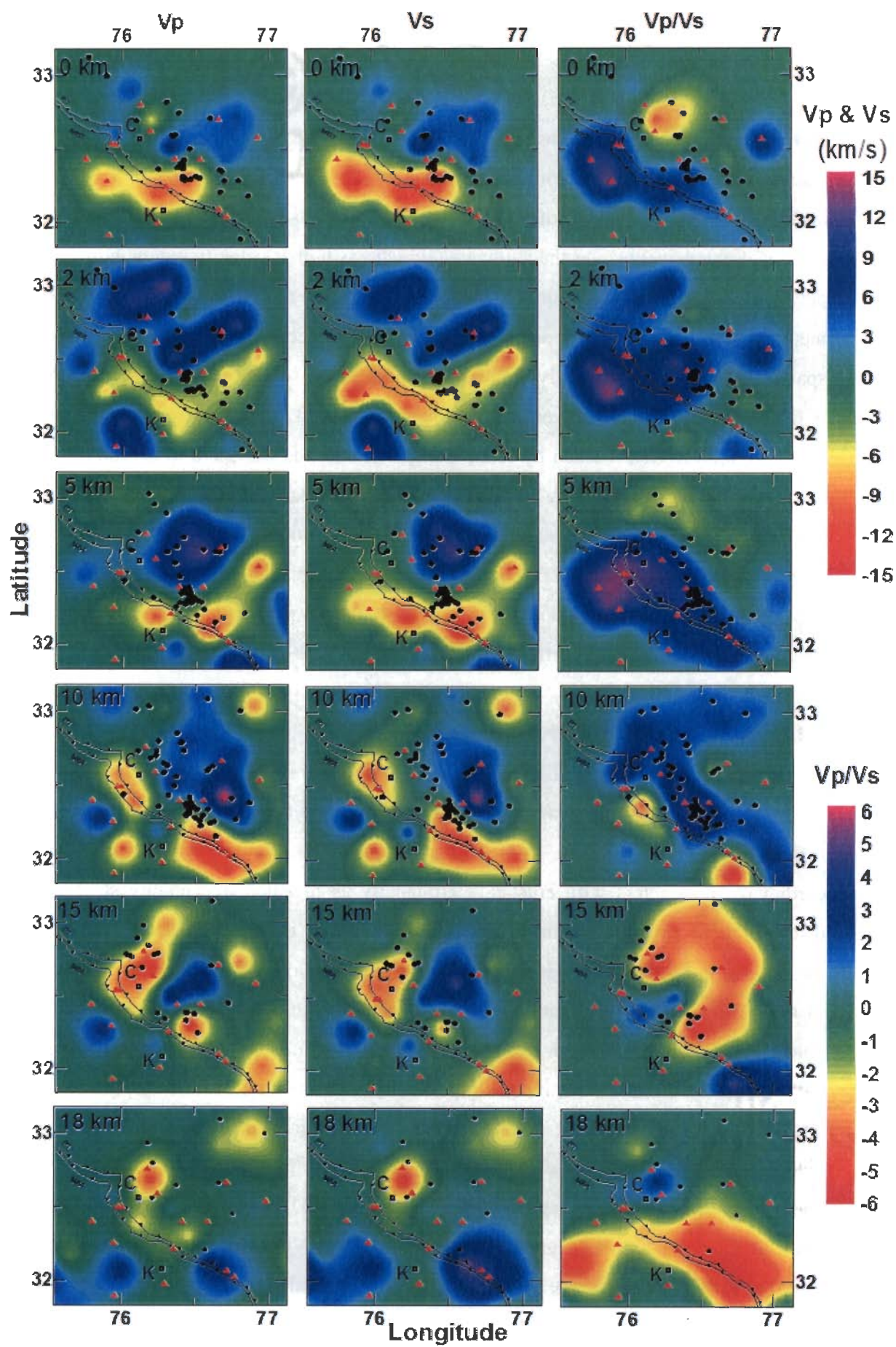
or physical state of the medium, e.g. saturation state, although plots of Vp and Vs in the present case exhibit identical picture. The profiles AB and CD are so selected that they cut the section of the crust orthogonally where the majority of seismic events are clustered in a narrow space and hence able to portray the 3D perspective of velocity-seismicity correlation. The profile CD is located in the northwestern part of Chamba region where the seismicity is evenly distributed. Hypocenters of all earthquakes that fall within 50 km wide corridor centered on the profiles are plotted to bring out most significant trends. On all cross-sections, numbers of well defined hypocenter alignments correlate well with resolved transition from high to low Vp/Vs ratio. Given their connotation with the surface expressions of tectonic elements of the region, such coincidences of seismic alignments with transitions in Vp/Vs structure can be best seen as sub-surface extensions of the active faults/thrusts of the study region.

4.4.3. Elements of Seismotectonic Model

On both profiles AB and CD in **Figure 4.16** the low Vp structure imaged is characterized by high Vp/Vs and low Vs. This is in agreement with the minimum 1D velocity model, deduced in Chapter 3, which indicated presence of anomalous low velocity layer in the depth range of 15-18 km. Attributing the low velocity to the presence of fluids and noting that presence of the LVZ zone was a conspicuous feature of the Garhwal (Arora, 2003; Kayal, 2003) and Nepal Hiamalaya (Schulte-Pelkun *et al.*, 2005), the top interface of the mid-crustal LVZ was interpreted as brittle-ductile transition. As observed in many seismically active zones, the brittle-ductile transition defines the sharp lower cut-off depth of crustal seismicity (Sibson, 1986). Except for a narrow section right beneath the clustered zone of epicenters, the top interface of the high Vp/Vs in **Figure 4.16** traces this brittle-ductile transition as a northeast low angle dipping interface placed at average depth of ~15 km near the MBT. The plunges of the axis of maximum stress for moderate to large earthquakes also tend to align with this interface as shown by (Kumar *et al.*, 2010) and as

---

Figure 4.15. The lateral variations in Vp, Vs and Vp/Vs at different depth levels. Velocity parameters are plotted as percentage perturbation relative to the initial 1D layer velocity. The hypocenter distribution in specific depth intervals is superimposed on the velocity tomograms of respective depth.

131
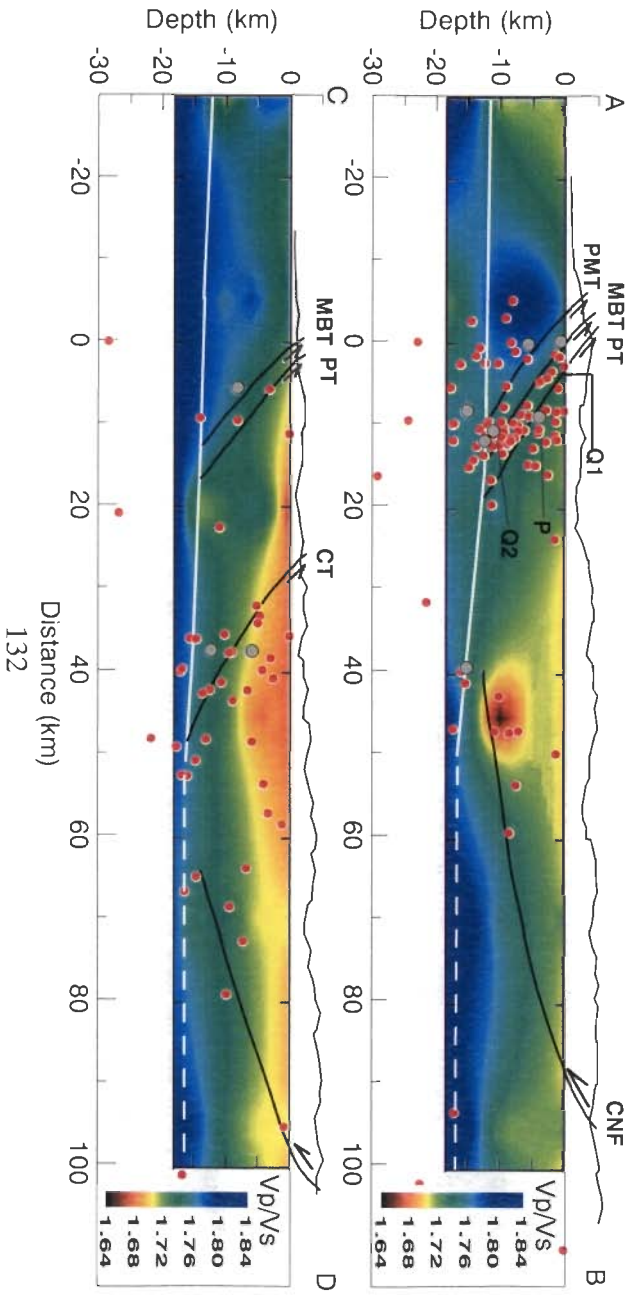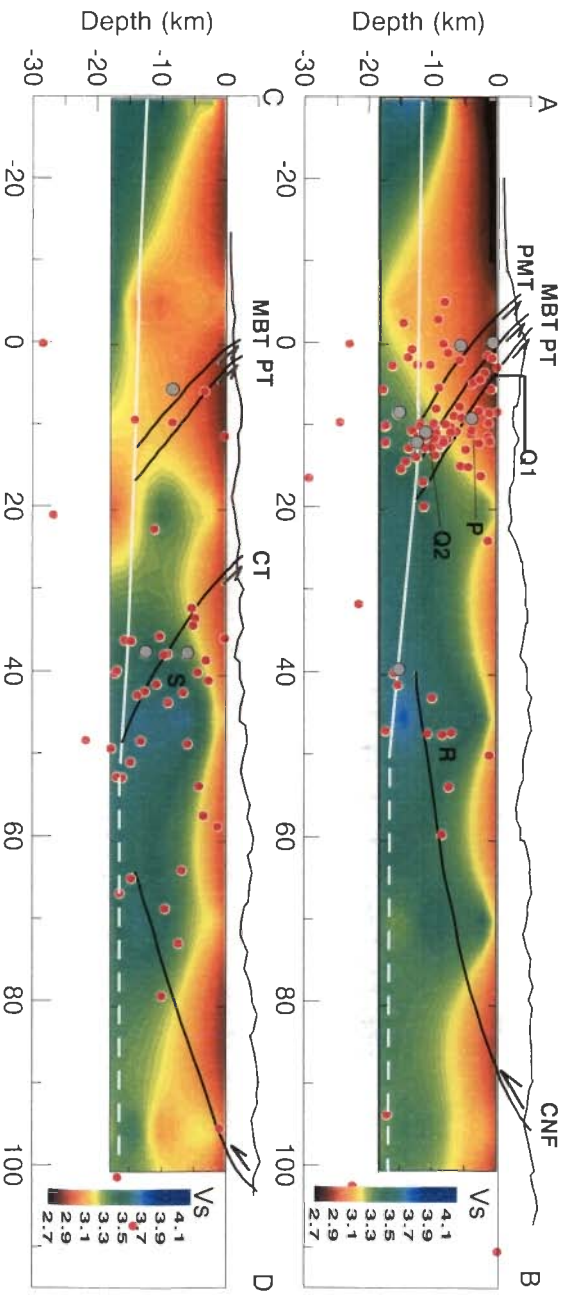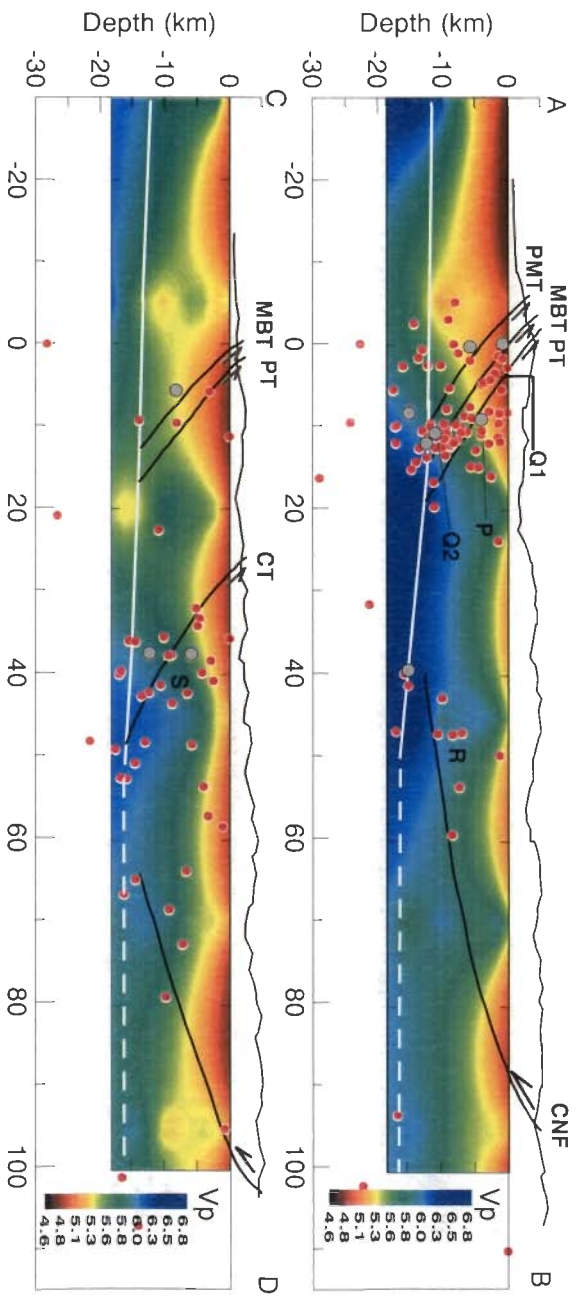
will be shown in Chapter 7. Such alignment of nodal planes on a single plane had led Ni and Barazangi (1984) to visualize such a linear plane as Basement Thrust Fault (BTF), separating the down going Indian Plate from the southward propagating sedimentary/metamorphic wedge of the Himalaya.

In the depth sections above the plane of detachment, most of the hypocenter concentrations are confined to the sharp transition in velocity structures, quite clearly reflected in Vp/Vs plots, demarcating major litho-tectonic boundaries (**Figure 4.16**). In this figure two profiles AB and CD taken perpendicular to the major tectonic units are used to obtain seismotectonic implications. For example on the profile AB, the seismicity is concentrated to the LH, which pinches out to a narrow belt of only few km. Two major concentrations are evident; one in the upper depth section of ~7 km on the northeast dipping PT (cluster P) and second on the lower section of the sub-parallel MBT (cluster Q). The later cluster is best developed where the northeast dipping MBT merges with the detachment zone. In addition, a weak cluster can also be inferred along a plane, which is best seen as sub-surface extension of the southwest dipping CNF. In comparison to this active nature of the PT and MBT on the profile AB, both these thrusts are seismically dormant along the profile CD. Instead, the hypocenter alignment is seen along the CT (cluster S). This marked difference in the behavior of seismicty on these two sectors appears to be related to the varying limits of southward extension of the CN. The southward extent of the CN on the western part of the study area is limited by the CT whereas on the eastern part, the CN extends right up to the PT/MBT. This varying limit of southward extension of the CN is consistent with field evidence of Singh (1994) who noted that the CT bordering the Chail formation to the north is well marked west of Chamba, whereas this contact is not traced east of Chamba. In the eastern part, the CN extends right up to the PT and geological evidence shows ductile deformation preserved in the form of mylonitized augen gneiss exposed at the base of the PT. (Rautela and Thakur, 1992).

Figure 4.16. Distribution of earthquake hypocenters in relation to velocity structure obtained for Vp, Vs and Vp/Vs on the depth sections along two profiles across the major tectonic units, profiles AB and CD shown in Figure 4.4. Well defined clusters, referred to in the text are also marked.

133
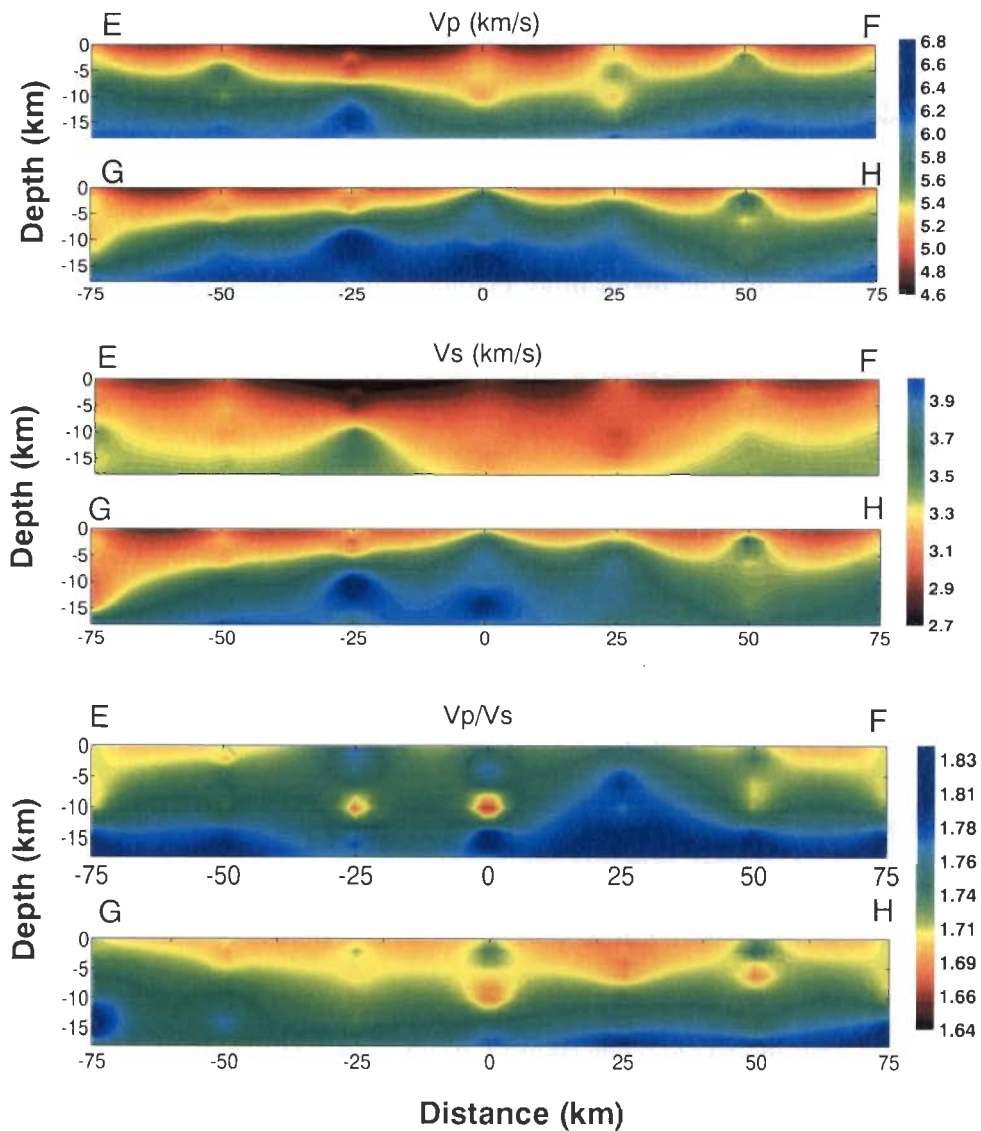
Figure 4.17. Velocity structure obtained for Vp, Vs and Vp/Vs on the depth sections along two profiles (EF and GH shown in Figure 4.4) taken parallel to the major tectonics units.

4.5. CONCLUDING REMARKS

The 3D variation of Vp, Vs and Vp/Vs is obtained in the source area of 1905 Kangra earthquake in the western Himalaya using LET for both P- and S-wave arrivals of well located set of local earthquakes recorded by a dense seismic network. The refined location of small magnitude earthquake using 1D and 3D velocity models shows that the

134

seismic activity in this region is shallow focused occurring mainly within upper 20 km crust with most of the events present within upper 10 km. The selected data set gave an appropriate resolution in the central part of the study area for a volume of about 100 x 100 x 18 km^3. The observed trend of velocities in the region of dense seismic rays shows a systematic and significant variation for all the parameters. The low and high velocity zones are extended in the east-west direction and are present in the southern and northern part of the study region respectively. At 2 and 5 km depths a NE-SW tending low velocity zone is observed in the eastern part (**Figure 4.15**), which may be the intrusion of low velocity material most probably caused by two perpendicular thrust tectonics. Northwest dipping low velocity zone is imaged from 15 to 18 km depth clearly from the vertical and horizontal cross sections and are in agreement with 1D velocity model indicating velocity variation along the main tectonic units of the region (**Figures 4.15 and 4.16**). Almost all the seismic events are located either on the boundary of low and high velocities or in the region of high velocity zone. Therefore, the uppermost brittle part of the crust is being ruptured by micro-earthquake activity and the brittle-ductile transition defines the sharp lower cut-off depth of crustal seismicity.

CHAPTER 5

STRESS FIELD INFERRED FROM FAULT PLANE SOLUTIONS

5.1. INTRODUCTION

Analysis of seismicity and focal mechanisms of earthquakes are basic tools for studying plate motions and reactivation of tectonic units. Boundaries of small and big tectonic plates are defined through intensity of seismic events and relative motion along these boundaries is scanned with the help of Fault Plane Solutions (FPS). Crustal behavior, displacement type and relative motion between the boundaries of tectonic plates are studied extensively through focal mechanism. The FPS is described through radiation pattern of energy emitted by an earthquake which is useful for obtaining fault geometry. Hence the location of earthquake hypocentre and its FPS helps us to better understand different aspects of tectonics and ongoing deformation of given region. Analysis of focal mechanisms also provides information about stress distribution on different faults of a region. Tectonic earthquakes, mainly govern release of stress in the crust and the behavior of stress helps to find the causes of interplate seismicity. Earlier convergence tectonics of the Himalayan region was mainly described using information about big sized earthquakes showing thrust dominated mechanism (Ni and Barazangi, 1984). Recently some work has been done using small magnitude earthquakes on local and regional scale (Mukhopadhyay and Kayal, 2003, Schulte-Pelkum *et al.*, 2005, Rai *et al.*, 2006, Kumar et al., 2009). It has been proved that the deformation in the Himalaya region is mainly through compression directed in N-S to NE-SW direction (Seeber et al., 1981; Ni and Barazangi, 1984); however the validity of this fact on regional basis has to be resolved for identification of regional compression regimes. The regional tectonic regimes can be inferred through focal mechanisms obtained for earthquakes of particular region to identify the principal stresses. The present study may help to decipher the regional tectonic deformation behavior of a part of NW Himalaya. This may be used to evaluate geodynamic implications. The Global Positioning System (GPS) measurement gives the deformation pattern only along the surface but the subsurface behavior is obtained through seismic activity and its source characterization.

137

5.2. METHOD OF DATA ANALYSIS

The study of displacements and forces at the focus of an earthquake is commonly referred to as focal (or earthquake) mechanism calculation. Focal Mechanism (FM) or FPS for an earthquake is obtained using the wave forms (particularly first polarity motion of body waves) recorded by seismographs at different stations around the earthquake generating source (Snoke *et al.*, 1984). The accuracy of solution depends upon the azimuthal distribution of seismographs around the epicenter and the number of observations/readings obtained for a single earthquake. Better the azimuthal coverage of earthquakes; better is the accuracy of FPS determination. The emitted energy radiation pattern through earthquake occurrence is recorded by the seismographs installed at earth's surface around the earthquake source. These radiation patterns describe the fault discontinuity or the reactivated fault plane through double force couple or simply double couple. The orientation of three orthogonal axes, P (compressive or pressure axis), T (tension axis) and N (null axis) are determined from this information. The fault plane contains N axis that is located at 45° from P and T axis. In each solution of double couple, two mutually perpendicular nodal planes are obtained in which one plane is the surface of tectonic fault and the other one is described as auxiliary plane having no structural significance. These two planes are at right angles with each other intersecting along N axis. Geologically significant information is required to determine which one is the fault plane. The different steps used to analyse the present data set are discussed in the following sub-sections.

5.2.1. Determination of Focal Mechanism

The polarities and amplitudes of the radiated seismic signals strongly depend on the directions in which the waves leave the source. This information is preserved along the travel path of the seismic waves. Based on seismic wave propagation, the seismograms recorded by several stations at locations around the epicentral area allow for the determination of the earthquake source process. The radiations produced by body waves are inverted to obtain the geometry of the earthquake source. This geometry is described by the focal mechanism (FM) of the earthquake. The FM of an earthquake can be obtained through first motion of P waves, the direction of P and S waves along with P/S amplitude ratios (Kisslinger *et al.*, 1981) and polarization and amplitudes of S waves (Khattri, 1973).
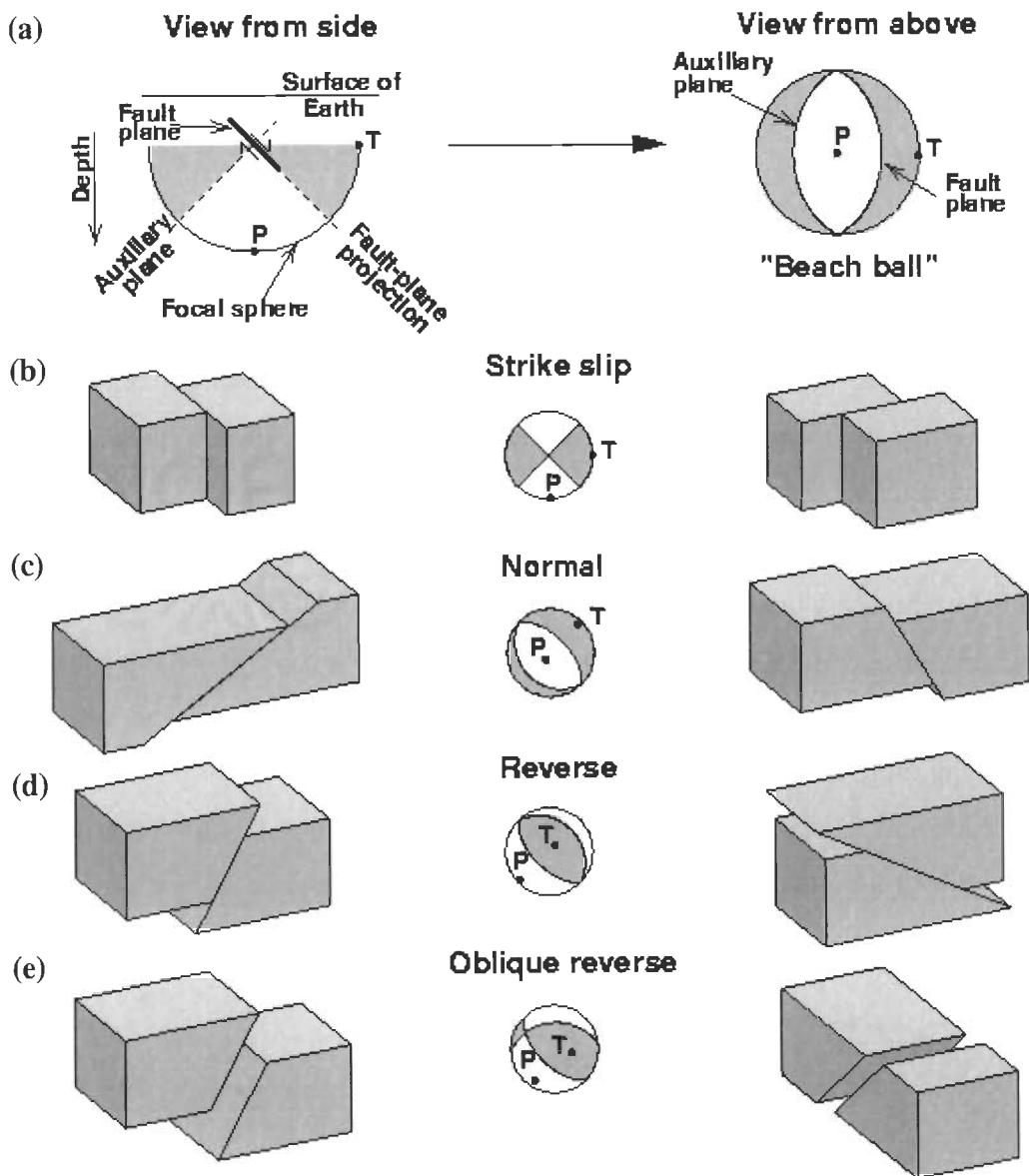
Figure 5.1: Schematic diagram of focal mechanism (USGS).

The lower-hemisphere stereographical projection is used to show the beach ball diagram describing the FM (**Figure 5.1**). The projection has four quadrants, two quadrants are black and the other two are white, these quadrants are separated from each other by great circle arcs oriented at 90° with each other. In case of pure normal or pure reverse/thrust fault one of the quadrants is not visible. The black quadrants represent the compressional while the white quadrants represent dilatational zones. The nodal planes are described by the great circle arcs for which one nodal plane represent the fault surface generated through tectonic slip. The line connecting two points of the two great

139

circles coinciding at the outer edge of the beach ball diagram represent the strike of the fault plane. The dip direction of the fault plane is indicated by a line that is at right angles to the strike and drawn from the center of the beach ball towards great circle. Simply stated the radiation pattern is represented in the beach ball in such a way that it shows the first P-polarity of the particle motion around the focus. The black quadrants show the movement of particles away from the focus and the white quadrants show movement towards the center of the focus. The slip along the fault plane represents the movement of either the hanging wall or the footwall or both in the form of possible four types of mechanisms as reverse, normal, strike-slip and oblique as shown in **Figure 5.1**. The schematic of FM representation described in **Figure 5.1** is as follow. The left panel of **Figure 5.1a** represents the beach ball view from side while the right panel is the view from above the surface of the earth for a pure normal fault. The fault plane and auxiliary plane are categorized using geo-tectonic background of the region. The probable movement along these two surfaces has been shown in **Figure 5.1c**. Figure 5.1b, d and e shows the block and fault plane solution representation of pure strike-slip, pure reverse and reverse with strike-slip component (oblique-slip) respectively.
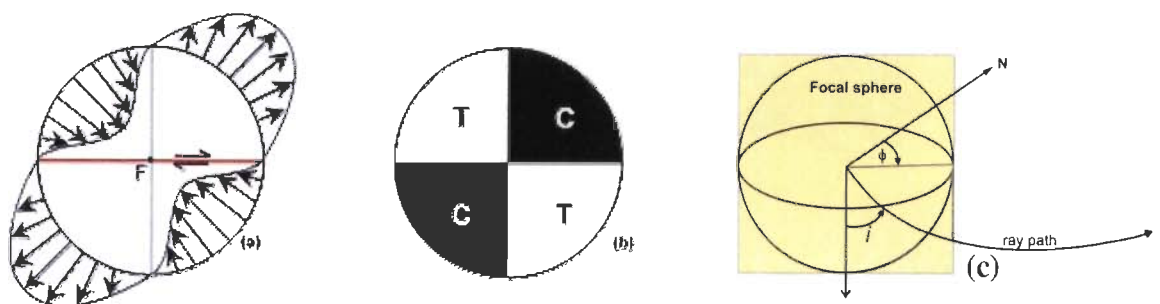
Figure 5.2: Schematic diagram (a) showing the direction of initial movement of particles around the focus (F) of an earthquake on a W-E dextral strike-slip fault, (b) equivalent zones of compressional (C) and tensional (T) sense of first motion of the seismic waves radiating outward from the source and (c) focal sphere representing ray path with azimuth ϕ and emergence angle i.

5.2.2. P-Wave First Motion

P-wave is the first motion recorded on a seismogram after occurrence of an earthquake. Vibration of medium particles due to P-wave propagation takes place in the

form of compression and dilatation in the direction of propagation of the wave. As shown in **Figure 5.2**, the amplitude of first P-wave motion varies depending on the position of the recording station with respect to the fault plane. In this case the wave recorded at stations lying in the direction of fault plane and orthogonal auxiliary plane has minimum amplitude while it is maximum in the directions at an angle of 45° to these two axes. These motions of first P-wave is taken from the vertical component seismogram. These observed motions are projected backwards from the recording station to the focal sphere of an earthquake to obtain the focal mechanism. The earthquake point source is represented by a conceptual homogeneous unit sphere named focal sphere. Thus, the geographical position of the seismometer is transformed to focal sphere which can be shown with lower hemisphere of a stereographic projection. Using these polarity motions the two orthogonal planes are obtained in which one is the nodal plane of the earthquake rupture. Along these four quadrants, the principal stress axes are drawn, one is the P-axis representing maximum compression and the other is the T-axis indicating minimum compression. As shown in **Figures 5.3** and **5.4**, the dilatational quadrant of first polarity plot contains the P-axis and the compressional quadrant contains T-axis. The axis formed at the point of intersection of P- and T-axes and perpendicular to the plane containing these two axes, is known as B- or (N) null axis. Therefore, the first motion of P-polarities can be used to fully describe the source region of an earthquake. The P-, T- and B-axes are obtained and using trend and plunge of these axes the FM solutions of the earthquakes of present study region are calculated for describing the stress environment.
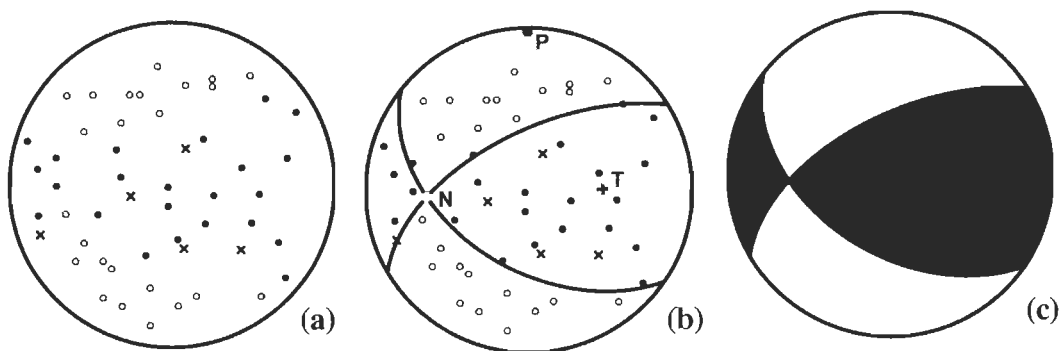
Figure 5.3: Fault plane solution obtained from first P-wave polarity motions (a) first P-wave polarity motion data for a hypothetical earthquake obtained from different seismographs, (b) Nodal planes along with N, P and T axes fitted to the data and (c) resulted beach ball plot showing obtained reverse oblique fault movement.
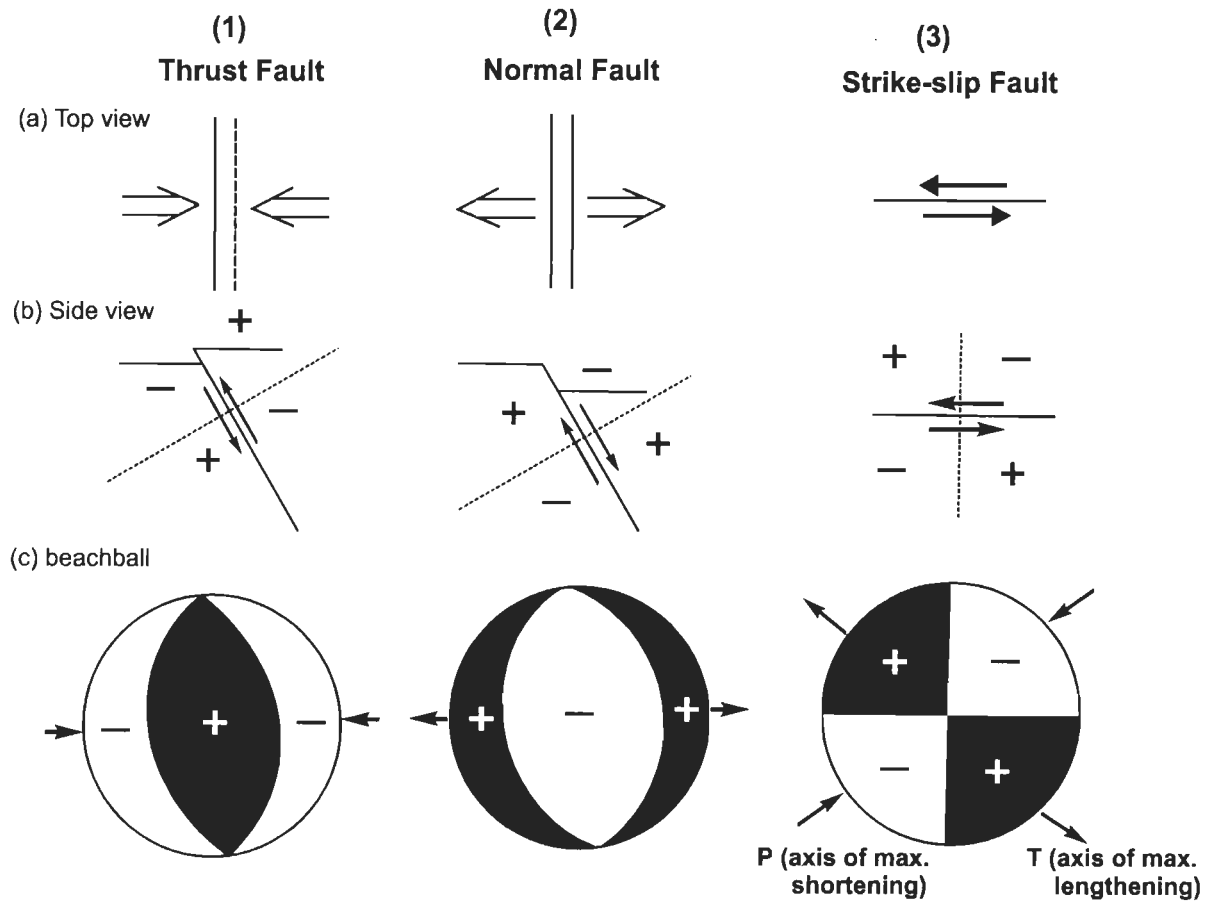
Figure 5.4: Three main types of fault plane solutions (after Snoke et al., 1984) as (1) Thrust fault (2) Normal fault and (3) Strike-slip fault and their representation through (a) Top view (b) Side view and (c) beach ball representation using lower hemisphere projection.

5.2.3. Technique Used to Obtain FPS

To obtain FPS from first motion, first the earthquake source is located using P- and S-wave recording time at each station and using appropriate velocity model of the region. Then azimuthally well covered earthquake source that have sufficient number of good quality first motions is used to obtain for FPS. The amplitudes of different waves depend upon magnitude of earthquake, hypocentral distance and the position of station with respect to the orientation of the fault plane. For an earthquake the epicentral/hypocentral distance is obtained for each station. The orientation of ray paths along which the wave has travelled from the source to the station is determined at the source. The ray path depends on the crustal velocity model around the source and the information of ray path is required to use the nomenclature of the polarity motion. Two

parameters, viz. azimuth (ϕ) and take-off angle (i) are obtained from the ray path. The azimuth is measured as the clock-wise angle to the line connecting the station and epicenter from the direction of north 'N' at the earthquake source (**Figure 5.2c**). The take-off angle is the angle the ray path makes at the source with imaginary vertical line connecting the source and the centre of the earth (**Figure 5.2c**). Based on these ray paths and P-wave first motion polarities the four zones of compressional and dilatational are estimated (**Figures 5.2b and 5.3**). In **Figure 5.2a** the zones showing the arrows diverting outward gives the compression at the recording station sensed by upward movement of the seismograph. While in other two zones the dilatation (extension of the region) is shown by the arrows pointing towards focus and the onset of P-wave will be recorded by downward movement on the seismograph. The first polarity motion using above mentioned information is marked on the equal-area stereo net on a lower hemisphere stereographic projection (**Figure 5.3a**) where the open circle represents dilatation and the filled circle represents compression. Few stations giving no clear indications are represented by 'x' sign where motion is identified as very weak. Such notation for each station is placed on a line extending from the centre of the stereonet towards the station azimuth measured from the earthquake focus. The calculated take-off angle gives the angular distance from the centre to the plotted symbol. After plotting all the points, the data is divided by incorporating two great circle arcs on the stereonet. These arcs represent two planes bisecting at right angles with each other (**Figure 5.3b**) and dividing the regions into compressive and dilatational regimes (open and filled small circles respectively). These two circular arcs separate the filled and open circles and pass near or through the 'x' marked symbols representing arrival of weak energy. These two circular arcs represent the nodal planes of the FPS; out of which one is the surface of the fault causing slip during earthquake occurrence. The compression (P) and tension (T) axes are marked on the stereonet, as their positions lie in the centre of the respective dilatation and compression quadrants and these are 45° away from the nodal planes. The intersection point of two planes bisects these planes at right angle with each other which is known as null point described by N or B.

Finally, the region between these great circles with compression polarities (filled circles) is filled with color (black) and the other region of dilatational polarities (open circles) is kept empty or filled with white color to complete the beach ball representation of the FM. Therefore, the compressional and dilatational quadrants are

143

separated as shown in **Figure 5.3c**. In these quadrants, the P-axis is in the middle of the dilatational (white) quadrant and T-axis is in the middle of compression (black) quadrant. In **Figure 5.1**, beach ball representation of the four different types (normal, reverse, strike-slip and oblique reverse) of FPSs is shown.
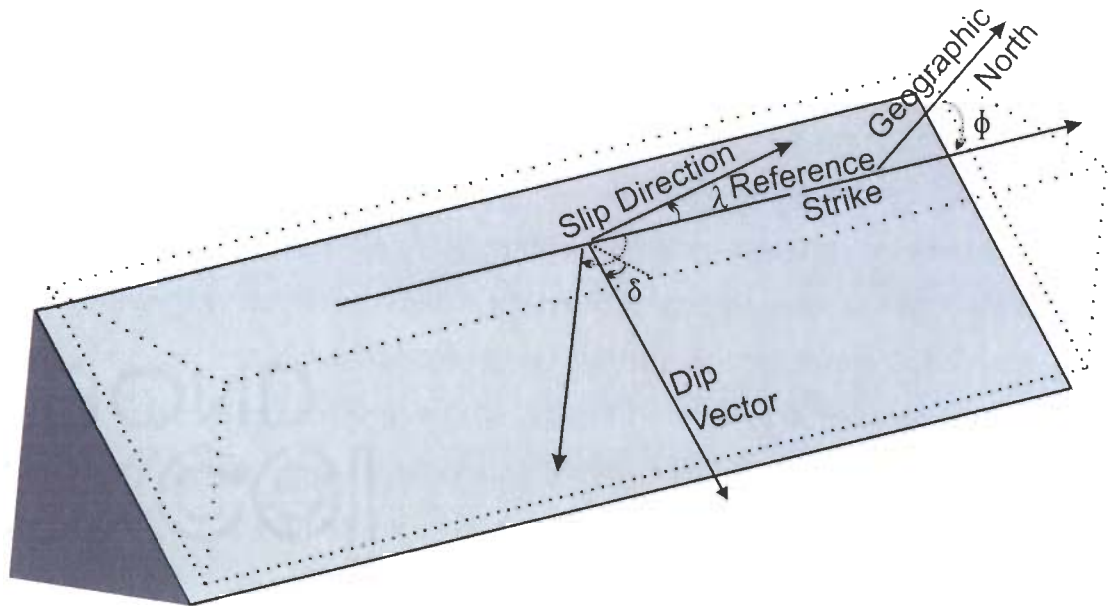
Figure 5.5. The schematic of Fault Plane Solution represented by strike, slip and dip directions (Aki and Richards, 1980).

Sometimes it is difficult to get a unique solution as the data may not be of sufficient quantity or of good quality. A grid search approach is adopted to obtain a compatible FPS for the event based on the available data. A systematic search is performed for a solution that gives minimum number of polarity errors. In this search a uniform step of angle provided by the user is used on input data (Snoke *et al.*, 1984). In this inversion the fault plane is represented by strike azimuth, dip angle and the rake (direction of slip movement) for the assumed double-couple mechanism as shown in **Figure 5.5** based on convention of Aki and Richards (1980). Using the information of strike, dip and rake the solution type is named as thrust/reverse, normal, strike-slip and oblique type as per the nomenclature given in **Table 5.1**. In the grid search the available polarities are matched with different options of these three parameters for the possible FPS assuming double-couple mechanism. The bad polarities along with their station information are given in the output file. In this case the minimum number of bad

polarities is first searched. This number is 0, 1, 2 etc based on the bad polarities in which the 0 number represent that all the available polarities are in agreement with one certain orientation of the fault. In the present study the maximum number of bad polarities for an event is 3 and majority of solutions have 0 and 1 bad polarity reading indicating reliable solutions. **Figure 5.6** depicts the reliability of the obtained solutions where in **Figure 5.6a** the percentage of matched (good) polarity with the solution is shown for all the events. In **Figure 5.6b**, the bar diagram shows the number of events having 0, 1, 2 and 3 bad polarities as 16, 17, 8 and 1 respectively.
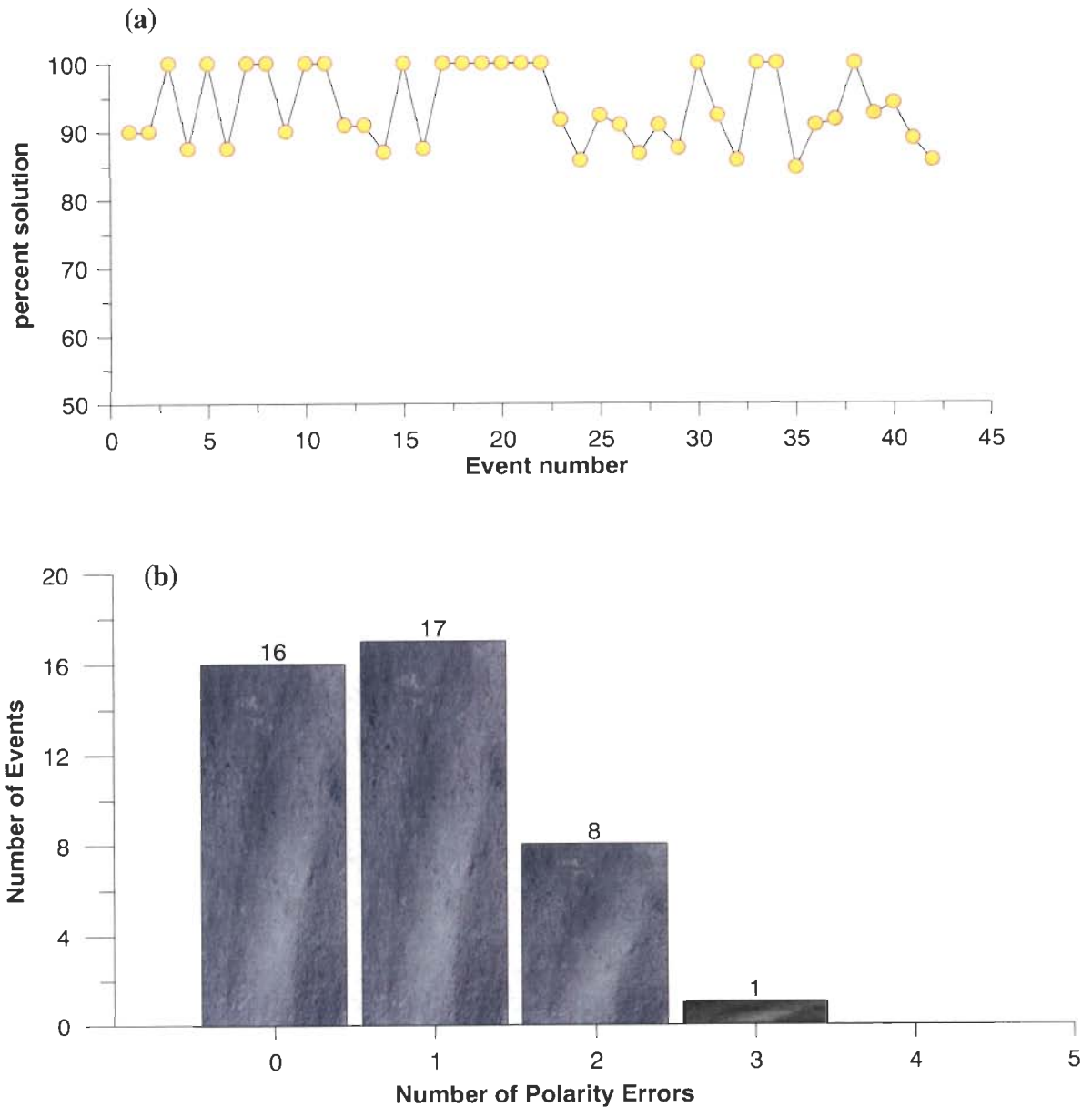
Figure 5.6. Solution stability observed through the number of P-polarity readings for the present data set of 42 earthquakes. (a) Percent variation of good polarity readings for each solution. (b) Observed polarity errors versus number of events.

Table 5.1: Description of Fault Plane Solution based on slip vector.

Rake of slip	Fault type
0° or 180°	pure strike-slip
90°	pure dip-slip reverse
-90°	pure dip-slip normal
-20° to 20°	left-lateral strike-slip
20° to 70°	reverse left-lateral oblique
70° to 110°	reverse
110° to 260°	reverse right-lateral oblique
-160° to 160°	right-lateral strike-slip
-110° to -160°	normal right-lateral
-70° to -110°	normal
-20° to -70°	Normal left-lateral oblique

5.2.4. Geometry of Fault Plane on the Basis of Focal Mechanism

The obtained beach ball is used to specify the geometry of the fault plane which indicates the type of deformation during an earthquake. The fault can be specified with three terms viz strike, dip azimuth and the slip vector as indicated in **Figure 5.5.** The strike of the fault plane is represented as the angle measured between the line connecting the centre of the focal sphere with geographical north and another one passing through the centre and along the strike of the fault. The strike of the fault plane is represented between 0° to 360° ($0° \leq \phi \leq 360°$). The angle is measured in clockwise direction from geographic north. The dip azimuth is at right angles to the strike direction. It gives the direction in which the fault plane dips. The dip angle is the angle between a horizontal plane and the dipping plane in the direction of the dip azimuth. The dip of the fault varies between 0° to 90° ($0° \leq \delta \leq 90°$). The third reference is the slip vector on the fault that is represented by the azimuth of the hanging-wall slip vector and is known as rake of the fault. The rake is measured in the fault plane relative to the reference strike of the fault plane. The rake is the angle giving clockwise or anticlockwise rotation of the hanging-wall relative to the reference strike of the fault (**Table 5.1**). If the angle of rotation is anticlockwise then it is taken as positive angle and if the rotation is clockwise then it is considered as negative. In other words we can say that the slip vector directed upward relative to strike has positive rake and the slip vector directed downward has negative strike. Hence the range of rake varies between

-180° to 180° (-180° ≤ λ ≤ 180°) in which the positive rake describe some component of reverse slip while the negative rake gives the movement of hanging-wall down to denote component of normal slip. The rake of the fault having value equal to 0° or 180° represents pure strike-slip movement. If the rake is 90° then it is a pure reverse fault movement. If the rake is equal to -90° then the movement of the hanging-wall gives pure normal fault slip. The other angles describe oblique faults of reverse and normal types having strike-slip component. In case of reverse fault if the dip angle is less than 30° then it is known as thrust fault. As fault plane solution gives two nodal planes based on double couple and moment tensor concept, the beach ball of FM has following properties:

(i)   Two nodal planes (main and auxiliary) are perpendicular to each other.

(ii)   The intersection of two nodal planes is coincident with the B-axis.

(iii)   The middle of the dilatational zone contains the P-axis while the T-axis lies to the middle of the compressional quadrant.

(iv)   The P- and T-axes are 45° from the nodal plane.

(v)   The P-, T- and B axes are orthogonal to one another.

(vi)   The slip vector lies in a plane defined by P- and T-axes.

Therefore, two nodal planes are obtained using the polarity motion or moment tensor inversion. However, which is the main fault plane has to be decided on the basis of surface tectonic features, seismotectonic models, aftershock distribution and field evidences for big sized earthquakes.

5.2.5. Average Focal Mechanism

A small fault or a small portion of big fault can be described as the average fault plane obtained through many FMs along that portion of the fault. A single rupture during an earthquake is fully described by orientation of P-, T- and B-axes. Conventionally, an average orientation of P-axis obtained from a number of earthquakes of a region is taken to be the representative of maximum compressive stress orientation. The orientation of the maximum compressive stress was utilized by Sbar and Sykes (1973) and Zoback and Zoback (1980) to infer the regional stress behavior. However, it is observed that in a single region the types of obtained focal mechanism differ. This may indicate that there is variation of stress pattern along tectonic units as well as with depth. Hence it is also important to see how focal mechanisms vary laterally as well as

with depth in a given region. This difference may be due to small scale perturbations in the stress field due to medium heterogeneity in the Himalayan region within small distance range. To overcome this problem average focal mechanism for different parts of the recent study region is also obtained. The utilized stress tensor inversion calculates the behavior of stress pattern using the focal mechanism of many events of one region. The stress tensor representation is useful in characterizing the tectonic characteristics of a given region.

5.2.6. Composite Focal Mechanism

In few tectonic processes of deformation, a small region is ruptured many times within a small duration of time giving rise to a cluster of events. These processes are aftershock and foreshock activities that occur respectively after and before the occurrence of a big earthquake. The other process is the occurrence of swarm activity in which numbers of earthquakes of almost similar size occur in a region within a short interval of time. In these processes the earthquakes are detected within a limited region for which the earthquake generating source process should be almost similar. In this case if the amount and azimuthal distribution of first motions is not sufficient to obtain individual focal mechanisms then composite focal mechanisms are constructed by superimposing the data of many events rupturing the same fault segment. The main objective behind this is to combine the data of many sources assuming that these earthquakes have similar FPS as the radiation are coming from a single zone so that polarity motions are same. This assumption is valid only if the earthquakes occur on a single fault segment such as the aftershocks or foreshocks that occur within the rupture extent of main shock. However sometimes the aftershocks induced activities are triggered by the adjacent fault having the source of main shock. In this case the focal mechanisms of the main shock and the aftershocks are sometimes quite different. It has also been observed that some aftershocks in a segment may occur on faults of much different orientation. Therefore these earthquakes should also be divided into different groups to observe the change in focal mechanisms with variation along depth and in horizontal direction. Hence the determination of focal mechanism through many earthquakes as a composite solution is a biased procedure that depends upon the selection criteria and may be different from one person to other.

5.3. DATA SET AND PROCESSING

Ever since the seismic network in the Kangra-Chamba region became dense in 2004 with Start experiment of WIHG, it has introduced a good azimuthal coverage for the region containing high micro-earthquake activity and therefore the latest well defined micro- and small magnitude earthquakes (2.5≤M≤5.0) are used to obtain FPS. On the basis of P-wave first motion polarity, the FPS of 42 events recorded at eight or more stations and having maximum azimuthal gap less than 100° are obtained. These earthquakes are well located with average RMS value of 0.1s. The amplitude of P- and S-waves observed at different azimuths is also determined and used to obtain the FPS. The focal mechanisms were determined from the first polarity information and the ratio of maximum amplitude of P and S waves (Snoke *et al.*, 1984). The observations for the current data shows that better solution can be obtained using at least 8 well distributed clear polarity readings of first P-wave around earthquake source. **Figure 5.7** shows the plot of number of P-polarity data for each earthquake versus earthquake magnitude. The number of polarity readings increases with increase in the size of earthquake as released seismic energy can propagate far away and get recorded at distant stations. The numbers of these polarity readings for earthquakes having magnitude around 3.0 have high variation from 8 to 20. This variation is dependent on the S/N ratio variation from station to station for which the identification of the polarity will depend upon the distance of that station from the earthquake source. Therefore it is influenced by the position of the source within the seismic network. It is also influenced by the sharpness of first motion due to the individual source time function. Using polarities of P-wave first motion recorded at 8 or more stations, the FPSs of 42 recent earthquakes were obtained for the Kangra-Chamba region (zone I in **Figure 5.8**). The program FOCMEC (Snoke *et al.*, 1984) was used to search the parameter space for possible double couple orientations for the focal mechanisms. Also 12 numbers of FPSs of the adjoining region (southeast of Kangra-Chamba region, zone II) are obtained from the data recorded during 2007 to 2008 for comparison of tectonic activities of adjoining regions. The FPSs are obtained for the earthquakes having magnitude range between 2.5 and 5.0 and the focal depth up to 40 km. For quantification of the tectonic regime the variable nature of FPS with focal depth is observed.
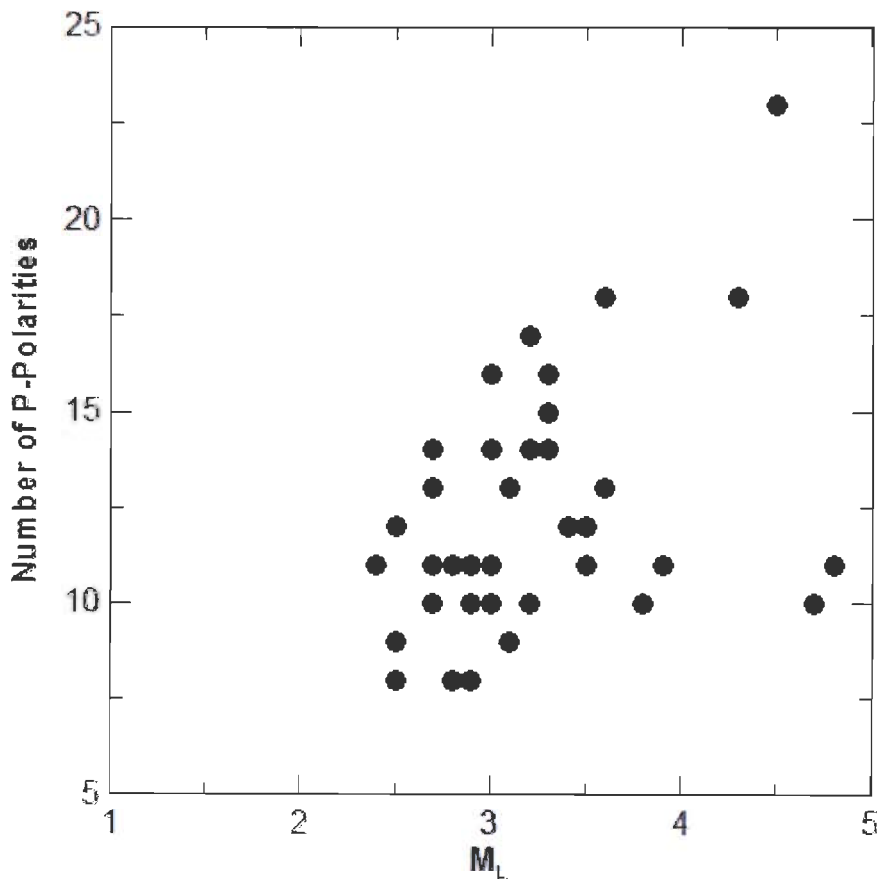
Figure 5.7. The plot showing the number of polarity readings with respect to the size of the earthquake. Generally the number of polarity reading increases with the increase of size.

5.3.1. Reliability of Solutions

It is important to check the reliability of the calculated FPS to quantify the focal mechanisms and stress patterns for the study regions. This reliability mainly depends on the quality of the selected data and the quality of the individual recording station. It also depends on the earth structure, mainly crustal structure for shallow focused earthquakes as the processing and ray path geometry are based on these factors and the recorded waveforms. If the utilized earth model (crustal structure) is not reliable then the calculated focal mechanisms will be incorrect. The number of polarity readings and their representation from all four quadrants around the earthquake source are important. Also these readings should be taken from different distance ranges from the earthquake source. Therefore, the quality of the selected data depends upon the number of used observations and the quality of recorded data. The quality can be improved by increasing the signal-to-noise (S/N) ratio by applying filters, by carefully reading the polarity of first motion readings and by increasing geographical distribution of data points by incorporating as many station data as possible.

150
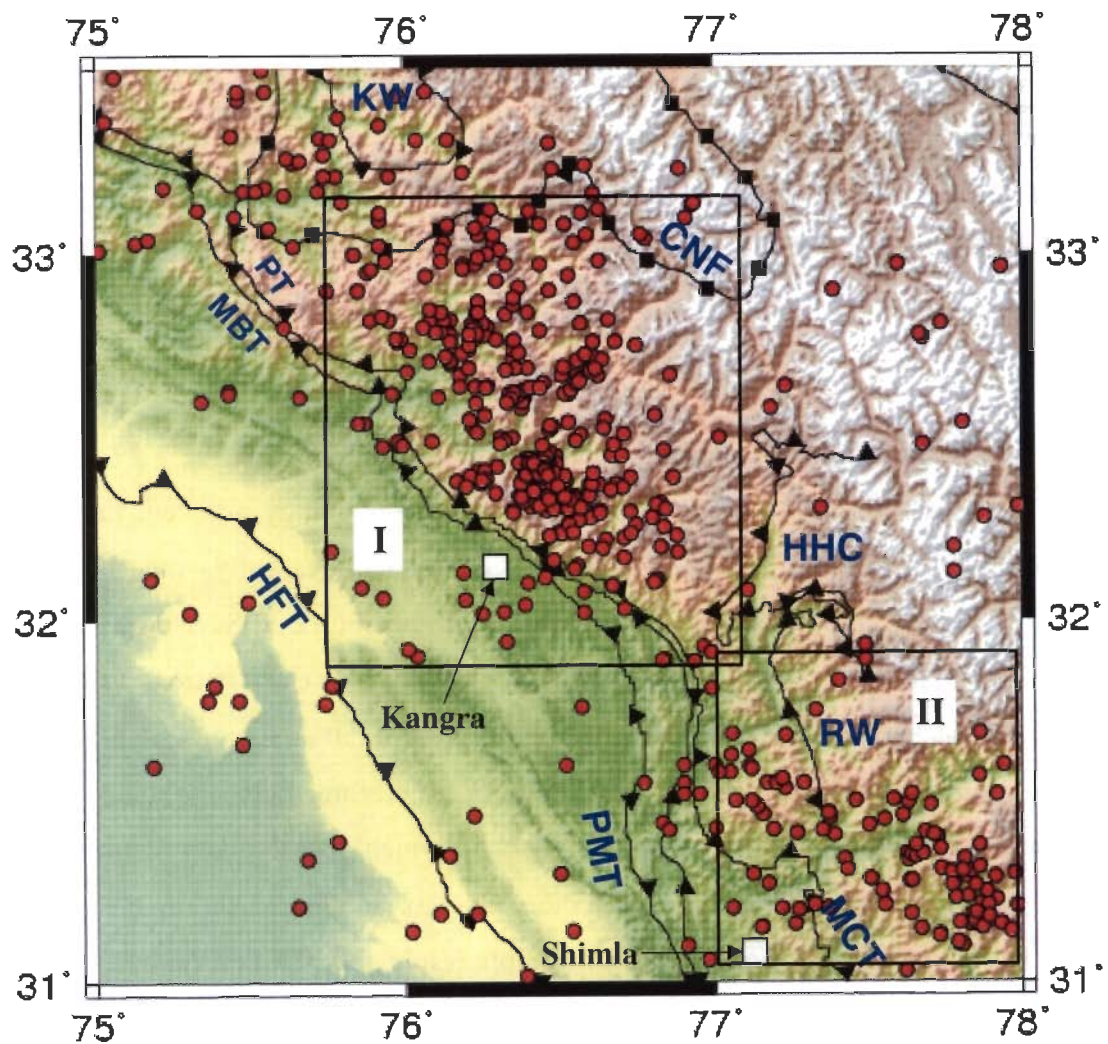
Figure 5.8. The recent seismic activity of the NW Himalaya (2004-2008). The region is divided into two zones; I-Kangra-Chamba region and II-SE zone. HFT: Himalayan Frontal Thrust, MBT: Main Boundary Thrust, MCT: Main Central Thrust, PT: Panjal Thrust, CNF: Chenab Normal Fault, HHC: Higher Himalayan Crystalline, RW: Rampur Window and KW: Kistwar window.

In the present study data of 42 earthquakes of magnitude M>2.5 are selected for the Kangra-Chamba region in the NW Himalaya. Each solution has utilized the data of at least 8 seismic stations. For this data the average, median and maximum numbers of polarities are 11.5, 11 and 23 respectively. It is evident from **Figure 5.7** that the number of polarities increases with the increase of the size (magnitude) of earthquake. However, two big size events (M~5) are also having polarity readings equivalent to average value because during the period of recording of these events few stations were not working

151

and therefore the events were recorded at limited stations. The minimum 1D velocity model obtained in Chapter 3 through joint inversion for the hypocenters and velocity using the data of 172 earthquakes is used for locating these earthquakes. This is the four layer crustal velocity model that has proved to be very useful in minimizing the error in epicenter location and the focal depth of the earthquakes. The take-off angles for all the FPS are determined using this 1D velocity model. The positions of the piercing-points of the seismic rays through the focal sphere are determined from the take-off angle (**Figure 5.2c**).

5.3.2. Data Quality and Error Analysis

The quality of the data depends up on the methodology adopted, procedure followed and the required inputs of the selected data. Presently, the micro- to intermediate magnitude earthquakes data is utilized to obtain the FPSs using P-polarity information along with the maximum amplitude recorded at each station. In case of micro-earthquakes the identification of the polarity is difficult at stations situated away from the source leading to errors in the solution. Therefore, only earthquakes with magnitude ≥ 2.5 are selected to reduce the error in which also the data of only those stations is used where the S/N ratio is more than 6. In this selection the size of earthquakes for existing network that gives reliable results fall between 2.5 and 4.8. The size of the earthquake alone is not important, the location of the earthquake source within the network is also important. If the earthquake source is within the network surrounded by seismic stations from all the sides then the minimum required numbers of polarities are also equally sufficient for small size earthquake as it is found for big size earthquake.

In the present data a detailed analysis has been done for assessing the quality of the solution on the basis of size of earthquake, the location of the epicentre in the network and the number of polarity readings. The solution of three earthquakes those occurred on 05/05/2005, 14/04/2005 and 28/10/2008 are shown in **Figure 5.9** having magnitude 2.5, 4.5 and 3.3 respectively. These earthquakes have 8, 23 and 14 polarity readings respectively indicating the increase of polarity readings with size of earthquake that is generally an overall trend of this data set. This is because S/N level of P-wave increases with the increase of earthquake size. Also it is observed that the amplitude of P-wave is more for higher size earthquake at equivalent distance from the source. However the position of the epicentre of the earthquake is also important as the quality

of solution with 8 numbers of polarities is comparable to that with 14 and 23 number of polarity readings (**Figure 5.9c and 5.9a**). Although the event having only 8 polarities gives many solutions (**Figure 5.9b**), they are similar to each other, i.e. the difference in the solutions are negligibly small.
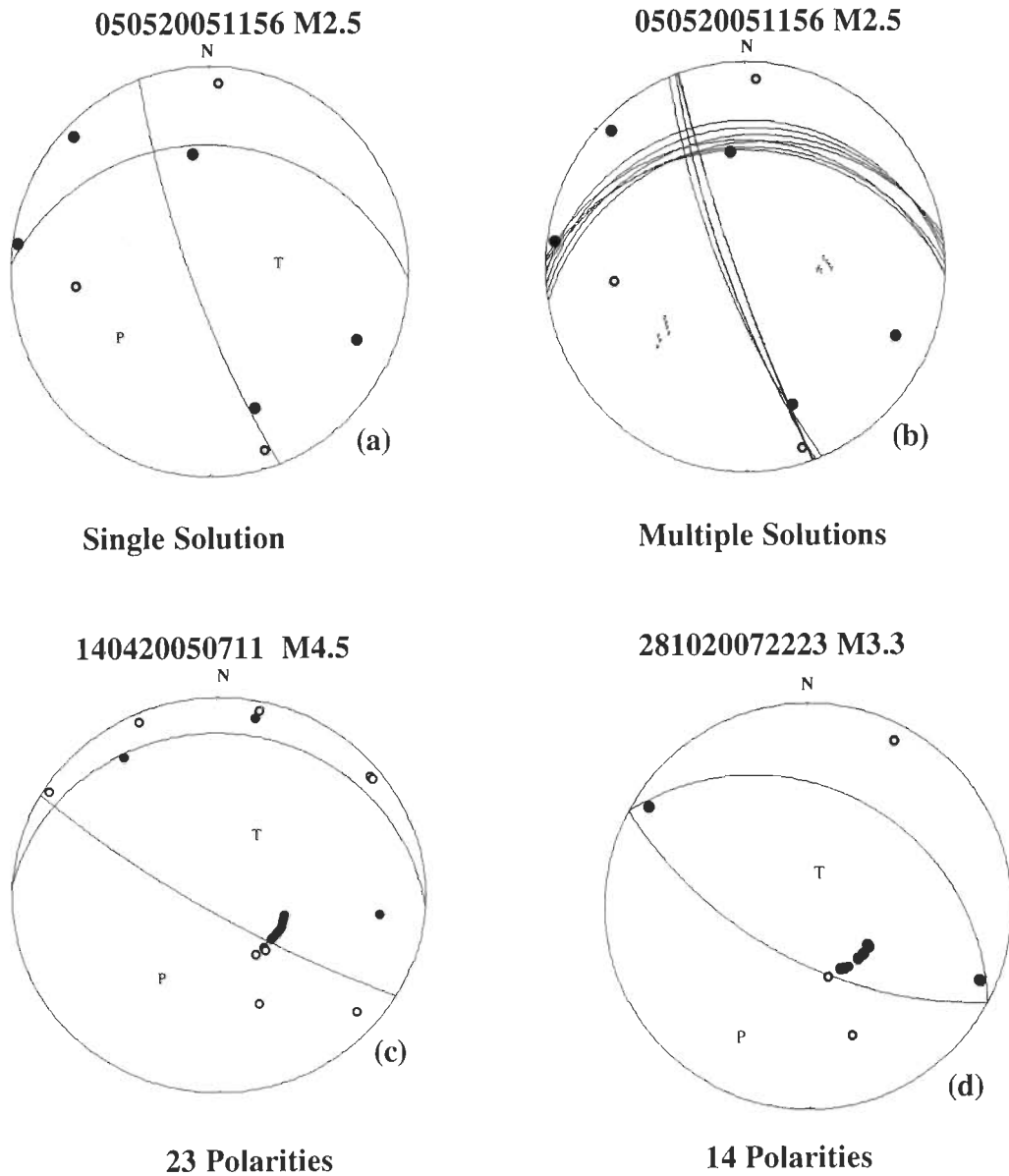
Figure 5.9. Stability of the FPS obtained by different number of polarities. (a) Single solution obtained using minimum 8 polarity readings for M2.5 earthquake. (b) Multiple solutions obtained for the same M2.5 earthquakes using 8 polarities that fit the data. (c) Solution obtained for M4.5 earthquake using 24 polarity readings (d) solution obtained for M3.3 earthquake using 14 polarity readings.

153

5.3.3. Sub-zonation of a Tectonic Regime Based on Focal Mechanism

Nature of deformation at and near the plate boundaries depends on the dominant stress regime. However, there may be small scale fluctuations in the stress regime caused by complex interaction of pre-existing faults. This would lead to variation in nature of faulting and resultant focal mechanism at one part of the plate boundary may modify stress regime of an adjacent region. Based on focal mechanism, a given plate boundary and its adjacent regions may be divided in to a number of sub zones.

The ongoing deformation, direction of deformation and exerted stress on different parts of plate boundaries and adjoining regions can be inferred using GPS observations. The vertical and horizontal velocity of the tectonic plate at the observation point on the surface of the earth can be inferred from such observation. However, GPS observation is more useful for study of deformation of earth's surface only. The subsurface deforming features can be studied using the source information of the earthquakes. During earthquake occurrence sudden deformation takes place due to rupture of the region in the source zone of the earthquake which is useful to describe the subsurface geometry of the tectonic fault. An earthquake releases the increased or stored stress due to ongoing tectonic deformation and thus it is useful in quantifying the stress regimes at different parts of the fault. The amount of released and remaining stress on any part depends upon the size or magnitude of the earthquake and the frequency of occurrence. The extent of region for which the stress is released depends upon ruptured area around earthquake source. The radius of this area varies from few millimeters to few hundreds of kilometers depending on the size of the earthquake.

The Kangra-Chamba and adjoining regions have been studied to observe the variation of stress and tectonic deformation governing different seismotectonic regimes. The results of adjoining parts are included to assess tectonic regimes and its relations with Kangra-Chamba region. The FPSs of recent earthquakes and available past earthquakes are discussed in detail in the following sections. Based on historical and recent seismicity, tectonic setup and focal mechanism distribution the study region was divided in to two subzones (**Figure 5.8**) as denoted by I and II. Kangra-Chamba region is described as zone I and its eastern part Shimla-Dehradun region as zone II. Based on the present analysis, the Kangra-Chamba region also shows variation of focal mechanism in the depth direction as well as in lateral direction. The Results are discussed in the next section.
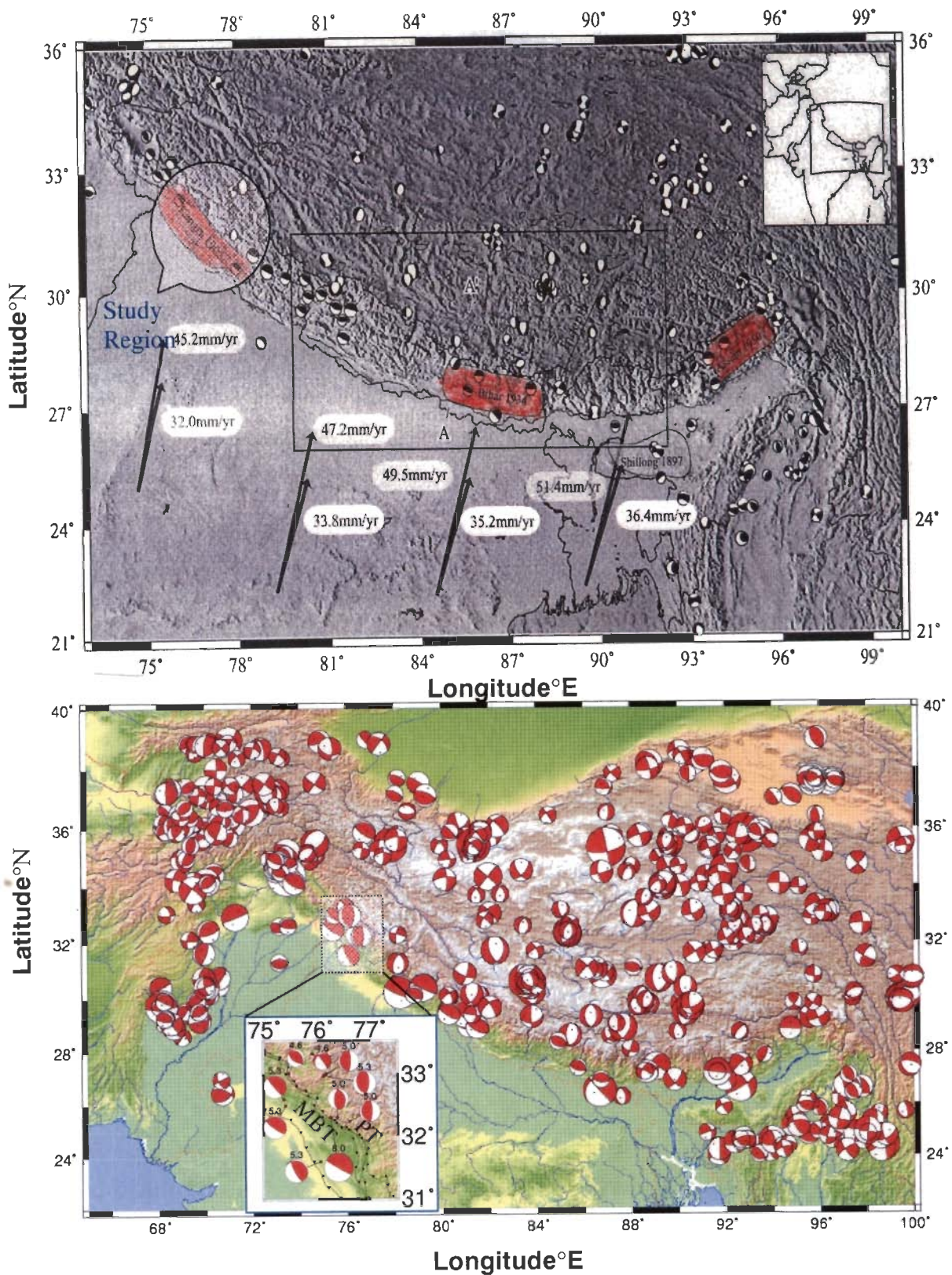
Figure 5.10: (a) Indian plate motion obtained from GPS and deformation obtained from focal mechanisms (after Bettinelli *et al.*, 2006). **(b)** The CMT solutions for the Himalayan region obtained by USGS during 1973 to 2005. Inset shows the solutions for the present study region.

5.4. CASE STUDIES OF PROMINENT EARTHQUAKES OF THE REGION

The historical records of last few centuries, the instrumental records of about last 100 years (**Figure 1.1**) and recent seismicity indicates that large number of earthquakes occur in the Himalayan region. The obtained focal mechanism mainly describes the state of deformation during earthquake occurrence. As shown in **Figure 5.10**, the Himalayan region is basically deformed due to compressive stress regime leading to shortening in northsouth direction which is also verified by the shortening of the surface of the Indian continent using GPS studies (Banerjee and Burgmann, 2002; Bettinelli *et al.*, 2006). The focal mechanisms of the large magnitude earthquakes for the present study region are given in the inset of **Figure 5.10b** and also in **Figures 5.11** and **5.12** for different depth ranges. The focal mechanism of these earthquakes for the Kangra-Chamba and adjoining regions are discussed in the following sections.

5.4.1 The great Kangra earthquake of 1905

Out of four great earthquakes of Himalayan region (1987, 1905, 1934 and 1950), the Kangra earthquake of 4th April, 1905 occurred in the study region and has caused maximum destruction among these earthquakes. No surface faulting was reported during any one of these great earthquakes, however the sub-surface rupture dimensions has been obtained (Molnar and Deng, 1984) using the reported intensities. Based on this criteria the fault length during Kangra earthquake was estimated to be 300 km (Seeber and Armbruster, 1981) using the intensities reported by Middlemiss (1910). As shown in **Figure 2.3**, the intensities during this earthquake aligned NW-SE parallel to the trend of Himalaya. Because this event occurred before the installation of well calibrated long-period seismographs, however using the approximate dimension of the rupture Molar and Deng (1984) has obtained fault orientation during this earthquake. In this work, thrust faulting is obtained striking to 300° and gently dipping plane towards northeast beneath the Himalaya. The evaluated source parameters are given in **Table 5.2** (ps1) and the focal mechanism is plotted in **Figure 5.12** having focal depth 25 km. Similar type of focal mechanism (**Figure 1.4a**) is obtained by CMT solution of USGS during devastating M7.6 Kashmir earthquake of 8th October, 2005 that occurred just northwest to the Kangra-Chamba region. The rupture fault plane of Kashmir earthquake is also dipping towards northeast, however the dip of the fault plane is more as compared to Kangra earthquake given by Molnar and Deng (1984).

156

Table 5.2. Previous Fault Plane solutions obtained in the Kangra-Chamba and adjoining regions.
Abbreviations: Sno – Serial number, dd/mm/yy – day/month/year, hr:min:sec – hour:minute:seconds, Lati – Latitude, Long – Longitude, Dep – Depth, M – Magnitude, PL - Plunge, AZM – Azimuth, ST – Strike, DP – Dip, RK – Rake, SRC - Source

Sno	Date dd/mm/yy	Time hr:min:sec	Lati (°)	Long (°)	Dep (km)	M	Type	Principal Axes						Nodal Plane 1			Nodal Plane 2			SRC
								P-axis		T-axis		N-axis		ST	DP	RK	ST	DP	RK	
								PL	AZM	PL	AZM	PL	AZM							
Ps1	04/04/1905	05:00:00.0	32.30	76.25	15.0	8.0	Mw							300	5	90				9
Ps2	20/02/1967	15:18:39.0	33.63	75.33	20	5.5	Mb	52	0	83	145	7	322	149	88		315	46		1
Ps3	21/02/1967	12:37:43.0	33.65	75.44	20	5.0		15	190	75	10	0	280	100	60		280	30		2
Ps4	11/02/1968	20:38:27	34.2	78.7	24	5.1		37	34	56	238			44*	80		180*	15		3
Ps5	05/11/1968	02:02:45	32.30	76.38	33.0	5.0	Mb	22	248	80	78			340	35	70	348	67	258	8
Ps6	16/01/1973	21:31:25.9	33.29	75.83	39	5.1		3	25	59	290	31	117	87	50		321	55		1
Ps7	24/10/1973	05:23:51	33.1	75.9		5.4		10	82	78	304	4	175	168	36		6	56		3
Ps8	19/01/1975	08:02:02.50	32.455	78.340	37.0	6.8	Ms	76	99	14	272	1	1							5
Ps9	19/01/1975	08:02:02.53	32.455	78.430		6.2	Mb	72	180	14	45	11	312							6
Ps10	19/01/1975	08:01:57.7	32.38	78.49	01	6.2	Mb	85	270	5	90	0	0	360	50		180	40		7
Ps11	19/01/1975	08:12:09.8	31.93	78.52	49	5.1	Mb	64	23	1	114	26	204	47	51		180	50		7
Ps12	29/07/1975	02:40:51.2	32.57	78.49		5.5	Mb	80	120	10	300	0	30	210	55		30	35		7
Ps13	11/12/1975	10:09:50	33.00	76.17	42.0	5.0	Mb	27	256	63	75	0	164	166	16	76	346	74	256	8
Ps14	07/01/1976	00:24:52	32.97	76.12	40.0	5.3	Mb	12	243	80	48			158	34	68	330	56	240	8
Ps15	19/02/1977	06:15:27.10	31.280	78.130	10.0	5.1	Mw	70	153	11	276	16	9	346	37	-118	199	58	-71	HRV
Ps16	14/06/1978	16:12:05	32.24	76.61	7.0	5.0	Mb	26	258	64	78			168	18	78	348	72	258	8
Ps17	23/08/1980	21:36:55.20	32.590	75.370	15.0	5.5	Mw	36	226	54	56	5	319	293	10	63	140	81	95	HRV
Ps18	23/08/1980	21:50:05.70	32.490	75.400	15.0	5.5	Mw	36	226	57	38	2	305	298	12	82	126	78	92	HRV
Ps19	27/02/1983	02:33:06.30	32.290	78.150	10.0	5.2	Mw	19	150	9	57	69	303	192	71	-7	284	83	-160	HRV
Ps20	26/04/1986	07:35:20.00	31.590	76.060	15.0	5.5	Mw	28	235	60	77	10	330	299	19	58	153	74	100	HRV
Ps21	16/07/1986	22:03:12.40	30.480	78.190	15.0	5.4	Mw	33	231	53	79	14	330	278	17	37	152	80	104	HRV
Ps22	19/10/1991	21:23:14.30	30.780	78.774	19.0	6.8	Mw	30	235	38	351	37	118	18	38	172	115	85	52	GS
Ps23	19/10/1991	21:23:21.60	30.220	78.240	15.0	6.8	Mw	32	207	57	14	6	113	317	14	115	112	78	84	HRV
Ps25	28/09/2001	04:37:58.70	33.000	75.460	40.5	4.9	Mw	14	222	74	10	8	130	323	32	105	125	59	81	HRV
Ps26	27/01/2002	22:33:43.40	33.320	75.910	28.8	5.2	Mw	45	215	38	73	20	326	225	20	-11	325	86	-110	HRV

* Dip Direction (deg)

Source (SRC):- 1- Chandra, 1978; 2-Rastogi, 1974; 3-Tabdon and Srivastava, 1975; 4-Gupta ; 4-Choudhary et al., 1974; 5- Khattri et al., 1978; 6-Bangar, 1976; 7-Molnar and Chen, 1983; 8-Dasgupta *et al.*, 1982; 9- Molnar and Deng, 1984; HRV- Harvard; GS: usgs
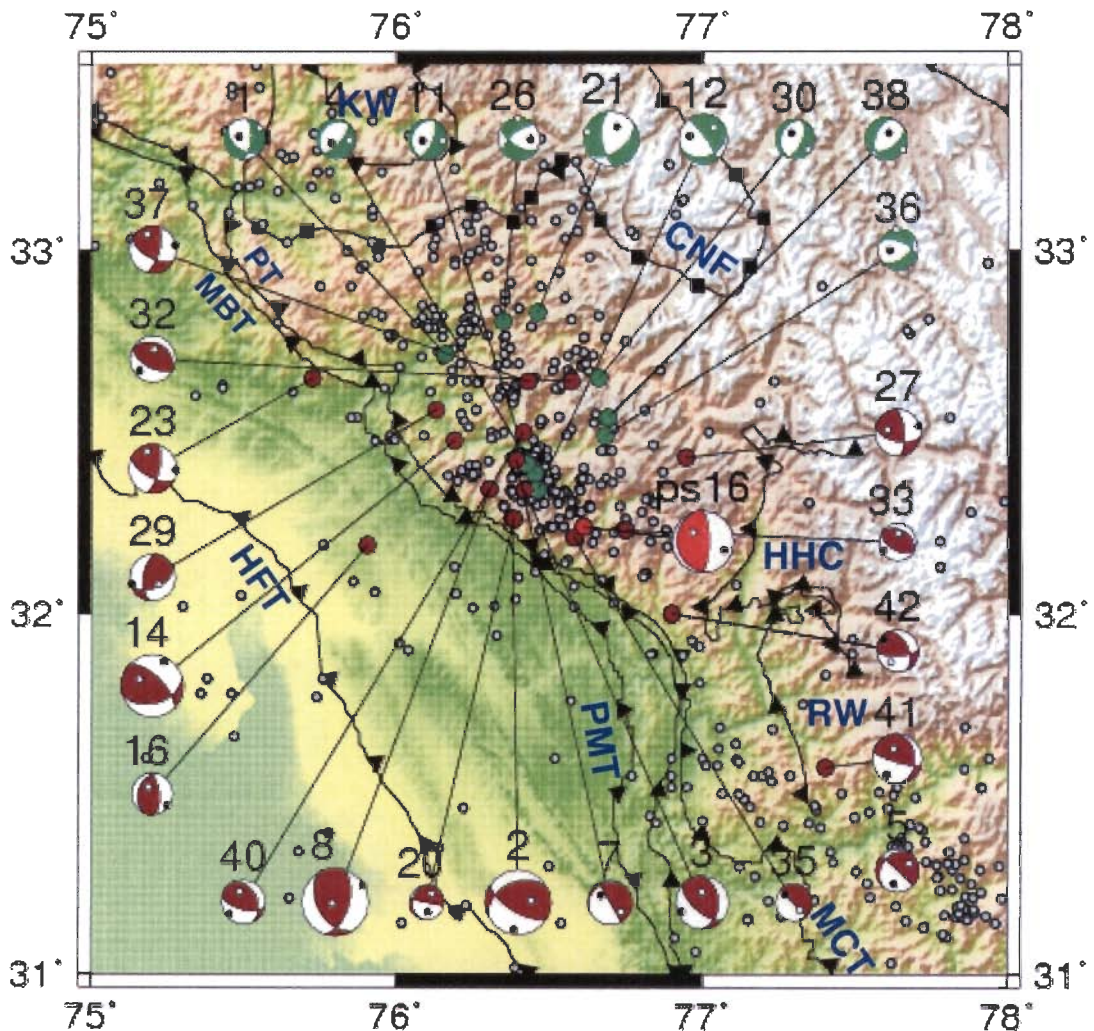
Figure 5.11. FPS obtained for recent data set for earthquake having focal depth less than 10 km. For event Ps16 (M5.1), data was taken from USGS. White and black dots within the beach balls represent T and P axes respectively. Red beach ball is of CMT solution by USGS, maroon beach balls show predominantly thrust mechanism of recent data, whereas green beach balls show predominantly normal faulting mechanism. MBT: Main Boundary Thrust, PT: Panjal Thrust.

5.4.2. The Ladakh Earthquake of 1968

This moderate magnitude (M5.1) earthquake occurred in Ladakh about 180 km northeast of the Zanskar thrust (Tandon and Srivastava, 1975). Along the Indus suture zone, the Zanskar thrust is wedged between the Pamir block and the Spiti Tethyan belt. Here the northern edge of the Indian plate coincides with the Indus suture line and the earthquake was located slightly north of this tectonic boundary. Its focal mechanism shows pure reverse/thrust type motion with one plane steeply dipping to southwest and

the other dipping at low angle to northeast. The later one is taken to be the fault plane (Tandon and Srivastava, 1975)
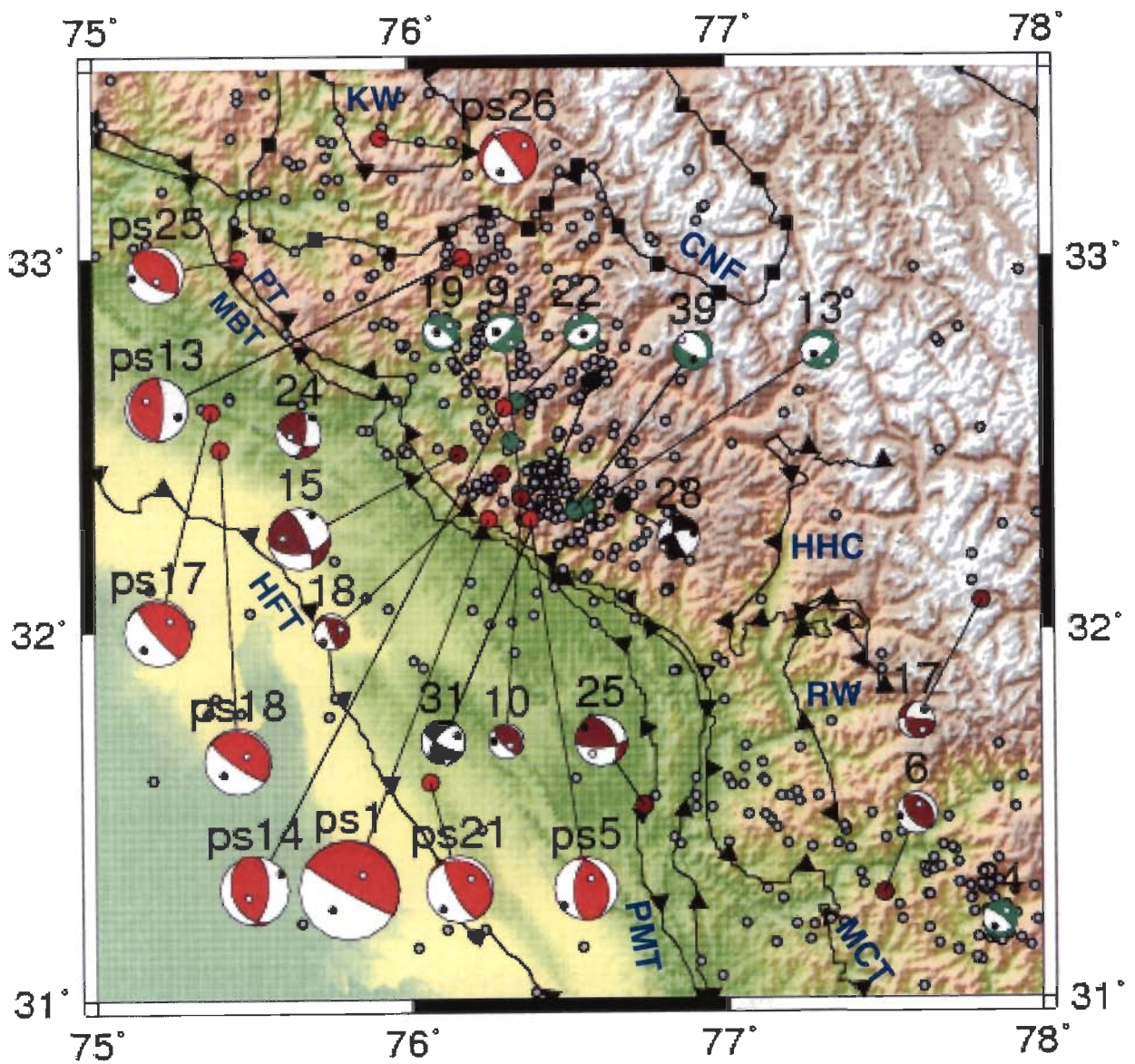
Figure 5.12. FPS obtained for recent data set for earthquake having focal depth more than 10 km. Maroon beach balls show predominantly thrust mechanism, black beach balls are predominantly strike-slip mechanism, whereas green beach balls show predominantly normal faulting mechanism. Red beach balls show predominantly thrust mechanism of CMT solutions obtained for M>5.0 earthquakes by USGS (Table 5.2).

Table 5.3. Source location of the seismic events for which the FPSs are obtained. Abbreviations: Sno – Serial number, dd/mm/yy – day/month/year, hr:min:sec – hour:minute/seconds, Lati – Latitude, Long – Longitude, Dep – Depth, M - Magnitude

Sno	Date dd/mm/yy	Time hr:min:sec	Lati (°)	Long (°)	Dep (km)	M
1	15/10/2004	21:22:31.80	32.716	76.160	2.5	2.9
2	11/11/2004	02:13:41.22	32.263	76.378	5.8	4.7
3	11/11/2004	02:46:47.80	32.340	76.419	6.4	3.8
4	09/12/2004	09:10:22.80	32.386	76.453	8.1	2.8
5	09/01/2005	16:43:32.50	31.295	77.640	2.8	3.1
6	25/02/2005	22:00:22.60	31.287	77.584	20.7	2.9
7	28/02/2005	16:04:45.00	32.422	76.392	8.1	3.2
8	28/02/2005	18:01:58.35	32.343	76.305	4.1	4.8
9	01/03/2005	15:20:02.45	32.369	76.352	12.5	2.7
10	03/03/2005	21:49:57.60	32.358	76.351	11.2	2.5
11	05/03/2005	02:36:09.70	32.413	76.426	5.9	2.8
12	06/03/2005	02:03:30.60	32.342	76.462	9.0	3.5
13	11/03/2005	20:01:58.99	32.336	76.556	15.2	2.7
14	14/04/2005	07:11:25.66	32.477	76.191	5.9	4.5
15	18/04/2005	20:10:33.07	32.476	76.155	12.3	4.3
16	01/05/2005	13:04:14.73	32.189	75.905	8.3	3.0
17	03/05/2005	00:00:08.20	32.077	77.808	39.1	2.5
18	05/05/2005	11:56:54.42	32.419	76.290	11.9	2.5
19	05/05/2005	20:56:37.60	32.485	76.310	9.8	2.5
20	07/05/2005	08:59:14.79	32.260	76.384	0.8	2.5
21	18/06/2005	04:01:43.30	32.740	76.377	6.3	3.9
22	19/06/2005	21:28:59.61	32.617	76.340	15.2	2.5
23	29/03/2006	10:56:48.70	32.647	75.724	7.6	3.5
24	07/07/2006	06:49:29.30	32.530	75.650	15.0	3.2
25	10/12/2006	08:19:28.82	31.526	76.734	23.0	3.6
26	21/12/2006	18:18:26.40	32.805	76.348	5.2	3.0
27	27/12/2006	06:03:45.80	32.430	76.946	8.5	3.3
28	04/10/2007	05:06:44.42	32.339	76.672	11.4	2.9
29	04/10/2007	05:14:16.37	32.564	76.127	6.5	3.3
30	08/10/2007	21:58:17.96	32.647	76.655	5.3	2.8
31	14/10/2007	09:14:53.34	32.668	76.591	15.3	3.1
32	28/10/2007	22:23:54.23	32.659	76.528	2.2	3.3
33	24/01/2008	01:23:24.95	32.246	76.741	7.5	2.7
34	01/02/2008	19:54:11.92	31.209	77.862	12.3	2.5
35	19/02/2008	22:18:37.94	32.206	76.581	0.0	2.7
36	23/02/2008	04:15:29.67	32.492	76.682	0.1	2.9
37	24/03/2008	09:48:34.40	32.639	76.428	1.2	3.4
38	13/04/2008	10:42:01.32	32.530	76.684	2.9	3.0
39	26/08/2008	07:58:10.58	32.320	76.520	10.5	2.7
40	14/09/2008	22:11:29.26	32.499	76.415	6.9	3.2
41	21/10/2008	15:09:07.27	31.575	77.403	6.8	3.6
42	30/12/2008	14:35:40.07	32.000	76.900	1.4	3.0

5.4.3. The Dharamshala Earthquakes of 1968 and 1978

On the basis of P-wave first motion data Srivastava *et al.* (1987) have obtained the focal mechanisms of M5.0 and M5.4 earthquakes that occurred in 1968 and 1978 respectively near the source zone of Kangra earthquake of 1905. The hypocenters of these earthquakes are very close to each other and the obtained focal mechanisms are also similar. The dip directions and dip angles of the nodal planes are N270°±2° and 70°±1° for plane I and N155°±5° and 48°±2° for plane II. The strike direction 270° is given as the direction of the main nodal plane which has been taken based on the trend of isoseismals studied by Kumar *et al.* (1981). They also suggested that this strike direction of nodal plane is well correlated with the local lineament identified by LANDSAT imagery and therefore defined it as the strike direction of main nodal plane. Therefore, the strike of the given main nodal plane is perpendicular to the regional trend of the major tectonic faults. Both the solutions have oblique mechanism, a reverse fault movement along with left-lateral strike slip component.

5.4.4. The Kinnaur Earthquake of 1975

This earthquake of M6.8 occurred on January 1975 and caused extensive damage in the Kinnaur and Lahul-Spiti districts of Himachal Pradesh. This region lies to the northeast of Kangra-Chamba region. The surface rupture due to this earthquake was investigated by Gupta and Virdi (1975); Bhargava *et al.* (1978); Khattri *et al.* (1978); Anand and Jain (1987). They associated the tectonic deformation of the region with Kaurik-Chango fault having strike towards north. The obtained fault-plane solution is of normal type with strike nearly N-S and one nodal plane steeply dipping towards west with a dip of 60°. The isoseismal contours are also elongated with a N-S trend with maximum intensity of VIII around Kaurik. It has caused extension of the region in the E-W direction with the development of step-faults.

5.4.5. The Dharamshala Earthquake of 1986

This earthquake of M5.5 occurred in 1986 and has epicentre in the same zone where two earthquakes reported in the previous sub-section occurred. Kumar and Mahajan (2001) obtained the FPS of this earthquake suggesting oblique reverse fault mechanism as was observed for the previous two earthquakes. However, during this earthquake the strike direction of both the nodal planes is quite different from that of previous two earthquakes obtained by Srivastava *et al.* (1987). Also there is variation in

the dip angles of both the planes. In this case oblique reverse fault mechanism with slight has right lateral strike slip motion was observed. In this case, they have obtained dip direction and dip angle of N223° and 29° respectively for plane I and N325° and 60° for plane II. This deformation was related with northeasterly movement of the Indian plate. The orientation of P-axis in this mechanism is towards south while in case of 1986 and 1978 earthquakes this direction was towards northwest.

5.5. FOCAL MECHANISMS AND TECTONIC STRESS

5.5.1. Regional Focal Mechanisms

The relative motion of the two plates moving in opposite directions is studied extensively using focal mechanism. The nature of faulting in the Himalayan region was studied earlier using the information of only intermediate and big size earthquakes by Molnar *et al.* (1973), Tandon and Srivastava (1975), Ni and Barazangi (1984), Rao *et al.* (2006), Bettinelli *et al.* (2006) and Angelier and Baruah (2009). The focal mechanisms reported by Bettinelli et al. (2006) for the Himalayan and adjoining region are given in **Figure 5.10a** indicating predominately compressive regime leading to thrust faults in the Himalayan region and extensional regime leading to normal fault movement in the Tibetan Plateau. I also collected the CMT solutions which are available at USGS website for the Himalayan and adjoining region. These solutions are given in **Figure 5.10b** for the period of 1973 to 2005 and indicate similar trends. These also include the focal mechanism of M8.0 Kangra earthquake of 1905 obtained by Molnar and Deng (1984). It clearly indicates that the Indian plate is under-thrusting below Asia.

The Kangra-Chamba region (Zone I) always has a dense cluster of micro-earthquake to low magnitude (M ≤ 5.0) earthquakes. The first P-wave polarity motions of 42 earthquakes are utilized to obtain the FPS through the grid search algorithm of Snoke (1984). The location parameters and the obtained FPSs of these earthquakes are given in **Tables 5.3** and **5.4** respectively. The majority of fault plane solutions show thrust movement. However strike slip and normal fault solutions are also present. The present study reveals the variability of focal mechanisms. In order to see whether there is distinctive variation in nature of deformation a region to the southeast of Kangra-Chamba region is selected as part II where the earthquakes of adjoining region are also combined. Further the region is also divided into two depth ranges for observation of variation of the sub-surface deformation in two different depth zones.

5.5.2. Tectonic Stress Regimes

The Kangra-Chamba and its immediate adjoining parts fall within compressive regimes in the Himalayan region. The region has complex tectonic setup compared to rest of the Himalaya indicating the influence of local tectonic faults. The density of the faults is more in this region as many local faults exist. The Siwalik Himalayan region between MBT and HFT is very wide and it contains local thrust faults striking parallel to these major faults. However the LH is very narrow which is marked in the southern side by the MBT and in the north by the PT. The MCT is missing in this part of the Himalaya as most of the LH is covered by the CN that contains the Tethyan overburden tectonically displaced from north and settled here. Due to this tectonic resettlement the MCT has been replaced by other tectonic thrust fault that is named as PT by Thakur (1992). In most part of this region the strike of these major and local thrust faults are nearly NW-SE parallel to the high Himalayan peaks. However in the eastern part of the region these tectonic faults turn to south and the strike direction changes to NS direction.

In the southern part of the region just north of PT, another local thrust exists that has been described as CT by Singh (1994) (**Figure 3.2**). The CN is bounded in the northern side by the CNF leading to extension environment in this part whereas in its southern boundary the region is compressive in nature. The FPS of recent earthquake also shows that tectonically the region is highly complex containing all three types (thrust, normal and strike-slip) of faults along with oblique types. The majority of the earthquakes show thrust/reverse focal mechanism. However, normal faults are also observed. The different types of mechanism are found in different depth levels in a given region as well as in different parts of a given depth level. To correlate them with the local tectonic features I have subdivided the region in to smaller parts in both horizontal and vertical directions.

Table 5.4. Obtained focal mechanisms for Kangra-Chamba region.
Abbreviations: Sno - Serial number, Pol Read – number of polarity readings, Pol Err – number of polarity error, Sol(%) – percent of readings showing wrong polarity, STR – Strike, DIP – Dip, RAK – Rake, SRC - Source

Sno	Pol read	Pol Err	Sol (%)	P-axis		T-axis		B-axis		Main Nodal Plane			Auxiliary Nodal Plane			SRC
				Trend	Plunge	Trend	Plunge	Trend	Plunge	STR	DIP	RAK	STR	DIP	RAK	
1	10	1	90.00	323	56	70	11	167	32	127	44	-140	5	63	-54	WIHG
2	10	1	90.00	189	15	74	57	287	28	245	38	41	121	65	121	WIHG
3	10	0	100.00	240	14	357	62	144	24	131	62	63	359	37	132	WIHG
4	8	1	87.50	132	66	312	24	42	0	221	21	-90	42	69	-90	WIHG
5	9	0	100.00	199	39	68	39	313	27	223	27	0	133	90	117	WIHG
6	8	1	87.50	231	11	51	79	141	0	141	56	90	321	34	90	WIHG
7	10	1	100.00	228	43	72	43	330	12	240	12	0	150	90	102	WIHG
8	11	0	100.00	85	4	345	64	177	25	150	46	54	16	54	121	WIHG
9	10	1	90.00	294	57	151	26	53	17	276	23	-43	48	73	-107	WIHG
10	12	0	100.00	228	25	48	65	138	0	318	20	90	138	70	90	WIHG
11	8	0	100.00	292	67	112	23	22	0	202	22	-90	22	68	-90	WIHG
12	11	1	90.91	263	45	31	32	141	28	67	29	-165	324	82	-61	WIHG
13	11	1	90.91	281	65	158	14	62	20	273	35	-53	51	61	-112	WIHG
14	23	3	86.96	19	11	273	56	116	32	75	44	40	314	63	126	WIHG
15	18	0	100.00	35	13	292	42	138	45	83	50	24	337	71	138	WIHG
16	16	2	87.50	93	15	232	71	0	12	200	32	113	353	61	76	WIHG
17	8	0	100.00	33	26	148	39	281	40	177	40	170	274	83	49	WIHG
18	8	0	100.00	230	30	97	50	335	24	272	27	25	159	79	114	WIHG
19	8	0	100.00	215	66	35	24	125	0	125	21	-90	305	69	-90	WIHG
20	9	0	100.00	172	41	33	41	283	22	192	22	0	102	90	112	WIHG
21	11	0	100.00	29	52	291	6	196	37	55	50	-39	171	61	-133	WIHG
22	9	0	100.00	154	76	334	14	64	0	64	31	-90	244	59	-90	WIHG
23	12	1	91.67	67	4	334	38	163	52	117	61	26	14	68	148	WIHG

24	14	2	85.71	66	5	333	36	164	53	116	59	28	16	64	145	WIHG
25	13	1	92.31	207	11	310	47	107	40	335	48	149	87	67	46	WIHG
26	11	1	90.90	87	45	177	0	267	47	122	60	-35	231	60	-144	WIHG
27	15	2	86.67	50	6	315	41	147	48	355	67	144	101	57	28	WIHG
28	11	1	90.91	115	25	207	6	309	64	159	76	-22	254	68	-165	WIHG
29	16	2	87.50	305	2	39	54	214	36	186	57	46	67	53	137	WIHG
30	11	0	100.00	290	75	110	15	20	0	200	30	-90	20	60	-90	WIHG
31	13	1	92.31	76	31	171	8	274	58	119	75	-29	217	62	-163	WIHG
32	14	2	85.71	208	15	28	75	118	0	118	60	90	298	30	90	WIHG
33	11	0	100.00	208	7	28	83	118	0	118	52	90	298	38	90	WIHG
34	8	0	100.00	238	57	25	29	123	15	307	76	-75	79	21	-135	WIHG
35	13	2	84.62	228	40	44	50	136	2	338	5	112	136	85	88	WIHG
36	11	1	90.91	257	55	353	4	85	35	291	58	-48	51	51	-137	WIHG
37	12	1	91.67	68	4	334	39	162	51	119	61	27	15	67	148	WIHG
38	10	0	100.00	30	69	128	3	219	21	57	51	-63	197	46	-120	WIHG
39	14	1	92.58	358	63	223	20	127	18	341	30	-51	119	67	-110	WIHG
40	17	1	94.12	214	14	331	62	118	24	105	63	63	333	38	132	WIHG
41	18	2	88.89	218	27	344	49	112	28	106	78	61	354	31	156	WIHG
42	14	2	85.71	207	11	309	48	107	40	335	48	149	87	67	46	WIHG

5.5.3. FPSs of Shallow focused earthquakes

The Indian plate is under-thrusting below the Eurasian plate dipping towards north or northeast direction. The boundary between the under-thrusting Indian plate and the overriding Himalayan wedge above it is described as the detachment zone. The depth of this detachment zone increases towards north. The FPS obtained for a small zone of dense cluster of seismic activity supports this concept and hence this data set has been divided into two parts. The solutions above the detachment plane (in the study region it is about 10-12 km below the mean sea level) are separated in one group and the remaining in the other group to observe the variation of mechanism in two depth ranges. In the shallow depth range (maximum depth 10 km), 27 solutions of recent data in the magnitude range of 2.5 to 4.7 is obtained for the investigation. The solutions and the epicentral location of the selected events are shown in **Figure 5.11** along with major tectonic units of the region. These are sallow focused earthquakes located within 10 km of upper crust in the Kangra-Chamba region. The available focal mechanisms of USGS and other previous studies for this part of the Himalayan region are available only for big sized earthquakes (M>5.0). Only the FPS solution of one event in this data set is included from the previous studies shown with bigger size beach ball of red color. This is the event number ps16, whose solution was taken from USGS and given in **Table 5.2.** Only this single event of previous solutions is available for this depth range which has thrust mechanism. One nodal plane of the pure thrust mechanism of this event is dipping to the west and has been considered as the fault plane. The westward dip direction is perpendicular to the trend of the general fault plane solutions and the trend of the Himalaya for this region. The epicentre of this earthquake is very close to the epicentre location of M8.0 Kangra earthquake of 1905. The remaining solutions of this group (shown in **Figure 5.11**) show all possible types of focal mechanisms.

18 of the 27 solutions obtained by me are of oblique types containing thrust/reverse displacement with small component of strike-slip motion in this region. This indicates that the accumulated stress is being released with thrusting of the Indian plate slightly obliquely to the tectonic trend of the area. These solutions are shown with maroon beach balls (size of ball is proportional to magnitude) in **Figure 5.11.** The event numbers mentioned in the figure are same as that given in **Table 5.4.** The thrusting nature of these events can be easily related with the northeast directed dipping thrust faults. These faults are PT, MBT and PMT (**Figure 5.11**). The remaining 9 solutions (36% of the events) show pure normal fault movement or oblique type with a small

strike-slip component along with normal mechanism. These solutions are shown with green beach balls in **Figure 5.11**. Most of these solutions are associated with CNF which causes displacement of CN towards south. CNF is the northern boundary of CN where the hanging wall portion of CN is displaced towards south through normal type of movement. Remaining normal mechanisms are in the region having dense cluster of seismicity in the epicentre zone of great Kangra earthquake of 1905 where both normal and thrust faults are observed. It shows that this portion of high seismicity has complex mechanisms.

5.5.4. FPSs of Deeper Focused Earthquakes

The other data set of earthquakes for the deeper part has 15 FPSs. The epicenter locations of these events are shown in **Figure 5.12** along with tectonic features of the region. In this data set, the solutions of large magnitude (M>5.0) earthquakes obtained by previous workers are 9, the FPS of these are shown in **Figure 5.12** by bigger sized red color beach balls. The beach balls of these events show that 8 out of 9 of them indicate thrust mechanism. Therefore the majority of these solutions are having thrust mechanism in agreement with the tectonic environment of the Himalaya. The main nodal planes of these solutions are dipping towards northeast or to the west direction. The major thrust faults of the region are also dipping towards northeast in most of the part of the study region however in the southeast corner of the region, these thrust faults are rotated and are dipping towards east. Hence in agreement with the tectonic set up of the region the available solutions also show fault planes dipping towards northeast or east direction. One earthquake (event number ps21) is located near the HFT which is an unusual behavior of this region because in the recent seismic data very few events are located near to this event. This event also indicates that the HFT is dipping towards northeast. The remaining single solution for large magnitude earthquake (M>5.0) is of normal type (event number ps26). This event is located to the northern part of the study region. In this part CNF exists. Therefore this solution supports the ongoing extension tectonic deformation in the northern part of study region.

It is clear from **Figure 5.12** that the remaining FPS obtained using the data of present seismic network have equal number of thrust and normal mechanisms in this depth range. 7 solutions out of total 15 that are about 46 percent have thrust type of movement along with some strike-slip component. These solutions are shown with maroon color in **Figure 5.12**, where the solutions of normal mechanism are shown with

167

green color. Normal mechanisms along with some strike-slip movement are 6 in number and 5 of these solutions are located in the region of high cluster of seismicity. The percentage of normal fault mechanism is therefore somewhat higher (40 percent) in this deeper part of the study region. These solutions show anomalous behavior where the tectonic features on the surface are of thrust nature. Kumar *et al.* (2009) too show that the dense cluster of seismic events in this part show different types of focal mechanisms that vary with depth. The possible reason for variation in characteristics of focal mechanism is that two type of convergence is going on at this part of the Himalaya in which the major tectonic features (e.g. PT, MBT) dip to northeast while the other local tectonic features, viz. Rampur Window and the HHC zone in the eastern side dip towards west (**Figure 3.2**). Besides the CNF also introduces extensional features in this part as it may extend to the south up to this region in the deeper depth ranges.

5.5.5. FPSs of Adjoining Southeast Region (zone II)

WIHG is operating a wide seismic network in the NW Himalaya. In this network sufficient numbers of stations are operated in the Kangra-Chamba and adjoining southeastern Garhwal Himalaya. This network shows (**Figure 3.1**), that the recent earthquake activity is concentrated in the central part of NW Himalaya. The seismicity is mostly located to the north of MBT and PT in the Kangra-Chamba region and it is more concentrated along MCT in the adjoining eastern part and Garhwal Himalaya. Data for 12 earthquakes were available for evaluation of FPSs for the adjoining southeastern part of present study region (zone II **Figure 5.8**). It was observed that most of the solutions in this data set are of thrust type along with small strike-slip component (**Figure 5.13**). The magnitude of these events is also in the same range as that of the present data set of the Kangra-Chamba region and only two events contained normal fault type mechanism. Majority of thrust mechanism indicate that the maximum compressive axis is oriented in the E-W to NW-SE direction unlike N-S or NE-SW direction observed for the Kangra-Chamba region (**Figures 5.11 and 5.12**). As shown in **Figure 5.8**, the strike of the major tectonic faults (MBT, PT) to the southeastern direction of Kangra-Chamba region is rotated to nearly NS direction as compared to Kangra-Chamba region where the strike direction is NS-EW. This changing behavior of the tectonic structures may indicate a different pattern in this part as compared to the Kangra-Chamba region. Similar results have been found by P and T axes or stress tensor inversion in the later sections.
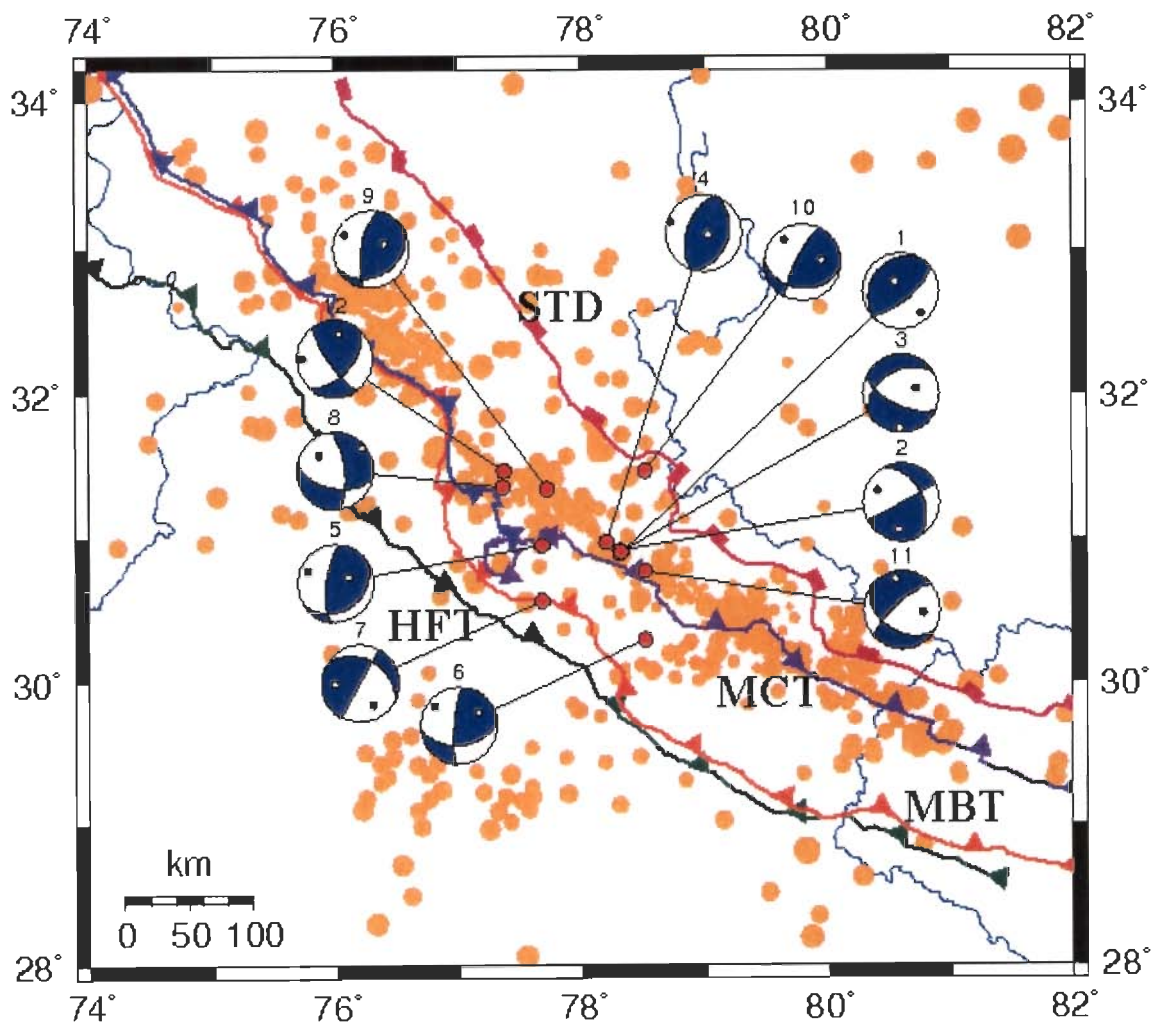
Figure 5.13. FPS obtained for recent data set for the earthquakes located towards southeast of Kangra-Chamba region (zone II).

5.5.6. FMS-Tectonic Linkage

The parameters of the FPSs obtained for 42 earthquakes (**Tables 5.4**) and few bigger size events collected from previous studies (**Table 5.2**) are used to obtain tectonic linkage with seismic activity. These solutions are shown in **Figures 5.11** and **5.12** where each FPS is represented with lower hemisphere equal area projection. It is well known that the stress field orientation near the focus of an earthquake can be constrained using focal mechanism. However, in a rock mass under stress, slip can occur on pre-existing zones of weakness. In such case the estimated stress field orientation may vary from the trend of the prevalent principal stresses of a particular tectonic province. These small scale stress fields are prominent for small size earthquakes having very localized rupture extent. In this case, the FPS of different

169

earthquakes may differ appreciably under a single major stress field of the region. On the basis of FPSs of big size earthquakes it was proposed by several workers (Kumar *et al.,* 1998; Ni and Barazangi, 1984) that along Himalayan arc, the Indian plate is under-thrusting the Tibetan plateau and the maximum compressive stress axis is oriented approximately N-S. However, the local and regional stress parameters may vary significantly (Yeh *et al.,* 1991) in the continental convergence region. As discussed in the previous sections, in the Kangra Chamba region also the rupture propagation during large magnitude earthquake is quite different as compared to smaller events. Therefore like other part of the Himalaya, the Kangra-Chamba region is very complex where majority of deformation is due to thrusting while normal and strike-slip movement also exist in localized part that is more visible while analyzing small magnitude earthquakes.

5.6. REGIONAL STRESS FIELD AND SUBZOING

5.6.1. Stress Tensor Inversion

Tectonic stress of the region can be obtained by inverting the fault plane solutions based on some predefined criteria. Different procedures have been suggested by Gephart and Forsyth (1984), Michael (1984), Angelier (1979) and Rivera and Cisternas (1990). Stress tensor inversion using the data of FPSs is performed with a program known as Focal Mechanism Solution Inversion (FMSI). The program is developed by Gephart and Forsyth (1984) and modified by Gephart (1990) for finding the orientation of the best fitting principal stress tensor to a group of earthquakes by grid search over a range of possible values. In this method the mechanism of the earthquake is regarded as passive indicator of the stress field and using multiple events within limited space and time the uniform stress of the region is obtained. The methodology utilized for stress tensor inversion is based on the assumption that the slip on a fault planes occurs in the direction of the resolved shear stress (Bott, 1959; Meckenzei, 1969). The misfit for each earthquake is defined as the smallest rotation angle about an axis of any orientation that matches with the direction and sense of slip vector. This orientation is associated with either of the obtained nodal planes in agreement with predicted slip of the stress model. The best fitting stress tensor is found by minimizing the average of the individual misfits. The parameters of the stress tensor obtained by this method are the azimuths and plunges of the three principal stresses and a measure of stress magnitude, R, indicating the magnitude ratio of the intermediate principal stress relative to the two extreme ones. R is obtained through the relation

$$R = \frac{\sigma_1 - \sigma_2}{\sigma_1 - \sigma_3} \qquad\qquad \text{-------------- 5.1}$$

Where, σ_1, σ_2 and σ_3 are the greatest, intermediate and least principal stresses respectively. The stress tensor inversion scheme tries to minimize the differences between the slip directions, computed from the stress tensor and the observed slip on each plane of the focal mechanisms. The difference between the computed slip and the observed slip is evaluated through an angular rotation (misfit), F, about an arbitrary axis. Thus, the misfit is the minimum rotation that brings the slip of one of the two nodal planes to match the resolved shear stress tensor. It is calculated through a grid search, systematically varying the orientation and magnitude of the principal stresses. The stress tensor that corresponds to the minimum average rotation angle is assumed to be the best stress tensor for the specific population of focal mechanisms (Kiratzi, 1999). The attitude of maximum principal axis closest to vertical indicates dominant normal type stress regime, minimum stress axis near vertical shows reverse stress regime and intermediate stress axis nearest to vertical indicates strike-slip stress regime. The oblique attitude of minimum and intermediate stress axes highlights the association of reverse and strike-slip or normal and strike-slip faulting types (Kao and Angelier, 2001).

5.6.2. Insight from distributions of P, T and B axes

The deformation of the regions around earthquake source location is provided through geometrical consideration of orientation of individual axis obtained using focal mechanism of earthquakes. The P and T axes reveal the direction of maximum compression and dilatation respectively. Therefore the P and T axes of individual event are studied in the later sections to provide geometrical and mechanical solutions of the region around earthquake source. To estimate the general trend of the stress tensors in Kangra-Chamba region the P, T and B axes orientation of the present data set is shown in compass rose diagram in **Figure 5.14** with 5° of bin while **Figure 5.15** has the similar plot of these events along with FPSs of previous studies (**Table 5.2**). The upper panel gives the distribution of the trend with respect to geographical north and the lower panel the plunges of these axes. The P axes show a preferred trend in NE-SW direction while the T and B-axes do not show any clear trend. The plunges of P-axes are mostly less that 20° while those of T-axes are aligned mostly along 45°. The B axes plunges are less

171

than 45° and mostly are less than 20°. The small value of P-axes plunge indicate that majority of the solutions are thrust type in nature which is in agreement with the results discussed in the previous section. The azimuthal trend of most of the P-axes is the NE-SW direction indicating the thrusting direction of the region that matches with the major tectonic trends of this area. However, almost each bin of this rose diagram has trend of the P-axis that also indicates a complex tectonic behavior. The azimuthal trend of T-axes show more scatter in comparision to P-axes however some trend is towards northwest and another trend is in the northeast. These trends may be due to the effect of CNF in the northern part and a complex tectonic regime in the southeastern part.
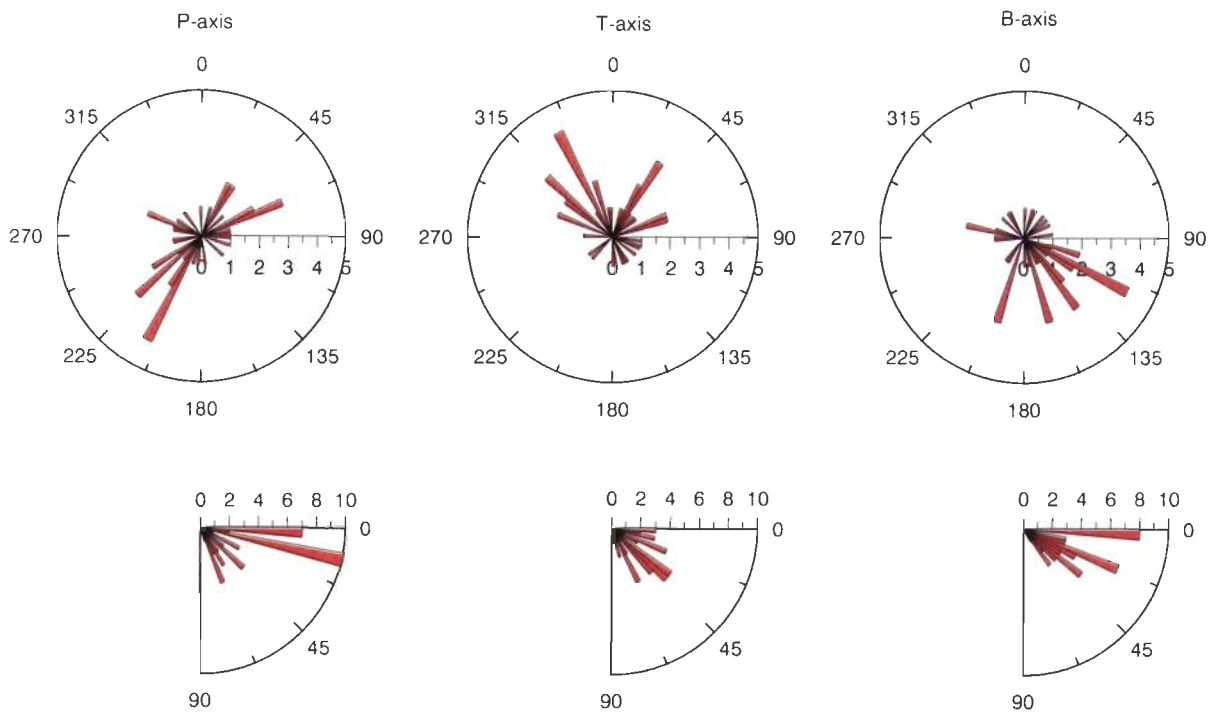
Figure 5.14: Rose diagram showing the distribution of trends (upper row) and plunges (lower row) of P-, T- and B-axes of the recent data set.

Similar analysis was done after combing the available data of bigger size events that is collected from previous studies (**Table 5.2**). As has been discussed in the previous sections and also quite clear from **Figures 5.11** and **5.12** most of the solutions of these events are pure thrust types. The addition of this data has strengthened the concept of thrusting tectonic behavior towards northeastern direction because now the azimuthal trend of most of the P-axes is towards this direction (**Figure 5.15**). Also the percentage of solutions with plunge of P-axes less than 30° is more in case. On the other hand orientation T-axes varies from NE to NW in both the figures (**Figures 5.1**4 and **5.15**).
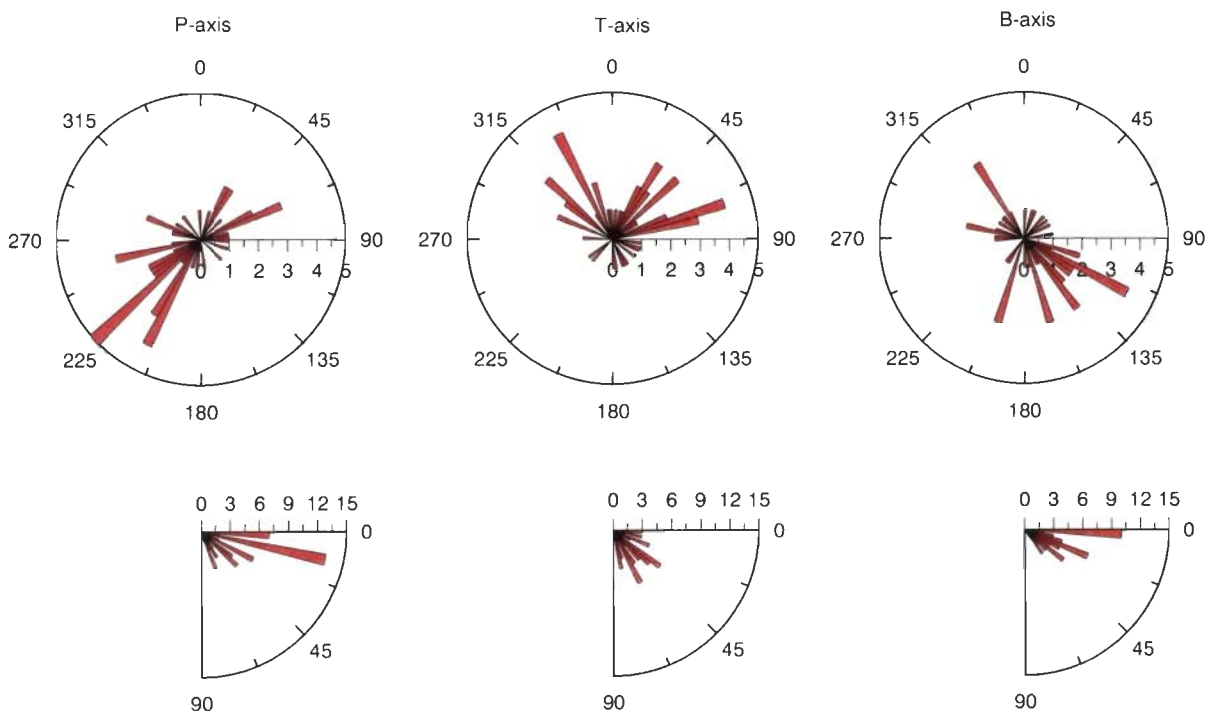
Figure 5.15: Rose diagram showing the distribution of trends (upper row) and plunges (lower row) of P-, T- and B-axes of recent data along with previous solutions.

5.6.3. Seismotectonic Regimes as a Function of Depth

The obtained focal mechanisms reveal diverse type of faulting in the central part of NW Himalaya where the crustal structural diversity is very high. It is remarkable to note that the zone of intense seismicity in the epicentral zone of Kangra earthquake of 1905 show different mechanism at different depths. The reason could be higher level of heterogeneity of tectonic activity in the study region.

Why does significant compression occur in the southern boundary of the Chamba Nappe along the Panjal imbricate zone? The possible reason could be southward movement of CN with respect to down-going Indian plate. Another major feature is the presence of Rampur window in the eastern part and also the HHC thrusting towards west for the northern part of this window. These complex tectonic settings of the region not only produce different focal mechanisms but also are the cause of higher level of seismicity as compared to the adjoining regions. Therefore it is important to analyse the distribution of seismicity and variation of focal mechanisms of this region.

5.6.4. Stress Tensor Results

The combined data of different solutions for a region obtained from the focal mechanism of each event is used to calculate the stress tensor of the region. It is obtained using the focal mechanism stress tensor inversion (FMSI) processing method through grid search technique (Gephart and Forsyth, 1984; Gephart, 1990) for obtaining best fit stress tensor. As per the procedure described in section 5.6.1, the stress tensor inversion is obtained for two data sets, one for the Kangra-Chamba region (Zone I) using 42 events and the second one Zone II (**Figure 5.8**) using data of 12 events. For each group the inversion results satisfies the acceptable criteria of 95% confidence for which the region of the greatest and least principal stress components do not overlap, and the misfits are $\leq 8^o$ for both the groups. The tectonic regime of the region is generalized using the combinations of greatest (S1), intermediate (S2) and least (S3) principal axes of each focal mechanism solution as per the convention of Anderson, 1951 and Zoback, 1992 as shown in **Figure 5.16**. The slip motion during earthquake occurrence is defined through the orientation of the principle stress axes for obtaining the type of mechanism i.e. any one out of thrust/reverse, normal, strike slip and oblique type.

The results of these two groups are plotted in **Figure 5.17** where the plot in part (a) is the result of the data of Kangra-Chamba region and in part (b) for the adjoining southeast region. In these plots, the greatest (σ_1), intermediate (σ_2) and least (σ_3) principal stress axes are represented by S_1, S_2 and S_3 respectively that gives the average values of trend and plunge for each axis. For the Kangra-Chamba region, the inversion is performed using FPS of 42 events solutions that gives average misfit of 5.7° and

stress magnitude value R=0.7. In this solution, the maximum principal stress axis (σ_1) has trend of N56° and plunge of 34°, intermediate principal stress axis σ_2 has trend N148° and plunge of 3° while least principal stress axis σ_3 has trend of N243° and plunge of 56° **(Figure 5.17a).** Therefore the resultant maximum compresive stress is aligned towards northeast in this part of NW Himalaya indicating thrusting tectonics towards northeast.
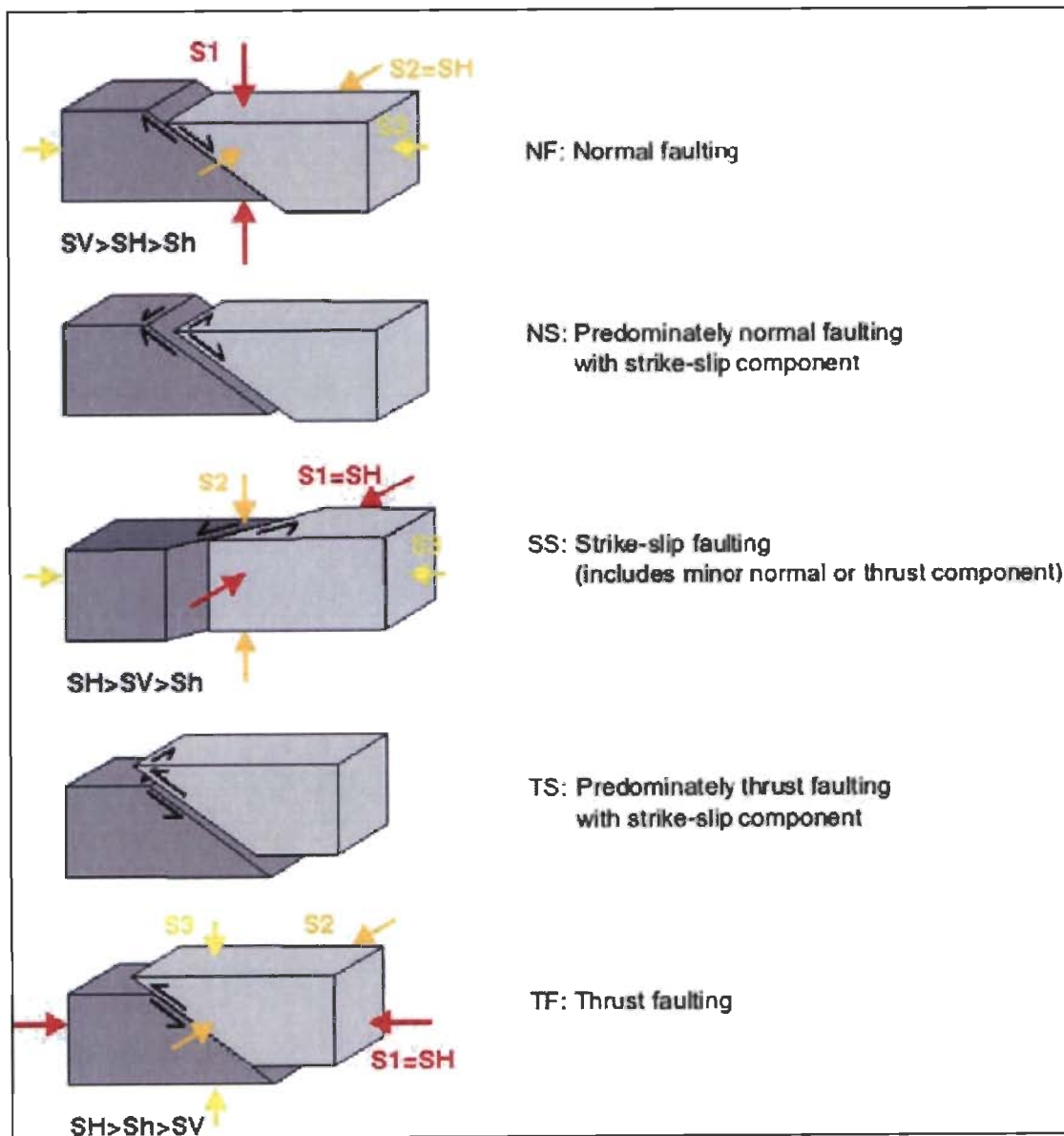
Figure 5.16: General illustration of tectonic regimes through the orientations of the principle stress axes (after Anderson, 1951, and Zoback, 1992)

(a)

R: 0.7
Misfit: 5.7
Phi: 3.7
S1: plunge: 34; trend: 56
S2: plunge: 3; trend: 148
S3: plunge: 56; trend: 243
Faulting style: Thrust

(b)

R: 0.4
Misfit: 7.9
S1: plunge: 14; trend: 282
S2: plunge: 65; trend: 159
S3: plunge: 20; trend: 17
Faulting style: Strike Slip
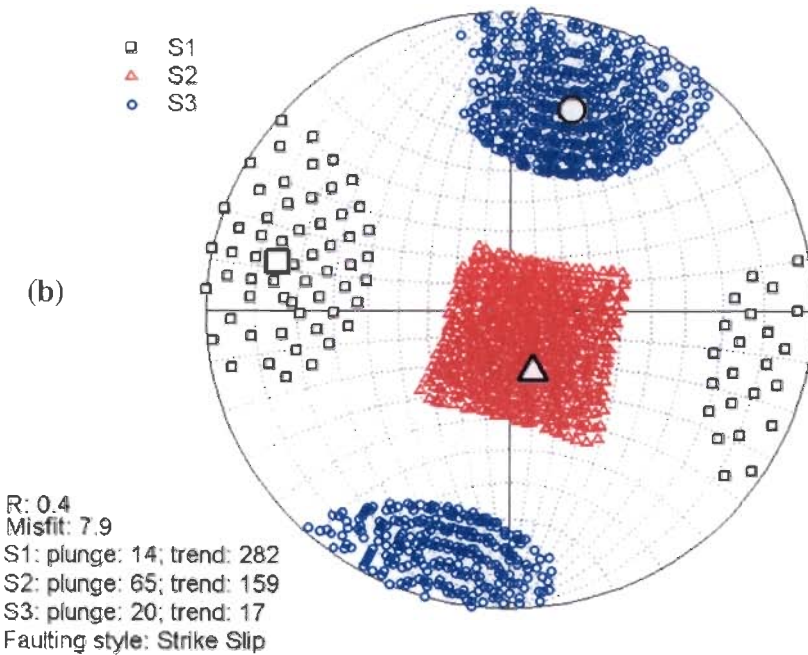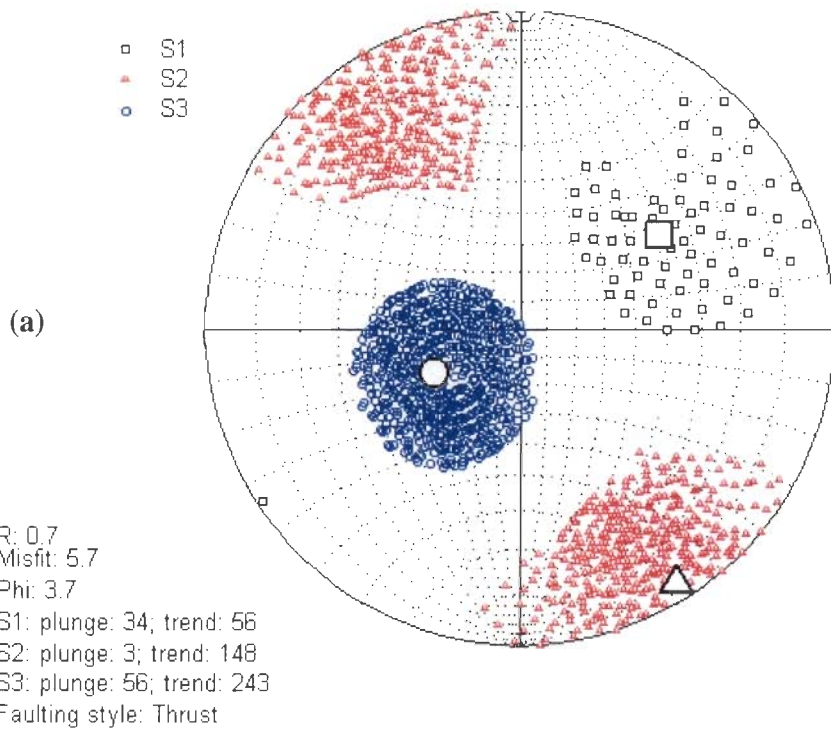
Figure 5.17: Stress Tensor Inversion obtained using FPS for two regions. The 95 percent confidence regions are defined by the black, red and the blue dots for the greatest (S1), intermediate (S2) and least (S3) principal stresses respectively. (a) Inversion for Kangra-Chamba region and (b) for the region lying to southeast of Kangra-Chamba.

The inversion results obtained for Zone II are plotted in Figure 5.17b showing strike–slip type of faulting. The result has a misfit 7.9° and the obtained stress magnitude ratio R is 0.4. The maximum principal stress axis σ_1 has a trend of 282° and have a shallow plunge of 14°, intermediate principal stress (σ_2) trend of 159° and a steep plunge of of 65° while the least principal stress axis (σ_3) has a trend of 17° and a shallow plunge of 20° respectively. The stress regime obtained from this analysis suggests reverse to strike-slip regime.

5.7 DISCUSSION AND CONCLUSION

This chapter divides the Kangra-Chamba and adjoining regions into different zones based on the FPSs and stress tensor inversion. The diversity in mechanism and hence the tectonic activity is observed along horizontal as well as vertical direction. The region also shows variation in seismic activity along both horizontal and vertical direction indicating complex nature of tectonic setup and heterogeneity. These issues are discussed here using the recent earthquake data.

5.7.1. Tectonic Heterogeneities and Stress

The surface topography and geotectonic information reveal that the northwest Himalaya has high level of tectonic heterogeneities produced due to continent convergence. The region contains many thrust/reverse and normal types of faults; the detail information of these faults is given in Chapter 1. It also contains the nappe and window type of geological structures. The present and past FPS data show that in the Kangra-Chamba and its adjoining regions tectonic activity is very complex due to interaction of different tectonic units. The dominant tectonic activity indicates NE directed underthrusting of Indian plate. The southward movement of CN is indicated by occurrence of large number of earthquakes with normal fault type focal mechanism. On top of this in zone II in the eastern part where the RW and the HHC zone are present, thrust type of motion in the westward direction at a large angle to the general trend of the Himalaya is observed.

5.7.2. Consistency between Stress Pattern and Kinematics

The FPS is a useful tool to reveal the relative movement direction of the two parts along tectonic fault that is represented using slip vector information (Molnar et al.,

1973; Mckenzie, 1969). However the direction of the maximum compressive stress obtained through FPS is revealed through the orientation direction of the P-axis or T-
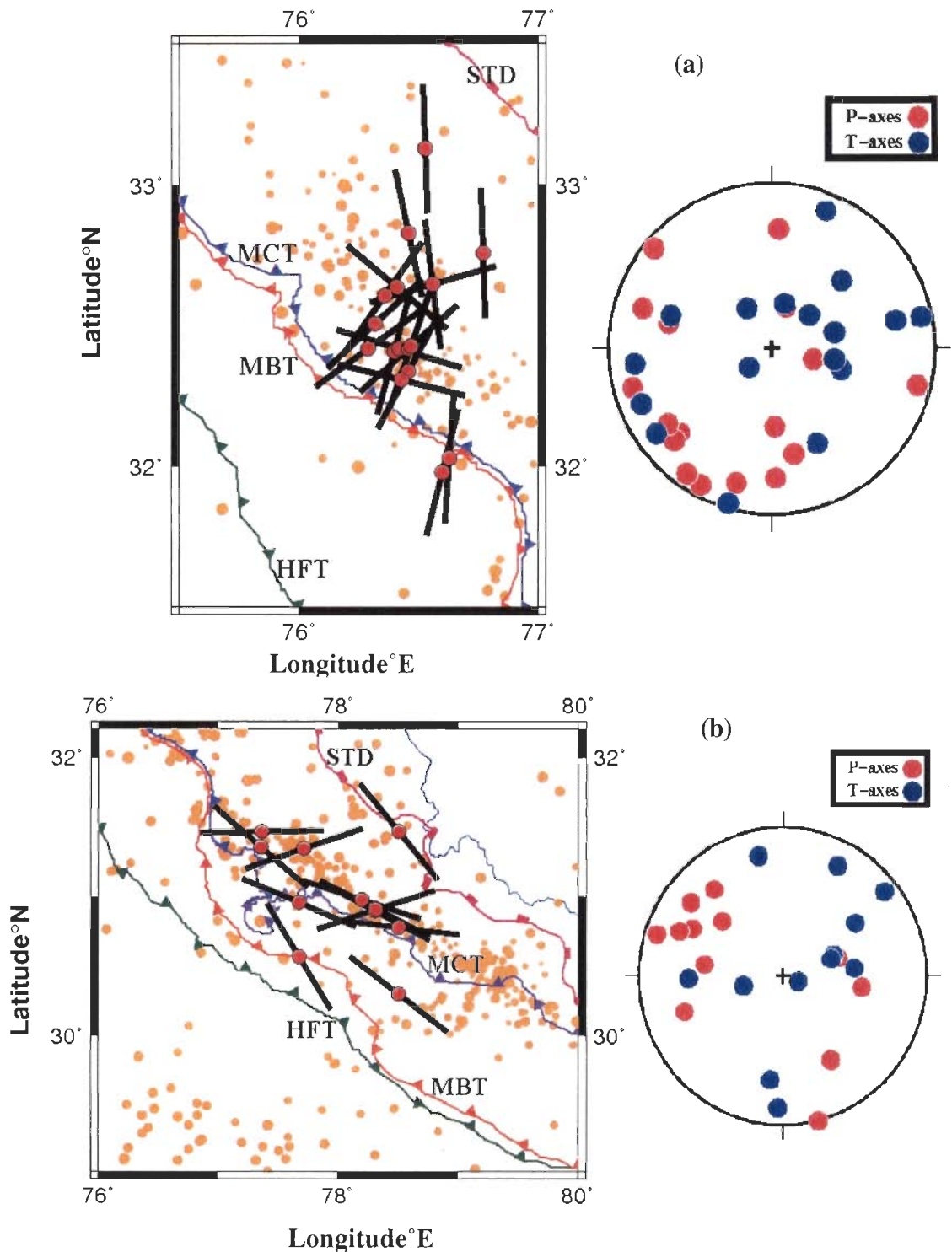
Figure 5.18: Projections of P-T axes using FPS of two regions. (a) Projections for events belonging to Kangra-Chamba region and (b) for events belonging to adjoing southeast region. In the left pannels, the thick black lines with red dots at the centre of each bar represent the direction of P-axes for the respective FPS. The Projection of P-axes (red) and T-axes (blue) on the focal sphere are also shown on the right side.

axis. The P-axis describes the orientation when the solution is thrust/reverse mechanism and T-axis for normal fault movement. Now the total deformation pattern for a region of single seismic regime may be obtained using the information of P-axes or T-axis. I used the trends of P- and T-axes to assess the stress regimes in the Kangra-Chamba (Zone I) and adjoining southeastern part (part II) region (**Figure 5.18**). The projections of these axes were also shown on the focal sphere to identify the difference in these two regimes. In the Kangra-Chamba region the compressive stresses appear to reveal the thrusting regime trending in N-S to NE-SW. However, the adjoining region to its southeast has oblique thrusting movement and the trend of movement is nearly E-W.

The FPSs give the principal compressive stress direction that appears to be aligned nearly perpendicular to the strike of the tectonic fault if it is reverse and normal fault solution. While in case of strike-slip solution, the principle stress axis is parallel to the strike. The oblique type of deformation has resultant stress direction in between to the above mentioned two slip directions. For Himalayan region generally the direction is aligned perpendicular to the tectonic discontinuities of the Himalayan fold belt. In case of Kangra-Chamba region the direction of principal compressive P-axis is towards NE-SW while for the southeastern adjoining region it is quite different. It reveals the geotectonic variation in these two regions.

5.7.3. Tectonic Linkage with Fault Plate Solutions in Kangra-Chamba Region

The obtained fault plane of earthquake rupture and the sense of displacements along the tectonic fault in the source zone of the 1905 Kangra earthquake help in identifying nature of faults. The FPS of 42 earthquakes was obtained using the first polarity motion of the P-wave. The complex tectonic setting of the sector is immediately evident from the fact that varieties of focal mechanisms are operative in the region. The three noted focal mechanisms are: thrust fault mechanism with strike slip component, strike slip movement with thrust component as well as normal motion with strike slip component. However, there is a variation of solutions in different parts but in general this quantification helped to divide the region into two parts, the upper crustal part about 10-12 km thick above the plane of detachment and dipping towards northeast have somewhat different nature compared to the deeper part. The solutions of these two data are shown in **Figures 5.11** (less than 10 km focal depth) and **5.12** (more than 10 km depth) for shallow and deeper sections respetivelly. In the upper section most of the solutions have reverse fault mechanisms and the resultant deformation

179
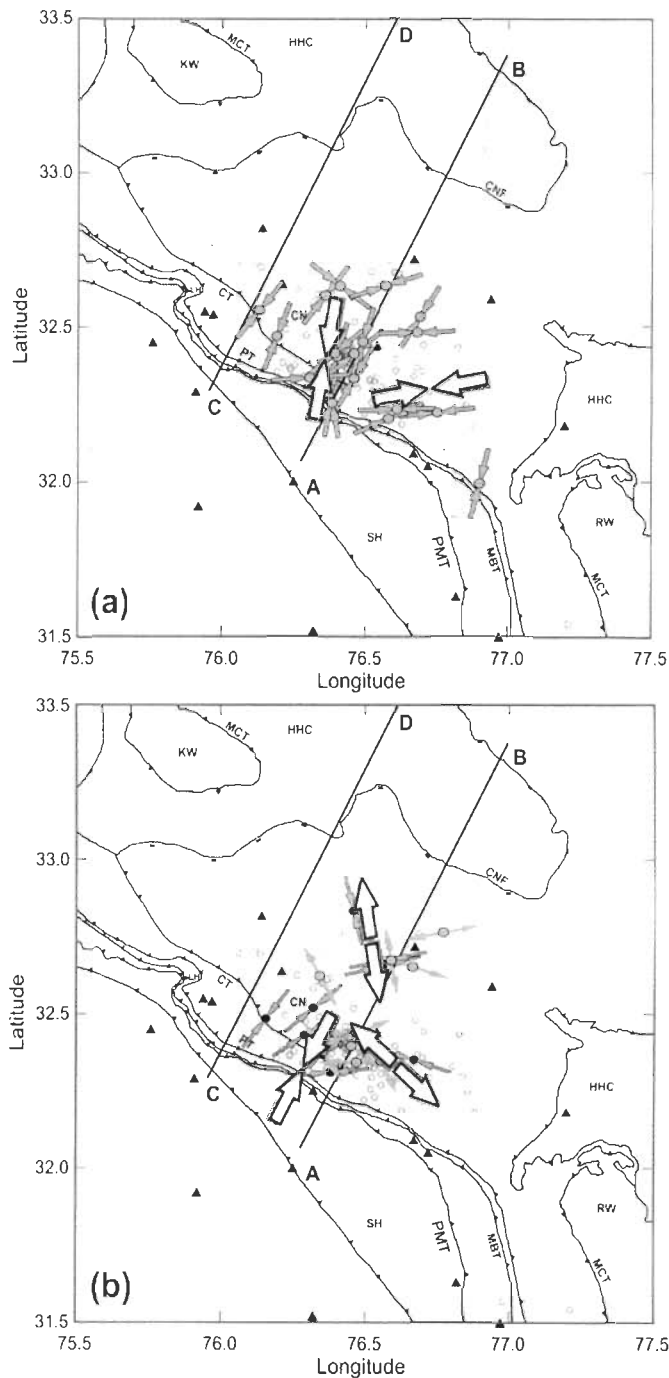
Figure 5.19: Distribution of the epicenters of well-located earthquake using the 3D velocity model, in relation to major tectonic features of the Kangra-Chamba sector of northwest Himalaya. The P- and T-axis obtained for 42 intermediate size earthquakes are denoted with the converging and diverging arrows respectively. Regional compressional and dilatational behavior obtained as the average trend of a small zone is shown with big size arrow. (a) Stress behavior obtained through earthquakes having focal depth < 10 km (b) Stress behavior obtained through earthquakes deeper than 10 km.

180

attained along parts of the tectonic faults near the earthquake source reveals the thrusting nature above the detachment plane that is related with the major tectonic units (MBT, PT shown with compression axis in **Figure 5.19a**) of the region. In addition of this, few solutions have normal fault mechanism and the varied mechanisms clearly depict complex tectonic activity. In the deeper part, the present solutions have reverse and normal fault mechanism in equal proportion where few normal mechanism coincide with CNF indicating NNW-SSE extension with gradual displacement of the CN towards south (**Figure 5.19b**). Few normal mechanisms are also located in the part having dense cluster of seismic activity showing NW-SE extension. Complex interaction of two tectonic environments may be reason of complex mechanisms as well as high seismic activity. The extension tectonics is described with extensional axis (T-axis) in **Figure 5.19b**.

5.8 CONCLUSION

FPSs of bigger earthquakes quantify the nature and plane of movement during the main rupture and are effective tools to constrain the active tectonics generating earthquakes in a given region. Further, the vector decomposition of FPS can help to define the direction and form of principal stresses operative in the given region. Therefore, as an independent mode to constrain the seismotectonic model of the Kangra-Chamba region, FPS of some 42 well located events (RMS value of <0.1s and M>2.5) are computed using P-wave first polarity motions recorded at 8 or more stations with maximum azimuthal station gap of less than 100°. The complex tectonic setting of the sector is immediately evident from the fact that three dominant fault mechanisms noted are: (1) thrust fault mechanism with strike slip component, (2) strike slip movement with thrust component and (3) normal fault motion with strike slip component. The FPSs of the larger earthquakes located at detachment highlight the dominance of the thrust environment. The earthquakes occurring along the shallow sections of the MBT and PT are characterized by thrust mechanisms with varying component of strike slip movement. The decreasing dip of the nodal planes with increasing depths on these thrusts favor the tectonic hypothesis that steeply dipping thrusts near the surface flatten out at depth to merge with the detachment plane zone marking top of the down-going Indian Plate. Similarly, earthquake occurring on the CT support that strain resulting from continued collision are being consumed by reverse-

fault movement on the CT. The normal fault mechanism along the plane which is the subsurface extension of the CNF (**Figure 5.19**) is consistent with the tectonic model which postulates NNW-SSE directed extensional tectonics responsible for the southward displacement of the CN along CNF which is a normal fault. Earthquakes located beneath the detachment zone in a localized cluster NE of the epicenter of the Kangra earthquake are also having normal fault mechanism (**Figures 5.12 and 5.19**). Orientation of P- and T-axes, obtained by tensor decomposition (Gephart and Forsyth, 1984; Gephart, 1990) of the FPS, indicates that stress pattern in the region is governed by two distinct tectonics; while the NE-SW compressive stress prevail over most of the study region at all depths, NNW-SSE to NW-SE extensional stress is also present at depths greater than 10 km.

CHAPTER 6

SOURCE PARAMETER DETERMINATION

6.1. INTRODUCTION

The accumulated stress along tectonic plate boundaries is released through occurrence of earthquakes due to deformation of weak portions of the region along tectonic faults. The area of deformation depends upon the size of the earthquake for one particular region; however the amount of slip, the stress drop and ability to rupture is different for different regions. The rupture area (shown in **Figure 6.1**), amount of slip, stress drop and size of earthquake are the properties of the earthquake source known as earthquake source parameters and can be determined through spectral analysis of waveforms recorded by local seismic network using models of Brune (1970, 1971) and Boatwright (1980). The theoretical investigations and the developed models have established significant relations among the earthquake source spectra, focal mechanism, spectra attenuation relation and characteristics of the tectonic faults. The realize of stress caused by earthquake occurrence is represented by the static stress drop which is defined as the average difference between the initial and final stress levels over the fault plane. The most common estimate of the dynamic stress drop is obtained using the circular model of Brune (1970, 1971). This method has been used in this study using far-field displacement spectrum and the corner frequency.

The micro- and low magnitude earthquake data recorded by local seismic network in the central part of NW Himalaya is used to calculate the earthquake source parameters and develop relations among these parameters for the Kangra-Chamba region. The studies for different regions (Aki, 1969; Brune, 1971) suggest that the spectral contents are influenced by the path-dependent attenuation in the crustal part embodying the earthquake source region. With the analogy of the electro-magnetic wave propagation theory, the attenuation is controlled by the function Q(f) that measure the loss of wave energy for each cycle of vibration along the path of propagated path of the wave in the medium. The Q(f) is the quality factor that is inversely related with the attenuation for frequency 'f'. The Q(f) obtained for this data set and also calculated earlier by others (Kumar et al., 2005; Mukhopadhyay and Tyagi, 2008) are used here to obtain the earthquake source parameters.
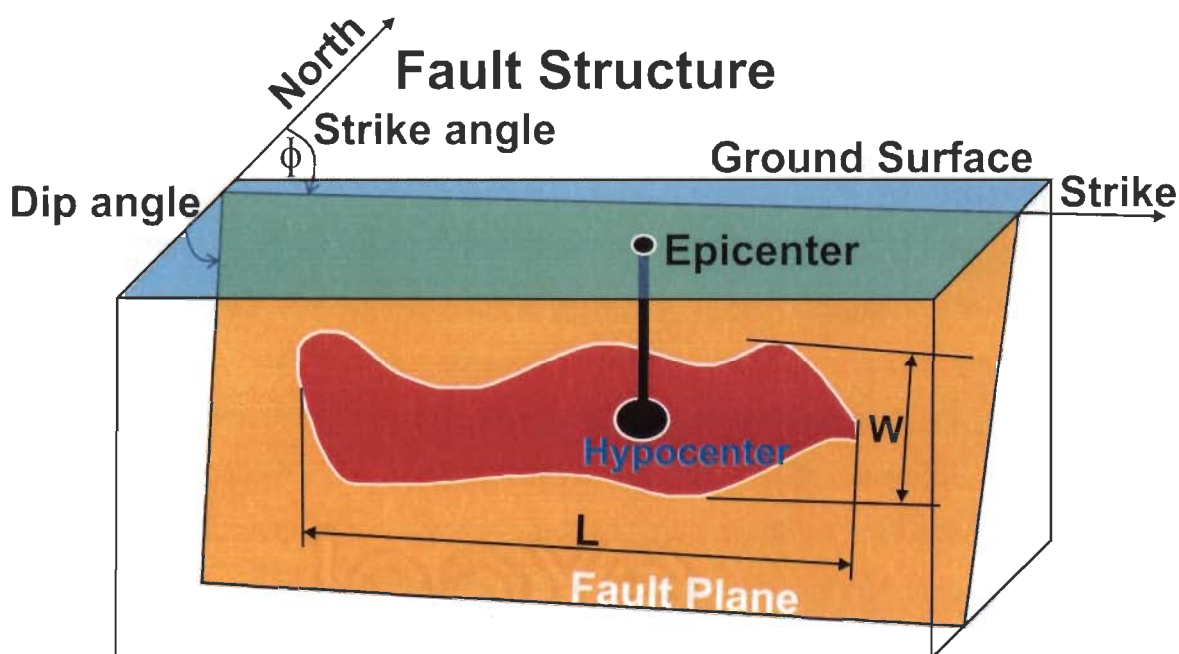
Figure 6.1. Schematic of the rupture fault plane shown with red color around the hypocentre of the earthquake. L and W are the approximate length and width of the fault plane respectively.

The purpose of this study is to examine any possible variation of source scale relation of well-located events for micro- to low magnitude earthquakes of the Kangra-Chamba region of NW Himalaya. Most of the earthquakes recorded during this study and in case of earlier observations (Kayal, 2003; Bhatahcharya and Kayal, 2005), are shallow focused that is restricted to seismogenic zone within the upper 20 km in the Kangra-Chamba and adjoining regions of NW Himalaya. This data set was also utilized to observe the variation of local stress drop with hypocentral depth.

6.2. METHODOLOGY TO CALCULATE DIFFERENT SOURCE PARAMETERS

The dislocation in the region around earthquake source depends upon the effective stress (σ), the rigidity (μ) and the shear wave velocity of the medium. This dislocation or the source geometry in the earthquake hypocentre zone can be characterized through near- and far-field source spectrum of displacements. The source geometry is obtained by converting the displacement into different types of functions. Aki (1968) represented dislocation as step function for near-source and Haskell (1969)

represented it as ramp function. According to Brune (1970), the near field displacement is given by

$$D(t) = \frac{\sigma\beta\tau(1 - e^{-t/\tau})}{\mu}$$ ---------------- 6.1

Where β, is the shear wave velocity and τ is of the order of dimension of the fault divided by the shear-wave velocity. The corresponding spectrum is

$$\Omega(\omega) = \frac{\sigma\beta}{\mu\omega(\omega^2 + \tau^{-2})^{1/2}}$$ ---------------- 6.2

Based on these assumptions, the rms average far-field spectrum is given by

$$\langle\Omega(\omega)\rangle = \langle\mathfrak{R}_{\theta\phi}\rangle\frac{\sigma\beta}{\mu}\frac{r}{R}F(\varepsilon)\frac{1}{\omega^2 + \alpha^2}$$ ---------------- 6.3

Where, $\langle\mathfrak{R}_{\theta\phi}\rangle$ is the rms average of the radiation pattern; r is the radius of an equivalent circular dislocation surface and R is the distance of the source from the recording site.

At distances beyond a few fault lengths, far-field effects dominate for which the source parameters are determined assuming source as a single point. Brune modeled the far-field displacement spectrum to give displacement of two blocks assuming the deformation region of circular dimension. Based on the study of Brune's (1970) circular model, the deduced source parameters are corner frequency, seismic moment, source radius and stress drop.

6.2.1. Calculation of the Spectra

Spectra of S-wave (all three components) recorded at stations of the Kangra-Chamba seismic network where installed digital instruments (shown with blue color huts in **Figure 3.2**) were used to obtain the source parameter of each earthquake. The seismic data on these stations is being recorded at a rate of 100 samples per second. Therefore, using the criteria of nyquist frequency, the spectra from natural frequency of the sensor to 50 Hz could be utilized for characterization of earthquake sources. The

185

spectra of these frequency ranges are corrected for the instrument response to obtain the required displacement spectrum for each event. The amplitude and phase spectra response of the CMG-3T broadband sensor of GURALP attached with REF TEK data recorder are shown in **Figure 6.2a** and CMG-40T broadband sensor of GURALP attached with data recorder of GURALP are shown in **Figure 6.2b**. Using this, in the frequency domain the total system response is removed from the recorded data to compute the displacement spectra as per **equations 6.1** to **6.3** given above. Then the displacement corrected spectra were used for further analysis to obtain the source parameters. The following parameters are obtained using the recorded spectra.

6.2.2. Corner Frequency (f_0)

The frequency at the intersection point of the asymptotes of low frequency and the high frequency portions of the displacement spectrum define the corner frequency. The amplitude of the displacement spectrum at a frequency less than corner frequency is constant while at higher frequency its decay is proportional to a frequency in the range of $f^{1.5}$ and $f^{3.0}$ (Haskell, 1966; Madariaga, 1976, 1978; Hanks, 1979; Andrews, 1986; Brune et al., 1986; Frankel, 1991; Hough and Seeber, 1991). In this case the asymptote point of low and high frequency portions of waveform displacement spectrum is described as the corner frequency that is estimated from the low-frequency level Ω of **equations 6.2** and **6.3** by relation

$$A(f) = \frac{\Omega}{1 + (f / fc)\gamma}$$ ---------------- 6.4

where, fc is the corner frequency and γ is the asymptotic high-frequency spectral decay exponent. γ varies from 1.5 to 3.0 and usually found to be about 2.0.

Corner frequency decreases with increasing earthquake size. Maximum energy is released around the corner frequency because at this frequency the ground velocity is highest. Magnitude of an earthquake is the measure of energy released and thus it strongly depends upon the position of the corner frequency in the source spectrum.

6.2.3. Seismic Moment (M_0)

The strength of a seismic shear source is measured through the scalar static seismic moment that is related to the source dimension through the relation

$$M_0 = \mu \, D \, A$$ ---------------- 6.5
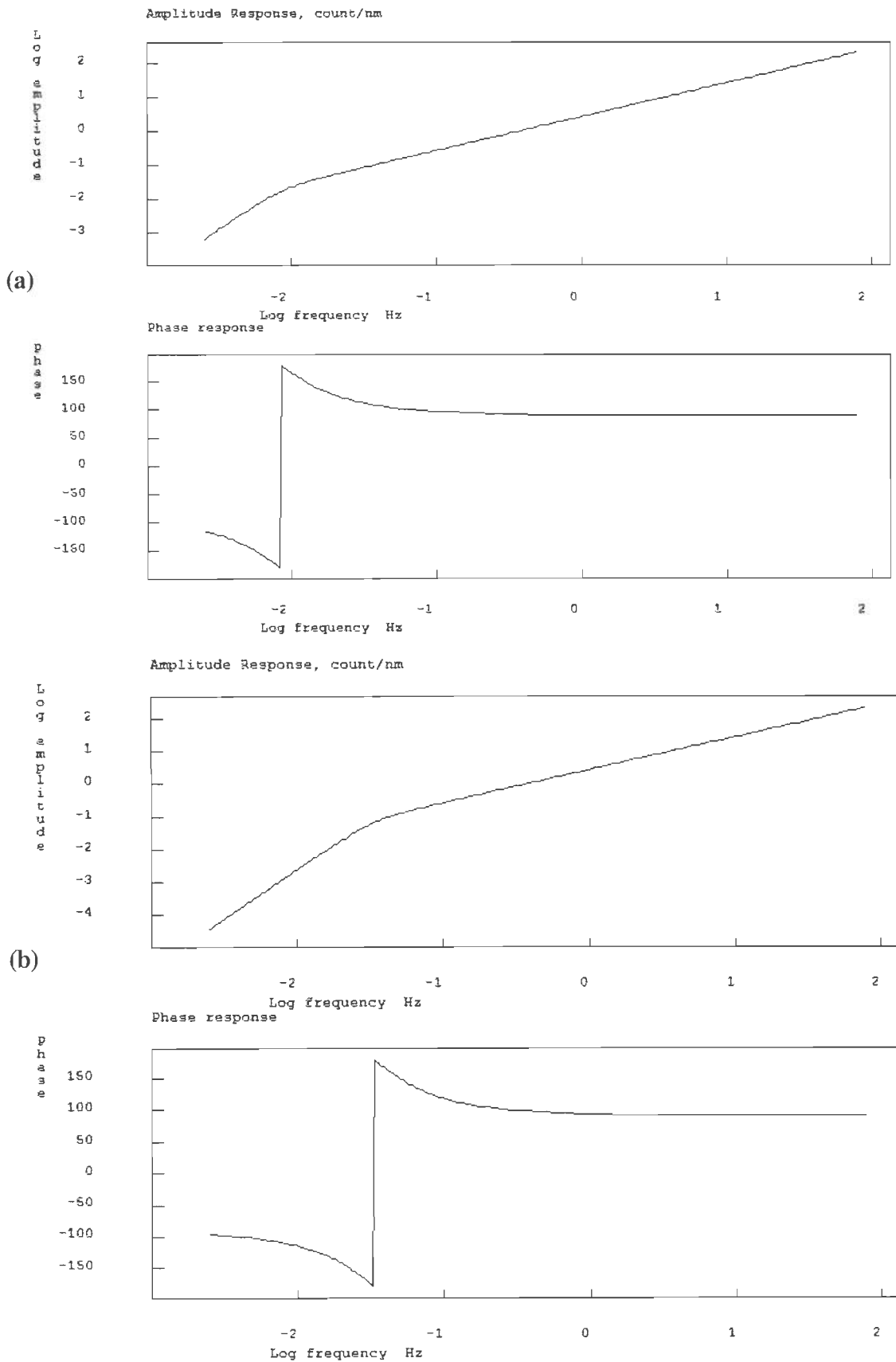
Figure 6.2. The amplitude and phase response of the two digital seismograph systems used in the Kangra-Chamba region (a) CMG-3T broadband sensor and REFTEK data acquisition system (b) CMG-40T broadband sensor and GURALP data acquisition system.

187

where, D is the average final static displacement across the rupture and A is the area of the surface of the rupture region around earthquake source. Although schematically an earthquake source is represented in roughly a rectangular form representing a portion of a fault on which slip has occurred, giving rise to the earthquake (**Figure 6.1**), however for calculation of the source parameters mostly the source is represented as a circular area according to the model proposed by Brune (1970). In reality the shape of the source could be irregular, which is approximated by a rectangular shape (**Figure 6.1**) or circular shape for making the calculations easier (Brune, 1970).

Kanamori (1977) has evaluated the strength of seismic moment that depends upon the stress drop assuming a constant value of $\Delta\sigma/\mu$. The M_0 calculated using above relation can be quantified according to the size of the surface rupture taking average displacement across the fault. The seismic moment is evaluated from the asymptote of low frequency earthquake motion, estimated from the low-frequency level Ω (calculated through **equations 6.2 to 6.4**) of the far-field displacement spectrum A(f). This seismic moment is measured from displacement spectrum amplitude through the relation

$$M_0 = \frac{4\pi G(r)\rho V^3 \Omega(\omega)}{\Re_{\theta\phi}} \qquad \text{---------------- 6.6}$$

where M_0 – seismic moment obtained in dyne-cm; ρ - average density of the rock; V – velocity of the body wave (P or S) around the source; $\Re_{\theta\phi}$ - radiation effect of the seismic source (0.52 and 0.63 for P- and S-waves, respectively and $\Omega(\omega)$ - low frequency amplitude of the displacement spectrum of the wave (P or S) corrected for the instrument response and the wave propagation effects of the earth medium. G(r) is the geometrical spreading effect that depends upon the distance between source and station and compensated for different distances based on the work of Herrmann and Kijko (1983) through the relation given below

$$G(r) = \begin{cases} r & r \le r_0 \\ (r_0 r)^{1/2} & r > r_0 \end{cases} \qquad \text{---------------- 6.7}$$

where, r_0 is the constant value of the medium around source described as the distance between source and recording station after which the geometrical spreading becomes less severe owing to surface wave arrivals. This value is estimated as 100 km by Herrmann and Kijko (1983).

6.2.4. Source Radius (R)

For dislocation fault geometry, Brune (1970) assumed that motion on the circular fault occurred with instantaneous stress release at the time of occurrence of the earthquake. The dimension of earthquake source is highly model dependent and its estimation is related to the accuracy of corner frequency determination from far field displacement spectra owing to the attenuation characteristic of high frequency perturbations. The radius of the ruptured circular fault is related to the velocity of the wave around the source and the corner frequency obtained from displacement spectra. The radius is obtained from these parameters assuming circular source model of Sato and Hirasawa (1973) as

$$R = \frac{KVs}{2\pi f_0} \qquad \text{--------------- 6.8}$$

Where K is a constant value of 2.34 based on Brune's circular fault model, Vs is the S wave velocity around the source.

The radius of circular fault model can also be related to the seismic moment (M_0) and the stress drop ($\Delta\sigma$) through the relation

$$R^3 = \frac{M_0}{16\Delta\sigma} \qquad \text{--------------- 6.9}$$

It is observed that the source radius is proportional to the size of the earthquake so that it increases with increase of seismic moment. Therefore, estimated stress drop based on **relation 6.9** should be constant as per the documentation by Kanamori and Anderson (1975) and Scholz (1990) that stress drop is "approximately constant" for earthquakes of all types and sizes.

6.2.5. Static Stress Drop

The stress drop is the difference between the state of stress at a point on the fault before and after rupture. This stress drop can vary with in the fault and the static stress drop is the integrated value of stress drop over total fault area divided by that area. The

static stress drop for a rectangular fault area with length L, width W and average displacement D is given by

$$\Delta\sigma = C\mu D/Lc \qquad\qquad \text{--------------- } 6.10$$

Where, Lc is a characteristic rupture dimension that relates the stress drop with the seismic moment and the source radius. It is measured as an instantaneous stress release from a circular crack/fault of radius R through Brune's source model. In this model a complete stress release is assumed approximating it as average static stress drop. On regional basis, the stress drop is independent of the source size (Kanamori and Anderson, 1975; Hanks, 1977; Hough, 1996) and is given by

$$\Delta\sigma = 7M_0/16R^3 \qquad\qquad \text{--------------- } 6.11$$

According to Brune's (1970) circular fault model, the effective stress refers to the difference between the applied and frictional stress opposing the rupture. Based on this model the source size increases with the increase of seismic moment. Therefore, on the basis of above relation, it is generally accepted that the seismic stress drops are relatively uniform over a wide magnitude range for one region.

The constant stress drop scaling law, $M_0 \propto f^3$ gives an indication of self-similar behavior of earthquakes over all magnitude range. However, some studies on source parameters for small magnitude earthquakes suggest a break-down in earthquake self-similarity behavior observing increase in the stress drop with the increase in seismic moment for micro-earthquakes (Chouet *et al.*, 1978; Fletcher *et al.*, 1986; Feltcher *et al.*, 1987; Garcia *et al.*, 2004). It is also suggested that the apparent breakdown at low magnitudes does not agree with predicted models and is simply an artifact of severe attenuation of the high frequency energy obscuring the corner frequency in the uppermost few kilometers of the earth's crust (Anderson and Hough, 1984).

The variation of the stress drop for crustal earthquakes depends upon attenuation characteristic of high-frequency energy. The local attenuation relations are very useful to estimate the seismic moment and the stress drop pattern on regional basis. It has been also observed that there is a difference in stress drop for earthquakes from stable continental intraplate region and those obtained from near plate margins, which was

190

observed in the Indian continent by Singh *et al.*, (1999, 2007). This discrepancy is considered to be caused by variation of release of the seismic energy at two different regions due to variation in the development of stress regime. Several studies have shown that intraplate earthquakes have higher stress drop with average value of 100 bar compared to interplate earthquakes whose average stress drop value is 30 bar (Kanamori and Anderson, 1975). The low stress drop near the plate boundary is related to high levels of earthquake activity with typically weak fault rheology. The interval of two earthquakes with similar magnitude is short in interplate region compared to in the intraplate region giving rise to accumulation of less stress energy in the former case. However, the effect of fault healing over time is more apparent in intraplate region where less numbers of seismic events occur. Therefore, initiation of rupture on new growth surface or healed fault asperities in stable regions gives rise to higher levels of stress release. Earthquakes in these regions possess relatively higher frequency ground motion and a short rupture duration which suggests a relatively small rupture size (Stork and Ito, 2004).

6.2.6. Average Dislocation (D) Along the Rupture Surface

The amount of dislocation can be measured through the displacement between two points on either side of the fault. The dislocation vary from one end to another end of the fault and the average dislocation is given by

$$D = \frac{M_0}{\pi R^2 \rho V^2} \qquad \text{---------------- 6.12}$$

6.2.7. Seismic Moment Magnitude

The rupture dimensions of earthquake source depend upon the released energy. Therefore the size of the earthquake can also be estimated using above mentioned earthquake source parameters. The earthquake size obtained through these parameters is described as seismic moment magnitude (M_W) as it is directly related to the seismic moment calculated through **relation 6.6** using displacement spectrum. Therefore, the M_W obtained here is the scaling of the earthquake size based on Brune's fault model (Brune, 1970). The empirical relation of seismic moment with seismic moment

magnitude is given by Kanamori (1977) and Hanks and Kanamori (1979). It is as follows:

$$M_W = 2/3 * \log (M_0) - 10.73 \qquad \text{---------------- 6.13}$$

In this relation the loss of energy due to the propagation of seismic body wave with increasing epicentral distance is compensated for using **equation 6.7**. In addition, the compensation of frequency dependent attenuation of these body waves are also used that are calculated through the coda attenuation factor obtained for S-coda wave for this region by Kumar *et al.* (2005) and Mukhopadhyay and Tayagi (2008) and for adjoining southeastern Garhwal region obtained by Mukhopadhyay *et al.* (2010). This attenuation factor is the quantity that varies on regional basis. It has been observed that attenuation characteristic also varies with the epicentral distance for Kangra-Chamba region (Kumar *et al.*, 2005).

6.3. RELATED PARAMETERS OBSERVED THROUGH OTHER METHODS

The above mentioned procedure of measurement of the earthquake source parameters including its size depends upon the recorded waveform spectra and the procedure given by Brune (1971, 1970) and modified by Aki (1970) and others (Boatwright, 1978). Beside this a number of methods are available for measuring the size of an earthquake for its proper quantification. They are discussed below.

6.3.1. Earthquake Magnitude

Earthquake magnitude scale gives a measure of size of an earthquake. Empirically, magnitude (M) is defined as the logarithm of the ratio of the maximum ground displacement amplitude (A_{max}) in micron and time period (T) of a particular wave added with a distance correction factor $C(\Delta)$ accounting for the attenuation and geometrical spreading of the wave with distance from the source. The general relation of magnitude is given as

$$M = \log_{10}\left(\frac{A}{T}\right)_{max} + \sigma(\Delta, h) + C_r + C_s \qquad \text{---------------- 6.14}$$

192

Where, $\sigma(\Delta, h)$ is the geometrical correction factor, C_r is the regional source correction factor and C_s is the site effect correction factor.

For observing the size of micro-earthquakes, two magnitude scales are often used. They are the local magnitude scale, M_L (Richter, 1935) and the coda duration magnitude M_d (Bistricsany, 1958).

6.3.2. Richter Local Magnitude

The well known Richter magnitude was designed by Richter (1942) for classification of local seismic events in Southern California. This is also known as local magnitude M_L that provides the first convenient measure of earthquake size from instrumental recordings and may be calculated using the relation

$$M_L = \log(A) - \log(A_0) + C \qquad \text{---------------- 6.15}$$

Where C is used for corrections, A is the recorded trace amplitude at hypocentral distance r and the $-\log(A_0)$ term is scaled such that for an event of M_L 3.0, A=1 mm recorded at an epicentral distance of 100 km on a standard horizontal-component Wood-Anderson seismograph (Richter 1935, 1958). The corrections are based on regional attenuation characteristics and the given relation is valid for southern California. Their shape and level may be different in other regions of the world with different velocity and attenuation structure, crustal age and composition, heat-flow condition etc.

6.3.3. Coda Duration Magnitude

The coda wave magnitude is calculated using the duration of coda envelopes measured from the start of P-wave to the end of the seismogram (Bistricsany, 1958). This magnitude scale was developed earlier to overcome the limitation of saturation of the waveform amplitude encountered in the earlier case for large magnitude earthquakes and generally used for the magnitude measurement using analogue seismograms for local seismic events. For the present data set, the coda wave magnitude is measured for both analogue and digital data. In this data set the coda magnitude was estimated using coda duration measured on records from vertical-component velocity sensors. The coda magnitude is calculated using the relation

$$Mc = C_1*\log(\text{coda}) + C_2*\text{dis} + C_3 \qquad \text{---------------- 6.16}$$

Where C_1, C_2 and C_3 are the coefficients, coda is the coda duration in seconds and 'dis' is the hypocenter distance in km. Based on the work of Lee and Lahr (1975), the C_1, C_2 and C_3 are taken as 0.054, 1.31 and -1.30 respectively. The present data set is used to obtain the relations of coda duration magnitude with the Richter magnitude and the seismic moment magnitude for Kangra-Chamba region.

6.4. METHOD OF DATA ANALYSIS

In order to determine earthquake source parameters accurately one needs to know accurate location of the earthquake hypocentre. Beside this the waveform characteristics depend on source characteristics as well as on the attenuation characteristic of the medium between source and recording station. Hence, in order to estimate source parameters it is necessary to determine hypocenter location and attenuation characteristics of the medium. The source locations of the earthquakes whose data are used in this study are refined using the new velocity model obtained using this data set (Chapter 4; Kumar *et al.*, 2010). The source parameters were obtained for 135 well located earthquakes (**Table 6.1**) having digital data from at least five stations in the Kangra-Chamba region. The SH and SV waves were inverted to calculate these source parameters. First, for each event the transverse and radial components were obtained using the back azimuths of the recorded data. The selected windows for these waves were taken in such a way that the data of many phases were not mixed and resolution and stability of the spectra were maintained. Therefore, the SH and SV components were selected with a window starting from the S-wave onset and the window length not exceeding more than 5 sec (**Figure 6.3**). The spectrum is corrected using the instrument response (Figure 6.2) of the seismograph of that station. Several corrections are applied to compute the source parameters of the earthquake. The observed velocity spectrum at a station located at distance R is described as

$$X(f, R) = I(f).G(R).DIM(f).S(f) \qquad \text{---------------- 6.17}$$

Table 6.1: The earthquake source parameters obtained using spectrum data. Abbreviations: dd/mm/yyyy – day/month/year, hr/min/sec – hour/minute/second, Avg. dist. – average distance, M_0 – static moment, Mw – moment magnitude, Lati. – Latitude, Long. – Longitude, f_0 – corner frequency, SR – source radius, SD – stress drop.

Date dd/mm/yyyy	Time hr/min/sec	Avg. Dist. (km)	M_0 (dyne-cm)	M_W	Lati.	Long.	Dep. (km)	f_0 (Hz)	SR (km)	SD (bar)
04/03/2004	20:27:55.30	113.8	1.34E+20	2.74	33.220	75.922	22.0	4.07	0.32	2.78
30/03/2004	08:49:19.10	59.5	1.22E+20	2.72	32.301	76.771	10.0	4.33	0.29	2.75
31/03/2004	20:22:52.51	32.2	2.55E+19	2.23	32.742	76.173	8.8	5.36	0.26	1.99
12/04/2004	20:06:14.48	52.8	4.64E+19	2.33	32.210	76.698	2.7	4.20	0.31	1.40
27/04/2004	18:24:34.88	48.8	1.02E+20	2.64	32.325	76.521	28.0	4.95	0.26	2.69
04/11/2004	21:43:55.71	34.2	7.14E+18	1.86	32.369	76.686	1.2	6.13	0.21	0.52
11/11/2004	02:13:41.22	44.0	1.44E+23	4.56	32.300	76.441	9.5	2.27	0.68	27.02
11/11/2004	02:46:48.73	37.7	6.40E+21	3.74	32.320	76.428	2.5	3.66	0.36	8.99
27/11/2004	18:55:24.27	23.3	2.79E+18	1.59	32.306	76.425	0.1	6.89	0.19	0.21
07/12/2004	18:32:10.34	24.6	5.46E+18	1.75	32.365	76.510	22.7	6.39	0.20	0.32
07/12/2004	20:12:45.06	51.3	6.10E+18	1.70	32.693	76.635	6.8	5.79	0.22	0.18
07/12/2004	21:51:30.11	50.8	4.79E+18	1.71	32.688	76.611	10.4	6.89	0.19	0.31
07/12/2004	22:02:05.97	53.5	1.73E+19	2.09	32.713	76.620	15.7	5.35	0.25	0.56
09/12/2004	02:20:41.56	22.5	3.00E+19	2.30	32.330	76.418	8.3	5.00	0.27	1.06
09/12/2004	09:10:23.30	31.2	2.66E+20	2.92	32.370	76.450	5.6	4.85	0.27	7.81
11/12/2004	16:56:35.02	23.7	6.31E+18	1.83	32.313	76.422	5.0	5.18	0.25	0.28
17/12/2004	05:13:45.42	21.0	2.16E+19	2.20	32.322	76.442	6.0	5.27	0.25	0.85
11/01/2005	17:47:27.50	36.8	1.67E+19	2.14	32.296	76.808	1.0	7.17	0.18	1.50
11/01/2005	20:30:15.90	20.1	2.05E+18	1.53	32.333	76.548	10.1	7.97	0.16	0.29
13/01/2005	01:46:38.15	55.3	1.58E+19	2.13	32.795	76.084	10.5	5.90	0.21	0.78
13/01/2005	04:21:50.96	40.4	3.62E+19	2.33	32.703	76.028	3.2	6.04	0.21	2.26
15/01/2005	17:20:58.09	15.0	2.85E+18	1.62	32.444	76.746	12.0	6.50	0.19	0.21
15/01/2005	17:43:25.09	13.4	1.53E+18	1.46	32.489	76.720	18.4	7.51	0.17	0.17
19/01/2005	20:40:50.59	73.6	2.40E+19	2.22	32.836	76.080	2.3	4.76	0.28	0.64
20/01/2005	21:35:28.87	43.4	1.12E+19	1.98	32.870	76.226	10.8	5.52	0.23	0.43
21/01/2005	06:58:28.01	50.4	2.56E+20	2.93	32.244	76.842	6.7	4.52	0.28	5.98
21/01/2005	07:03:34.44	43.8	6.14E+19	2.49	32.099	76.797	26.6	5.15	0.28	2.48
31/01/2005	08:04:23.60	50.0	4.73E+19	2.20	32.505	76.366	5.5	7.07	0.18	8.67
04/02/2005	15:12:04.76	55.6	9.14E+19	2.51	32.372	76.440	12.0	7.04	0.18	7.88
10/02/2005	19:10:23.39	29.5	7.77E+18	1.92	32.377	76.422	0.1	7.54	0.17	1.01
24/02/2005	21:58:31.48	104.6	1.80E+19	2.12	31.503	77.015	0.0	6.09	0.21	0.96
28/02/2005	00:51:54.57	53.3	6.33E+19	2.54	32.295	76.716	1.3	5.04	0.25	2.22
28/02/2005	01:37:37.19	39.6	9.15E+18	1.95	32.186	76.872	0.0	7.07	0.19	1.17
28/02/2005	07:56:11.30	94.2	3.49E+19	2.32	33.306	76.144	0.1	5.06	0.26	0.93
28/02/2005	16:04:45.80	103.3	2.77E+21	3.57	32.389	76.403	6.5	2.75	0.49	20.71
28/02/2005	17:38:31.86	23.9	6.61E+18	1.79	32.390	76.422	0.1	7.01	0.18	0.59
28/02/2005	17:52:56.42	48.3	1.02E+20	2.55	32.391	76.440	12.2	5.32	0.24	3.25
28/02/2005	18:01:58.35	116.9	3.72E+22	4.27	32.418	76.410	5.4	2.43	0.56	10.73
28/02/2005	18:09:05.47	30.3	8.61E+19	2.61	32.389	76.450	12.4	5.27	0.26	2.91
28/02/2005	18:36:05.31	17.4	2.02E+19	2.19	32.411	76.414	3.7	5.73	0.25	0.97
28/02/2005	18:58:31.64	15.6	4.83E+18	1.77	32.374	76.467	9.9	6.42	0.21	0.30
28/02/2005	19:03:47.99	23.6	1.38E+19	2.02	32.404	76.440	9.1	6.21	0.23	0.94
28/02/2005	20:40:57.39	24.0	2.03E+19	2.18	32.403	76.430	8.6	6.28	0.21	1.13
28/02/2005	20:54:55.31	31.9	2.78E+19	2.23	32.404	76.426	7.3	7.22	0.18	3.06
28/02/2005	21:13:10.88	31.8	9.10E+18	1.86	32.402	76.425	6.5	7.94	0.18	1.10

28/02/2005	21:14:39.59	31.9	1.17E+19	1.98	32.399	76.427	5.2	7.54	0.19	1.72
28/02/2005	21:36:22.20	28.3	5.56E+18	1.75	32.394	76.442	7.1	7.34	0.17	0.51
28/02/2005	21:50:35.77	29.1	2.56E+19	2.21	32.407	76.435	8.6	6.39	0.20	1.49
28/02/2005	23:18:53.37	25.4	1.14E+19	2.02	32.409	76.441	7.6	7.11	0.17	0.92
01/03/2005	12:02:07.83	15.3	2.65E+19	2.28	32.383	76.442	7.6	6.19	0.21	1.48
01/03/2005	12:11:09.60	30.0	2.09E+19	2.20	32.414	76.431	4.9	7.21	0.17	1.88
01/03/2005	14:22:25.81	15.1	3.65E+18	1.70	32.350	76.499	5.9	7.19	0.18	0.32
01/03/2005	15:20:02.45	48.8	1.34E+20	2.62	32.422	76.458	8.9	5.88	0.22	4.53
01/03/2005	16:24:06.06	12.8	2.64E+18	1.61	32.430	76.413	2.8	8.23	0.15	0.35
02/03/2005	02:49:31.64	14.7	3.03E+19	2.32	32.388	76.394	2.9	9.19	0.14	5.33
02/03/2005	09:39:41.54	37.7	5.12E+19	2.40	32.445	76.393	10.1	4.40	0.28	1.01
02/03/2005	09:58:53.92	21.8	3.93E+19	2.40	32.395	76.458	10.1	5.17	0.24	1.31
02/03/2005	13:40:03.46	33.4	6.45E+19	2.47	32.394	76.480	10.4	5.84	0.22	3.00
03/03/2005	10:15:29.02	35.9	1.12E+19	1.97	32.415	76.451	6.0	5.76	0.22	0.52
03/03/2005	12:05:14.90	21.6	3.89E+18	1.73	32.414	76.409	0.0	4.72	0.26	0.10
03/03/2005	12:37:03.15	85.4	5.59E+19	2.46	33.207	76.979	0.0	5.74	0.22	2.92
03/03/2005	15:22:36.49	22.5	1.71E+19	2.07	32.424	76.449	10.1	6.82	0.20	0.93
03/03/2005	17:47:14.77	26.2	9.57E+18	1.97	32.422	76.414	6.5	6.70	0.21	0.75
03/03/2005	21:49:57.60	30.7	6.39E+19	2.49	32.411	76.450	7.5	4.56	0.29	1.48
04/03/2005	02:39:05.96	33.4	1.84E+19	2.17	32.417	76.460	10.4	7.27	0.17	1.68
04/03/2005	20:58:03.02	26.6	3.84E+18	1.72	32.399	76.445	6.4	7.00	0.18	0.33
05/03/2005	02:36:10.22	42.3	7.51E+19	2.53	32.402	76.427	2.0	6.37	0.20	5.20
05/03/2005	16:01:26.17	22.6	2.63E+18	1.60	32.275	76.599	8.4	8.46	0.16	0.50
05/03/2005	18:15:11.11	18.5	5.42E+18	1.81	32.410	76.424	0.0	6.91	0.20	0.51
06/03/2005	02:03:31.15	25.9	3.59E+20	2.98	32.335	76.460	9.5	4.93	0.28	16.07
06/03/2005	18:22:18.40	39.7	1.60E+19	2.06	32.408	76.440	3.8	5.49	0.24	0.88
06/03/2005	21:36:57.76	35.4	1.65E+19	2.13	32.435	76.447	5.2	6.33	0.21	0.95
09/03/2005	02:52:25.67	113.4	2.48E+20	2.90	33.162	76.631	15.0	4.00	0.31	4.62
11/03/2005	20:01:58.99	57.0	2.11E+20	2.82	32.290	76.627	10.0	4.68	0.29	10.21
17/03/2005	21:47:10.94	79.6	6.34E+19	2.51	33.068	76.815	9.4	4.81	0.27	1.72
17/03/2005	22:06:21.66	92.7	1.09E+19	2.01	33.071	76.930	20.0	6.37	0.20	0.85
22/03/2005	01:58:13.20	33.6	6.15E+18	1.82	32.388	76.734	1.6	10.01	0.12	1.44
24/03/2005	23:54:54.27	23.8	1.46E+19	2.09	32.396	76.432	2.7	5.88	0.21	0.66
27/03/2005	10:14:48.81	66.3	1.55E+19	2.11	32.705	76.125	14.0	5.40	0.24	0.71
30/03/2005	22:11:30.07	22.7	3.67E+18	1.68	32.292	76.349	5.9	6.63	0.19	0.26
01/04/2005	22:43:36.03	74.3	1.04E+19	1.97	33.120	76.152	7.3	5.76	0.22	0.44
03/04/2005	21:32:32.03	28.6	2.33E+19	2.24	32.323	76.380	6.4	7.45	0.17	2.36
04/04/2005	00:33:41.74	33.3	5.56E+20	3.10	32.465	76.452	9.7	2.63	0.52	2.48
12/04/2005	12:19:20.14	25.2	1.59E+19	2.13	32.433	76.445	3.5	6.95	0.19	1.52
13/04/2005	12:56:40.62	33.4	3.01E+19	2.24	32.400	76.444	5.4	6.23	0.20	1.92
13/04/2005	18:16:25.65	42.0	3.53E+19	2.36	32.553	76.337	10.0	5.87	0.22	1.78
14/04/2005	07:11:25.66	141.6	4.12E+22	4.33	32.611	76.367	7.6	1.14	1.15	12.32
14/04/2005	07:56:21.46	40.8	3.71E+19	2.37	32.608	76.352	10.0	5.89	0.22	1.81
14/04/2005	08:25:49.97	41.4	1.07E+20	2.66	32.631	76.400	1.7	5.71	0.22	4.57
15/04/2005	23:43:36.86	47.1	4.05E+19	2.38	32.632	76.403	0.0	5.59	0.22	1.71
18/04/2005	20:10:33.07	155.2	2.12E+22	4.00	32.616	76.349	5.3	2.62	0.51	9.71
01/05/2005	13:04:14.73	7.6	4.82E+20	3.12	32.485	75.980	8.6	3.10	0.40	3.39
01/05/2005	22:13:00.30	30.6	1.42E+18	1.38	32.525	76.483	0.1	9.72	0.13	0.33
02/05/2005	03:28:02.99	28.9	1.56E+19	2.05	32.354	76.486	5.6	6.51	0.20	0.96
02/05/2005	23:36:48.80	30.4	5.60E+18	1.76	32.411	76.427	8.4	6.22	0.23	0.48
05/05/2005	11:56:53.90	21.3	2.07E+19	2.20	32.419	76.290	11.9	6.52	0.21	1.86
06/05/2005	21:39:00.20	89.0	1.70E+19	2.08	33.119	76.527	7.1	5.00	0.25	0.45
07/05/2005	08:59:14.79	21.2	2.67E+19	2.28	32.296	76.443	0.8	7.03	0.19	2.57

07/05/2005	14:48:19.69	90.8	2.14E+19	2.15	32.162	75.486	0.5	5.97	0.21	0.87
08/05/2005	17:45:23.41	34.5	1.40E+19	2.02	32.403	76.445	5.9	6.32	0.20	0.95
11/05/2005	19:32:21.32	42.7	6.23E+18	1.82	32.686	76.664	3.3	6.47	0.20	0.36
13/05/2005	10:13:26.29	69.3	8.78E+18	1.96	32.739	76.694	5.2	4.53	0.27	0.19
15/05/2005	04:33:53.80	79.1	7.18E+19	2.53	33.033	76.131	0.8	3.48	0.39	0.72
18/05/2005	20:24:12.79	30.9	2.53E+18	1.55	32.513	76.223	21.5	6.43	0.20	0.20
19/05/2005	14:01:43.49	123.2	6.97E+19	2.51	31.560	77.249	10.1	4.93	0.26	2.39
19/05/2005	17:08:14.97	32.4	7.81E+18	1.87	32.379	76.240	13.8	6.15	0.21	0.46
20/05/2005	16:51:02.51	28.9	5.32E+18	1.72	32.340	76.289	13.8	6.28	0.20	0.34
23/05/2005	01:33:52.83	43.0	4.50E+19	2.38	32.473	75.957	24.8	5.43	0.23	1.70
02/06/2005	16:41:06.87	22.0	5.71E+18	1.83	32.239	76.539	17.2	3.95	0.32	0.08
02/06/2005	20:52:02.92	28.5	6.30E+18	1.83	32.770	76.215	11.1	7.41	0.17	0.56
05/06/2005	07:02:37.51	7.7	1.22E+19	2.06	32.787	76.060	14.6	6.66	0.19	0.86
05/06/2005	15:01:17.60	38.2	4.69E+19	2.36	32.388	76.467	7.4	5.80	0.22	2.85
07/06/2005	17:59:46.28	23.2	1.34E+19	2.06	32.397	76.460	6.0	6.12	0.22	0.77
11/06/2005	16:57:28.50	40.1	1.21E+19	2.02	32.803	76.209	13.5	5.85	0.22	0.75
13/06/2005	15:01:54.13	88.1	2.06E+20	2.85	33.183	76.476	0.0	5.96	0.22	11.36
18/06/2005	04:01:43.17	133.6	7.12E+21	3.73	32.800	76.422	7.3	3.68	0.43	14.22
19/06/2005	10:12:02.22	46.6	2.86E+19	2.28	32.658	76.567	11.0	5.35	0.26	1.01
20/06/2005	11:39:39.81	123.0	2.06E+20	2.87	33.023	75.898	1.5	3.87	0.34	3.03
01/07/2005	16:51:03.76	69.8	1.89E+19	2.18	31.891	76.820	3.3	5.11	0.25	0.69
01/07/2005	19:03:42.64	58.6	2.21E+19	2.17	32.421	76.868	10.9	6.08	0.21	1.40
01/08/2005	16:09:43.73	32.4	9.25E+18	1.98	32.375	76.589	10.0	6.33	0.20	0.55
03/08/2005	19:48:56.36	27.9	3.16E+18	1.66	32.639	76.274	9.1	7.41	0.17	0.31
11/08/2005	14:33:22.79	36.3	4.23E+18	1.74	32.801	76.023	14.1	6.65	0.19	0.34
12/08/2005	18:27:07.48	60.9	1.05E+19	1.91	32.735	76.127	36.9	5.44	0.23	0.33
13/08/2005	18:40:53.62	31.7	3.61E+18	1.71	32.356	76.194	4.1	5.45	0.23	0.15
14/08/2005	19:57:17.81	37.3	1.21E+18	1.32	32.920	76.367	11.9	7.04	0.18	0.13
16/08/2005	19:44:59.44	64.0	6.29E+18	1.85	32.998	75.837	0.0	5.75	0.23	0.29
17/08/2005	16:21:00.55	109.6	1.96E+19	2.10	33.370	75.788	0.5	5.81	0.22	0.75
22/08/2005	12:03:22.92	36.3	1.29E+19	2.07	32.849	76.084	10.6	6.18	0.20	0.79
22/08/2005	12:54:33.37	48.7	5.38E+19	2.45	32.796	76.224	4.8	5.36	0.24	2.26
24/08/2005	01:25:45.94	54.2	1.77E+19	2.15	32.958	75.894	10.0	4.92	0.26	0.49
25/08/2005	04:10:22.17	52.6	6.93E+20	3.18	32.770	75.974	3.3	3.12	0.44	5.69
27/08/2005	10:16:43.97	50.6	5.08E+19	2.46	32.829	75.928	12.9	5.83	0.22	2.50
28/08/2005	11:59:54.48	64.9	1.42E+20	2.67	32.761	76.683	7.4	3.58	0.39	1.79
29/08/2005	18:06:31.92	84.3	6.81E+19	2.54	32.960	76.190	4.9	4.64	0.30	1.66

where f is the observational frequency in Hz, I(f) is the instrument response function at frequency f (Figure 6.2) for the present data set, G(R) is the geometrical spreading correction for the body waves which is taken as per equation **6.7**, DIM(f) is diminution function due to anelastic attenuation and S(f) is the amplitude source spectrum. Anelastic attenuation is assumed as frequency dependent loss and described by quality factor Q.
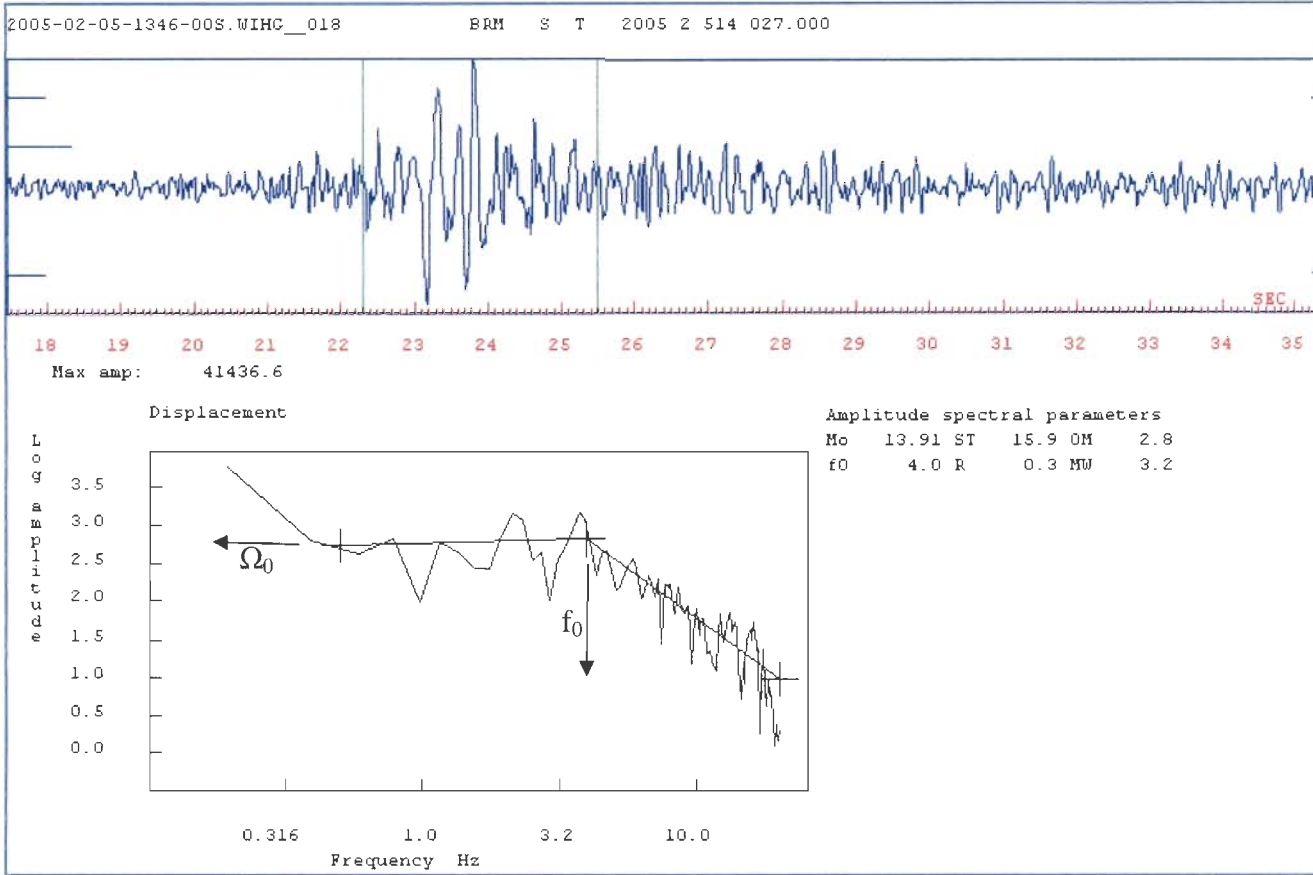
Figure 6.3. The S-wave window (above within green lines) of the transverse component of M3.0 earthquake recorded at Bharmour station. The displacement spectrum of this window is in the lower panel. Ω_0; the low frequency level, f_0; the corner frequency.

6.4.1. Applied Procedure

The source parameter analysis is performed based on circular fault model of Brune (Brune, 1970, 1971). On the basis of this analysis for each event, the average values are computed for seismic moment, source radius, corner frequency, moment magnitude and stress drop using the recorded data of different stations. These average values $\langle x \rangle$ are estimated following the relation of Archuleta et al. (1982)

$$\langle x \rangle = anti \log \left(\frac{1}{N_s} \sum_{i=1}^{N_s} \log x_i \right) \qquad \text{--------------- 6.18}$$

where N_s is the number of stations used to record the seismic event and x_i is the data of ith station. This procedure of averaging the calculated data gives equal weight to each observation. However, in the case of simple arithmetic average, the result would be biased towards larger values. Also the errors associated with low frequency

198

displacement spectrum amplitude and source radius are log-normally distributed. Therefore the average seismic moment of single event is evaluated using the relation

$$\left\langle M_0 \right\rangle = anti\log\left(\frac{1}{N_s} \sum_{i=1}^{N_s} \log M_{0i} \right) \qquad \text{--------------- 6.19}$$

where, M_{0i} is the seismic moment computed at each station. The other parameters such as stress drop, source radius, corner frequency and moment magnitude are also computed similarly using the data of different stations.

For calculation of the source parameter, the crustal structure has to be defined for inclusion of the information of the medium around the source and the characteristics of the path along which seismic wave travels. The seismic events are located using 1D velocity model obtained from the same set of data as discussed in Chapter 3. Three layered velocity structure is taken for the upper crust of 25 km thickness (as given in section 3.3 of 1D velocity model) with 6.80 km/s P-wave velocity for lower crust of 21 km thick and 8.25 km/s for the underlying half space. The seismic events have been located using the P- and S-wave data of at least five stations of digital and analogue seismographs and having good station azimuthal coverage. The waveforms of S-phase of the event recorded by at least three digital stations were inverted for obtaining average values of different source parameters. The same dataset is also used to obtain the frequency dependent attenuation relation for S-coda wave. The average value of coda quality factor at 1 Hz frequency is taken as 125 and the frequency parameter is 1.07 (Kumar *et al.*, 2005) as the average attenuation parameter obtained for coda wave of 30 sec window length. The obtained value of quality factor is used to correct the effect of attenuation characteristic from the displacement spectra.

The displacement spectrum of appropriate time window length (**Figure 6.3**) is taken from the start of S-wave to compute the S-wave spectra for obtaining the source parameters. The signal windows of variable lengths are taken in order to avoid contamination from other phases and to maintain good resolution and stability of the spectra. Similar to equation **6.17** for velocity spectra, the observed displacement spectra at a distance R from the source is described as
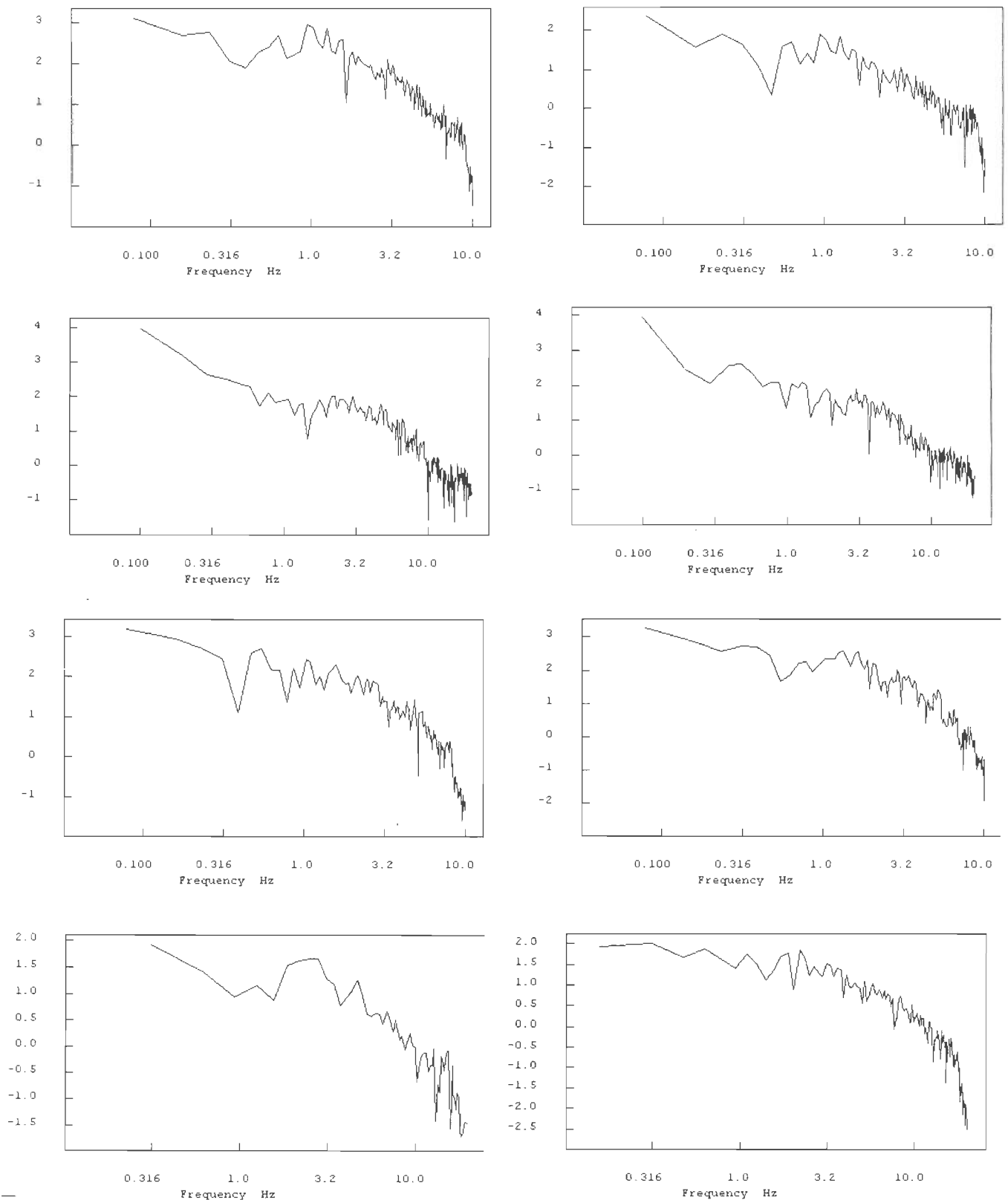
Figure 6.4. Typical displacement spectra obtained for SH (left panel) and SV (right panel) for Kangra-Chamba region.

$$D(f,R) = I_d(f).G(R).DIM(f).S(f) \qquad \text{---------------- 6.20}$$

where $I_d(f)$ is the recording instrument displacement transfer function for frequency f and S(f) is the calculated amplitude source spectrum.

The observed spectra are corrected for instrumental response, geometrical spreading, diminution factor and the site response to get the exact amplitude at the site. The correction for geometrical spreading is applied with epicenter distance based **relation (6.7)**. This relation is for body waves for which the decay of energy (amplitude) is inversely proportional to the hypocentral distance with the assumption of spherical shape of wave front. The earthquake source spectra are obtained using the S-wave of the recorded data and the attenuation characteristic was adopted through the available coda Q values for this region (Kumar et al., 2005). The coda Q values, Q_c is used instead of Q_β (Q value for S wave) as both are nearly equal for one particular region based on the observations of Rautian and Khalturin (1978) and Aki (1980). Some representative examples of the corrected amplitude spectra obtained for different earthquakes at different stations are shown in **Figure 6.4**.

The observed source model is based on the response of far-field displacement spectrum after applying the correction for propagation, site and other effects. This displacement spectrum has a characteristic shape that is flat at low frequencies less than corner frequency and at higher frequencies its amplitude falls-off with the increase in frequency (**Figure 6.4**). The far-field observation is based on the assumption which will be truly justified after taking the distance between source and station several times greater than the wavelengths under study. This interpretation is taken from Brune's source model with low frequency amplitude level (Ω_0) and corner frequency (f_0) as the usual spectral parameter (Hanks and Wyss, 1972). The results are discussed in the next section.

6.4.2. Calculation of Seismic Moment and its relation with Magnitude

Seismic moment for each event of present data set was obtained using the displacement spectrum as per the relation given in **equation 6.6** for each recording station. The radiation coefficient used in this equation is 0.6 which is an average global value for S-wave (Aki and Richard, 1980; Bore and Boatwright, 1984). The reliability of the displacement spectrum obtained from single record is not stable (Yalcinkaya and Alptekin, 2003), therefore the average value for a single event is obtained using relation

given in **equation 6.18** for the data of all records for the same event. The computed average values of the seismic moment are given in **Table 6.1** which reveals that the range of seismic moment is 1.2×10^{18}dyne-cm to 1.4×10^{23}dyne-cm. The obtained seismic moment was used to obtain the size of the seismic event which is defined as the moment magnitude. This moment magnitude was measured from the seismic moment using **equation 6.13**. Generally, the source size of the seismic events is calculated based on Richter relation (Richter, 1935) for local magnitude scale, M_L and the duration magnitude, M_c using the appropriate parameters described in **equations 6.15 and 6.16** respectively. Relationships among the source parameters vary from one region to another and therefore the empirical relations were obtained for the local magnitude scales routinely obtained for the study region with respect to moment magnitude obtained in present work. For Kangra-Chamba region the estimated relation is as follows:

$$M_L = 0.743 * Mw + 0.620 \qquad \text{---------------- 6.21}$$

The variation of Richter magnitude with moment magnitude is shown in **Figure 6.5a**. A straight line fit is obtained by least square regression analysis to obtain the empirical relationship between M_L and Mw. The obtained relation is given in **equation 6.21** for which regression relation gives a good correlation for these magnitude scales with 0.889 correlation coefficient and small residual of 0.042. Thereofore, the obtained relation has a good fit to data and the relation indicates that for smaller sized earthquakes the local magnitude is comparatively higher but with the increase of size this difference decreases.

Similarly the empirical relation is obtained between Mc and Mw (**Figure 6.5b**) for which the straight line of least square regression fit gives lesser correlation having correlation coefficient value of 0.697 and a slightly higher residual of 0.118. The empirical relations obtained for these magnitude scales are given as:

$$Mc = 0.859 * Mw + 0.323 \qquad \text{---------------- 6.22}$$

However, the correlation of Mc with Mw is comparatively lower than that of M_L with Mw but the values of the constants in **equation 6.22** indicates that the duration

magnitude is close to the moment magnitude for this data set. Therefore, this relation can be used to directly calculate the moment magnitude of the local earthquake and vice-versa.
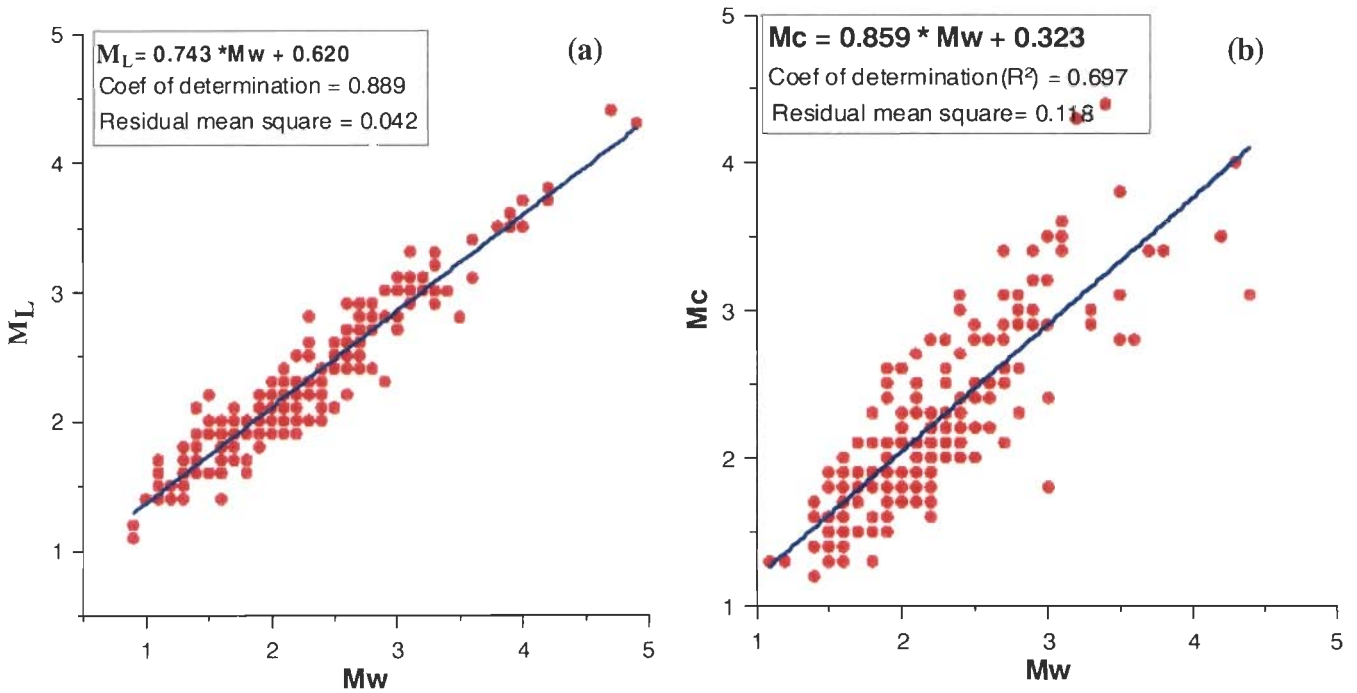
Figure 6.5: Empirical relationships computed to obtain the relation of different magnitudes with moment magnitude. (a) Richter magnitude and moment magnitude (b) Duration magnitude and moment magnitude.

This data set was also used to obtain the relation between local magnitude, M_L and the coda duration magnitude, Mc. The data of these two parameters is plotted in **Figure 6.6** as a scatter plot. The least square regression fit is applied between these parameters to obtain the straight line fit and incorporate a relation of the variation of one parameter with respect to other. The obtained relation is as follow

$$M_C = 0.799 * M_L + 0.632 \qquad \text{---------------- 6.23}$$

The regression relation between these two parameters is not as good as it has been observed in case of other two above mentioned relations. In this case the

correlation coefficient value is only 0.661 while the residual of 0.310 is higher than other two relations.

These relations can be utilized to calculate one type of magnitude using the information of available data of other one. It is clear that the relation of local magnitude is well correlated with the moment magnitude.
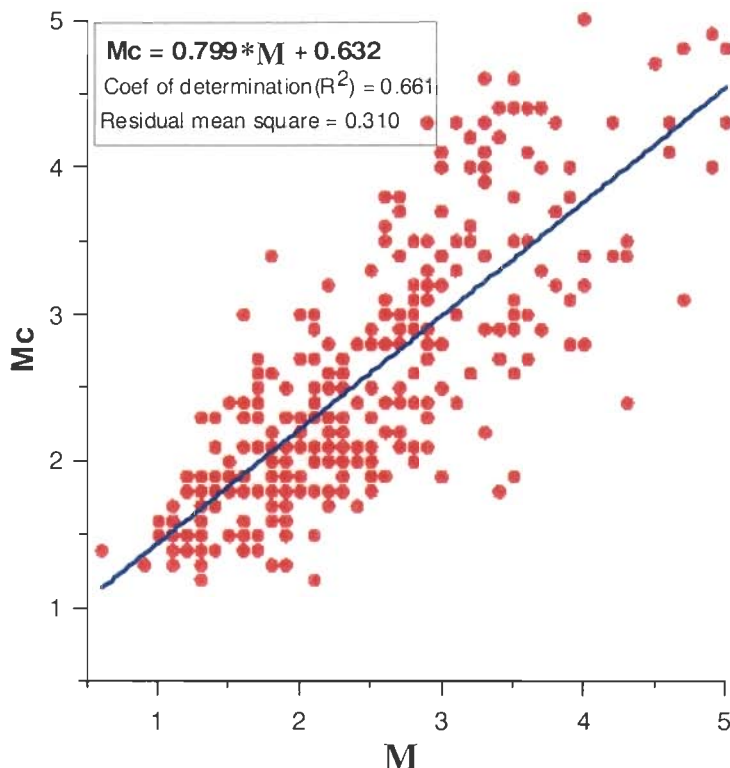
Figure 6.6. The empirical relation obtained for the local magnitude and coda duration magnitude of Kangra-Chamba region.

6.4.3. Calculation of Corner Frequency and Source Radius

It has been mentioned in the previous sections that the waveform inversion is used to obtain the circular source size. The radius of this circular source is calculated for each spectrum through the relation 6.8 using the S-wave velocity in the medium around earthquake source and the estimated corner frequency. First of all the corner frequency of each component of the recorded data is selected from the recorded displacement spectrum at the intersections of two straight lines drawn on the spectrum as shown in **Figure 6.3**. The S-wave velocity around the source is taken as per 1D velocity model obtained in Chapter 3. The average source radius for each earthquake is computed from

the spectra obtained from all the records for that events using equation 6.8 and based on the average relation of 6.18. The computed source radius of these events varies from 0.1 km to 1.15 km (**Table 6.1**).

6.4.4. Calculation of Stress Drop

The calculated average seismic moment and the average source radius for each event are used in **equation 6.11** to obtain the average stress drop during the occurrence of the earthquake. The average stress drop for bigger events is 18 bar with maximum value of 27 bar while for micro-earthquakes it increases linearly from 0.1 bar to 10 bar with the increase of earthquake size. Hence, the observed stress drop is different for micro-earthquakes and the larger magnitude earthquakes. It is quite clear from **Figure 6.7** and **Table 6.1** that for lower seismic moment (micro-earthquakes M≤3.0) of the earthquakes the stress drop increases with the increase of earthquake size. However, based on the relation of the **equation of 6.11** it is not appropriate to say that the stress drop should vary with magnitude for one local region. The difference in stress drops for higher and lower moment values indicate either the break down in the similarity behavior of earthquake generation processes or it may be the effect of variation in attenuation with frequency which has been also observed in other regions (Archuleta, 1986; Dysart et al., 1988; Garcia et al., 2004) for seismic moment smaller than about 20 dyne-cm.

6.5. RESULT AND DISCUSSION

The analyzed data has a wide range of source size from micro-earthquake events (minimum Mw of 1.5) to big earthquakes of maximum size Mw 4.6. The calculated seismic moment of these events vary from 1.20 x 10^{18} dyne-cm to 1.44 x 10^{23} dyne-cm. The observed stress drop is also variable that increase with the increasing source size (**Figure 6.7**). However this increase is observed only for events of smaller magnitude having seismic moment less than 1 x 10^{21} dyne-cm. Its value is higher and nearly constant for bigger events. The average stress drop for these events is 18 bar and the maximum value is 27 bar. The stress drop for smaller events increases from 0.1 bar to 10 bar. As shown in **Figure 6.7**, the increase of stress drop for smaller events is linear.

The seismic moment obtained for the data of NW Himalaya is also used to incorporate the relation of variation of stress drop, source radius and corner frequency calculated for these earthquakes. The plot of stress drop with respect to seismic moment

states that the stress drop generally increases with the increase of seismic moment. However the relation given by Brune model in **equations 6.11 and 6.8** states that the stress drops for one region is constant for all range of magnitudes. The constant stress drop based on the evaluated relations state that as the magnitude of the seismic event increases its corner frequency decreases and the source radius increases (Aki and Richards, 1980). The assumption for this observation is the similarity in the behavior of generation of all types of earthquakes for single region. But it is generally seen that this is valid only for big sized (M>3.0) earthquakes but not for micro-earthquakes. The different scaling for micro size events may be either due to break down in the similarity or the cause of attenuation. The observation for Kangra-Chamba region of NW Himalaya also

$$\ln(\sigma) = 0.5591118018 * \ln(M_0) - 25.05992826$$

Coef of determination, $(R^2) = 0.801$
Residual mean square = 0.277
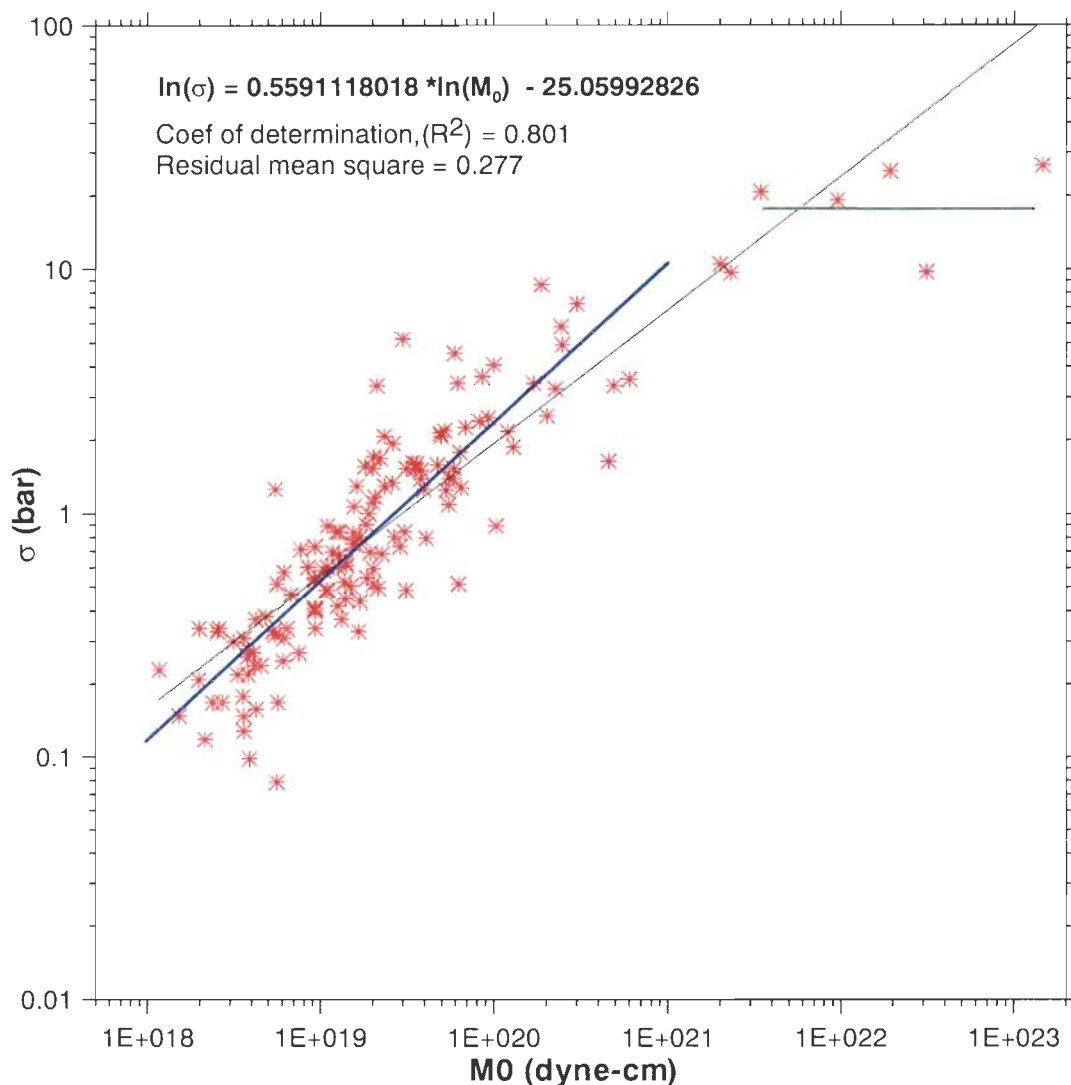
Figure 6.7. The variation of stress drop with seismic moment. Straight-line fit obtained using least-square regression analysis for different moment ranges are also shown. The black line is for the entire data set taken together, the blue line is for the smaller sized events and the green line is for the larger sized events.

indicates that stress drop increases with magnitude from micro-earthquakes events to low magnitude having maximum seismic moment of 1.44 x 10^{23} dyne-cm. However, as shown in **Figure 6.7** the stress drop is nearly constant for the seismic events of higher seismic moment. It states that the similarity behavior in earthquake generation for the present data set is valid for the events having moment magnitude greater than 3.2. Using least-square regression analysis, we applied a straight-line fit to obtain the relationship between stress drop and seismic moment. The empirical relation obtained from straight-line fit with correlation coefficient of 0.801 using the entire data set is give as:

$$\log(\sigma) = 0.56 * \log(Mo) - 25.06 \qquad \text{---------------- 6.24}$$

However, as shown in the **Figure 6.7**, the straight-line fit is not valid for all the data set and there should be another fit which can be the resultant of two straight-line fits applied to two segments of data. The straight-line fit shown with blue color is for the micro-earthquakes having maximum seismic moment of 1.0 x 10^{21} dyne-cm and the other one of green color is for larger magnitude events having seismic moments more than 3.0 x 10^{21} dyne-cm. In Brune's model, the dimension of the source rupture is assumed a circular area whose two parts are displaced relative to each other. The dimension of this circular region is proportional to the size of seismic moment so that the rupture area of the circular region increases with the increase of the magnitude of the earthquake. However, the change in the source dimension with the seismic moment is different for different regions (Aki and Richards, 1980). The present data is also used to observe the variation of the size of the rupture with the seismic moment. The variation of the source radius with the seismic moment is plotted in **Figure 6.8**.

It is observed that the source dimension linearly increases with the increase of the seismic moment. The data is also used to develop the relationship of the source radius with the seismic moment. A straight-line fit is obtained by least square regression to determine the empirical relation. The straight-line fit has correlation coefficient of 0.717 and the obtained relation is given by

$$\text{Log}(R_0) = 0.15 * \log(M_0) - 8.04 \qquad \text{---------------- 6.25}$$

207
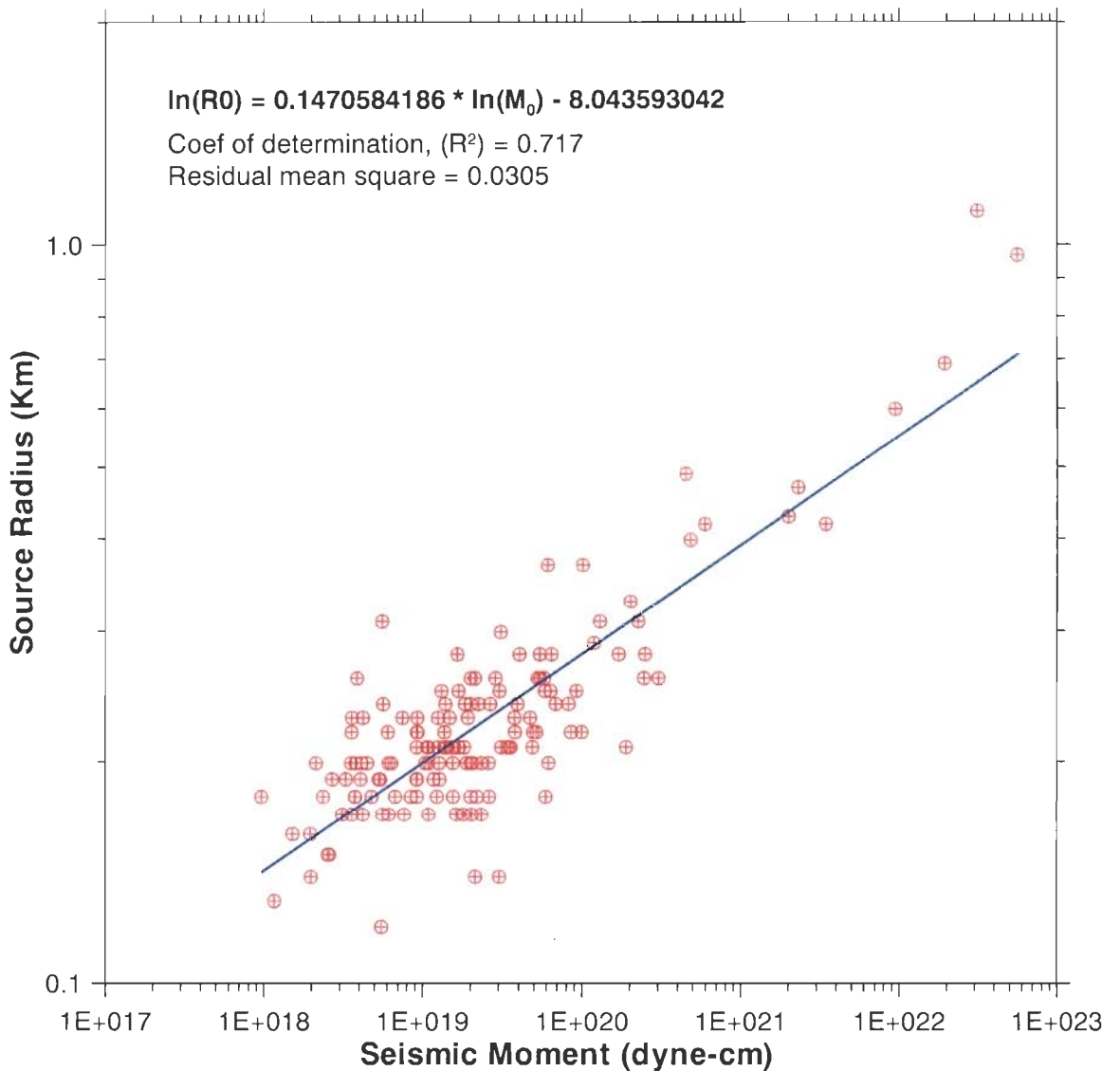
Figure 6.8. Source radius of Brune's circular model as a function of seismic moment. Straight-line fit obtained using regression analysis.

Another important parameter of the rupture source is the corner frequency. It is the intersection of the asymptotes of the low frequency and the high frequency portion in the displacement spectrum. The amplitude of displacement spectrum is constant at a frequency less than the corner frequency. At this frequency the velocity of earthquake rupture is maximum; therefore the maximum energy is released along the corner frequency. As shown in **Figure 6.9**, the corner frequency decreases with the increase of seismic moment. We obtained a relation from the best fit of least-square regression

between these two parameters **(Figure 6.9)**. The resultant relation having correlation coefficient 0.714 is given as

$$Log(f_0) = -0.15 * log(M_0) + 8.24 \qquad\text{---------------- 6.26}$$

The source parameters are determined for micro and moderate magnitude earthquake for NW Himalayan region. The range of moment magnitude of the data set is 1.3 to 4.6. The resultant parameters are used to derive the relation among different source parameters and the different magnitude scales.

$\ln(f0) = -0.1469203616 * \ln(M_0) + 8.244245205$

Coef of determination, (R^2) = 0.714
Residual mean square = 0.0309
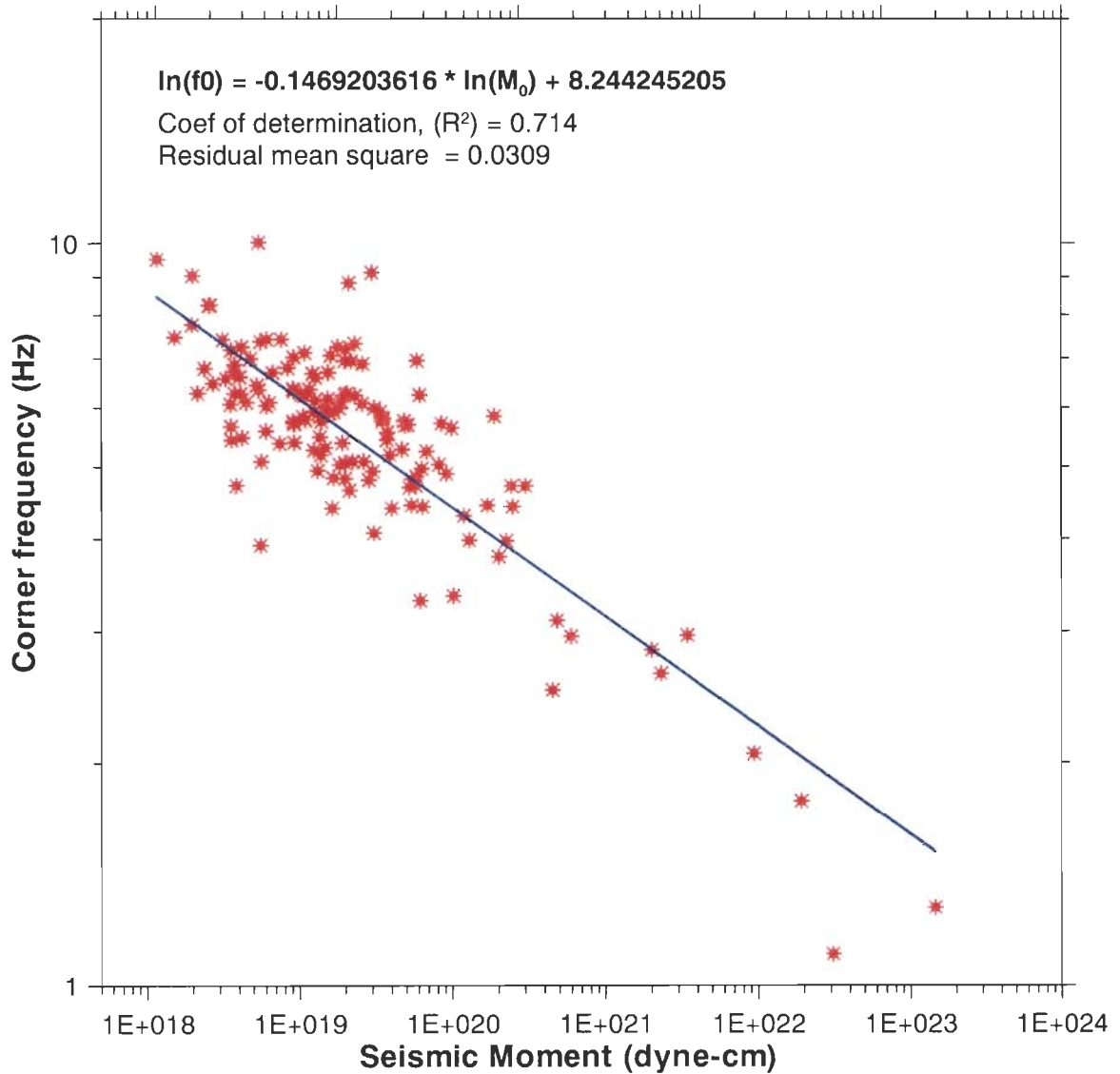
Figure 6.8: The corner frequency as a function of seismic moment. Straight line fit obtained using regression analysis.

The determined corner frequency is in the range 1 to 10 Hz for the earthquakes recorded between 1.3 and 4.6 moment magnitude. The range of seismic moment for the same events is 1.20×10^{18} dyne-cm to 1.44×10^{23} dyne-cm. The source radius is found to range from 0.1 to 1.15 km. The variation of stress drop is different for micro-earthquakes and the earthquakes having moderate magnitude. The average stress drop for all events is 2.5 bar with maximum value of 27 bar while for micro-earthquakes it increases linearly from 0.1 bar to 10 bar with the increase of earthquake size. The different stress drops indicates either the break down in the similarity behavior of earthquake generation processes or it may be the effect of attenuation for different frequency range.

6.5.1. Variation of Stress drop with depth

As mentioned in the previous section, the stress drop measured with local earthquake data indicates increase of its value with the increase of earthquake source size. It has also been observed that on an average the stress drop also increases with the increase of focal depth for upper most 15 km crustal medium (**Figure 6.10**). Few events located in the deeper part also have smaller stress drop for which the size of the earthquake is low. Allen *et al.* (2004) have done an extensive study for the variation of seismic source parameters with focal depth for southeastern Australia and found that shallow focus earthquakes (less than 6 km) produce lower stress drop compared to deeper earthquakes. According to that study, the b values of the Gutenberg-Richter magnitude-frequency relation (Gutenberg and Richter, 1944) decrease with depth for the upper crust suggesting that both rock strength and yield stress increases with depth. They suggested that this decrease of b values with source depth implies that the bigger size earthquakes having higher stress drop occur in the deeper part in that region. From **Figure 6.10** it is observed that in the Kangra-Chamba region of NW Himalaya also bigger size events were located in the deeper part of the upper crust. However enough data is required to observe the variation of b value with depth. The observations of present data also indicate the increase of stress drop with focal depth (**Figure 6.10**) which is related with the increase of size of the earthquake. Therefore, it appears that the upper most crust have less strength to withhold larger stress and therefore the stress drop appears to increase with depth along with the increase of earthquake size for which Stork and Ito (2004) states that the lower stress drop in the uppermost crust is due to
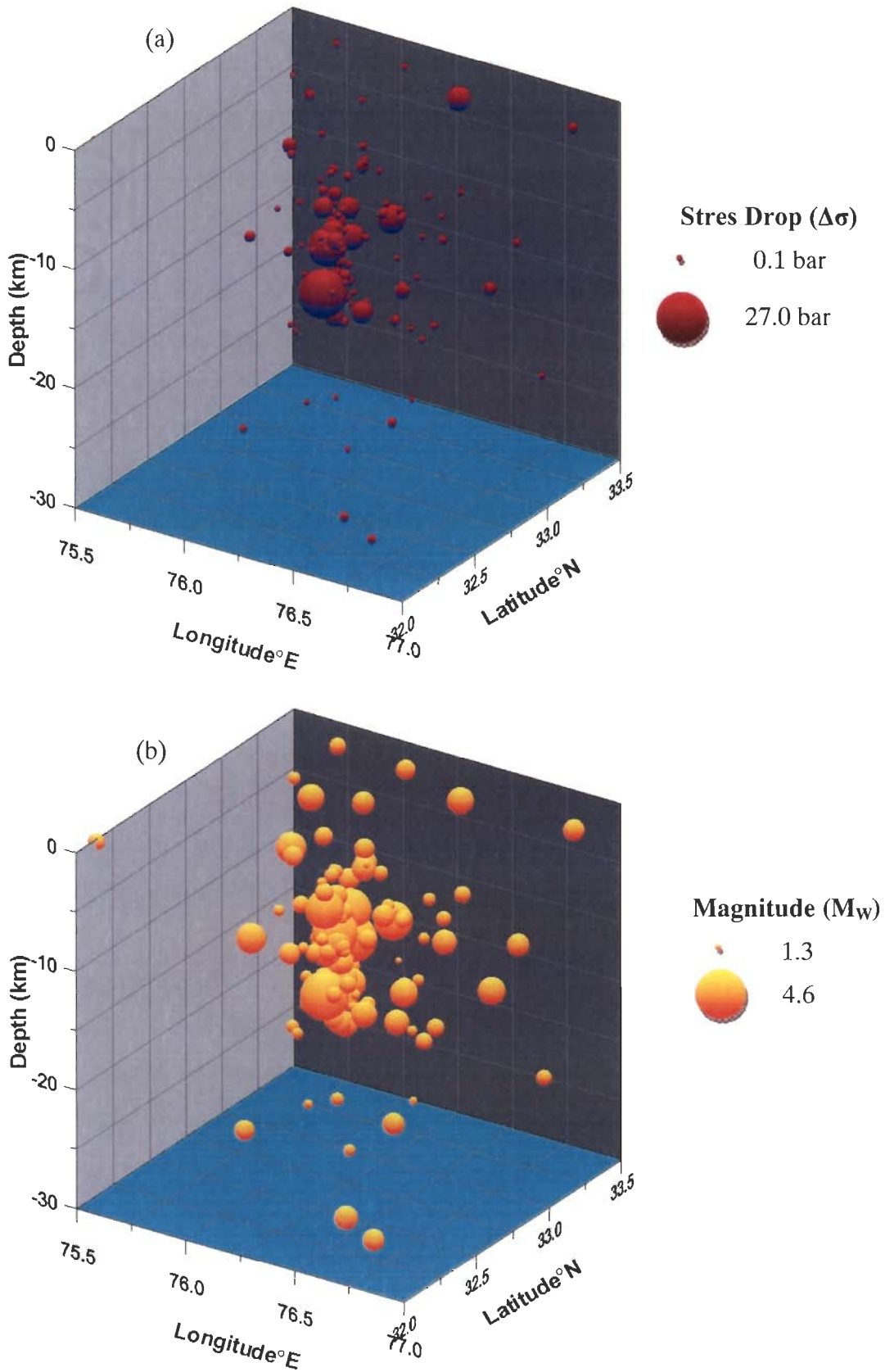
Figure 6.10. Assessment of stress drop and moment magnitude variation with depth (a) the variation of stress drop in the range of 0.1 to 27.3 bars (b) the seismic moment variation for the respective earthquakes.

weak crustal rocks. However there is a need to relate this observation with the variation of b value using more data which will also be useful for quantification of earthquakes for hazard studies.

6.6. CONCLUSION

Earthquake source parameters are estimated for 135 local seismic events having moment magnitude range 1.5<M_L<4.8. In this inversion the S-wave spectra of over 2000 seismograms are used. The source parameters of the earthquakes are obtained using Brune's circular model (Brune, 1970) after correction of amplitude spectra for geometrical spreading and site effect. For these earthquakes the determined corner frequency of the spectrum is in the range 1 to 10 Hz. The seismic moment of these events is 1.20 x 10^{18} dyne-cm to 1.44 x 10^{23} dyne-cm. The specified relation of Brune is used to convert the seismic moment into moment magnitude (M_w). The linear regression analysis to the set of seismic events is performed to obtain relations between M_w and the local magnitude M_L as well as coda magnitude M_C. The source radius for these earthquakes is in the range 0.1 km to 1.15 km showing increase with increase in seismic moment. The obtained stress drop is different for the micro-earthquakes compared to bigger size events. The maximum stress drop is 27 bar with a majority in the range 0.1 bar to 10 bar showing increase in value with the earthquake size irrespective of given relation. The different stress drops for different sized earthquakes indicate the break down in the similarity behavior of earthquake generation processes.

For earthquake up to Mw 4.6 a systematic increase of Brune stress drop is observed with increase of earthquake size for upper crust which may be related with compact source dimensions and high-frequency ground motion in the deeper part. The validation of this aspect for larger events (M > 5.0) can be done in future when enough data for such earthquakes become available. The slight increase of stress drop with hypocentral depth also suggests the increase of rock strength and thus yield stress with depth. These two aspects can be useful for hazard studies that may be addressed in future analysis.

CHAPTER 7

INTEGRATED INTERPRETATION, DISCUSSION AND DIRECTION FOR FUTURE RESEARCH

7.1. INTRODUCTION

The collision of Indian and Eurasian plates beginning some 50 m.y. ago has given rise to the Himalaya orogen (Gansser, 1964; Valdiya, 1980; 1984). Strains resulting from continued collision of these two plates make the entire Himalayan arc seat of profuse seismicity. The occurrences of major and great earthquakes along the Himalayan arc are the extreme examples of the plate boundary ruptures marking penultimate state of strains accumulation exceeding the frictional/material strength of the crustal rocks. The reactivation of faults in response to accumulating strain or adjustments of crustal blocks to decaying strains following major and great events account for the large fraction of micro and small earthquakes during inter-seismic periods. The space-time distribution of earthquakes, their inter-linkage to tectonic features, understanding of earthquake source processes and the medium characterization provides the basic tools to unveil the geodynamic processes, deeper seismogenic structures, physical state of rocks, constrain the alternative tectonic evolution models of the Himalaya as well as pave way for the assessment, mitigation and reduction of seismic hazards. Over past one hundred and twenty years, four great earthquakes, namely, the 1897 Shilong (M ~ 8.7); 1905 Kangra (M~8.0); 1934 Bihar-Nepal (M~8.3), and 1950 Assam (M~8.7) earthquakes have occurred along the length of the Himalayan arc. Assuming a steady elastic strain accumulation due to plate convergence, the return period of great plate boundary earthquakes (M > 8.0) in the Himalaya has been estimated to be a few hundred years (Molnar, 1990; Sukhija *et al.*, 1999) and thus the sections of the Himalayan arc between the ruptured zones of these great earthquakes are recognized as seismic gaps, where the probability of occurrence of future great earthquakes is high (Khattri, 1987). The GPS measurements corroborate such inference as accumulated strains in the central seismic gap between the ruptured zones of 1905 Kangra and 1934 Bihar-Nepal earthquakes are estimated to be large enough to drive one or more great earthquakes (Bilham *et al.*, 2001; Gahalaut, 2008). However, the paleo-seismological and historical evidences that two major earthquakes have occurred in 1505 and 1803 in the central seismic gap (Ambraseys and Jackson, 2003; Kumar *et al.*,

2001) have begun to question the validity of central Himalaya being a seismic gap (Rajendran and Rajendran, 2005). Even it has been estimated through paleo-seismology (Bilham and Szeliga, 2008) that the earthquake producing a slip of around 20m or even more has occurred in the Himalaya region at three zones. In this, one zone is in the NW Himalaya starting from Kangra and extended to southeast upto India-Nepal border. Occurrence of such earthquakes in future would lead to huge loss of human life and tremendous amount of economic loss; because population has increased many fold in this region of Himalaya and surrounding areas. The revisit to the records of pre-instrumentation period or earlier phase of skeleton seismometer network raise doubts about whether some of the earthquakes either did not release strain from the Himalaya or from the point of energy released fail to qualify as great Himalayan earthquakes (Rajendran and Rajendran, 2005; Gahalaut, 2008). Clearly, our understanding of space-time distribution of great Himalayan earthquakes, their return period as well as exact source mechanism is far from satisfactory. Curiously, the past 60 years have been exceptionally quiet in terms of great earthquake and this has raised concern about when and where the next one might occur.

Much of the earlier studies on Himalayan earthquakes relied on the observations at distant and widely spaced regional stations, largely outside the Himalaya and thus provided information on moderate and large earthquakes. Lack of information on small magnitude earthquakes coupled with large errors in hypocenter locations prevented correlation of observed seismicity of the Himalaya with mega-thrusts and other tectonic features of the Himalaya. Over the last decade, micro-earthquake data collected from temporary networks reveal clear segmentation of seismicity along the Himalayan arc with well-defined segments of intense/low seismicity, seismic gaps or tectonically stable zones (Srivastava *et al.*, 1987; Khattri and Tyagi, 1983; Gaur *et al.*, 1985; Khattri *et al.*, 1989; Kayal 2001, 2003). Such space-time segmentation of earthquake activity along the entire length of the Himalayan arc signifies complexities of the tectonic setting and crustal structures controlling strain accumulation/release that may be responsible for varied earthquake mechanisms in different parts of the Himalaya (Pandey *et al.*, 1995; Kayal, 2003; Bollinger *et al.*, 2004). The Kangra-Chamba region in NW Himalaya that formed the center of devastating 1905 Kangra earthquake (M8.0, location shown in **Figures 2.1 and 3.2**) has been one of the most active seismotectonic segments of the Himalaya. The region falls in the risk zone V on the seismic zoning map of India (http://www.gsi.gov.in/zonation.htm). From geological and tectonic

214

considerations also the Kangra-Chamba region exhibits certain distinctive character and is dominated by Nappes and Windows with variable extent well marked by highly undulating topography. The lack of good regional velocity model coupled with limited azimuthal distribution in existing seismological stations, particularly from north of the high seismicity zone, restricted the robust determination of the hypocenters and, thus, inhibited detailed insight into the tectonic setting associated with localized zone of the high seismicity. The special campaign mode arrays operated either to monitor local seismicity (Thakur *et al.*, 1997; Pandey *et al.*, 1995) or aftershock activities of 1991 Uttarkashi and 1999 Chamoli earthquakes (Kayal, 2001) have proved an effective tool to analyse the complex seismotectonic environment of the NW Himalaya on local scale. To generate area specific seismic velocity model and to improve the location of seismic events for better understanding of seismicity and seismotectonics of the Kangra-Chamba segment of the NW Himalaya, a special experiment with an array of closely spaced seismometers was started in April 2004. The present thesis discusses and presents the various aspects of this experiment, starting from the basic rationale, distinctive tectonic setting, design and upgradation of seismic network, data acquisition, application of more advanced processing tools to derive local velocity models, robust determination of hypocenters and their bearing on the tectonic interpretation to arrive ultimately at the seismotectonic model for the Kangra-Chamba region.

7.2. CHARACTERISTICS OF NW HIMALAYAN SEISMIC REGIMES

7.2.1. Seismic Regimes of NW Himalaya

The epicentral distribution of micro, small and moderate size earthquakes shows high concentration in nearly eastwest extended central part of the NW Himalaya (**Figure 3.2**). This high seismicity zone is mainly bounded between MBT and MCT and is viewed as a ramp structure in the detachment zone separating Indian plate and overriding Himalayan wedge (Pandey *et al.*, 1995; Thakur *et al.*, 1997). In NW Himalaya the topography suddenly changes in this part as measured by RMS deviation of elevation (**Figure 2.12**). The distribution of the larger size (M > 6) well located earthquakes is also concentrated in this zone in the NW Himalaya. The modeling of new GPS measurements suggests large concentration of strain that may lead to rupture of the section of mega thrust that has remained partially or fully locked (Banerjee and Burgmann, 2002). It is further argued that intense micro-seismic activity is triggered by

the inter-seismic stress accumulation around the down-dip end of the locked portion of the Main Himalayan Thrust fault (Bilham *et al.*, 1998 and Bollinger *et al.*, 2004).

Given the observation that rupture due to large and moderate size earthquakes occurred along the major thrusts of Himalaya, suggesting release of the accumulating strain by the seismogenic slips on these structures. Several duplexes and transfer structure exist in the Lesser Himalaya (Valdiya 1976, Arora *et al.*, 1982, Srivastava and Mitra, 1994) but how exactly they contribute to the pattern of the seismicity is not well understood and calls for continued monitoring of seismicity by wide aperture seismic network. The START 2004 experiment in the Kangra-Chamba region and the recent broad band seismic network in whole NW Himalaya established by WIHG is a step to fill vital gaps in our knowledge on the rarity of great earthquakes and more frequent occurrence of moderate and large magnitude earthquakes in this part of the Himalaya. The micro-earthquake activity being recorded by this network will help to further understand the different aspects of physics of the earthquake source. The data set from this network coupled with GPS monitoring at widely spaced GPS stations could also help to test the alternative hypothesis to the generating mechanism of earthquakes.

7.2.2. Longitudinal Seismic Segmentation Along NW Himalaya

As discussed in Chapter 2 the earthquakes of micro- to small magnitude size are not uniform in NW Himalaya and longitudinal seismic segmentation exists. The observation emerging from temporary seismic networks operated during last 10-20 years (Pandey *et al.*, 1995; Kayal, 2003; Bollinger *et al.*, 2004) support this concept for whole Himalayan arc indicating well defined segments of intense/low seismic zones. Therefore the so called high seismicity described as MHSB of about 100 km width between MBT and MCT in the Himalayan arc has longitudinal inequalities. In the last century knowledge of Himalayan seismicity has been gained through moderate to large magnitude earthquakes using the information of regional and global seismic network. It was summarized in Chapter 2 that the magnitude threshold of the seismic catalogue of NW Himalaya was M4.5 since the introduction of World Wide Seismic Station Network (WWSSN) in 1965 and it came down to M2.5 in 1999. This lowered threshold basically is due to addition of more seismic stations in regional and local seismic networks. Now this threshold for the NW Himalaya is nearly M2.5 (Arora *et al.*, 2008) and the current distribution of seismicity in this part of Himalaya highlights the concentration of seismicity to a narrow belt around the surface trace of MCT. Therefore

216

now we are in a position to compare the aspects of seismic zonation for micro, small and major earthquakes. The epicentre locations given in **Figures 2.1** and the release of seismic energy in **Figure 2.8** highlight the concentration of seismicity around MCT in NW Himalaya with segments of intense/low seismicity zones. The present work along with the previous studies also indicates that micro-earthquakes are also concentrated in nearly eastwest direction around MCT in NW Himalaya again with longitudinal segmentations. The possible reason for this segmentation may be the heterogeneous accumulation of strain in the inter-seismic period due to local tectonic features and persistent asperities (Bollinger *et al.*, 2004). The high concentration of seismic activity in the Kangra-Chamba region of NW Himalaya has been correlated with the variation of asperities (Arora *et al.*, 2008) that is well revealed by topography, geotectonics and varied earthquake mechanisms.

7.2.3. Space-Depth Distribution of Seismicity in Kangra-Chamba Region

The earthquake sources in the Kangra-Chamba region of NW Himalaya are shallow focused, i.e. mainly concentrated in the upper crust. The micro to small magnitude earthquakes data used in the present work for obtaining 1D and 3D velocity structure, focal mechanisms and earthquake source characteristics has focal depth up to 40 km from the surface of the earth. However, about 90 percent of these events are located above the detachment plane, the plane defining the under-thrusting Indian plate located between 10 and 20 km in the study region and dipping towards northeast. The epicentral zone of the devastating Kangra earthquake of 1905 is a zone of high seismicity where few events are also located below the detachment plane having different type of focal mechanism as compared to the solutions above detachment zone. This concentration of high seismicity and the variable behavior of focal mechanism are related to perpendicular directed tectonics in this part in which the major tectonic units are dipping towards northeast and in the eastern part the HHC and RW are dipping towards west (**Figure 3.2**).

7.3. NEW UNDERSTANDING ABOUT CRUSTAL STRUCTURE AND ITS IMPLICATIONS

7.3.1. Optimum Crustal Velocity Structure

While locating the earthquakes using 36-stations seismic network it was observed that the error in location could not be minimised using the existing crustal

velocity model (Kamble *et al.*, 1974; Mukhopadhyay and Kayal, 2003) even though the station coverage was strengthened. Therefore, first of all the data set using 36-stations of NW Himalaya is used to obtain the optimum velocity crustal structure of the region. This data set contained 350 regional and local earthquakes recorded by 36 stations. This data set was divided into two parts to incorporate 1D velocity structure of the crust for the NW Himalaya using two different methods. In one method, travel time-distance curves for 285 shallow focused earthquakes were utilized to get 1D velocity model of the crust along with Moho depth. Regression analysis of travel time-distance curves showed that the crust mainly consists of two layers with thicknesses of nearly 21 km and 24 km for upper and lower crust respectively. The obtained P-wave velocity of the second layer and underlying half-space (8.27 km/s) are typical of the continental lower crust and uppermost mantle (Kennett *et al.*, 1995).

This seismic network of 36 stations was denser in the Kangra-Chamba region comprising 21 stations which covers about one-fifth part of the NW Himalaya. 172 local earthquakes of Kangra-Chamba region were used to obtain 1D velocity model using simultaneous inversion of P- and S-wave phase data. Due to the shallow nature of seismicity in the Outer and Lesser Himalaya, the inversion of travel time paths could be used to estimate velocity structure only for the upper crust. The minimum 1D vertical velocity model obtained from simultaneous inversion permitted division of the upper crustal region to a depth of 20 km in to a 3-layer structure. Therefore, the combination of two approaches helped to divide the crust beneath Kangra-Chamba region of the NW Himalaya, with a total thickness of 45 km into 4-layers with Vp (Vs) velocities of 5.23 (3.04) km/s, 5.66 (3.26) km/s, 5.71 (3.18) and 6.38 (3.72) km/s with intervening interfaces at 10, 15, ~18-20 km. The merit of this 4-layer velocity model over the simple 2-layer crustal model, obtained either from travel-time plots or that reported in Kamble *et al.* (1974) is immediately obvious from the fact that travel time residual for all the 172 events has reduced from 0.50s to 0.32s.

A salient feature of the inverted velocity model is that both Vp and Vs increase with depth except in the third layer. In third layer (depth 15 to ~18 km), the proportional enhancement of Vp is lower, while Vs is slightly less than upper layer, resulting in high Vp/Vs ratio of 1.81. In the compression regime of Himalaya, the frictional heat generated by under-thrusting processes is favorable to initiate dehydration reactions at mid crustal depths where temperatures are in the range of 350-400°C (Hyndman and Shearer, 1989). The present evidence of anomalous layer marked by high Vp/Vs ratio

due to relatively low shear wave velocity in the depth range of 15 km to ~18 km is consistent with the closing of saturated micro-cracks with increasing confining pressure (Nicholson and Simpson, 1985). The top 10 km thick layer with P-wave velocity of 5.23 km/s, much lower than the typical velocity of upper continental crust, can be related to the thick sheet of weakly metamorphosed sediments of the CN that encompass the seismically active zone, the Kangra-Chamba sector. This geological attribute strongly supports the view of Thakur (1998), who based on the stratigraphic morpho-tectonic consideration, postulated the CN sequence to be approximately 8 km thick. In this tectonic scenario, the 5 km-thick second layer with Vp and Vs of 5.66 km/s and 3.26 km/s, respectively can be viewed as meta-sediments of under-thrusted sequence of the LH or the over-thrusted sedimentary wedge of the Himalaya overriding the down-going Indian plate.

7.3.2. Lateral Velocity Inequalities and Station Corrections

While plotting the average station delay times (**Figure 3.12**) for P- and S-phases a systematic variation from southwest to northeast was observed. The contour plots of station corrections of both waves with reference to BRM station are dominated by strong relative high value in the southwest part that signifies true lower velocities than the 1D model in the southwest part of the study area and its values change to pronounced low in the northeast corner which corresponds to relatively higher velocity zone. These station corrections are the deviation of the velocity from 1D model that strongly depends upon topography and lateral velocity variations associated with heterogeneous near-surface structure (Kissling, 1995). The area of relatively higher station delays broadly encompasses low-velocity alluvial/sediments of Indo-Gangetic Plains and Siwaliks whereas the region of low station delays, northeast of the Chamba thrust, is covered by the Tethys sequence of CN. However, this distinctive pattern in the eastern part, where similar contrast in lithology prevails across the Siwalik, is either almost absent (P-wave) or is greatly subdued in magnitude (S-wave). It seems likely that in addition to surface lithology, a substantial part of station corrections may relate to alternative near surface or deeper crustal velocity structure. On the P-wave map, the zone of relatively higher station delays terminates sharply in a prominent NE-SW trend. A critical examination of the delay patterns reveals that the region of transition embeds a zone of local high striking NE-SW, both on the P-wave and S-wave velocity model obtained using 3D inversion. The anomalous trend does not correlate with any

topographic or surface tectonic feature. The inversion of present earthquake data sets, using formulation of 3D local earthquake tomography (Chapter 4 and Kumar *et al.*, 2010), map lateral velocity heterogeneity. It suggests presence of a low velocity zone, coincident with this NE-SW trend, in the depth range of 2-5 km range, which is underlain by high velocity body.

7.3.3. Joint Hypocenter Determination

The Joint Hypocenter Determination (JHD) performed, using the optimum 1D velocity model, permits relocation of hypocenters with higher precision because it allows for elevation changes from station to station and lateral velocity variations associated with heterogeneous near-surface structures (Kissling *et al.*, 1995), termed station correction. The improved locations of epicenters show close cluster of seismic events in the epicentral track of 1905 Kangra earthquake, while away from this zone the seismicity in the Chamba sector has more even distribution **(Figure 3.15)**. The earthquake parameters obtained after incorporating station corrections result in considerable improvement, particularly in estimation of the depth values. This is clearly borne out in the space-depth distribution plots of the hypocenters obtained after incorporating the station corrections **(Figure 3.15)**. Both sectional plots are in vertical plane and are along two representative profiles perpendicular to the strike of the Himalaya. The profile AB traverses the section of the Kangra where majority of the seismic events are clustered in a narrow space. The second profile CD is placed on the Chamba Nappe where the seismicity is evenly distributed. On both the profiles, hypocenters of all earthquakes that fall within 25 km on either side of the cross-section line are plotted. The space-depth distribution also shows some distinctive pattern in the cut off depth of seismicity. The relocated hypocenters of earthquakes show clear alignments with the major faults/thrusts of the region and help view their subsurface extension.

7.4. INTERPRETATION AND DISCUSSION

7.4.1. Mid-Crustal Low Velocity Layer and Its Seismotectonic Significance

It is known that in the Himalayan collision regime, the Indian Plate flexes and under thrusts at gentle dip resulting in the increase in the thickness of the overriding wedge from frontal Himalaya to higher Himalaya. The lateral variation in the thickness of overriding wedge is examined as an alternative source of long-term trend in station

corrections. The nature of variations in the absolute value of S-wave station corrections is shown along two selected profiles, AB and CD (upper panels of **Figure 3.15b**). As noted earlier, these long-term trends in station corrections may relate to variation in thickness of the over-thrusted sedimentary wedge; the first rough estimate on the geometry of the dipping under-thrusting Indian plate is approximated by converting the station corrections to thickness of the wedge corresponding to the average velocity. In such a transformation, the averaged 1D velocity structure can be viewed as northeast dipping layers. As an example, the overall geometry of the upper surface of the mapped anomalous low-velocity layer in the depth range of 15–18 km will be seen as marked in **Figure 3.15** for both profiles. It is interesting to note that, except for a narrow section directly beneath the clustered zone of epicenters, the inferred geometry of the low-velocity layer defines the lower depth boundary of crustal seismicity.

This anomalous layer characterized by low S-wave velocities and high Vp/Vs ratio is interpreted to be caused by the presence of the fluids at depth (Scarft *et al.*, 2003). Presence of fluid saturated layer tends to simulate the onset of ductile behavior and hence, the brittle-ductile transition in the crust is shown in many seismically active areas to define the cut-off depth of micro-seismicity caused by crustal stresses (Stanley *et al.*, 1990). Mukhopadhyay and Kayal (2003), based on the inversion of aftershocks data of 1999 Chamoli earthquake in Garhwal Himalaya, noted similar low S velocity and higher Vp/Vs ratio zone that demarcate the lower limit of crustal seismicity. More recent high quality receiver functions also reveal almost continuous mid-crustal low velocity interface imaged at 17-20 km depth beneath the frontal Nepal Himalaya (Schulte-Pelkum *et al.*, 2005). The deep geo-electric model of the Himalaya also suggests presence of low-angle north dipping conducting layer beneath the Outer Garhwal Himalaya at mid-crustal depths of 15-20 km (Reddy and Arora, 1993; Arora, 2003).

It can be visualized that in the compressive regime, adjusting to differential tectonic stresses brittle and ductile sections due to rheological differences can facilitate development of new thrust/detachment plane at brittle-ductile transitions (Bailey, 1990; Jodicke, 1992). The presence of fluids produced by dehydration reaction or driven off from the down going sediments may act as lubricants reducing the sliding resistance along the thrust/detachment plane creating conditions favorable for the concentration of tectonic failure manifested by alignment of earthquake foci along such a plane (Arora, 2003). The foci of many moderate to large magnitude earthquakes align on the NE

dipping plane of decollment and are consistent with this seismotectonic model of the Himalaya (Ni and Barazangi, 1984). The FPS of the three moderate (M~4) earthquakes (FPS 4,5,7 of Kumar *et al.,* 2009) with their nodal plane dipping at low angles of 10° - 15° are placed on the upper surface of a plane defined by anomalous low velocity layer. The earthquakes of November 5, 1968 (M_L 5.0) and June 14, 1978 (M_L 5.4) from the same region revealed similar dips in thrust movement (Srivastava *et al.,* 1987).

7.4.2. 3D Velocity Structure and Refinement of Earthquake Locations

The recently derived 3D velocity model has improved the earthquake source locations describing close association of seismicity with tectonic structures of the region. The 3D variation of Vp, Vs and Vp/Vs is obtained in 100 x 100 x 18 km^3 crustal part in the source area of 1905 Kangra earthquake. The location of micro- and small magnitude earthquakes obtained using 1D velocity model are further refined through 3D velocity models. The refined locations show that the seismic activity in this region is shallow focused occurring mainly within upper 20 km crust with most of the events are within upper 10 km. A systematic and significant variation in Vp, Vs and Vp/Vs were observed. The low velocity zones of Vp and Vs are extended roughly in the east-west direction and its adjoining northern part of CN has high values. At 2 and 5 km depth a NE-SW tending low velocity zone is observed in the eastern part, which may be the intrusion of low velocity material most probably caused by two perpendicular thrust tectonics. Northeast dipping low velocity zone is imaged from 15 to 18 km depth clearly from the vertical and horizontal cross sections. This is in agreement with 1D velocity model indicating velocity variation along the main tectonic units of the region. Almost all the seismic events are located either on the boundary of low and high velocities or in the region of high velocity zone. Therefore, the uppermost brittle part of the crust is being ruptured by micro-earthquake activity and the brittle-ductile transition defines the sharp lower cut-off depth of crustal seismicity. Vp/Vs being direct measure of Poisson's ratio image boundaries related with intrinsic lithogic transitions of physical state of the medium (saturation state). It is observed that most of the earthquakes are located at the boundary between high and low Vp/Vs zones.

7.4.3. Tectonic Linkage with Fault Plate Solutions

The obtained FPSs of earthquake rupture and the sense of displacements along the tectonic faults in the source zone of the 1905 Kangra earthquake help in identifying

nature of faults. The FPS of 42 earthquakes was obtained using the first polarity motion of the P-wave. The refined epicentre locations (**Table 5.3**) of these events are shown in **Figures 5.11 and 5.12** and tectonic linkage in the study region was evaluated (**Figure 5.19**). The complex tectonic setting of the sector is immediately evident from the fact that varieties of focal mechanisms are operative in the region. There is a variation of solutions in different parts but in general this quantification helped to divide the region into two parts, the upper 10 km thick crust above the plane of detachment have somewhat different nature compared to the deeper part. In the upper section most of the solutions have reverse fault mechanisms and the resultant deformation attained along parts of the tectonic faults near the earthquake source reveals the thrusting nature above the detachment plane that is related with the major thrust faults (MBT, PT shown with compression axis in **Figure 7.1**) of the region. In the deeper part, the present solutions have reverse and normal fault mechanism in equal proportion where few normal mechanism coincide with CNF indicating northsouth extension with gradual displacement of the CN towards south (**Figure 7.2**). Few normal mechanisms are also located in the part having dense cluster of seismic activity where the perpendicular interaction of two tectonic environments may be reason of complex mechanisms as well as high seismic activity.

The previous available solutions of bigger size events describe the deformation for the longer portion of the tectonic fault as compared to present solutions. These are mainly in the deeper part (**Figure 5.12**) and having thrust mechanisms indicating overall deformation due to thrusting tectonics mainly along the plane of detachment.

7.4.4. Stress Pattern Subzonation Obtained Through P- and T-Axes Inversion

The focal mechanism stress tensor inversion (FMSI) method of Gephart and Forsyth (1984) and Gephart (1990) was used to obtain best fitting stress tensor through 42 seismic events for the Kangra-Chamba region. For comparison, the stress tensor inversion was also done for the adjoining southeastern region. The results of these two data sets are plotted in **Figure 5.17** where the plot in part (a) is the result of the data of Kangra-Chamba region and in part (b) for the adjoining southeast region. Using this, the maximum principal stress axis (σ_1) for Kangra-Chamba region is found to have average trend towards N56° along with a plunge of 34°. Therefore the resultant stress is aligned towards northeast in this part of NW Himalaya. The principal stress axis is dominant in this inversion indicating predominantly thrust type of environment. However, the results

obtained for the adjoining southeast region are plotted in **Figure 5.17b** showing reverse to strike-slip type of faulting. The maximum principal stress axis trends to N282° and have a shallow plunge of 14°. The stress regime suggests reverse to strike-slip regime due to oblique attitude of intermediate and minimum stress axis.

7.4.5. Characterization of Earthquake Sources Using Waveform Spectra

The waveform spectra of the earthquakes were used to measure the source characteristics using Brune circular model. The determined corner frequency of the spectrum for the local earthquakes having moment magnitude between 1.3 and 4.6 is in the range 1 to 10 Hz. For these earthquakes, the seismic moment, M_0 varies between 1.20×10^{18} dyne-cm to 1.44×10^{23} dyne-cm with larger seismic moment for the higher magnitude. The source radius for these earthquakes is in the range 0.1 to 1.2 km showing increase of radius with the increase in seismic moment. The variation of stress drop is different for micro-earthquakes and the earthquakes having small to medium magnitude. Its value is higher and nearly constant for bigger events. The average stress drop for these earthquakes is 18 bar with maximum value of 27 bar while for micro-earthquakes it increases linearly from 0.1 bar to 10 bar (**Figure 6.7**) with the increase of earthquake size. However, the general assumption is that the stress drop for one region is constant due to similarity in the behavior of generation of all types of earthquakes. But it is generally seen that this is valid only for medium and big size of earthquakes but not for micro-earthquakes. The difference in stress drop pattern indicates either the break down in the similarity behavior of earthquake generation processes or it may be the effect of attenuation for different frequency range. The observation for NW Himalaya also indicates that the stress drop increases with the magnitude for micro-earthquakes upto maximum seismic moment of 1.0×10^{21} dyne-cm equivalent to moment magnitude of 3.2.

Figure 7.1: Plot of compression (P) axes obtained for few earthquakes of recent data set, denoted by converging arrows superimposed on Vp, Vs and Vp/Vs tomograms at different depth levels. Hypocenter distributions in specific depth intervals are also superimposed on velocity tomograms with black dots.
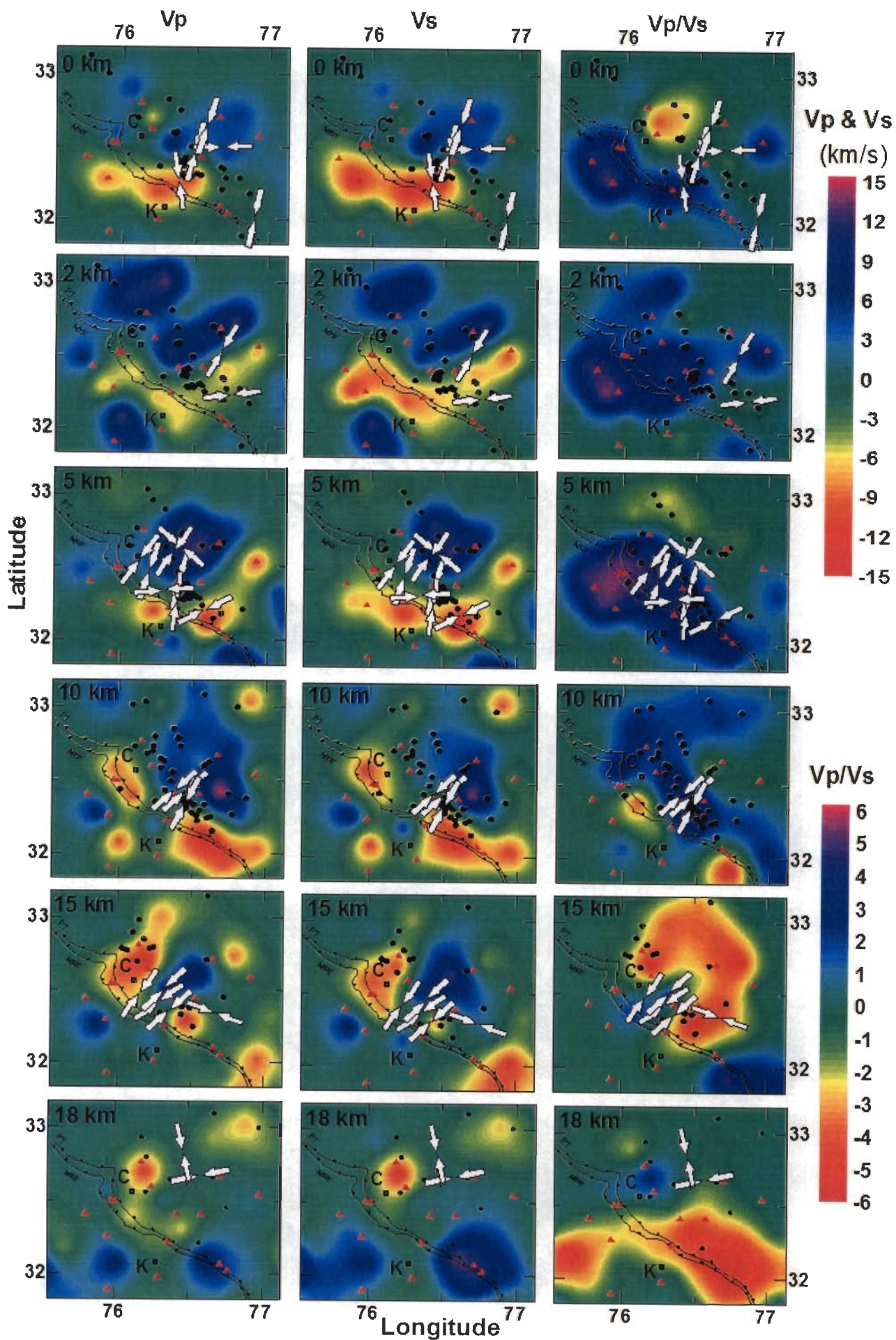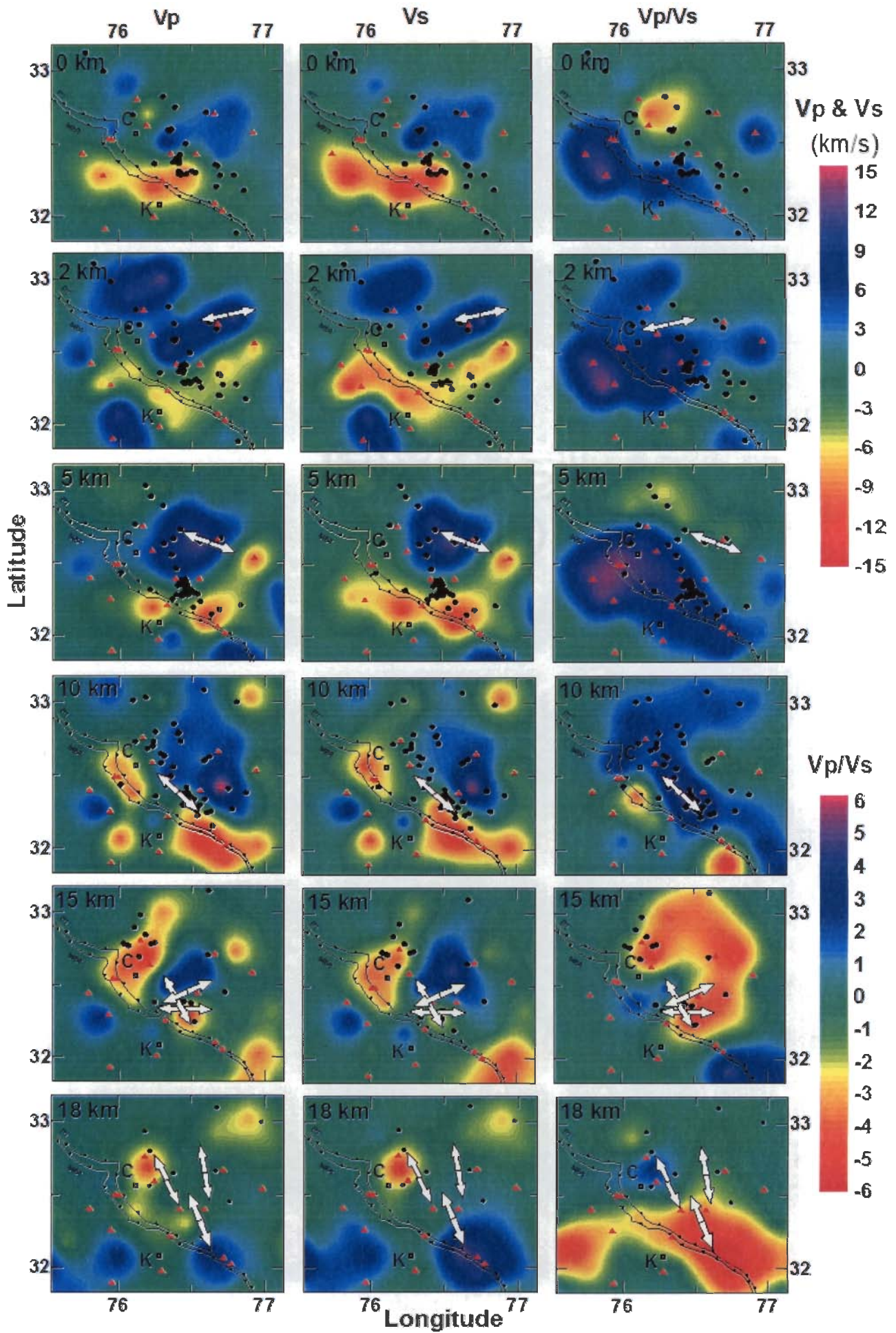
7.4.6. Variation of Stress Drop with Depth

In the current data set on an average the magnitude of the earthquake increases with the increase in focal depth up to a depth of 15-18 km. Also as given in the previous section the stress drop of micro-earthquakes increases with the increase of the earthquake size. Therefore the average aspect of this data set indicates that the stress drop increases with the increase in focal depth up to a depth of 15-18 km. However, few deeper events in this upper crust of 15-18 km are also of smaller size but having higher stress drop (**Figure 6.10**) compared to shallow focused of similar magnitude. The low stress drop indicates that the region is not able to withstand higher stress and prone to release the accumulated energy with small increase of stress. In opposite case more is the stress drop in a region higher is the capability to withhold the ongoing tectonic stress. Therefore with the increase of the depth in the Kangra-Chamba region the strength of holding stress is more. However this is valid only for the micro-earthquake activity and in case of medium and big size earthquake generally the observed stress drop is constant.

7.4.7. Elements of Seismotectonic Model and Clustered Seismicity

The improvement in earthquake location through recent 1D crustal velocity model and its further refinement using JHD and 3D tomographic inversion helped to develop the close relation of seismicity with tectonic features of the region. Profiles AB and CD (**Figures 3.15**) are taken to observe the sub-surface behavior of seismicity, tectonics and velocity variations. On both profiles, the low velocity zone is observed in the depth range of 15-18 km in 1D velocity model inversion (**Figure 3.15**) and it is characterized by high Vp/Vs (**Figures 4.16, 4.17 and 7.3**) and lowest Vs through 3D inversion (**Figures 4.16 and 4.17**). Attributing low velocity to the presence of fluids and noting it a conspicuous feature of the Garhwal (Arora, 2003) and Nepal Himalayas (Schulte-Pelkum et al, 2005), the top interface of mid-crustal LVZ was interpreted as brittle-ductile transition. As observed in many seismically active zones, brittle-ductile transition defines sharp lower cut-off depth of crustal seismicity (Sibson, 1986). Top

Figure 7.2: Plot of tension (T) axes obtained for few earthquakes of recent data set, denoted by converging arrows superimposed on Vp, Vs and Vp/Vs tomograms at different depth levels. Hypocenter distributions in specific depth intervals are also superimposed on velocity tomograms with black dots.

interface of low velocity (**Figure 3.15**) and high Vp/Vs in (**Figure 7.3**) in general traces this brittle-ductile transition as a northeast low angle dipping interface placed at average depth of ~15 km near MBT. Dip of fault planes for moderate to large earthquakes also tends to align with this interface (**Figure 7.3**).
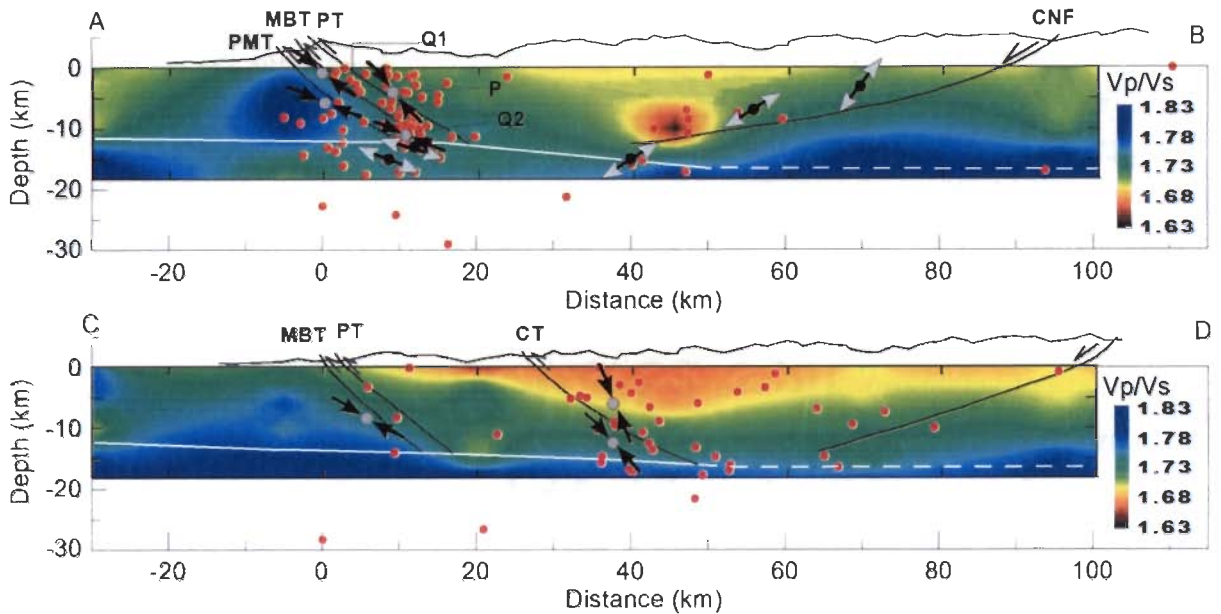
Figure 7.3: Distribution of earthquake hypocenters in relation to change in Vp/Vs ratio on depth sections along profiles AB and CD (Figure 3.15) are shown where well defined clusters, referred to in the text are also marked. Arrows indicate nature of stress, compression or extension, slope of these lines with respect to horizontal denotes dip of nodal plane of FPS.

Such alignment of nodal planes on a single plane had led Ni and Barazangi (1984) to visualize linear plane as basement thrust fault (BTF), separating down going Indian plate from southward propagating sedimentary/metamorphic wedge of the Himalaya. The seismotectonic model of Seeber et al., (1981) also indicates low angle dipping detachment plane towards north where the rupture of large magnitude earthquakes occurred along this plane propagating up to the frontal Himalaya. Figure 7.4 shows a cartoon representation of the tectonics of the study area. Here the local features like CN are superimposed on the general tectonic model of the Himalaya given by Seeber et al. (1981). As shown in **Figure 7.4**, the low magnitude earthquakes are aligned on the junction of detachment plane and the MCT, however the micro earthquake activity is occurring (Khatri, 1987; Kayal, 2001) in a 50 km wide zone

between MBT and MCT described as MHSB. In the present study also the micro-earthquake activity is mainly concentrated along of MBT/PT and mostly associated with the basement of the CN along these northerly dipping major tectonic faults of the region. Therefore on the basis of present study and the earlier work for the Himalayan region, the seismotectonic model developed is shown in **Figure 7.4** that indicates following three concepts (1) the micro-earthquake activity is shallow focused mostly occurring in the uppermost crust upto 15 km depth above the plane of detachment and is mainly associated with major tectonic faults of thrust nature dipping towards north or northeast (2) the large magnitude earthquakes are occurring on the detachment plane causing northly dipping gentle angle thrust rupture and propagating upto frontal Himalaya.
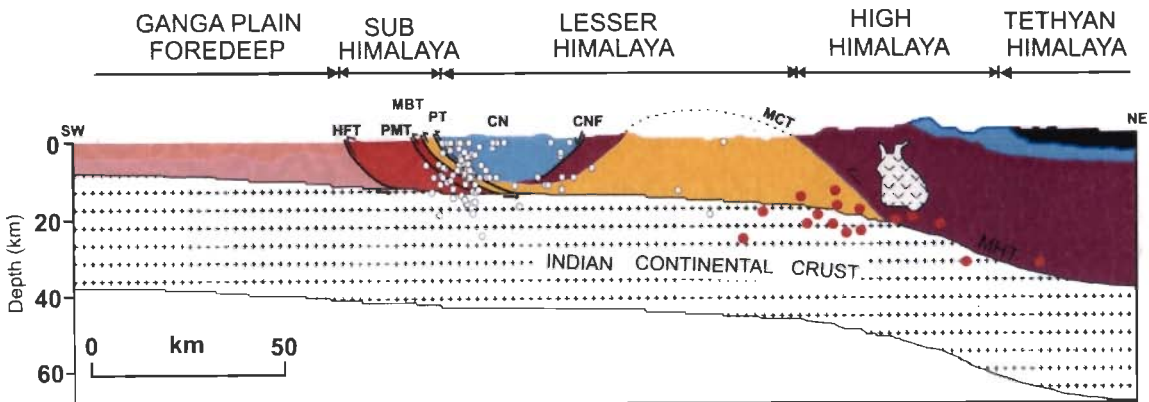
Figure 7.4: Seismotectonic Model developed based on present and previous earthquake data of NW Himalaya. Previous earthquakes are shown as orange dots and present data set are shown as white dots.

7.4.8. Direction for Future Work

This work was carried out with a small data set of local seismic events. However, the obtained parameters of the data were refined and highly accurate. There is need to strengthen these results using more data with more number of seismic stations. The obtained crustal structure, its refinement with additional data and combination of information obtained though other methods using regional and tele-seismic events will be useful for better understanding the seismic regimes. The structure will be improved further using other geophysical investigations. With addition of more stations in this network, the installation of more networks in the adjoining regions and the addition of

other geophysical parameters will be useful for improving understanding the geodynamic processes operating in the Himalaya.

7.5. CONCLUDING REMARKS

An overview of the space time distribution of seismicity resulting from continuous monitoring using local and regional network within and outside the Himalaya has given insight in to the nature and extent of seismicity. The synthesis of seismicity pattern, velocity structure, distinctive focal mechanisms coupled with nature of stress distribution allow new insight in to operative dynamics that control the seismotectonics of the Kangra-Chamba region. In the inverted velocity model, the depth range of 15-18 km is characterized by low S-wave velocity and high Vp/Vs ratio and is defined as a fluid-filled detachment plane that defines the cut-off depth of crustal seismicity in the region. The velocity structure of the lower crust and Moho is established through the time-distance plot, which suggests an average crustal thickness of 44 km. Future studies using teleseismic tomography may help to resolve the velocity of the lower crust and the upper mantle. Beside the well-known association of seismicity with the MBT/PT/CT that sole down to merge with the detachment plane, the space-depth distribution of hypocenters brings out the alignment of hypocenters along the CT and possibly along the CNF.

Proposed model envisages that strains resulting from continued collision in the Himalaya are partitioned differentially at distinct tectonic features to produce characteristic seismicity pattern at different depths and varied mechanisms. In the first place accumulating strains are partly consumed by normal-fault type displacements along CNF and reverse-fault movements on CT/PT/MBT, which account for low magnitude wide spread seismicity in upper 8-10 km of the crust. At intermediate depths from 8 to 15 km, adjusting to residual compressive stresses, the detachment or the lower end of MBT/PT slips episodically in stick slip manner to produce thrust dominated focused seismicity. Local NE-SW oriented structure in southeast corner of the study area appears to play important role in producing local stress concentration. Nucleation of such secondary stresses at the base of northeast dipping MBT may lead to extensional stresses producing normal type earthquakes seated below plane of detachment. Since in small localized block, three source regions of seismicity at different depths are vertically coincident, epicenter distribution map shows intense clustering of earthquakes of different mechanisms.

230

REFERENCES

1. Aki, K., (1968), Seismic displacement near a fault, J. Geophys Res, 73, 5359-5375.

2. Aki, K., (1969). Analysis of the seismic coda of local earthquakes as scattered waves. J. Geophys. Res 74, 615-631.

3. Aki, K. (1970), Geophysics, In Seismic Design for Nuclear Power Plants, (Hamsen, R.J. Ed). MIT Press, Cambridge, Mass. 91-113.

4. Aki, K. and Lee, W. H. K., (1976). Determination of three-dimensional velocity anomalies under a seismic array using first P arrival times from local earthquake, I, A homogenous initial model. J. Geophys. Res., 81, 4381-99.

5. Aki, K., and Richards, P.G., (1980). Quantitative Seismology: theory and Methods. W.H. Freeman, New York, pp. 932.

6. Allegre, C.J ., et al ., (1984) . Structure and evolution of the Himalayan – Tibet orogenic belt. Nature 307 , 17-22.

7. Allen, T. I., G. Gibson, A. Brown, and Cull, J.P., (2004). Depth variation of seismic source scaling relations : implications for earthquake hazard in southeastern Australia, Tectonophysics 390, 5-24.

8. Alsdorf, D., Makovsky, Y., Zhao, W.J., Brown, L.D., Nelson, K.D., Klemperer, S.L., Hauck, M., Kuo, J. (1998b). INDEPTH (International deep profiling of Tibet and Himalaya) Multi Channel Seismic reflection data: Description and availability. Journal of Geophysical Research, 103.. 26,993-26,2999.

9. Ambraseys, N.N. and Douglas, J., (2004). Magnitude calibration of north Indian earthquakes. Geophys. J. Int., 158, 1-42.

10. Ambraseys, N.N. and Jackson, D., (2003). A note on early earthquakes in northern India and southern Tibet. Curr. Sci., 84, 570-582.

11. Anand, A., and Jain, A.K., (1987). Earthquakes and deformational structures (seismites) in Holocene sediments from the Himalayan-Andaman arc, India. Tectonophysics, 133, 105-120.

12. Anderson, J, G., Hough, S.E., (1984). A model for the shape of the Fourier amplitude spectrum of acceleration at high frequencies. Bull. Seism. Soc. Am. 74, 1969-1993.

13 Anderson, E. M., (1951). The dynamics of faulting and dyke formation with application to Britain, 2nd ed., Edinburgh, Oliver and Boyd.

14 Andrews, D.J., (1986). Objective determination of source parameters and similarity of earthquakes of different size. In: S.Das, J. Boatwright and C.H.

Scholtz (Editors), proc. 5th Maurice Ewing Symp. Earthquake Source Mechanics. Am. Geophys. Union, Washington, DC, pp. 259-267.

15   Angelier, J., (1979). Determination of the mean principal directions of stresses for a given fault population. Tectonophysics, 56, pp. T17-T26.

16   Angelier, J. and Baruah, S., (2009). Seismotectonics in Northeast India: a stress analysis of focal mechanism solutions of earthquakes and its kinematics implications. Geophys. J. Inst. Doi: 10.1111/j.1365-246X. 2009.04107 .x pp. 1-24.

17   Archuleta, R., Cranswick, E., Mueller, C., Spudich, P., (1982). Source parameters of the 1980 Mammoth Lakes, California, earthquake sequence. J. Geophys. Res. 87, 4595-4607.

18   Archuleta, R.J., (1986). Downhole recordings of seismic radiation.In: Das, S., Boatwright, J., Scholz, C.H. (Eds), Earthquake source Mechanics, Proceedings of the 5th Maurice Ewing Symposium. American Geophysical Union, Washington, D.C, pp 319-329.

19   Arora, B.R., Lilley, F.E.M., Sloane, M.N., Singh, B.P., Srivastava, B.J. and Prasad, S.N., (1982). Geomagnetic induction and conductive structures in northwest India. Geophys. J.R. astr. Soc., 69, 459-475.

20   Arora. B.R., (1993). Implications of Electrical conductivity structures int the tectonic framework of Northwest India. Curr Sci, Vol. 64, NOS 11&12, 10&25. Pp 848-855.

21   Arora, B. R. (2003). Seismotectonics of the Frontal Himalaya through the electrical conductivity imaging, In: Eds. N. Fujinawa and A. Yoshida, Seismotectonics in Convergent Plate Boundary, Terra Publications, Tokyo. 261-272.

22   Arora, B.R., Unsworth, M.J., Rawat, G., (2007). Deep resistivity structure of the northwest Indian Himalaya and its tectonic implications, Geophys. Res. Lett. 34, L04307.

23   Arora, B. R., Kumar, N., Rawat, G. and Paul, A., (2008). A peep into the Himalayan Seismicity. Mem. Geol. Soc. India, 72, 29-46.

24   Avouac, J.P., (2003). Mountain building, erosion, and the seismic cycle in the Nepal. Advances in Geophysics 46, 1-80.

25   Bailey, R. C. (1990). Trapping of aqueous fluids in the deep crust, Geophys. Res. Lett. 17, 1129-1132.

26   Banerjee, P., and Burgmann, R., (2002). Convergence across the northwest Himalaya from GPS measurement. Geophys. Res. Lett., 29 (13), 30.1-30.4.

27   Bangar A.R., (1976). Mechanism of Kinnaur (Himachal Pradesh, India)

earthquake of January 19, 1975. Tectonophysics, Vol. 31, pp. T5-T11.

28   Baranowski, J., Armburster J, Seeber L, Molnar, P., (1984). Focal depths and fault plane solutions of earthquakes and active tectonics of the Himalaya. J. Geophys Res 89: 6918-6928.

29   Bettinelli, P., Avouac, J.P., Flouzat, M., Jouanne, F., Bollinger, L., Willis, P., and Chitrakar, G.R., (2006). Plate motion of India and interseismic strain in the Nepal Himalaya from GPS and DORIS measurements, Journal of Geodesy, doi: 10.1007//s00190-006-0030-3.

30   Bhargava, O. N., Ameta, S. S., Gaur, R. K., Kumar, S., Agarwal, A. N., Jalote, P. M., and M. L., Sadhu, (1978). The Kinnaur (H.P. India) Earthquake of 19 January, 1975: Summary of geoseismological observations Bull. Ind. Geol. Assoc., 11(1), 39-53.

31   Bhattacharya, S.N., and Kayal, J.R., (2005) Seismicity of The Himachal Himalaya: Constraints from Local Seismic Network. Geol. Surv. Ind. Spl. Pub. 85, pp. 71-79.

32   Bilham, R., K. Larson, J. Freymueller and Project Idylhim members, (1997). GPS measurements of present day convergence across the Nepal Himalaya, Nature (lond). 386, 61-64 1997.

33   Bilham, R., F. Blume, R. Bendick, and V. K. Gaur (1998). Geodetic constraints on the translation and deformation of India: Implications for future great Himalayan Earthquakes, Curr. Sc. 74, 213-229.

34   Bilham, R., and Gaur, V.K., (2000) Geodetics contributions to study of seismotectonics in India, Current Science 79(9), 1259-1269.

35   Bilham, R., Gaur, V.K. and Molnar, P., (2001). Himalayan seismic hazard. Science 293, 1442-1444.

36   Bilham, R., Bendick, R., and Wallace, K., (2003). Flexure of the Indian Plate and Intraplate Earthquakes, Proc. Indian Acad. Sci. (Earth Planet Sci.), 112(3) 1-14.

37   Bilham, R., and Ambraseys, (2004). Apparent Himalayan slip deficit form the summation of seismic moments for the Himalayan earthquakes, 1500-2000, Current Science, in the press.

38   Bilham, R., and Szeliga, W., (2008). Interaction Between the Himalaya and the Flexed Indian Plate-Spatial Fluctuations in Seismic Hazard in India in the Past Millennium? American Inst. Of Physics Conf. Proc., 224-231,978-0-7354-4/08/. pp 1-9.

39   Bisztricsany, E., (1958). On the problem of magnitude determination. Zeitch. f. Geophys., Bd. 24, pp .153-160.

40   Boatwright, J., (1978).Detailed spectral analysis of two small NewYork State

earthquakes. Bull. Seis. Soc.Am 68, 1177-1131.

41   Boatwright, J., (1980). A Spectral theory for circular seismic sources simple estimates of source dimension, dynamics stress drop, and radiated seismic energy. Bull. Siesm. Soc. Am. 70, 1-26.

42   Bollinger, L., Avouac, J. P., Cattin, R. and Pandey, M. R., (2004). Stress Buildup in the Himalaya, J. Geophys. Res., 109, B11405, doi: 10.1029/2003JB002911.

43   Boore, D.M., Boatwright, J., (1984). Average body-wave radiation coeffeciants. Bull. Seism. Soc. Am 74, 1615-1621.

44   Bott, M.H.P., (1959). The Meachnics of oblique faulting. Geol. Mag.96, 109-117.

45   Brookfield, M.E., (1993), The Himalayan passive margin from Precambrian to Cretaceous times: Sedimentology Geology, v. 84, p. 1-35.

46   Brune, J.N., Flectcher, J., Vernon, F., Haar, L., Hanks, T., Berger, J., (1986). Low stress-drop earthquakes in the light of new data from the Anza, California telemetered digital array. In: Das, S., Boatwright, J., Scholz, C.H. (Eds.), Earthquake Source Mechanics, Proceedings of the 5th Maurice Ewing Symposium. American Geophysical Union, Washington, DC, pp. 237-245.

47   Brune, J.N., (1970). Tectonic stress and the spectra of seismic shear waves from earthquakes. Jour. Geophys. Res. 75: 4997-5009.

48   Brune, J.N., (1971). Corrections to: Tectonic stress and the spectra of seismic shear waves from earthquakes. Jour. Geophys. Res. 76, 5002.

49   Burchfiel, B.C., Chen, Z., Hodges, K.V., Liu, Y., Royden, L.H., Deng, C., Xu, J., (1992). The south Tibet detachment system, Himalayan orogen: Extension contemporaneous with and parallel to shortening in a collisional mountain belt. Geol. Soc. Am. Sp. 269, 1-41.

50   Burg, J.P., Chen, G.M., (1984). Tectonics and structural formation of the southern Tibet, China. Nature 311, 219 – 223.

51   Burg, J.P., Brunel, M., Gapais, D., Chen, G.M., Liu, G.H., (1984a). Deformation of leucogranites of the crystalline main central sheet in southern Tibet(China). Journal of structural Geology 6 , 535-542.

52   Caldwell, W. B., Klemperer, S. L., Rai, S. S., and J. F., Lawrence, (2009). Partial melt in the upper- middle crust of the northwest Himalaya revealed by Rayleigh wave dispersion. Tectonophysics, (accepted).

53   Calvert, A. J., Klemperer, S. L., Takahashi, N., and B. R., Kerr, (2008). Three-dimensional crustal structure of the Mariana island from seismic tomography. Jour. Geophy. Res., 113, B01406, doi: 10.1029/2007JB004939.

54   Cattin, R., and Avouac, J.P., (2000). Modeling mountain building and the seismic cycle in the Himalaya of Nepal. J.Geophys. Res, 105, 13389-13407.

55   Chandra, U. (1992). Seismotectonics of Himalaya, Curr. Sci. 62, 40-71.

56   Chatterjee, S. N., and Bhattacharya, S.N., (1992). Microearthquake survey and seismicity of northwest Himalaya, in Himalayan Seismicity, G. D. Gupta (Editor), Mem. Geol. Soc. India, Vol. 23, 23–44.

57   Chaudhary, H.M. and Srivastava, H.N., and J. Subba Rao (1974). Seismotectonics investigations of the Himalayas, Himalayan Geol. 4, 481-491.

58   Chaudhary, H.M. and Srivastava, H.N., (1976). Kinnaur earthquake of January 1975 and its aftershocks. Proc. 6th World Conf. on Earthquake Engineering, New Delhi.

59   Chou, C. W. and Booker, J.R., (1979). A backus-Gilbert approach to the inversion of travel time data for three dimensional velocity structure. Geophys. J.R. Astron. Soc., 59, 325-44.

60   Chouet, B., Aki, K., and Tsujiura, M., (1978), Regional variation of the scaling law of earthquake source spectra: Bull. Seism.Soc. Am, 68, 49-79.

61   Corfield, R.I., Searle, M.P ., and Pederson. R.B., (2001). Tectonic setting, origin, and obduction history of the spontaneous Ophiolite, Ladakh Himalaya, NW India. The Journal of Geology Vol 109, pp 715-736.

62   Critelli, S., Garzanti, E., (1994). Provenence of the lower Tertiary Murree redbeds (Hazara-Kashmir syntax, Pakistan) and the initial rising of thr Himalayas . Sedimentary Geology 89, 265-284.

63   Crosson, R.S., (1976). Crustal structure modeling of earthquake data 1.Simultaneous least squares estimation of hypocenter and velocity parameters. J. Geophys. Res., 81, 3036-46.

64   Curray, J.R., Emmel, F.J., Emmel, D.G., Moore, R.W. Raitt., (1982). Structure, tectonics and geological history of the NE Indian Ocean, in The ocean Basins and Margins, edited by E.M. Narrin and F.G Sehli, 6, 399-450.

65   Das Gupta, A., Srivastava, H.N. and Basu Malik, S. (1982). Source mechanism of earthquakes in Kangra-Chamba region of Himachal Pradesh, India. Bull. Ind. Sec. Earth Tech., v.19, pp.102-116.

66   Das Gupta, A., et al., (2000). Seismotectonic Atlas of India and its environs, Geological society of India (GSI), pp 86.

67   DeCelles, P.G., Robinson, D.M., Quade, J., Ojha, T.P., Garzione, C.N., Copeland, P., Upreti, B.N., (2001). Stratigraphy, structure and tectonic evolution the Himalayan fold- thrust belt in western Nepal. Tectonics, 20,

487-509.

68   Dezes, P.J., (1999). Tectonic and Metamorphic evolution of the central Himalayan domain in southeast Zanskar (Kashmir India). PhD Thesis. University of Lausanne, Lausanne Switzerland, 160 pp.

69   DiPietro, J.A., Pogue, K.R., (2004). Tecnostratigraphic subdivisions of the Himalaya: a view from the west. Tectonics 23, TC5001, doi: 10.1029/2003TC001554.

70   Dysart, P. S., Snake, J. A., Sacks, I.S., (1988), Source parameters and scaling relations for the small earthquakes in the Matsushiro region, southwest Honshu, Japan: Bull. Seism .Soc. Am, 78, 571-589.

71   Eberhart-Phillips, D., (1986). Three dimensional velocity structure in the northern California coast ranges from inversion of local earthquake arrival times, Bull, Seismol. Soc. Am. 76, 1025-1052.

72   Eberhart-Phillips, D., (1993). Local earthquake tomography: earthquake source regions, in Seismic Tomography: Theory and Practice, edited by H. M. Iyer and K. Hirahara, Chapman and Hall, New York, 613-643.

73   England, P., and P. Molnar., (1997). The field of crustal velocity in Asia calculated from quaternary rates on slip of faults, Geophys. J. Int, 130, 551-582,

74   Feldl, N., and Bilham, R., (2006). Great Himalayan earthquakes and the Tibetian plateau. CIRES and Dept. Geol. Sci. University of Colorado Vol. 444/9. pp 165-170.

75   Fletcher, J. B., L. Haar, F. L. Vernon, J. N. Brune, T. C. Hanks, and J. Berger (1986). The effects of attenuation on the scaling of source parameters for earthquakes at Anza, California, in Earthquake Source Mechanics, S. Das, J. Boatwright, and C. H. Scholz (Editors), American Geophysical Union Monograph 37, 331-338.

76   Fletcher, J., Haar, L., Hanks, T., Baker, L., Vernon, F., Berger, J. and Brune, J., (1987). The digital array at Anza, California, Processing and initial interpretation of source parameters. J. Geophys. Res., 92: 369-382.

77   Frank, W., Grasemann, B., Guntli, P., Miller, C., (1995). Geological map of the Kishwar- Chamba-Kulu region (NW Himalayas India). Jahrbuch der Geologischen Bundesanstalt 138, 299-308.

78   Frankel, A., (1991). Mechanisms of seismic attenuation in the crust: Scattering and anelasticity in New York State, South Africa, and Southern California , J. Geophys. Res. 96, 6269-6289.

79   Gahalaut, V.K. (2008). Major and great earthquakes and seismic gaps in the Himalayan arc. Golden Jubilee Mem. Geol. Soc. of India 66, 373-393.

80   Gahalaut, V. K., and Kalpna (2001). Himalayan mid-crustal ramp, Curr. Sci., 81(12), 1641.

81   Gansser, A., (1964). Geology of the Himalaya Interscience, New York, N.Y., 287 pp.

82   Gansser, A., (1981). The geodynamic history of the Himalaya. Amer. Geophy. Unin. Washington, Geod. Ser., 3, 111-121.

83   Garcia Garcia, J.M., Romacho, M.D. and Jimenez, A., (2004). Determination of near-surface attenuation, with k parameter, to obtain the seismic moment, stress drop, source dimension and seismic energy for microearthquakes in the Granada Basin (Southern Spain). Phys. Earth. Planetary. Interiors. 141 9-26.

84   Gardner, J.K., Knopoff, L., (1974). Is the sequence of Earthquakes in Southern California with aftershocks removed, Poissonian?: Bull. Seism. Soc. Amer., v.64, pp. 1363-1367.

85   Garzanti, E., (1999). Stratigraphy and sedimentary history of the Nepal Tethys Himalaya passive margin. Journal of Asian Earth Sciences 17, 805-827.

86   Gaur, V. K., Chander, R., Sarkar, I., Khattri, K. N. and Sinhval, H., (1985). Seismicity and state of stress from investigations of local earthquakes in the Kumaun Himalaya, Tectonophysics 118, 243-251.

87   Gephart, J. W., and Forsyth, D. W., (1984). An improved method for determining the regional stress tensor using earthquake focal mechanism data: Application to the San Fernado earthquake sequence. Jour. Geophy. Res., 89, pp 9305-9320.

88   Gephart, J. W., (1990). FMSI: A FORTRAN program for inverting fault/slickensides and earthquake focal mechanism data to obtain the original stress, Comput. Geosci. 16, pp. 953-989.

89   Gitis, V. G., Osher, B. V., Pirogov, S. A., Ponomarev, A. V., Sobolev, G. A. and Jurkov, E. F., (1994), A System for Analysis of Geological Catastrophe Precursors, Journal of Earthquake Prediction Research, 3, 540.

90   Gitis, V., Yurkov, E., Arora, B. R., Chabak, S., Kumar, N., and P. Baidya, (2008). Analysis of seismicity in north India. Russ. Jour. Earth Sci., 10, ES5002, 1-11.

91   Gupta, V. J., and Virdi, N. S., (1975). Geological aspects of the Kinnaur Earthquake Himachal Pradesh. J. Geol. Soc. Ind., 16(4), 512-514.

92   Gutenberg, B., Richter, C. F., (1944). Frequency of earthquakes in California. Bull. Seismol. Soc. Amer., 34, 185-188.

93   http://www.gsi.gov.in/zonation.htm

94   Hanks, T.C. (1977). Earthquake stress drops, ambient tectonic stresses and stresses that drive plates, Pure Appl.Geophys. 115, 441-458.

95   Hanks, T.C. and Wyss, M., (1972). The use of body-wave spectra in the determination of seismic-source parameters. Bull. Seismol. Soc. Am., 62(2), 561-589.

96   Hanks, T.C., and Kanamori, H., (1979). A moment magnitude scale, J. Geophys. Res. 84, 2348-2349

97   Hanks, T.C., (1981). The corner frequency shift, earthquake source models, and Q. Bull. Seismol. Soc. Am., 71(3): 597-612.

98   Haskell, N.R.,(1966). Total energy and energy spectral density of elastic radiation from prpagaing faults, Part II. A statistical source model. Bull. Seismol. Soc. Am., 56: 125-140.

99   Haskell, N.A., (1969). Elastic Displacement int the near field of a propagating fault. Bull. Seismol. Soc. Aner., 59, 865-908.

100   Haslinger, F., Kissling, E., Ansorge, J., Hatzfeld, D., Papadimitriou, E., Karakostas, V., Makropoulos, K., Kahle, H.G. and Peter, Y., (1999). 3-D crustal structure from local earthquake tomography around the Gulf of Arta (Ionian region, NW Greece), Tectonophysics 304, 201-218.

101   Hauck, M.L., Nelson, K.D., Brown, L.D., Zhao, W.J., Ross, A.R., (1998). Crustal Structure oh the Himalayan orogen at similar to 90 degrees east longitude from Project INDEPTH deep reflection profiles. Tectonics 17, 481-500.

102   Havskov, J., and Alguacil, G., (2004). Instrumentation in Earthquake Seismology. Modern App. Geophy., Springer Publication, 349 pp.

103   Havskov,J., and Ottemoller,L., (2008). SEISAN:The Earthquake Analysis Software version 8.2.1. pp 1-267.

104   Hawley, B.W., Zandt, G. and Smith, R.B., (1981). Simultaneous inversion for hypocenters and lateral velocity variations; an iterative solution with a layered model. J. Geophys. Res., 86, 7073-76.

105   Heim, A., Gansser, A., (1939). Central Himalaya geological observations of Swiss, pp 1-246.

106   Herrmann, R. B., Kijko, A., (1983). Modeling Some empirical vertical component Lg relation. Bull. Seismol. Soc. Am. 73, 157-171.

107   Honneger, K., Dietrich, V., Frank, W.,. Gansser, A., Thoni, M., Trommsdorff,

V., (1982). Magnetism and metamorphism in the Ladakh Himalayas(the Indus-Tsangpo suture Zone)Earth and Planetery Science Letters 60, 253-292.

108   Hough, S.E. (1996). Observational constraints on earthquake source scaling: understanding the limits in resolution, Tectonophysics 261, 83-85.

109   Hubbard, M.S., Harrison, T.M., (1989). $^{40}Ar/^{39}Ar$ age constraints on deformation and metamorphism in the MCT Zone and the Tibetian Slab , eastrern Nepal Himalaya. Tectonics 8, 865-880.

110   Hyndman, R. D., and Shearer, P. M., (1989). Water in the lower Continental crust: modeling magnetotelluric and seismic reflection results. Geophys. J. Int. 98, 343-365.

111   Iyenger R.N., Sharma D.,(1998) . Earthquake history of India in medieval times, Rep. Central Build. Res. Inst., 124pp, Roorkee.

112   Jackson, D. D. and matsu'ura, M., (1985). A Bayesian approach to nonlinear inversion. J. Geophys. Res., 90, 581-91.

113   Jodicke, H. (1992). Water and graphite in earth's crust- an approach to interpretation of conductive models. Surv. Geophys. 13, 381-407.

114   Johnson, M.R.W., (1994). Culmination and domal uplift in the Himalaya . Tectonophysics 239, 139-147

115   Jordan, T. A., & Watts, A.B. (2005) Gravity anamolies, flexure and the elastic thickness structure of the India-Eurasia collisional system. Earth and Planetary Science Letters, 236, 732-750.

116   Kaila, K.L. and Sarkar, D., (1978). Atlas of Isoseismal maps of major earthquakes in India. Geophys. Res. Bull., Vol. 16(4), pp 233-267.

117   Kamble, V. P., Verma, R. K. and Chaudhury, H. M. (1974). Crustal studies in the Himalayan region: Part-I Dalhousie-Mandi section. Ind. Jour. Met. Geophys. 25, 229-236.

118   Kanamori, H., Anderson, D.L., (1975). Theoretical basis for some empirical relations in seismology. Bull. Seismol. Soc. Am. 65, 1073-1095.

119   Kanamori, H., (1977). The Energy Release in Great Earthquakes. Jour. Geophys. Res., Vol. 82, pp. 1981 – 1987.

120   Kao, H., and J., Angelier, (2001). Stress Tensor Inversion for the Chi-Chi earthquake Sequence and its implications on Regional Collision. Bull. Seismol. Soc. Amer. 91(5), pp. 1028-1040.

121   Kayal, J. R. (2001). Microearthquake activity in some parts of the Himalaya and the tectonic model, Tectonophysics. 339, 331-351.

239

122 Kayal, J. R. (2003). Seismotectonic structures of the Western and Eastern Himalayas: Constraint from microearthquake data, Mem. Geol. Soc. India. 53, 279-311.

123 Kennett, B. L. N., Engdahl, E. R. and Buland, R. (1995). Constraints on seismic velocities in the earth from travel times, Geophys. J. Int. 122, 108-124.

124 Khattri, K., (1973). Earthquake focal mechanism studies – A review. Earth Sci. Rev., 9, pp. 19-63.

125 Khattri, K.N., Rai, K., Jain, A. K., Singhvi, H., Gaur, V. K., and R. S., Mittal, (1978). The Kinnaur earthquake Himachal Pradesh India of 19 January 1975. Tectonophysics, 49, 1-21.

126 Khattri, K. N., and Tyagi, A. K., (1983). Seismicity patterns in the Himalayan plate boundary and identification of the areas of high seismic potential. Tectonophysics, 96, 281-297

127 Khattri, K. N., (1987), Great earthquakes, seismicity gaps and potential for earthquake disaster along the Himalaya Plate boundary. Tectonophysics, Vol. 138, pp. 79-92.

128 Khattri, K. N., R. Chander, V. K. Gaur, I Sarkar, and S. Kumar (1989). New seismological results on the tectonics of the Garhwal Himalaya. Proc. Indian Acad. Sci. (Earth Planet. Sci.). 98, 91-109.

129 Kiratzi, A.A., (1999). Stress Tensor Inversion in western Greece using earthquake focal mechanisms from the Kozani-Greneva 1995 seismic sequence. Annali Di Geofisca, Vol.42, No.4, pp. 725-734.

130 Kissling, E. (1988). Geotomography with local earthquake data. Rev. Geophys. 26, 659-698.

131 Kissling, E., Ellsworth, W. L., Eberhart-Phillips, D., and U. Kradolfer (1994). Initial reference models in local earthquake tomography. J. Geophys. Res., 99, 19'635-19'646.

132 Kissling, E., (1995). Program VELEST USER'S GUIDE – Short Introduction (second draft version), Institute of Geophysics and Swiss Seismological Service, ETH-Hoenggerberg CH-8093 Zurich, Switzerland, 1-26.

133 Kisslinger, C., Bowman, J. R., and Koch, K., (1981). Procedures for computing focal mechanisms from local (SV/P) data. Bull. Seismo. Soc. Am., 71, pp. 1719-1729.

134 Kumar, M. R., Rao, N. P., and Bhatia, S. C., (1998). Analysis of Harvard centroid moment tensor solutions and computation of strain rates in the Himalaya and Tibetan plateau regions. Curr. Sci., 75(3), pp. 311-316.

135 Kumar, S., and Mahajan, A.K., (2001). Seismotectonics of the Kangra region, Northwest Himalaya. Tectonophysics, 331, 359-371.

136 Kumar, N., Parvez, I. A., and Virk, H. S., (2005). Estimation of coda wave attenuation for NW Himalayan region using local earthquakes. Phys. Earth Plant. Inter. 151, 243-258.

137 Kumar, N., Sharma, J., Arora, B.R. and Mukhopadhyay, S. (2009). Seismotectonic model of the Kangra-Chamba sector of NW Himalaya: Constraints from joint hypocenter determination and focal mechanism. Bull. Seismo. Soc. Am. 99(1), 95-109.

138 Kumar, S., Wesnousky, S. G., Rockwell, T. K., Ragona, D., Thakur, V. C., and G. G., Seitz, (2001). Earthquake recurrence and rupture dynamics of Himalayan frontal thrust, India. Science, 294, 2328-2331.

139 Kumar, N., Sharma, J., Arora, B. R., and S., Mukhopadhyay, (2006). Imaging deep structures through the inversion of earthquake data: An example from Kangra-Chamba region of Himachal Himalaya. DCS-DST News letter, 7-10.

140 Kumar S., Gupta, S.K. and Jalote, P.M., (1981). A macroseismic study of 14th June, (1978) Dharamsala earthquake, Himachal Pradesh. Rec. Geol. Surv. Ind. Vol. 112(VIII).

141 Kumar, N., Arora, B.R., Mukhopadhyay, S., and Yadav, D.K., (2010). Seismogenesis of Clustered Seismicity Beneath the Kangra-Chamba Sector of Northwestern Himalaya: Constraints from 3D Local Earthquake Tomography.

142 Kumar, S. and Mahajan, A.K., (1990). Study of intensities of 26th April, 1986 Dharamsala earthquake (Himachal Pradesh) and associated tectonics. Jour. Geol. Surv. Ind, Vol. 35, pp.213-219.

143 Lee, W. H. K., and Lahr, J. C., (1975). HYPO71PC: A computer program for determing the Hypocenter, Magnitude and First-motion pattern of local earthquakes, USGS Open File Report 75-311, 1-116.

144 Lee, J.M. and Crosson, R.S., (1989). Tomographic inversion for three-dimensional velocity structure at Mount St. Helens using earthquake data. J. Geophys. Res., 94, 5716-28.

145 LeForte, P. (1975). Himalayas - the collided range - present knowledge of the continent arc. Am. Jour. Sci, 275, 7-44.

146 Le Pichon X. (1968). Sea-florr spreading and continental drift. J. Geophys. Res 73: 3661-3697.

147 Leveque, J., Rivera, L., Wittlinger, G., (1993). On the use of checker board test to assess the resolution of tomographic inversion. Geophys. J. Int. 115, 313– 318

148 Lyubushin, A.A., Arora, B.R., Kumar, N., Chabak, S.K., Baidya, P.R., submitted (2010). Investigating the seismic regime in the western Himalaya, J. Seismol.

149 Lyon-Caen, H., Molnar, P., (1983). Constraints on the strucutre of the Himalaya from an analysis of gravity anomalies and a flexural model of the lithosphere. J. Geophy. Res., 88, pp 8171-8191.

150 Lyon-Caen, H., and P. Molnar, (1985). Gravity anomalies, flexure of the Indian plate, and the structure, support and Evolution of the Himalaya and Ganga Basin. Tectonics, 4(6), 513-538.

151 Madariaga, R., (1976). Dynamics of an expanding circular fault, Bull. Seismol. Soc. Am. 66 pp. 639–666.

152 Madariaga, R. (1978), A relation between seismic moment and stress drop of complex earthquakes, in Proceedings of the fault mechanics conference at Stanford, edited by J. F. Evernden, U.S.G.S., Men-lo-Park.

153 Mahajan, A.K. and Virdi, N.S., (2005). Macroseismic study of shallow earthquakes in the Himachal and Garhwal Himalaya, Northwest Himalaya, India. Geol. Soc. Ind. Spl. Pub. 85, pp. 205-215.

154 Mahajan, A.K., Kumar, N. and Arora, B.R., (2006). Quick look isoseismal map of 8 October 2005 Kashmir earthquake. Current Science, Vol. 91, No. 3.

155 Mc Kenzie, D.P., (1969). The relation between fault plane solutions for earthquakes and the directions of the principal stresses. Bull. Seimol. Am. 59, pp. 591-601.

156 Mc Kenzie, D.P. & Scalter, J.C (1971). The evolution of the Indian ocean since the Late Cetaceous. Geophys. J.r. astron. Soc. 24,437-528.

157 Meigs, A. J., Burbank, D.W., Beck, R.A., (1995). Middle-late Miocene (>10 Ma) formation of the Main Boundary Thrust in the western Himalaya. Geology 23, 423-426.

158 Michael, A. J., (1984). Use of focal mechanisms to determine stress: A control study. J. Geophys. Res., 92, pp. 357-368.

159 Michelini, A., M. Zivcic, and P. Suhadolc (1998). Simultaneous inversion for velocity and hypocenters in Slovenia, J. Seismology 2, 257-265.

160 Middlemiss, C.S., (1910). The Kangra earthquake of 4th April, 1905. Mem. Geol. Surv. India, Vol. 37, pp. 1-409.

161 Miller, C., Thoni, M., Frank, W., Grasemann, B., Klotzli, U., Guntli, P., Draganitis, E., (2001). The early Paleozoic magmatic event in the northwest Himalaya. India: Source, Tectonic setting and age of emplacement. Geological magazine 138, 237-251.

162 Mishra, D.C, and Rajshekhar R.P., (2006) Crustal structure at the epicentral zone of 2005 Kashmir (Muzzafarabad) earthquake ans seismotetonic significance of lithospheric flexure. Curr Sci 90:1406-1412.

163 Mitchell, B., (1981). Regional variation and frequency dependence of Q_β in the crust of the United States. Bull. Seismol. Soc. Am., 71: 1531-1538.

164 Molnar, P., Fitch, T. J., and F. T., Wu, (1973). Fault plane solutions of shallow earthquakes and contemporary tectonics in Asia. Earth Planet. Sci. Let., 19, pp. 101-112

165 Molnar, P., Tapponnier, P., (1978). Active tectonics of Tibet. Journal of Geophysical Research 83, 5361–5375.

166 Molnar, P., and Chen, W. P., (1983). Focal Depths and fault plane solutions of earthquakes under the Tibetan Plateau. J. Geophys. Res. 88, 1180-1196.

167 Molnar, P., W.P Chen, T.J. Fitch, P. Tapponier, W. E. K. Warsi, and F.T. Wu, (1977). Structure and tectonics of the Himalaya: A brief summary of the relevant geophysical observations, collogue internationaux du CNRS, No. 268, Himalaya: Sciences de la Terre, Editions du Center National de la Recharche Scientifique, Paris, 269-294.

168 Molnar, P. and Deng, Q., (1984). Faulting associated with large earthquakes and the average rate of deformation in central and eastern Asia. J. Geophys. Res., 89 (7), 6203-6227.

169 Molnar, P., (1987). The distribution of intensity associated with the 1905 Kangra earthquake and bounds on the extent of rupture. J. Geol. Soc. India, 29, 221.

170 Molnar, P.and H. Lyon-Caen, (1988). Some simple physical aspects of the support, structure, and evolution of the mountain belts, in Processes in Continental Lithospheric Deformation, Geol. Soc. Am Spec. Pap. 218, S.P. Clark,Jr. (ed.), in Press.

171 Molnar, P. and Tapponnier, P., (1975). Tectonics of Asia: consequences and implications of a continental collision. Science, 189: 419-246.

172 Molnar, P. (1990). A review of the seismicity and the rates of active underthrusting and deformation at the Himalaya. J. Himal. Geol., 1(2), 131-154.

173 Moser, T.J., (1991). Shortest path calculation of seismic rays. Geophysics, 56, 59-67.

174 Mukhopadhyay, S., and J. R. Kayal (2003). Seismic Tomography structure of the 1999 Chamoli Earthquake source area in the Garhwal Himalaya, Bull. Seism. Soc. Am. 93(4), 1854-1861.

175 Mukhopadhyay, S., Mishra, O. P., Zhao, D., and J. R., Kayal, (2006). 3-D seismic structure of the source area of the 1993 Latur India, earthquake and its implications for rupture nucleations. Tectonophysics, 415, 1-16.

176 Mukhopadhyay, S., Tyagi, C., (2008). Variation of intrinsic and scattering attenuation with depth in NW Himalayas. Geophys. J. Int. 172, 1055-1065.

177 Mukhopadhyay, S., Sharma, J., Del-Pezzo, E., Kumar, N., (2010). Study of attenuation mechanism for Garwhal-Kumaun Himalayas from analysis of coda of local earthquakes. Phys. Earth. Planetary. Interiors. 180 7-15.

178 Nakanishi, I., (1985). Three-dimensional structure beneath the Hokkaido-Tohoku region as derived from a tomographic inversion of P-arrival times. J. Phys. Earth, 33,241-56.

179 Narula, P.L. and Shome, S.K., (1992). Macroseismic investigations of Uttarkashi earthquake of 20th Oct. 1991. Geol. Surv. India, Sp. Pub. No. 30.

180 Narula P.L., Shome, S.K., Kumar, S. and Pande, P., (1995). Damage pattern and delineation of isoseismals of Uttarkashi earthquake of 29th October, 1991. Mem. Geol. Soc. India, Vol. 30, pp. 1-17.

181 Narula P.L., Shankar, Ravi, and Chopra, S., (2000). Rupture mechanism of Chamoli earthquake on 29th March 1999 and its implications for seismotectonics of Garhwal Himalaya. J. Geol. Soc. Ind., Vol. 55(5), pp.493-503

182 Ni, J., and M. Barazangi, (1984). Seismotectonics of the Himalayan collision zone: Geometry of the underthrusting Indian plate beneath the Himalaya. Jour. Geophys. Res., 89, 1147-1163.

183 Ni, F. J., and A. Ibenbrahim (1991). Three-Dimensional Velocity Structure and Hypocenters of Earthquakes Beneath the Hazara Arc, Pakistan: Geometry of the Underthrusting Indian Plate, J. Geophys. Res. 96(B12), 19865-19877.

184 Nicole, B., S. Christian, P. Anne, V. Jean, F. Julien, T. Francois, and C. Marco (2007). Local tomography and focal mechanism in south-western Alps: Comparison of the methods and tectonic implications, Tectonophysics 432, 1-19.

185 Nicholson, C., and D. W. Simpson (1985). Changes in Vp/Vs with depth: implications for appropriate velocity models, improved earthquake locations, and material properties of the upper crust. Bull. Seism. Soc. Am. 75(4), 1105-1123.

186 Ojeda, A., and J. Havskov (2001). Crustal structure and local seismicity in Colombia. J. Seismology 5, 575-593.

187 Pandey, M. R., R. P. Tandukar, J.-P. Avouac, J. Lave, and J. P. Massot (1995).

Interseismic strain accumulation n the Himalayan crustal ramp Inepal), Geophys. Res. Lett., 22, 741-754.

188 Pandey,M.R., Tandukar , R.P., Avouac , J-P., Vergne, J., Heritier , T., (1999). Seismotectonics of the Nepal Himalayas from a local seismic network. Journal of Asian Earth Sciences 17, 703-712.

189 Pecher, A., (1991). The contact between the higher Himalaya crystallines and the tibetian sedimentary series: Miocene large scale dextral shearing. Tectonics 10, 587-598.

190 Pedersen, R.B., Searle, M.P., & Corfield, R.I., (2001). U-Pb zircon ages from the spontag Ophiolite. Journal of the Geological Society. London, 158, 513-520.

191 Pei, S., Zhao, J., Sun, Y., Xu, Z., Wang, S., Liu, H., Rowe, C. A., Toksöz, M. N., and X., Gao, (2007). Upper mantle seismic velocities and anisotropy in China determined through Pn and Sn tomography. Jour. Geophys. Res., 112, B05312, doi: 10.1029/2006JB004409.

192 Pisarenko, V. (1989), About frequency-magnitude relationship of earthquakes, in Discret properties of geological environment, p. 47, Nauka, Moscow.

193 Powers, P.M., Lillie, R.J., and Yeats, R.S., (1998). Structure and shortening of the Kangra and Dehra Dun reentrants, Sub-Himalaya, India. Geological Society of America Bulletin 1998; 110;1010-1027 doi: 10.1130/0016-7606(1998).

194 Raffaele, R., H. Langer, S. Gresta, and F. Moia (2006). Tomographic inversion of local earthquake data from Gioia Tauro basin (south-western Calabria, Italy), Geophys. J. Int., 165, 167-179.

195 Rai, S.S., K.Priestley, K. Suryaprakasam, D. Srinagesh, V. K. Gaur, and Z.Du (2003), Crustal shear velocity structure of the south Indian shield, J.Geophys. Res., 108(B2), 2088, doi: 10.1029/2002JB001776.

196 Rai, S. S., K. Priestley, V. K. Gaur, S. Mitra, M. P. Singh, and M. Searle (2006). Configuration of the Indian Moho beneath the NW Himalaya and Ladakh, Geophys. Res. Lett. 33, L15308, doi 10.1029/ 2006GL026076.

197 Rajendran, C.P. and K. Rajendran (2005). The status of central seismic gap: a perspective based on the spatial and temporal aspects of the large Himalayan earthquakes. Tectonophysics, 395, 19-39.

198 Rajesh. R.S, and Mishra, (2004). D.C., Lithospheric thickness and mechanical strength of the Indian shield. Earthand Planetry Science letters 225, 319-328.

200 Rao, P. N., P. Kumar, Kalpna, T. Tsukuda and D.S. Ramesh (2006). The devastating Muzaffarabad earthquake of 8 October 2005: New insights into Himalayan seismicity and tectonics, Gondwana Research, 9, 365-378.

201 Rastogi, B.K., (1974). Earthquake mechanisms and plate tectonics in Himalayan region, Tectonophysics 19, 47-56.

202 Rautela, P., and V. C. Thakur (1992). Structural analysis of the Punjal Thrust Zone, Himachal Himalaya, India. J. Him. Geol. 3(2): 195-207.

203 Rautian, T.G. and Khalturin, V.I., (1978). The use of the coda for the determination of the earthquake source spectrum. Bull. Seismol. Soc. Am., 68(4), 923-948.

204 Reddy, C. D., and B. R. Arora (1993). Qunatitative interpretation of the geomagnetic induction response across the thrust zones of the Himalaya along the Ganga-Yamuna valley, J. Geomagn. Geoelectr. 45, 775-785.

205 Richter, C.F., (1935). An instrumental earthquake magnitude scale. Bull. Seismol. Soc. Am. 25, 1-32

206 Richter, C.F., (1958). Elementary seismology, W. H. Freeman and Co., San Fransisco, p.768.

207 Rivera, L. and A., Cisternas, (1990). Stress tensor and fault plane solutions for a population of earthquakes. Bull. Seismo. Soc. Amer., 80, pp. 600-614.

208 Sarkar, d., Kumar, M., Saul, J., Kind, R., Raju, P., Chadha, R., & Shukla, A., (2003). A Reciever function perspective of the Dharwar craton (India) crustal structure , Geophys, J. Int 154,205-211.

209 Sato, T. and Hirasawa, T., (1973). Body wave spectra from propagating shear cracks. J. Phys. Earth. 21: 415-431.

210 Sbar, M.L., Sykes, L.R., (1973). Contemporary compressive stress and seismicity in eastern North America, An example of intraplate tectonics. Geol. Soc. Am. Bull., 84: 1861-1882.

211 SCHOLZ, C. H., *The Mechanics of Earthquakes and Faulting* (Cambridge University Press, Cambridge (1990) 439 pp.

212 Schulte-Pelkun, V., G. Monssalve, A. Sheehan, M. R. Pandey, S. Sapkota, R. Bilham, and F. Wu (2005). Imaging the Indian subcontinent beneath Himalaya, Nature 435, 1222-1225, doi:10,1038/nature03678.

213 Scarft, L., H. Langer, and S. Gresta (2003). High precision relative locations of two microearthquakes clusters in Southeastern Sicily, Italy, Bull. Seism. Soc. Am. 93, 1479-1497.

214 Searle, M.P., (1986) . Structural evolution and sequence of thrusting in the high Himalayan Tibetian Tethyan and Indus suture zones of Zanskar and Ladakh , Western Himalayan. Journal of Structural geology 8 , 923-936.

246

215 Seeber, L., and J.G. Armbruster, (1981). Great detachment earthquakes along the Himalayan arc and the long-term forecasting, in earthquake prediction-An international review, edited by D.E. Simpson, and Richards, P.G., pp. 259-277, Maurice Ewing Series 4, The American Geophysical Union.

216 Seeber, L., J. Armbruster, and R. Quittmeyer (1981). Seismicity and continental subduction in the Himalayan arc, in Zagros, Hindu Kush, Himalaya, Geodynamic Evolution, Geodyn. Ser. 3, In: Eds. H. K. Gupta and F.M. Delany, 215-242, AGU, Washington, D. C.

217 Sibson, R.H., (1986). Rupture interaction with fault jogs, in Earthquake Source mechanics, Geophys. Monogr. Ser., vol. 37, edited by S.das, J. Boatwright, and C.H. Scholz, pp. 157-167, AGU, Washington, D.C.

218 Singh S.K., Pimprikar, S.D., Bansal, B.K., Pacheco,J.F., Dattatrayam, R.S., and Suresh , G., (2007). An Analysis of the M_w 4.7 Jabalpur, India, Earthquake of 16 October 2000: Toward Ground-Motion Estimation in the region from Future Events. Bull. Seismol. Soc. Am vol. 97, No.5. pp 1475-1485.

219 Singh, K., (1994). Structural framework of the Chamba Thrust Sheet, Himachal Himalaya, India, Geoscience Journal XV, 85-92.

220 Singh, S. K., Dattatrayam, R. S., Shapiro, N. M., Mandal, P., Pacheco, J. F., and R. K., Midha, (1999). Crustal and upper mantle structure of peninsular India and source parameters of the 21 May 1997, Jabalpur earthquake (Mw = 5.8): Results from a new regional broadband network. Bull. Seismo, Soc., 89(6), 1631-1641.

221 Singh, K., (2010). Tectonic evolution of kishtwar window with respect to the main central thrust, northwest Himalaya, India . J. Asian Earth Sci. 39(2010) 125-135.

222 Sinha. A.K., (1989). Geology of the Higher Central Himalaya. John Wiley & Sons. pp 219.

223 Smirnov, V. (1995). Earthquake recurrence and seismic regime parameters,. Volcanol. Seism., 3, 59

224 Snoke, J. A., Munsey, J., W., Teague, A. G., and G. A., Bollinger, (1984). A program for focal mechanism determination by combined use of polarity and SV-P amplitude ratio data. Earthqauke notes, 55, p15.

225 Sorkhabi, R.B., Stump, E., Foland, K,. Jain, A.K., (1999). Tectonic and cooling history of the Garhwal higher Himalaya (Bhagirathi valley): constraints from thermochronological data. In Jain , A.K Manickavasagam, R.M (Eds) Geodynamics of the NW Himalaya. Gondwana Research group Memoir . Vol 6 ,pp 217-235.

226 Spencer, C. and Gubbins, D., (1980). Travel time inversion for simultaneous earthquake location and velocity structure determination in lateral varying

media. Geophys. J.R. Astron. Soc., 63, 95-116.

227 Srivastava, H.N., R.K. Dube and H. Raj (1987). Space and time variation in the seismicity patterns preceding two earthquakes in the Himachal Pradesh, India, Tectonophysics, 138, 69-77.

228 Srivastava, P. and G. Mitra, G. (1994). Thrust geometries and deep structure of the outer and lesser Himalaya, Kumaon and Garhwal (India): implications for evolution of the Himalayan fold-and-thrust-belt. Tectonics 13, 89-109.

229 Stanley, W. D., W. D. Mooney, and G. S. Fuis (1990). Deep crustal structure of the Cascade range and surrounding regions from seismic refraction and magnetotelluric data, J. Geophys. Res. 95, 19419-19438.

230 Steck, A., (2003). Geology of the NW Indian Himalaya. Eclogae geol. Helv. 96, 147-196.

231 Steck, A., Spring, L., Vannay, J.C., Masson, H., Bucher, H., Stutz, E., Marchant, R., & Tieche , J.-C. (1993): Geological transect across the North-Western Himalaya Eastern Ladakh and Lahul (A Model for the continental collision of India and Asia). Eclogae geol. Helv. 86, 219-263.

232 Steck, A., Epard, J.L., Vannay, J.C., Hunziker, J., Girard, M., Morard, A., & Robyr, M., (1998): Geological transect across the Tso Morari and Spiti areas: The nappe structures of the Tethys Himalaya. Eclogae geol. Helv. 91, 103-121.

233 Stephenson, B.J., Searle, M.P., Waters, D.J., Rex, D.C., (2001). Structure of the main central thrust zone and extrusion of the high Himalayan deep crustal wedge, Kishtwar-Zanskar Himayala. Journal of the geological soc. 158 , 637-652.

234 Stork, A. L., and Ito, H., (2004). Source parameter scalling for small earthquakes at the Western Nagano 800-m-Deep Borehole, Central Japan. Bull. Seismol. Soc. Am., 94(5), 1781–1794.

235 Sukhija, B. S., Rao, M. N., Reddy, D. V., Nagabhushanam, P., Hussain, S., Chadha, R. K., and Gupta, H. K. (1999). Paleoliquefaction evidence and periodicity of large prehistoric earthquakes in Shillong Plateau, India, Earth Planet. Sci. Lett., 167, 269-282.

236 Tandon, A.N. (1992). Seismology in India-An Overview Upto 1970.

237 Tondon, A. N., and H. N., Srivastava, (1975). Focal mechanisms of some recent Himalayan earthquakes and regional plate tectonics. Bull. Seismo. Soc. Amer., 64(4), pp. 963-969

238 Telford, W.M., Geldart, L.P., Sheriff, R.E., and Keys, D.A. (1976). Applied Geophysics, Cambridge University Press. pp 843.

239 Thakur, V. C. (1992). Geology of Western Himalaya, pp363, Pregamon Press, Oxford.

240 Thakur, V.C., V. Sriram, and A.K. Mundepi (1997). Seismotectonics of the great 1905 Kangra earthquake meizoseismal region in Kangra-Chamba, NW Himalaya, Tectonophysics 326, no. 3-4, 289-298.

241 Thakur, V. C. (1998). Structure of the Chamba nappe and position of the Main Central Thrust in Kashmir Himalaya, J. Asian Earth Sci. 16, 269-282.

242 Thakur, V.C., Sriram, V. and Mundepi, A.K., (2000), Seismotectonics of the great 1905 Kangra earthquake meizoseismal region in Kangra-Chamba, NW Himalaya. Tectonophysics, 326, 289-298.

243 Thakur, V.C., (2004). Active tectonics of Himalayan Frontal Thrust ans Seismic hazard to Ganga plain, Curr. Sci., 86 (11), 1554-1560.

244 Thurber, C. H. and Ellsworth, W. L., (1980). Rapid solution of ray tracing problems in heterogenous media. Bull. Seismol. Soc. Am., 70, 1137-48.

245 Thurber, C. H., (1983). Earthquake locations and three-dimensional structure in the Cyote Lake area, central California. Jour. Geophy. Res., 88, 8226-8236.

246 Thurber, C. H., (1986). Analysis methods for kine, atic data from local earthquake. Rev. Geophys., 24, 793-805.

247 Thurber, C. H., (1993). Local earthquake tomography velocities and Vp/Vs – theory. In: H.M Iyer and K. Hirahara, Editors, Seismic tomography, Champan & Hall, London (1993), 563 – 580.

248 Tiwari, V.M., Rajasekhar, R.P., and Mishra, D.C (2009). Gravity anomaly , lithospheric structure and seismicity of western Himalayan Syntaxis. Jour.Seismol 13 (pp 363-370).

249 Toomey, D., and G. Foulger (1989), Tomographic inversion of local earthquake data from the Hengill-Grensdalur central volcano complex, Ice-land, J. Geophys . Res., 94, 17,497-17,510.

250 Valdiya, K.S. (1976). Himalayan transverse faults and folds and their parallelism with subsurface structures of north India plains. Tectonophysics, 32, 353-386.

251 Valdiya, K.S, (1980). Geology of the Kumaon Lesser Himalaya. Wadia institute of Himalaya, Dehradun, India, 291 pp

Valdiya, K.S. (1984). Lithosphere: Structure, Dynamics and Evolution. Elsevier Sciences Publishers B.V., Amsterdam. Tectonophysics, 105, 229-248

253 Vidale, J.E., (1990). Finite-difference calculation of travel times in three

dimensions. Geophys, 55, 521- 26.

254   Wadati, K., (1933). On the travel time of earthquake waves, 2nd Geophysical Magzine pp. 101-113.

255   Wagner, L., Beck, S. L., and G., Zandt, (2005). Upper mantle structure in the south central Chilean subduction zone (30 to 36S). Jour. Geophys. Res., *110*, B01308, doi: 10.1029/2004JB003238.

256   Wagner, L., Beck, S. L., Zandt, G., and M. Ducea, (2006). Depleted lithosphere, cold, trapped asthenosphere, and frozen melt puddles above the flat slab in central Chile and Argentina. Earth Planet. Sci. Lett., 245, 289-301.

257   Walck, M.C., and Clayton, R.W., (1987) P wave velocity variations in the Coso Region California, derived from local earthquake travel times . J. Geophys. Res 92, 393-405.

258   Walker, J.D., Martin, M.W., Bowring, S.A., Searle, M.P., Waters, D.J., Hodges, K.V., (1999). Metamorphism, melting, and extension: age constraints from the high Himalayan slab of Southeast Zanskar and Northwest Lahaul. Journal of geology. 107, 473-495.

259   Windley, B.F. (1995). The evolving continents (3rd edn). John Wiley and Sons, Chichester.

260   www.asc-india.org.

261   Yadav, D.K., Kumar, N. and Paul, A., (2009). Recent Seismicity and Stress pattern in NW Himalaya. Himalayan Geology, Vol. 30 (2), pp. 139-145.

262   Yalcynkaya, E., and Alptekin, O., (2003). Relationships among source parameters of aftershocks of the October 1, 1995 Dinar (Turkey) earthquake. Journal of the Balkan Geophysical Society, Vol. 6, No. 2, pp. 53-65.

263   Yeh, H −Y., Barrier, E.., Lin, C. H., and J., Angelier, (1991). Stress tensor analysis in the Taiwan area from focal mechanisms of earthquakes. Tectonophysics, 200, pp. 267-280.

264   Yin, A., (2006). Cenozoic tectonic evolution of the Himalayan orogeny as constrained by along-strike variation of structural geometry, exhumation history, and foreland sedimentation. Earth Sci. Rev., 76, 1-131.

265   Yeats, R.S., and V.C. Thakur (1998), Reassessment of earthquake hazard based on a fault-bend fold model of the Himalayan plate-boundary fault, Curr. 74(3), 220

266   Zhao, D., Hasegawa, A., Horiuchi, S., (1992). Tomographic imaging of P and S wave velocity structure beneath northeastern Japan. J. Geophys. Res. 97, 19909–19928.

267 Zoback, M. L., 1992. First- and second-order patterns of stress in the lithosphere: The World Stress Map project. J. Geophys. Res., 97, 11, 703-11, 728.

268 Zoback, M. L., and M. D., Zoback, (1980). Faulting pattern in north-central Nevada and strength of the crust. Jour. Geophy. Res., 85, pp. 275-284.